Radiation Damage in Silicon Particle Detectors

– microscopic defects and macroscopic properties –

Dissertation
zur Erlangung des Doktorgrades
des Fachbereichs Physik
der Universität Hamburg

vorgelegt von

Michael Moll

aus Ratzeburg

Hamburg

1999

Abstract

Silicon microstrip and pixel detectors are the key devices for the measurement of particle trajectories in elementary particle collision experiments. In present-day and future high luminosity experiments (e.g. ATLAS, CMS, LHCb and HERA-B) they have to operate in extremely intense hadronic radiation fields where radiation damage of the detector bulk material leads to severe deterioration of the detector properties. It is even foreseeable that some of the devices produced from standard detector grade silicon and exposed to the highest irradiation levels will not survive the envisaged operational period of the experiments. Hence, the improvement of the radiation tolerance of the detector bulk material is of prime importance and was the main goal of this thesis.

The radiation induced changes in the effective doping concentration and the leakage current have been systematically investigated and parameterized as function of particle fluence, annealing temperature and annealing time. Furthermore, as a possibility for defect engineering, the dependence on the oxygen content and the resistivity of the bulk material was studied. The oxygen concentration of the investigated materials reached from below $2 \times 10^{14}\,\mathrm{cm}^{-3}$ to $9 \times 10^{17}\,\mathrm{cm}^{-3}$ and the resistivity of the n-type silicon from $110\,\Omega\mathrm{cm}$ to about $25\,\mathrm{k}\Omega\mathrm{cm}$.

It has been found that a high oxygen concentration leads to an improved radiation hardness of the bulk material with respect to the changes in the effective doping concentration for neutron and especially charged hadron irradiation. While for the neutron damage the so-called *donor removal* is suppressed by the oxygen the main effect after charged hadron irradiation is a reduced introduction of negative space charge (so-called *stable damage*).

The current related damage rate α is not influenced by the oxygen concentration or the resistivity of the material. Furthermore, the value of α in a well defined annealing state was found to be independent of the fluence in a range from $10^{11}\,\mathrm{cm}^{-2}$ to $10^{14}\,\mathrm{cm}^{-2}$. Based on this result and the NIEL hypothesis an easy to use method has been suggested for the determination of particle fluences, respectively hardness factors.

Microscopic defect studies using the Deep Level Transient Spectroscopy (DLTS) and Thermally Stimulated Current (TSC) techniques led to the detection of about 20 radiation induced defect levels. Besides the well known defects VO_i, C_iO_i, C_iC_s and VV also defects so far not reported in the literature were found and characterized. Furthermore, the material dependence of the defect introduction rates and the defect annealing behavior was investigated in isothermal and isochronal annealing experiments. On the basis of these studies the relations between the microscopic defects and the macroscopic detector properties were discussed in very detail. It was e.g. found that the annealing of an electron trap with a level of $E_C - 0.46\,\mathrm{eV}$ is most probably responsible for the *short term annealing* of the leakage current and the effective doping concentration. Furthermore, relations between other defects and the *reverse annealing*, the *stable damage*, the leakage current and the charge collection efficiency have been investigated.

Finally, the present and future possibilities for the production of radiation hard material are discussed and it is argued that for the moment oxygen enriched FZ silicon is the best choice.

Kurzfassung

Silizium-Mikrostreifen- und Pixeldetektoren sind die Schlüsselelemente für die Messung von Teilchenbahnen in Experimenten der Hochenergiephysik. In gegenwärtigen und zukünftigen Experimenten mit hoher Luminosität (z.B. ATLAS, CMS, LHCb und HERA-B) werden diese in intensiven hadronischen Strahlungsfeldern eingesetzt, in denen die Strahlenschädigung des Siliziumsubstrats zu einer erheblichen Verschlechterung der Detektoreigenschaften führt. Dabei ist absehbar, daß die am stärksten belasteten Detektoren die angestrebte Betriebsdauer der Experimente nicht überstehen werden. Die Verbesserung der Strahlenhärte des Siliziumsubstrats ist daher von großer Bedeutung.

In dieser Arbeit wurden die strahlungsinduzierten Veränderungen der effektiven Dotierungskonzentration und des Volumengenerationsstromes systematisch untersucht und als Funktion der Teilchenfluenz, der Ausheiltemperatur und der Ausheilzeit parametrisiert. Desweiteren wurde die Abhängigkeit der Schädigung von der Sauerstoffkonzentration ($2 \times 10^{14}\,\mathrm{cm}^{-3}$ bis $9 \times 10^{17}\,\mathrm{cm}^{-3}$) und dem spezifischen Widerstand des Substratmaterials (110 Ωcm bis 25 kΩcm) untersucht. Es konnte gezeigt werden, daß eine erhöhte Sauerstoffkonzentration zu einer verbesserten Strahlenhärte im Hinblick auf die Veränderungen der effektiven Dotierung nach Neutronenbestrahlung und insbesondere nach Bestrahlung mit geladenen Hadronen führt. Während sich der Einfluß des Sauerstoffs nach Neutronenbestrahlung in einem unterdrückten *donor removal* zeigt, liegt der wesentliche Effekt nach Bestrahlung mit geladenen Hadronen in einer reduzierten Generation von negativer Raumladung (*stable damage*).

Die Schädigungskonstante α, die den Anstieg des Volumengenerationsstromes beschreibt, wird nicht durch die Sauerstoffkonzentration oder den spezifischen Widerstand des Ausgangsmaterials beeinflußt. Weiterhin konnte gezeigt werden, daß der Wert von α für einen wohldefinierten Ausheilzustand in einem Bereich von $10^{11}\,\mathrm{cm}^{-2}$ bis $10^{14}\,\mathrm{cm}^{-2}$ unabhängig von der Fluenz ist. Aufbauend auf diesen Ergebnissen und der NIEL-Hypothese wurde eine einfach handhabbare Meßmethode vorgeschlagen, die es ermöglicht Teilchenfluenzen bzw. Härtefaktoren zu bestimmen.

Mit Hilfe der Techniken *Deep Level Transient Spectroscopy* (DLTS) und *Thermally Stimulated Current* (TSC) konnten über 20 strahleninduzierte Defektniveaus nachgewiesen werden. Neben den Defekten VO_i, C_iO_i, C_iC_s und VV wurden auch einige bisher unbekannte Defekte entdeckt und charakterisiert. Basierend auf den gemessenen Defekteigenschaften und den Ergebnissen der Untersuchungen zur Materialabhängigkeit und Ausheilkinetik der Defekte wurde der Zusammenhang zwischen den Defekten und den Detektoreigenschaften diskutiert. So konnte z.B. gezeigt werden, daß die Ausheilung einer Elektronenhaftstelle mit $E_C - 0.46\,\mathrm{eV}$ höchstwahrscheinlich für das sogenannte *short term annealing* des Volumengenerationsstromes und der effektiven Dotierung verantwortlich ist. Desweiteren wurden Zusammenhänge zwischen weiteren Defekten und dem *reverse annealing*, dem *stable damage* und der Ladungssammlungseffizienz untersucht.

Abschließend wurden die gegenwärtigen und zukünftigen Möglichkeiten für die Herstellung von strahlenhartem Material diskutiert. Dabei zeigte sich, daß sauerstoffangereichertes zonengezogenes Silizium die derzeit beste Wahl darstellt.

Contents

1 Introduction **1**

2 Silicon and Silicon Detectors **4**
2.1 Detector grade silicon – growth techniques 4
2.1.1 Polysilicon 5
2.1.2 Czochralski silicon (Cz) 6
2.1.3 Float zone silicon (FZ) 9
2.1.4 Epitaxial silicon 11
2.1.5 Silicon wafers 12
2.2 Detector manufacturing 13
2.2.1 Process technologies 13
2.2.2 Test structures used in this work 15
2.3 Basic features of silicon diodes 21
2.3.1 p-n junction 21
2.3.2 Capacitance 23
2.3.3 Forward current 24
2.3.4 Leakage current 25
2.4 Operation of silicon detectors 26
2.4.1 Basic principle of detector operation 26
2.4.2 Why silicon? 27
2.4.3 Signal to noise ratio 29
2.4.4 Microstrip and pixel detectors 29

3 Radiation damage – Defects in silicon **31**
3.1 Damage mechanism 31
3.2 The NIEL scaling hypothesis 33
3.2.1 Displacement damage cross sections 33
3.2.2 Hardness factors 35
3.3 Classification of defects 36
3.3.1 Clusters 36
3.3.2 Point defects 36
3.4 Electrical properties of point defects 38
3.4.1 Occupation statistics for traps in thermal equilibrium 38
3.4.2 Basic semiconductor equations 44

3.4.3 Occupation of traps in the space charge region 45
3.4.4 Occupation of traps under forward bias 46
3.4.5 Occupation of traps under high leakage current 46
3.5 Defect annealing 48
3.5.1 Annealing mechanisms 48
3.5.2 Rate of reaction 49
3.5.3 Annealing temperature 51
3.6 Review of point defects 52
3.6.1 Radiation induced defects 52
3.6.2 Thermal donors 57
3.7 Impact of defects on detector properties. 59

4 Experimental Methods and Experimental Equipment 63
4.1 Materials and devices 63
4.2 Irradiation facilities 66
4.2.1 The Be(d,n) source at the PTB–Braunschweig 66
4.2.2 Further neutron sources 69
4.2.3 Proton and gamma sources 70
4.3 Diode characteristics 70
4.4 Deep Level Transient Spectroscopy (DLTS) 75
4.4.1 Principle of operation 75
4.4.2 Determination of defect parameters 77
4.4.3 Transient analysis 81
4.5 Thermally Stimulated Current (TSC) 88
4.5.1 Principle of operation 88
4.5.2 Determination of defect parameters 90
4.6 DLTS and TSC setup 94

5 Change of Detector Properties 97
5.1 Leakage current 98
5.1.1 Introduction 98
5.1.2 Fluence dependence 98
5.1.3 Annealing 99
5.1.4 Material dependence 104
5.2 Experimental determination of hardness factors 106
5.3 Effective doping concentration 110
5.3.1 Introduction 110
5.3.2 Short term annealing 112
5.3.3 Reverse annealing 115
5.3.4 Stable damage – Material dependence 122
5.3.5 Particle dependence 127
5.4 Charge collection efficiency 130

6 Microscopic Defects **131**
6.1 Labelling of defects . . . 132
6.2 Accuracy of defect concentrations . . . 135
6.2.1 Measurement results – DLTS, TSC, TSCap . . . 135
6.2.2 Comparison – DLTS, TSC, TSCap . . . 141
6.3 Cooling and filling conditions (C_iC_s and VO_i) . . . 142
6.4 Capture cross sections of the C_iO_i . . . 146
6.5 Field strength dependence . . . 152
6.6 ^{60}Co-gamma irradiations . . . 155
6.7 Comparison: Neutron and ^{60}Co-gamma irradiations . . . 158
6.8 Annealing at room temperature . . . 162
6.8.1 DLTS measurements . . . 163
6.8.2 TSC measurements . . . 169
6.9 Isochronal annealing . . . 172
6.10 Material dependence – Annealing at 60°C . . . 174
6.10.1 High resistivity FZ - 3 kΩcm . . . 175
6.10.2 Low resistivity FZ - 6 Ωcm . . . 177
6.10.3 Cz silicon with high oxygen content - 110 Ωcm . . . 178
6.10.4 FZ silicon with low oxygen content - 4 kΩcm . . . 180
6.10.5 Comparison . . . 180

7 Relation between Macroscopic Detector Properties and Microscopic Defects **185**
7.1 Leakage current . . . 187
7.1.1 Magnitude of current . . . 187
7.1.2 Annealing . . . 188
7.2 Effective doping concentration . . . 190
7.2.1 Short term annealing . . . 191
7.2.2 Stable damage – Donor removal . . . 191
7.2.3 Reverse annealing . . . 196
7.3 Charge collection efficiency . . . 199

8 Radiation Hard Material - Outlook **201**
8.1 Oxygen enriched FZ silicon . . . 201
8.2 Magnetic Czochralski silicon (MCz) . . . 205
8.3 Compensated silicon . . . 206

9 Summary and Conclusions **208**

A Constants and Silicon Properties **215**
A.1 Fundamental constants . . . 215
A.2 Basic properties of silicon . . . 215
A.3 DLTS - Determination of trap concentration . . . 217

B Review: Defects and Impurities in Silicon **219**

List of figures **225**

List of tables **228**

List of publications **230**

Bibliography **232**

Acknowledgements **251**

Chapter 1

Introduction

Silicon microstrip and pixel detectors are at present the most precise electronic tracking detectors for charged particles in high energy physics experiments. With an achieved position resolution of a few micrometers they have already contributed significantly to the study of τ-leptons, heavy quarks like charm and beauty and last but not least to the recent discovery of the top quark. In addition to their excellent position resolution and two particle separation, their signal collection time is short ($O(10$ ns$)$), they can be operated in strong magnetic fields and their thickness of $\approx 300\,\mu$m represents a radiation length of only $\approx 0.3\%$.
Silicon detectors have also been chosen as central tracking detectors for the next generation of high energy physics experiments like ATLAS[1] and CMS[2] at the CERN[3] Large Hadron Collider (LHC) [ATL97, CMS94]. To achieve some of the LHC prime physics goals – the discovery and possible study of the Higgs-particles and supersymmetric particles – a center of mass energy of pp-interactions of 14 TeV and an unprecedented luminosity[4] of $L = 10^{34}\,\mathrm{cm}^{-2}\mathrm{s}^{-1}$ is required. As a result the silicon detectors, which are located as close as 4 cm from the beam line, will have to operate in a very harsh radiation environment.
As a representative example the expected particle fluences for the ATLAS tracking detector in dependence of the distance from the beam line are shown in Fig. 1.1. The fluences are normalized to a 1 MeV neutron equivalent fluence on the basis of the NIEL (Non-Ionising Energy Loss) scaling hypothesis (see Sec. 3.2). The positions of the pixel and the microstrip tracking detectors are indicated in the figure. The pixel detector will be exposed to a pion ($\pi^{\pm}$) dominated fluence of up to $\Phi_{eq} \approx 3 \times 10^{14}\,\mathrm{cm}^{-2}$ per operational year and the microstrip detectors (SCT[5]) will face up to $\Phi_{eq} \approx 2 \times 10^{13}\,\mathrm{cm}^{-2}$ per operational year. In the latter case the fluence is dominated by neutrons (an important difference as will become obvious within this work).
These irradiation levels will cause an appreciable deterioration of the detector per-

[1] ATLAS - A Toroidal LHC Apparatus
[2] CMS - Compact Muon Solenoid
[3] CERN - European Laboratory for Particle Physics, Geneva, Switzerland
[4] The luminosity L is related to the event rate R by the interaction cross section σ_{int}: $L = R/\sigma_{int}$.
[5] SCT - Semiconductor Central Tracker

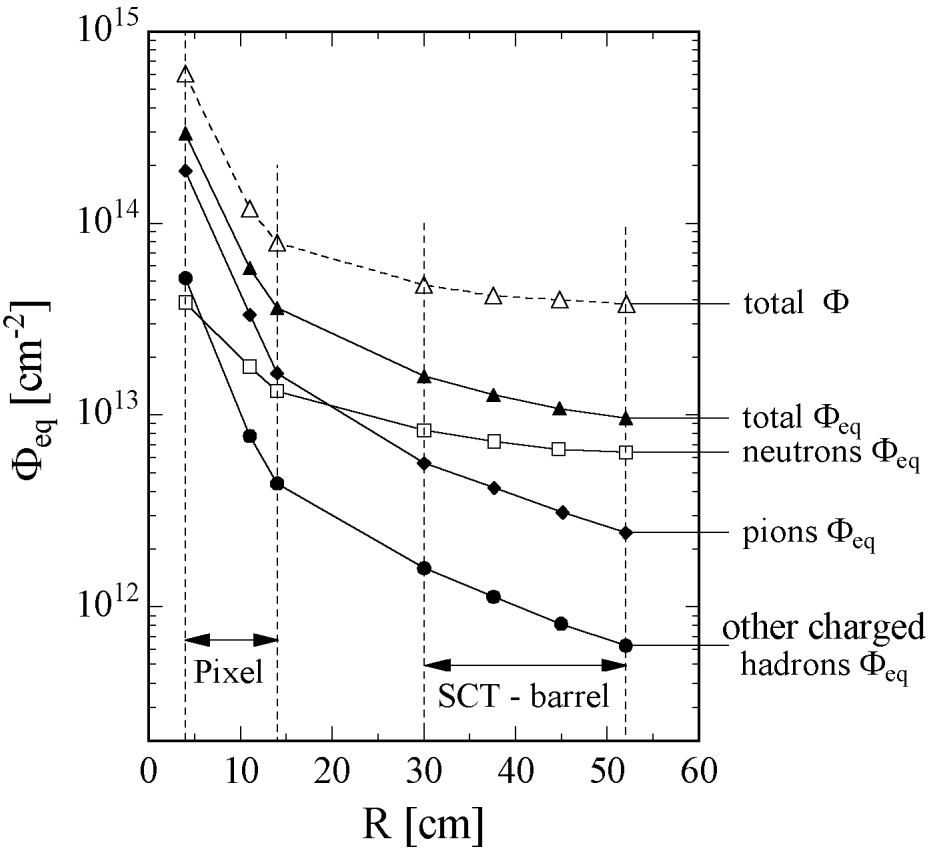

Figure 1.1: Expected particle fluences for the ATLAS detector within one operational year (10^7 s) of high luminosity ($10^{34} cm^{-2} s^{-1}$) assuming an inelastic pp interaction cross section of 80 mb [Vas97b].

formance. The main damage effects are a fluence proportional increase of the leakage current, a dramatic change of the depletion voltage, needed to maintain a full sensitivity of the whole detector thickness, and a decrease of the charge collection efficiency. All these effects have been measured so far in a number of impressive systematic studies, covering the fluence dependence for protons, neutrons and pions of different energies and including also the annealing effects observed after irradiation (e.g. [Wun92, Zio94, Lem95, Li 95a, Sch96a, Fei97a]). A comprehensive modeling had been developed allowing reliable projections for prolonged operations in the forthcoming experiments [Chi95, Fei97a]. Such estimates have shown that especially for the areas close to the interaction points the radiation tolerance of present state of the art detectors may not be sufficient for the envisaged operation lifetime, which is however needed for cost effectiveness [ATL98, Fei98a, HB95]. The radiation tolerance of these devices has therefore become of supreme interest and led to intense efforts for the development of radiation hard material world-wide. Along with the developments for

the LHC experiments these projects were coordinated within the ROSE[6]-collaboration CERN-RD48 [R48]. This thesis was performed in close co-operation with this collaboration. On the one hand a substantial part of the experimental data was obtained with silicon materials produced under the auspices of the ROSE-collaboration and on the other hand many of the results have already been included into the collaboration status reports [ROS98a, ROS97].

The radiation induced changes in the *macroscopic* detector performance are caused by electrical active *microscopic* defects. Therefore, a strategy for the development of radiation hard material should be based on the understanding of the defect kinetics and the relation between the defects and the *macroscopic* properties. With such a knowledge it is possible to influence the defect kinetics, e.g. by the enrichment of the silicon with certain impurities, in such a way that less macroscopic damage is produced (*defect engineering* strategy). Several groups have therefore studied possible correlations between the macroscopic radiation damage effects and microscopic defects analyzed by using e.g. DLTS (Deep Level Transient Spectroscopy), TSC (Thermally Stimulated Current) and other microscopic tools (e.g. [Bor94, Mac96a, Wat96, Li 97, Fei97c]).

This work is regarded as a further step to a more fundamental understanding of the radiation damage effects in silicon with the goal of a *defect engineered* radiation hard silicon. A first success in these efforts will be presented.

The text is organized in 9 chapters. In the following chapter an overview of silicon growth techniques for monocrystalline silicon will be given. Subsequently the production process of silicon detectors, the different types of test structures used in this work and the basic features of silicon detectors are described. In Chapter 3 the basic radiation damage mechanisms and the radiation induced defects in the silicon bulk are reviewed and classified with respect to their electrical properties. Furthermore, the impact of the microscopic defects on the macroscopic detector properties is described. Chapter 4 illustrates the used microscopic and macroscopic characterization techniques. The experimental results on the leakage current and the effective doping concentration are presented in Chapter 5 and the ones on the microscopic defects and their properties in Chapter 6. In Chapter 7 the relation between the detected microscopic defects and the measured macroscopic detector properties are investigated. Subsequently, the possibilities for the production of radiation hard material are discussed in Chapter 8 and, finally, a summary with some conclusions is given in Chapter 9.

[6]ROSE - Research and development On Silicon for future Experiments

Chapter 2

Silicon and Silicon Detectors

Silicon is the most abundant solid element on earth, being second only to oxygen and it makes up more than 25% of the earth's crust. However, it rarely occurs in elemental form, virtually all of it is existing as compounds. In this chapter the question will be answered how very pure sand (SiO_2) is converted into monocrystalline silicon and later on into silicon detectors and how these detectors are operated.
After a description of the different growth techniques for monocrystalline silicon with special interest in the material used in this work it is shown which kind of detectors have been used and how they have been produced. Subsequently the basic diode properties – p-n–junction, capacitance and leakage current – are explained and finally a short description of detector operation in high energy physics experiments is given.

2.1 Detector grade silicon – growth techniques

The material requirements for the manufacturing of silicon particle detectors used for high energy physics applications have to meet two basic demands: High resistivity and high minority carrier lifetime. A very high resistivity ($\geq 1\text{k}\Omega\text{cm}$) is needed in order to fully deplete the detector bulk with a thickness of $\approx 200 - 300\,\mu\text{m}$ by an adequate voltage below about 300 V. Together with the demand for a reasonable price and a homogeneous resistivity distribution – not only over a single wafer but also over the whole ingot – float zone silicon is the best choice of material and is therefore exclusively used for detector applications today. Further requirements for detector grade silicon are often a high minority carrier lifetime and a very low bulk generation current respectively high generation lifetime in order to avoid detector noise. However, these requirements should not be taken too strictly for particle detectors that will be exposed to severe radiation levels since already after small radiation fluences the lifetimes are reduced by orders of magnitude and therefore the good initial lifetime qualities are of no use any more.
In the search for radiation harder material and in order to perform radiation tests on an as wide as possible range of material also silicon grown by the Czochralski and epitaxial method have been investigated in this work. While for the epitaxial technique the price and the *substrate problem* might rule out largely its application as detector material

the Czochralski method could become of interest for the production of radiation hard material if it is possible to make high resistivity ($\geq$ 1kΩcm) Cz commercially available (see Chapter 8).

In this section the production of silicon with the three growth techniques mentioned above will shortly be reviewed with special interest in the high resistivity silicon production and the possibilities of defect engineering respectively the controlled incorporation of impurities into the crystal.

2.1.1 Polysilicon

2.1.1.1 Metallurgical Grade Silicon (MGS)

The production of silicon crystals starts with the mining of silicon dioxide in form of quartzite or, nowadays more often, very pure sand. The main impurities are Al_2O_3 and Fe_2O_3 (in the order of a few tenth of a percent). The silicon dioxide is melted together with coke and wood chips in a submerged electrode arc furnace at about 1780°C. While a number of reactions take place in the furnace, the overall reaction can be described as

$$SiO_2 + 2C \rightarrow Si + 2CO.$$

The leftover liquid silicon drains away and is already 99% pure. When the liquid cools to a solid the result is called Metallurgical Grade Silicon (MGS).

2.1.1.2 Semiconductor Grade Silicon (SGS)

The MGS is ground into a fine powder and by exposing it to hydrogen chloride gas (HCl) at about 300°C is converted into trichlorsilane

$$Si + 3HCl \rightarrow SiHCl_3 + H_2.$$

Trichlorsilane is a liquid at room temperature and boils at 31.7°C. Many impurities have much higher boiling points. Therefore, repeated distillation is used to refine the trichlorsilane until the concentration of the electrically active impurities is below 1 ppb [Amm84]. Finally the pure trichlorsilane gas is passed together with hydrogen over the surface of a hot (900–1100°C) silicon rod where the reaction mentioned above is reversed. Polysilicon is deposited on the silicon rod with a fairly low deposition rate (< 1 mm/h) [Amm84]. Typical concentrations of the dominant electrically active impurities in polysilicon, as used by the company Wacker in 1998 [WAC99], are $\approx 5 \times 10^{12}\,\mathrm{cm}^{-3}$ for aluminum and $\approx 1 \times 10^{11}\,\mathrm{cm}^{-3}$ for phosphorus, boron and arsenic. Furthermore, the typical concentration of carbon is about $2 \times 10^{15}\,\mathrm{cm}^{-3}$ and the one of oxygen below about $5 \times 10^{14}\,\mathrm{cm}^{-3}$. However, due to the further processing steps (see below) these values differ from the ones in the monocrystalline silicon wafers used for the detector production.

2.1.2 Czochralski silicon (Cz)

The vast majority of the commercially grown silicon is Czochralski silicon due to the better resistance of the wafers to thermal stress, the speed of production, the low cost and the high oxygen concentration that offers the possibility of *Internal Gettering*. The industrial standard crystals range in diameter from 75 to 200 mm, are typically 1 m long and of <100> orientation. For a detailed description of the different Czochralski silicon growth techniques with main focus on the incorporation of oxygen into the crystal the reader is referred to [Lin94]. In the following only a short review is given.

2.1.2.1 Standard Cz

The Czochralski method is named after J.Czochralski [Czo18], who determined the crystallisation velocity of metals by pulling mono- and polycrystals against gravity out of a melt which is held in a crucible. The pull-from-melt method widely employed today was developed by Teal and Little in 1950 [Tea50]. A schematic diagram of a Czochralski-Si grower, called *puller*, is shown in Fig. 2.1. The puller consists of three main components:

1. a furnace, which includes a fused-silica crucible, a graphite susceptor, a rotation mechanism (clockwise as shown), a heating element, and a power supply;
2. a crystal-pulling mechanism, which includes a seed holder and a rotation mechanism (counter-clockwise); and
3. an ambient control, which includes a gas source (such as argon), a flow control and an exhaust system.

The Czochralski method begins by melting high purity polysilicon (SGS) with additional dopants as required for the final resistivity in the rotating quartz crucible. A single crystal silicon seed is placed on the surface and gradually drawn upwards while simultaneously being rotated. This draws the molten silicon after it which solidifies into a continuous crystal extending from the seed. Temperature and pulling speed are adjusted to first neck the crystal diameter down to several millimetres, which eliminates dislocations generated by the seed/melt contact shock, and then to widen the crystal to full diameter. During the production process the quartz crucible (SiO_2) gradually dissolves, releasing large quantities of oxygen into the melt. More than 99% of this is lost as SiO gas from the molten surface, but the rest stays in the melt and can dissolve into the single crystal silicon [Ewe97]. Another impurity, however with smaller concentrations, that is also introduced into the melt by the production process itself is carbon. The silicon monoxide evaporating from the melt surface interacts with the hot graphite susceptor and forms carbon monoxide ($SiO + 2C \longrightarrow SiC + CO$) that re-enters the melt. As the crystal is pulled from the melt, the impurity concentration incorporated into the crystal (solid) is usually different from the impurity concentration of the melt (liquid) at the interface. The ratio of these two concentrations is defined as the *equilibrium segregation coefficient* $k_0 = C_s/C_l$ where C_s and C_l are the equilibrium concentrations of the impurity in the solid and liquid near the interface, respectively. The equilibrium segregation coefficient k_0 is displayed in Tab. 2.1 for some impurities.

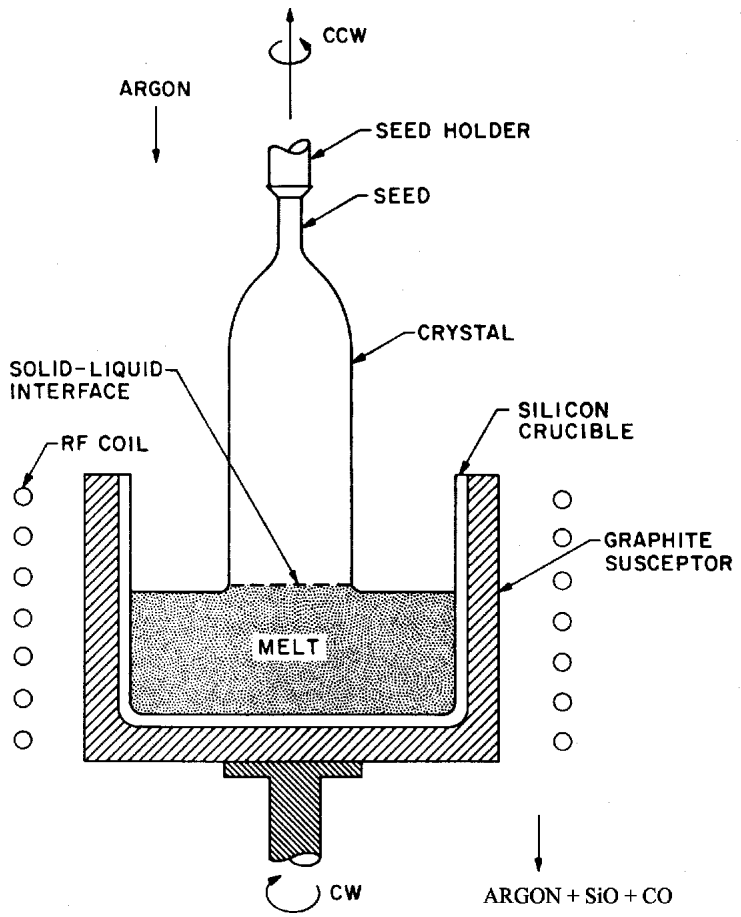

Figure 2.1: Schematic setup of a Czochralski crystal puller (after [Sze85]).

Impurities with $k_0 < 1$ prefer to stay in the melt where their concentration is increasing during the pulling process. Therefore an inhomogeneous impurity distribution $C_s(x)$ along the ingot is observed that can be described by [Lin94, Sze85]

$$C_s(x) = C_0\, k\, (1-x)^{k-1}. \tag{2.1}$$

Here x is the fraction of solidified melt ($\approx$ axial position/final ingot length) and C_0 the initial impurity concentration in the melt. k denotes the effective segregation coefficient that for a first approximation can be assumed to be k_0 (usually $k > k_0$) but is strongly depending on the process parameters like rotation speed, pulling speed and convection in the crucible. Thus the homogeneity of the impurity distribution in Cz silicon is strongly depending on the production technology used by the specific producer.

Oxygen is always the impurity with the highest concentration in Cz silicon. Typical oxygen and carbon concentrations are $[O] \approx 5 - 10 \times 10^{17}\,\mathrm{cm}^{-3}$ and $[C] \approx 5 - 50 \times 10^{15}\,\mathrm{cm}^{-3}$, respectively. The solubility of O in Si is $\approx 10^{18}\,\mathrm{cm}^{-3}$ at the melting point[1] but drops by several orders of magnitude at room temperature, hence there is

[1]Silicon melting point: 1420°C.

element	k_0	Ref.	element	k_0	Ref.	element	k_0	Ref.
B	0.8	(1)	N	7×10^{-4}	(1)	C	0.07	(2)
Al	0.002	(1)	P	0.35	(1)	O	$0.3^{(\dagger)}$	(2)
Ga	0.008	(1)	As	0.3	(1)	Fe	8×10^{-6}	(1)
In	4×10^{-4}	(1)	Sb	0.023	(1)	Sn	0.016	(1)

References: (1) [Mad89]; (2) [Lin94].
$^{(\dagger)}$ For oxygen there exists a wide range of segregation coefficients in the literature, ranging from greater to less than unity and including unity (for details see [Lin94]).

Table 2.1: Equilibrium segregation coefficients for some elements. Further segregation coefficients in silicon can be found in [Mad89].

a driving force for oxygen precipitation. Furthermore the high oxygen concentration can lead to the formation of unwanted electrically active defects. These are oxygen related thermal double donors (TDD) and shallow thermal donors (STD) which can seriously change the resistivity of the material and will be discussed therefore in more detail (see Sec. 3.6.2). However, oxygen has also good properties. Oxygen acts as a gettering agent for trace metal impurities in the crystal (*Internal Gettering*) and it can pin dislocations which greatly strengthens the crystal. Oxygen precipitates in the wafer core suppress stacking faults, and oxygen makes the Si more resistant to thermal stress during processing. This is the reason why Cz-Si is used for integrated circuit production, where there are many thermal processing steps.
However, the most important property of a high oxygen concentration from the point of view of this work is the improved radiation hardness, as will be shown in Chapter 5. The main problem for the application as detector grade material arises from the resistivity of Cz silicon. Due to contamination with boron, phosphorus and aluminum from the dissolving quartz crucible the highest commercially available resistivity is about 100Ωcm for n-type and only slightly higher for p-type material. Therefore standard Cz silicon is not suitable for detector production. However, a first experiment to compensate the *natural* p-type background doping by adding a small quantity of phosphorus to the melt have been performed in collaboration with MEMC in Italy [MEM]. The results will be discussed in Chapter 8.

2.1.2.2 Magnetic Field Applied Cz (MCz)

MCz may be the future standard Cz technology since today's approaches to solve the challenge[2] of the 300 mm and later on also the 400 mm crystal diameter are based on this technology [Moz97]. The MCz method is the same as the Cz method except that it is carried out within a strong horizontal (HMCz) or vertical (VMCz) magnetic field. This serves to control the convection fluid flow, allowing e.g. with the HMCz method to minimise the mixing between the liquid in the center of the bath with that at the edge. This effectively creates a liquid silicon crucible around the central silicon bath,

[2]According to the *Semiconductor Industry Association Roadmap on VLSI-Technology* [SIA94] 300 mm and 400 mm wafer diameter shall become standard in the year 2001 and 2007, respectively.

which can trap much of the oxygen and slow its migration into the crystal. Compared to the standard Cz a lower oxygen concentration can be obtained and the impurity distribution is more homogeneous.
This method offers also the possibility to produce detector grade silicon with a high oxygen concentration. Since the MCz technology is still a very young one, it is hard to get such material with reproducible impurity concentrations on a commercial basis. However, a first test material of 4 kΩcm p-type with an oxygen concentration of $7 - 8 \times 10^{17}\,\mathrm{cm}^{-3}$ and a carbon concentration below $2 \times 10^{16}\,\mathrm{cm}^{-3}$ was obtained from KOMATSU in Japan [KOM] (for details see Chapter 8).

2.1.2.3 Continuous Cz (CCz)

With the CCz method a continuous supply of molten polycrystalline silicon is achieved by using a double quartz crucible. In the first one the crystal is grown and in the second one, connected to the first one, a reservoir of molten silicon is kept, that can be refilled by new polysilicon during the growth process. This allows for larger crystal length and improves the throughput and operational costs of the Cz grower. Furthermore the resulting single crystals have a uniform resistivity and oxygen concentration and identical thermal history. In combination with the magnetic field method the Continuous Magnetic Field Applied Cz technique (CMCz) offers the possibility to grow long and large diameter Cz. However, silicon produced by this technology has so far not been used for radiation damage experiments.

2.1.3 Float zone silicon (FZ)

The role of detector grade silicon compared to FZ silicon for other applications like high voltage and high power devices has been described by one of the leading companies as follows [Amm84]:

> Regarding the quantities, it has always been very small and – despite its high price – its contribution to the turnover or benefit of a silicon manufacturer is negligible. However, the extraordinary purity requirements have always been a challenge and – if successful – an image for a silicon supplier.

Thus detector grade silicon may be interesting for the silicon industry but it is very hard to find industrial partners for growing specially doped detector grade FZ ingots for radiation hardness tests and the RD48 Collaboration is very grateful to the ITME company in Poland [ITM] for doing so. Without their help part of this work would not have been possible.

2.1.3.1 The float zone method

The float zone (FZ) method is based on the zone-melting principle and was invented by Theuerer in 1962 [The62]. A schematic setup of the process is shown in Fig. 2.2. The production takes place under vacuum or in an inert gaseous atmosphere. The process starts with a high-purity polycrystalline rod and a monocrystalline seed crystal that

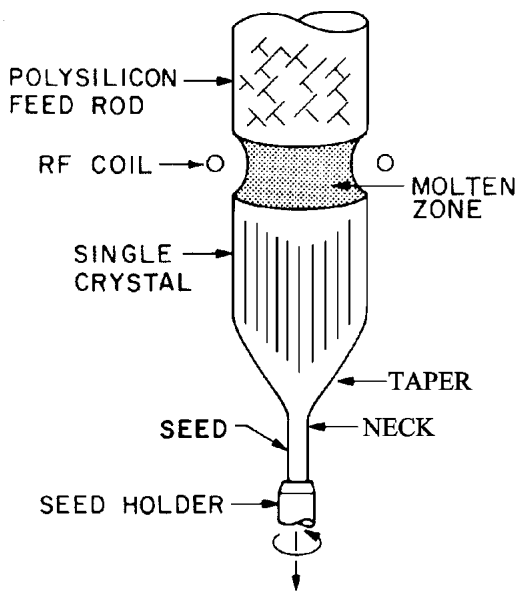

Figure 2.2: Schematic setup for the Float zone (FZ) process (after [Sze85]).

are held face to face in a vertical position and are rotated. With a radio frequency field both are partially melted. The seed is brought up from below to make contact with the drop of melt formed at the tip of the poly rod. A necking process is carried out to establish a dislocation free crystal before the *neck* is allowed to increase in diameter to form a taper and reach the desired diameter for steady-state growth. As the molten zone is moved along the polysilicon rod, the molten silicon solidifies into a single crystal and, simultaneously, the material is purified [Lin94].
Typical oxygen and carbon concentrations in FZ silicon are below $5 \times 10^{15}\,\mathrm{cm}^{-3}$ [WAC99]. FZ crystals are doped by adding the doping gas phosphine (PH_3) or diborane (B_2H_6) to the inert gas for n- and p-type, respectively. Unlike Cz growth, the silicon molten zone is not in contact with any substances except ambient gas, which may only contain doping gas. Therefore FZ silicon can easily achieve much higher purity and higher resistivity. Additionally multiple zone refining can be performed on a rod to further reduce the impurity concentrations. Once again the effective segregation coefficient k plays an important role. Boron, for example, has an equilibrium segregation coefficient of $k_0 = 0.8$ (Tab. 2.1) while the effective segregation coefficient[3] k is close to 1 and no purification can be reached. In contrast to this phosphorus cannot only be segregated ($k_0 = 0.35$) but also evaporates from the melt at a fairly high rate [Amm84]. This is the reason why on the one hand it is easier to produce more homogeneous p-type FZ than n-type FZ and on the other hand high resistivity p-type silicon can only be obtained from polysilicon with low boron content.
Dopants with a small k_0 like Sn (see Tab. 2.1) can be introduced by pill doping[4] – holes are drilled into the ingot into which the dopant is incorporated – or by evaporating a dopant layer on the whole ingot[5] before the float zoning process.

[3]The effective segregation coefficient k is strongly depending on the pulling speed.
[4]E.g. used by TOPSIL for Sn doping of experimental ingots [TOP98]
[5]E.g. used by ITME for Sn doping of ROSE test material [Nos98]

2.1.3.2 Neutron Transmutation Doping (NTD)

Due to the very nature of the FZ growth configuration, the small *hot zone* lacks thermal symmetry. As a result, temperature fluctuations, remelting phenomena and dopant segregation cause FZ silicon to display more microscopic dopant inhomogeneity or dopant striations than observed in the Cz silicon [Lin94]. Furthermore, as mentioned above, high resistivity n-type silicon is always less homogeneous than p-type. This can be improved by NTD. In NTD, a high purity p-type FZ ingot is subjected to thermal neutron bombardment in a reactor, causing some part of ^{30}Si ($\approx 3.1\%$ of Si) to form the unstable isotope ^{31}Si by neutron capture ($\sigma_{capt.} = (0.11 \pm 0.01)$ barn [Ber68]), which decays with a half life time of 2.62 hours into the stable phosphorus isotope ^{31}P

$$Si^{30}_{14}(n,\gamma) \quad \longrightarrow \quad Si^{31}_{14} \quad \stackrel{2.62\,\mathrm{h}}{\longrightarrow} \quad P^{31}_{15} + \beta^{-}. \tag{2.2}$$

Because the penetration depth of thermal neutrons is about 100 cm, doping is very uniform across the diameter. However, the neutron bombardment induces radiation damage (mainly due to the unavoidable fast neutron component in the reactor) that must be annealed out at about 800°C for defect annihilation and for activation of the phosphorus dopant. Thus, starting with high resistivity homogeneous p-type silicon, high-resistivity n-type silicon can be produced with a homogeneity that cannot be reached with the standard float zone doping.

In this work it will be shown that a high oxygen concentration improves the radiation hardness of silicon detectors. Thus the idea arises to perform the NTD process on p-type Cz silicon in order to get high resistivity n-type silicon with a very high oxygen concentration. However, commercially available Cz does not fulfill the requirements of high resistivity and high homogeneity in the dopant distribution. Also the high resistivity (650 Ωcm) p-type Cz material investigated in this work (see Tab. 4.1) – such material is not commercially available and was produced on an experimental basis only – is not usable. The initial resistivity variation of about ±6% over a single wafer would result after an NTD process to 1 kΩcm n-type in a resistivity variation of about ±30% which is not acceptable for detector grade silicon.

2.1.4 Epitaxial silicon

There are many different epitaxial[6] growing methods [Sze85]. However, the most important for silicon device production is the vapor-phase epitaxy (VPE) that has also been used to grow the epitaxial material investigated in this work. In a VPE process a low resistivity substrate wafer (usually Cz) acts as a seed crystal on which silicon is decomposited from a compound like silicon tetrachloride ($SiCl_4$), dichlorosilane (SiH_2Cl_2), trichlorosilane ($SiHCl_3$) or silane (SiH_4). Among those compounds tetrachloride is the most studied and also widest used in industry. Furthermore, it was also used for the production of the epitaxial silicon investigated in this work. The typical reaction

[6]The word *epitaxy* is derived from Greek and means *to arrange upon.*

temperature is around 1200°C and the overall reaction can be described as

$$SiCl_4(\text{gas}) + 2\,H_2(\text{gas}) \longrightarrow Si(\text{solid}) + 4\,HCl(\text{gas}).$$

An additional competing reaction takes place reducing the solid silicon growth rate:

$$SiCl_4(\text{gas}) + Si(\text{solid}) \longrightarrow 2\,SiCl_2(\text{gas}).$$

Therefore the optimum $SiCl_4$ concentration has to be carefully chosen. Using small concentrations results in small growth rates and using too high concentrations results in etching of silicon rather than growing it. A typical growth rate lies in the order of 1 μm/min [ITM]. The dopant is introduced in the epitaxial reactor together with the trichlorsilane. As for the FZ method gaseous diborane (B_2H_6) or phosphine (PH_3) can be used for p- or n-type doping, respectively. A detailed description of the process parameters for the epitaxial samples produced at the Institute of Electronic Materials Technology (ITME) in Poland can be found in [Dez97].
During the crystal growth impurities are diffusing from the substrate (Cz silicon) into the epitaxial layer. Thus, it is possible to find higher concentrations of oxygen and carbon in epitaxial wafers than in float zone wafers.
For the application as detector material the substrate that for reasons of mechanical strength has a thickness of $\approx 600\,\mu$m is problematic since it introduces a *non active layer* in the final detector. The possibility to lap the substrate off after production is difficult and expensive. Thus this material is not an attractive material for the application as detector material but offers the possibility to study the influence of impurities that can be included from the gaseous phase in a very controlled way and homogeneously into the silicon.

2.1.5 Silicon wafers

After the crystal growth the tails of the ingots are cropped and the whole ingot is ground to a uniform diameter with an orientation flat[7]. With an inner diameter blade saw or a multi wire saw the ingot is sliced into *wafers* and the edges of the wafers are ground into a round profile. In order to remove surface roughness from saw cuts and process damage, the wafers are mechanically lapped (Al_2O_3 powder and water). Then the wafers are etched (e.g. using a a sodium hydroxide (NaOH) based solution) to remove the remaining micro cracks of surface damage introduced by the alumina abrasive in the previous lap-stage. Finally the wafers are polished to get a good surface flatness and are now ready for processing. Wafers for IC production may undergo further treatments before polishing like gettering and oxygen donor killing processes.

Doping of silicon is not only possible during the crystal growth but also by diffusion of dopants into wafers. This has most recently been demonstrated again for oxygen doping of high resistivity FZ silicon in Ref. [Ruz99b]. An approximately 300 nm dry oxide was

[7]For 200 mm wafers it is standard to carve a notch down the backbone of the wafer instead of using a flat

grown on a 300 μm thick double side polished high resistivity FZ wafer. Afterwards the wafer was heated to 1150°C in a nitrogen atmosphere to allow desorption of oxygen from the SiO_2 at the interface and it's diffusion into the bulk. After a heating period of 72 h a homogeneous distribution of oxygen with a concentration of $\approx 2 \times 10^{-17}$ cm^{-3} was measured by SIMS[8] in a depth profile of up to 150 μm.

2.2 Detector manufacturing

Radiation hardening of silicon detectors is not only achieved by using radiation hard bulk material but also by choosing a proper detector design and process technologies enabling operation even under high bias voltages after severe radiation damage (see e.g. [And98]). Also the oxidation technique is a very important aspect since the high amount of ionizing radiation in HEP detector applications leads to strong surface damage effects (for details see e.g. [Ma 89, Nic82]).
However, the study of the radiation induced changes of silicon bulk properties can be performed using very simple device structures. A single pad diode with or without a guard ring (*test structure*) is sufficient. In this work many different kinds of test structures (Schottky–, implanted–, diffused– and MESA–diodes) produced by different companies (ITE, ELMA, MPI-Halbleiterlabor München, Sintef, Canberra, Diotec and in our own laboratory) have been used. After a short description of the main process steps of the planar technology the used test structures are described in more detail. Finally the basic principle of detector operation is explained and silicon is compared to other detector materials.

2.2.1 Process technologies

In 1980 J. Kemmer [Kem80] applied the *planar technology* to manufacture silicon detectors with extremely low leakage currents (low noise). This technique is now common practice and will be described briefly. The basic process steps are shown in Fig. 2.3. The process starts with oxidation of polished and thoroughly cleaned wafers at temperatures of about 1000°C. Thermal oxidation can be done in oxygen (*dry oxidation*: $Si + O_2 \rightarrow SiO_2$) or in water vapor (*wet oxidation*: $Si + 2H_2O \rightarrow SiO_2 + 2H_2$) [Sze85]. Often small percentages of HCl or TCE (trichloroethylene) are added to getter impurities and therefore improve the bulk properties (higher minority carrier life times) [Kem84]. The main effect of the oxidation is the elimination of surface leakage current, and therefore it is also called *passivation*. Furthermore the oxide layer protects the wafer during the processing and later on the detector itself from contaminations.
Using photolithographic equipment and proper etching techniques, windows are opened in the oxide to enable the doping of these areas by ion implantation while the oxide masks the rest of the surface. For the n^+–contact phosphorus or arsenic (e.g. As; 30 keV; 5×10^{15} ions/cm^2 [Kem84]) and for the p^+ contact boron (e.g. B; 10–15 keV;

[8]SIMS - Secondary Ion Emission

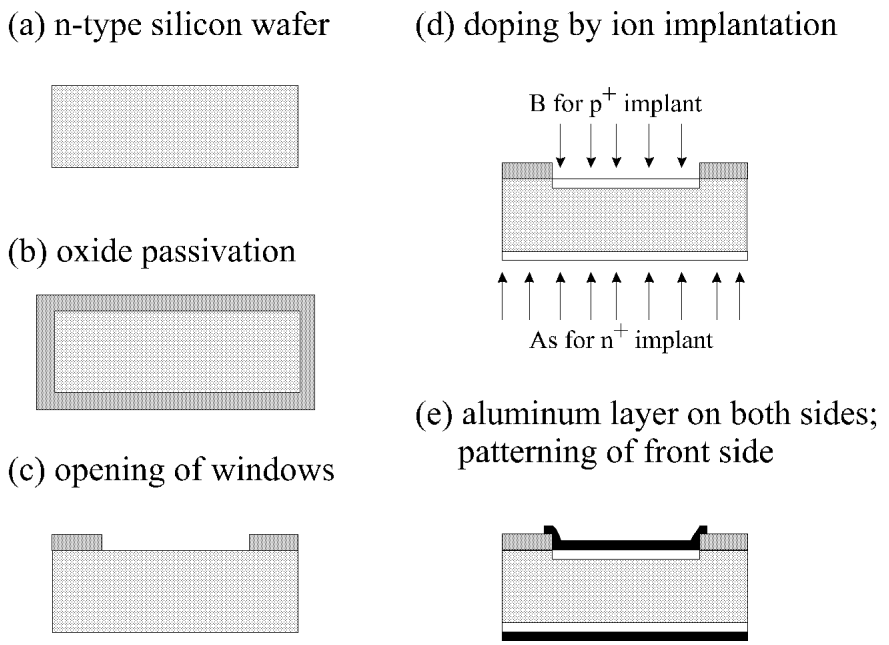

Figure 2.3: Basic process steps for the fabrication of an ion implanted planar $p^+ - n - n^+$ pad detector (after [Kem84]).

5×10^{14} ions/cm^2; R_p[9] ≈ 500Å; [Kem84]) is used. After implantation the wafers have to be annealed (e.g. 30 min in dry nitrogen at $\approx 600°$C [Kem84]) in order to anneal the radiation damage in the implanted layers and activate the dopants. Finally metal patterns are generated (typically aluminum) for good electrical contacts, again using photolithographic techniques. Now the wafer can be cut and the detectors used.

The junctions can also be achieved by diffusion. Since the diffusivities of the commonly used dopants B, P and As are considerably smaller in the oxide than in the silicon, the oxide can still be used as an effective mask. The typical diffusion process itself is performed in two steps. During the first step, the dopant impurities (e.g. phosphorus in the form of P_2O_5 or $POCl_3$ vapor) react with silicon dioxide to form a glass. As the process continues the thickness of the glass increases until the entire silicon oxide layer above the later junction is converted into glass (e.g. phosphosilicate glass). The thicker oxide on top of the non-junction areas is not completely converted and thus masks these areas during the second step. After the glass formation, the second step begins. The dopant impurity diffuses through the glass; upon reaching the glass-silicon interface, it enters and diffuses into the silicon [Sze85]. Note that there exist also other techniques for forming diffused junctions (e.g. the technique used by ITE [ITE] for boron and arsenic diffusion; see Sec. 2.2.2.2).

A third possibility to produce a junction is a metal-semiconductor (*Schottky*) contact. Schottky-diodes are formed by evaporation of e.g. a gold layer on n-type silicon for the front contact and an aluminum layer for the ohmic back contact (see e.g. [Rho88]).

[9] R_p = projected range

2.2.2 Test structures used in this work

Although different manufacturers may use in principle the same process technology, there are many details that are individually optimized in order to ensure reliable and robust production and operation. These informations are usually treated as commercially sensitive information. Therefore not all details about the test structures are known and as a result the description given here can only be incomplete. However, as will be shown in Chapter 5, no influence of the different process technologies and producers was found in this work on the observed radiation induced changes of the silicon bulk materials.
Although many different detector types have been used in this work only the three major ones with different junction processes – implantation from MPI-Halbleiterlabor München, diffusion from ITE-Warsaw and Schottky barriers as produced in our own lab – will be described in some more detail. The main features of all other diodes are summarized in the last part of this section.

2.2.2.1 Implanted diodes produced by MPI - Munich

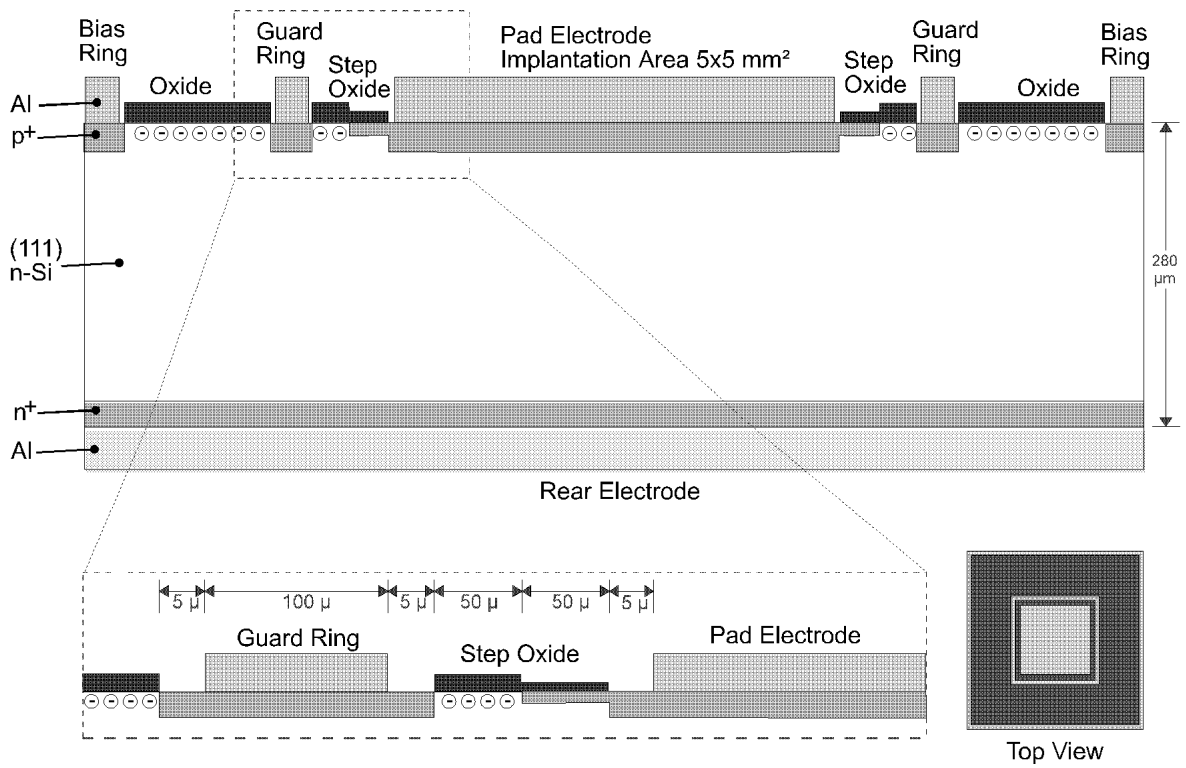

Figure 2.4: Schematic cross section of a MPI München $p^+-\nu-n^+$ structure with a p^+ guard ring around an active area of a $p^+-\nu$ junction (structures labelled WM2-3kΩcm in Tab. 2.2).

Fig. 2.4 shows a cross section of a diode with implanted junctions (labelled WM2-3kΩcm, see Tab. 2.2) provided by the semiconductor laboratory of the MPI München

[MPI]. On the rear side the oxide is completely removed and the n^+-implant is covered with a 370 nm thick aluminum layer ($100\,\mu g/cm^2$). On the front side there are two different oxide layers. While the unimplanted regions are covered by a 110 nm thick oxide (used to fully mask the silicon during the 12.5 keV boron implantation) a thinner oxide (about 50% of the full oxide thickness) covers the edge regions of the implanted junction. This so-called *step oxide* does not fully mask the silicon during the implantation. Therefore the edges of the implanted junction are tailored and the problems arising from high fields at those edges are minimized. The implanted regions are covered with a 1.2 μm thick aluminum metallization. The implanted junction area is 25 mm^2 and surrounded by a single *guard ring* and a *bias ring*. The guard ring is operated under the same bias conditions as the front electrode and is therefore capable of sinking leakage currents generated outside the pad area. In all the measurements in this work the guard ring, if used, was connected to ground and the pad to the low potential input of the measurement equipment (essentially ground too). The bias ring is thought to bias (high voltage) the device from the front side. However, due to a contact resistance between the bias ring p^+– and the backside n^+–implant the possibility to bias the diode in such way was not used and instead the biasing was achieved via the back side aluminum contact.
These diodes (same bulk material) have previously been used for investigations on bulk radiation damage ([Sch96a, Fei97a]) and lateral extension of the space charge region probed by a scanning proton micro beam [Osi95, Wun96].

2.2.2.2 Diffused diodes produced by ITE – Warsaw

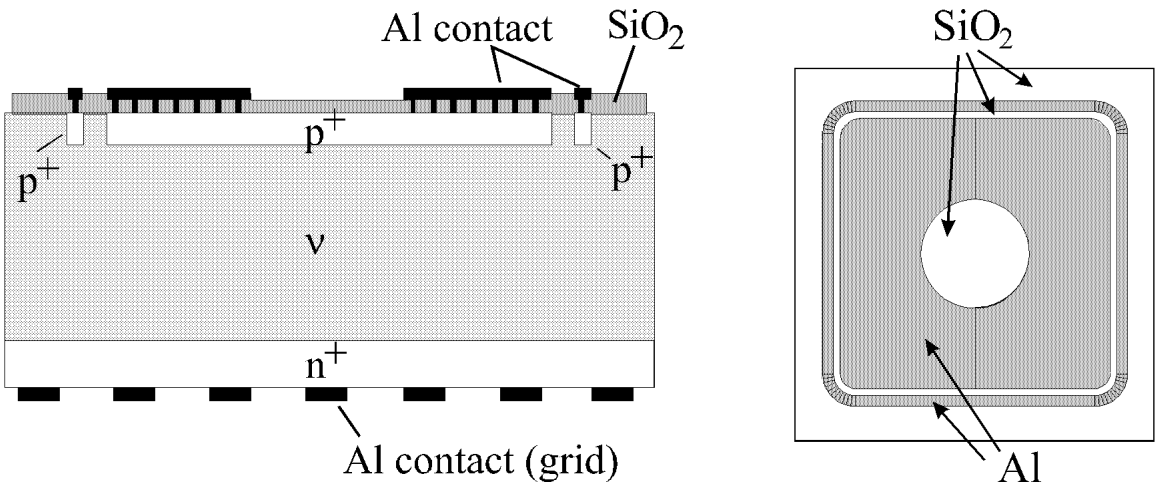

Figure 2.5: Schematic cross section (left) and top view (right) of an ITE p^+–ν–n^+ structure with a p^+ guard ring around an active area of a p^+–ν junction (after [Weg98]). The structures are labelled WI# or II# in Tab. 2.2.

Two types of diodes produced by ITE – Warsaw have been used in this work. A schematic cross section of the first one – used for n-type material and named FLM3A – is shown in Fig. 2.5. The active area of 5×5 mm^2 is surrounded in a distance of 100 μm by a guard ring of 200 μm width. The p^+ junction depth is about 0.6 μm and

the surface boron concentration is $> 5 \times 10^{19}\,\mathrm{cm}^{-3}$. The n^+ (back) side is phosphorus diffused with a junction depth of $\approx 7\,\mu$m and a surface concentration of $> 10^{21}\,\mathrm{cm}^{-3}$. The final oxide thickness is about 110 nm on top of the p^+ regions and about 550 nm on the rest of the front side. A grid of holes in the oxide ($20\,\mu\mathrm{m} \times 20\,\mu\mathrm{m}$) with a distance of $100\,\mu$m from each other allow the contact between the diffused phosphorus layer and the aluminum metallization on the front side. A hole of 2 mm diameter is left in the front metallization as a transparent window for optical charge injection techniques. For the same reason the back side metallization is realized as an aluminum grid structure directly deposited on the silicon with a strip thickness of $40\,\mu$m and openings of $370 \times 370\,\mu\mathrm{m}^2$. The grid is 45° rotated with respect to the quadrangular chip. The overall cut detector has an area of 7×7 mm^2 from cutting edge to cutting edge [Weg98].
ITE is one of the companies that is relatively freely distributing some more detailed information about the used detector production process. Therefore this kind of detector was chosen as an example to describe the production process in more detail. The indicated high temperature process times are corresponding to the highest temperature during a specific process step and do not include ramping times [Weg98, Weg99].

- Preliminary cleaning
- Oxidation at 1000°C for 190 min; thickness of oxide $d_{ox} = 750$ nm
- Forming of back side ohmic n^+–ν contact:
  - Oxide etching of back side (front side is masked)
  - Forming of phosphorus-silicon glass with $POCl_3$ vapor (23 min at 1050°C). During the heating process phosphorus diffuses from the glass into the silicon (front side is masked by the thick oxide). For details see description in Sec. 2.2.1.
  - Glass etching (whole wafer).
  - Oxidation at 1000°C for 86 min (+phosphorus re-diffusion); thickness of oxide on back side $d_{ox} = 400$ nm.
- Forming of front side p^+–ν junction:
  - Photolitography of p^+ region (pad area and guard ring).
  - Oxide etching on front side (back side is masked with photoresist)
  - Photoresist removing
  - Deposition of a thin boron doped amorphic silicon layer by LPCVD[10] method.
  - Heating - diffusion of boron from the deposited layer into the silicon (the areas other than the front side junction and guard ring are masked by the oxide). During the heating the amorphic layer is oxidized and converts into boron-silicon glass.
  - Glass etching (whole wafer).
  - Boron re-diffusion for 6 min at 1085°C from the thin boron layer diffused in last heating step. At the same time oxidation takes place.
- Photolithography; oxide etching; photoresist removing
  - front side: windows for contact holes
  - back side: oxide completely removed ($\rightarrow$ diodes have no oxide on back side)
- Evaporation of Al:Si on front side
- Evaporation of Al on back side
- Al photolithography of front side (pad and guard); Al etching (back side is masked); photoresist removing

[10]LPCVD = Low Pressure Chemical Vapor Deposition

- Al photolithography of back side (grating); Al etching (front side is masked); photoresist removing
- Al alloying at 450°C

Meanwhile this structure has widely been used within the ROSE-collaboration (see e.g. [ROS98b]) and is now a standard tool for radiation damage investigations on n-type materials.

The second detector type produced by ITE – used for p-type material and named FLM3B – has in principle the same layout as shown in Fig. 2.5 with only two basic differences. First, the front contact and guard ring consist of arsenic diffused junctions (LPCVD–method) and the back contact of a boron implanted one and second, an additional boron implanted channel stopper (a p^+–ring with a thickness of 200 μm and located in a distance of 100 μm around the guard ring) protects the detector area (the n^+–diffused regions) from surface currents originating from the contact with positive SiO_2/Si interface charges. However, one important drawback of this structure is a missing second channel stopper between the pad and the guard. In radiation tests with ionizing particles this has already led to some problems (see Chapter 8). The n^+ junction depth is 0.5 μm with a surface arsenic concentration of $> 5 \times 10^{19}$ cm^{-3}. The implanted boron junction depth is $\approx 3.5\,\mu$m with a surface concentration of $> 10^{21}$ cm^{-3}. One special feature of this diode is the metallization. A titanium–tungsten–aluminum layer is deposited without any subsequent high temperature treatment. This has been done to avoid the final aluminum alloying step at about 450°C since at this temperature thermal donors are produced in highly oxygenated materials that change the effective space charge density of the detector bulk material (for details see Sec. 3.6.2).

2.2.2.3 Surface Barrier Diodes produced in Hamburg

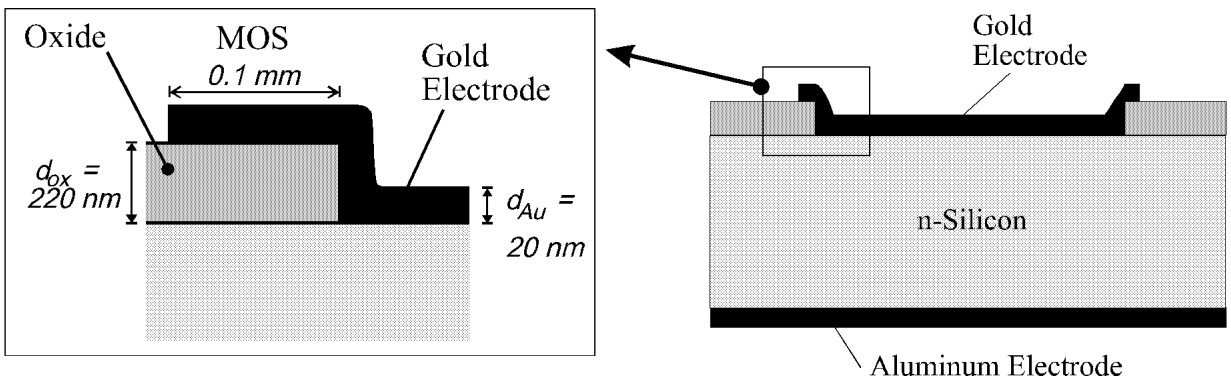

Figure 2.6: Schematic cross section of a surface barrier structure produced in the Hamburg laboratory.

A schematic cross section of a surface barrier diode produced in the Hamburg laboratory is shown in Fig. 2.6. The relatively simple process for such a diode starts with the oxidation of n-type wafers. Afterwards windows for the front contact (normally

a circle with a diameter of 7 mm) are defined in a photolitographic step and etched into the oxide in a subsequent etching step. Furthermore the oxide on the rear side of the wafer is completely removed. The front electrodes are then evaporated through an aligned mask which results in a metallization overlapping the oxide edge by about 100 μm (MOS-structure[11], see Fig. 2.6). Gold or palladium ($40\,\mu g/cm^2$) is used for forming the Schottky contact on the front side while the whole back side forms an ohmic contact via an evaporated aluminum layer ($100\,\mu g/cm^2$). Finally the wafers are surface protected with a standard varnish and cut to their exact sizes using a high speed diamond saw. The surface protection is removed before the diodes are used for radiation damage experiments. A detailed description of the production process in the Hamburg laboratory can be found in [Fre87, Fre90].
Although these structures do not have a guard ring and it is therefore difficult to determine the exact bulk generation current the effective doping concentration can be determined very accurately via the depletion voltage. Furthermore they offer the advantage of a fast manufacturing process since only the oxidation has to be ordered from an external company. The production has even been accelerated for some of the used materials by completely abandoning the oxide surface protection and evaporating the contacts directly on the naked silicon. This results in a very high leakage current due to surface generation current (up to several $10\,\mu A$) but still enables the possibility of measuring the depletion voltage. Since DLTS measurements (see Sec. 4.4) are not seriously influenced by high leakage currents these structures are very well suited for defect analysis. Because no high temperature step is needed for device production there is also no danger of contaminating the material with process induced defects, like observed in some of the commercially processed structures.

2.2.2.4 Further diodes and labelling of devices

ELMA
The test structures produced by Elma [ELM] were exclusively processed on standard high resistivity float zone n-type silicon and have mainly been used for fluence normalization via the so-called alpha–value (see Sec. 5.2). The junctions are implanted and the active area (provided the guard ring is properly used) is $0.24\,cm^2$. Around the inner guard ring three additional potential rings are disposed in order to stabilize the electric field.

Canberra and Sintef
Further test structures, used for only a few experiments in this work, have been produced by Sintef [SIN] (diffused junctions) and Canberra [CAN] (implanted junctions). Both companies used the so-called CERN II mask (produced by Canberra for the ROSE collaboration) that is described in more detail in Refs. [Dez97, Cas98b].

Diotec
Another kind of production technology has been used by DIOTEC [DIO] to fabricate so-called mesa diodes. Here non-oxidized HF-etched silicon wafers are stacked in a

[11] MOS = Metal–Oxide–Semiconductor

producer	technology	guard ring	area [cm^2]	front and back contacts & comments	devices (label)
Hamburg	Schottky	No	0.442	cross section shown in Fig. 2.6 passivation: thermal oxide front: Pd – circle back: Al – fully covered	974, 975, 97F 97G, 97H (PH-140Ωcm) (IH-140Ωcm)
		No	0.442	passivation: non front: Pd – circle back: Al – fully covered	962, 963 (PH-110Ωcm)
		No	0.442	passivation: non front: Au – circle back: Al – fully covered	933
MPI	implanted	Yes d:50 μm w:110 μm	0.25	cross section shown in Fig. 2.4 front: B, Al, circle or square back: P, Al, fully covered	M1, M2 (WM2-3kΩcm)
		Yes d:10 μm w:100 μm	0.25	double sided structure, square front: Al with hole + guard back: Al with hole + guard	M3D (WM3-3kΩcm)
ITE	diffused	Yes d:100 μm w:200 μm	0.25	mask: FLM3A (see Fig. 2.5) front: B, Al square with hole back: P, Al–grid	WI, II
	diffused(As) and implant.(B)	Yes d:100μm w:200μm	0.25	mask: FLM3A + p-stop ring front: As,Ti:W:Al square/hole back: B, Ti:W:Al grid	MI
ELMA	implanted	Yes d$\approx$30 μm w$\approx$30 μm	0.24	front: Al, square back: Al, fully covered	60, 61, 72, (WE-7kΩcm), (WE-25kΩcm)
Sintef	diffused	Yes	0.25	mask: CERN II	ST
Canberra	implanted	Yes	0.25	mask: CERN II	C142
Diotec	mesa	No	0.25	front: B, Ni-Au fully covered back: P, Ni-Au fully covered	IB, IBP

Table 2.2: Labelling and some properties of the used test structures provided by different producers (see text). Approximate values, indicated by a ($\approx$), were determined by measuring the size of the metallization.

sandwich-like pile with boron and phosphorus containing paper sheets. This pile is put into an oven at 1150°C for about 3 to 4 hours. Thus, the diffusion of the front junction and the ohmic contact is achieved simultaneously. Afterwards both sides of the wafer are covered with a Ni-Au layer. Then the wafers are cut into quadrangular pieces (diodes) of 5×5 mm and the cut edges are passivated with so-called silicon rubber. A more detailed description of the diode production can be found in [Dez97]. Although this production technology is a very fast one and does neither need oxidized wafers nor any diffusion or implantation masks it has an important drawback. The single diffusion step for boron and phosphorus at the same time from papers attached to the wafer surfaces can lead to inhomogeneous junctions. SIMS (Secondary Ion Emission) and spreading resistivity depth profiles of the boron and phosphorus concentrations have revealed junction depths of up to $20\,\mu$m on both the p^+ and n^+ side [Dez97].

Labelling of devices
Tab. 2.2 gives some properties of the used test structures provided by the different producers. Furthermore the abbreviations used for the labelling in this work are displayed. The individual test structures are labelled by an 8 digit alphanumerical name[12]. The leading digits, as given in the last column of Tab. 2.2, identify the detector producer and the material (see also Tab. 4.1) while the following digits identify the individual test structures on the corresponding wafers. The value A given for the area is the effective area of the pad provided the guard ring is properly used. This value has also been used for the calculation of detector properties (effective doping concentration, bulk generation current density, etc.) if not mentioned otherwise. For the Schottky diodes the active area is bigger than the pad area since the lateral extension of the electric field has to be taken into account [Fre87, Wun92]. For the guard rings d denotes the distance between the implanted (or diffused) pad and the implanted (or diffused) guard ring while w gives the width of the guard ring. Further information in the table describes the front and back contacts in more detail.

2.3 Basic features of silicon diodes

2.3.1 p-n junction

In order to explain the operation of a p-n diode one may imagine the opposite sides of the junction originally isolated, and then brought into intimate contact. Thermal equilibrium is established as equal numbers of highly mobile electrons and holes, from the n-type and the p-type material, respectively, recombine. A potential difference Φ_{bi} which prevents further charge flow is maintained by the static space charge built up around the junction by the ionization of the donor and acceptor atoms in the doped semiconductor. This region is effectively depleted of all mobile charge carriers and the voltage corresponding to the potential difference is called *built-in voltage* V_{bi}. In the case of an abrupt p-n junction one side is more heavily doped than the other

[12]Restriction to 8 digits due to the used DOS version for data storage.

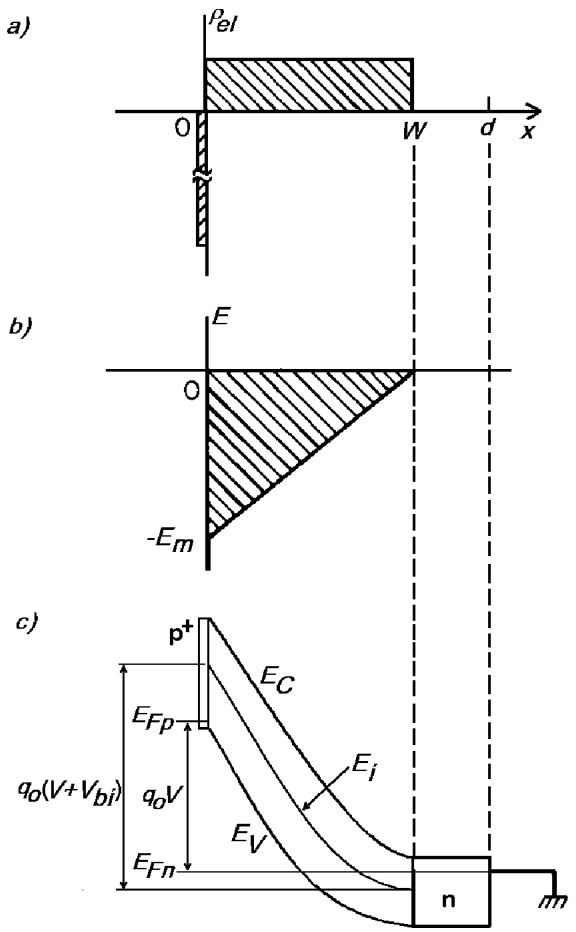

Figure 2.7: Schematic figure of a p^+-n abrupt junction: a) electrical charge density, b) electric field strength, c) electron potential energy.

and overall charge neutrality then implies that the depletion region of thickness W extends much further into the less heavily doped side of the device. This is displayed in Fig. 2.7 a) for a reverse biased abrupt $p^+ - n$ diode of thickness d under the assumption of a homogeneous distribution of dopant atoms. Furthermore the so-called *depletion approximation* is assumed to be valid which demands that the space charge is constant in the region $0 < x < W$, although it is known that the diffusion of electrons from the n-type bulk into the depletion zone results into a smooth distribution of the charge around x = W. The electric field strength and electrochemical potential can be calculated by solving Poisson's equation:

$$-\frac{d^2\Phi(x)}{dx^2} = \frac{\rho_{el}}{\epsilon\epsilon_0} = \frac{q_0\, N_{eff}}{\epsilon\epsilon_0}. \tag{2.3}$$

Here N_{eff} denotes the effective doping concentration which is given by the difference between the concentration of ionized donors and acceptors in the space charge region. Furthermore $\epsilon\epsilon_0$ stands for the permittivity of silicon with $\epsilon_0 = 11.9$. The first integration of Eq. 2.3 with the boundary conditions $E(x=W) = -\frac{d}{dx}\Phi(x=W) = 0$ leads to an expression for the electrical field strength which depends linearly on x (see Fig. 2.7 b))

and reaches the maximum field strength of

$$E_m(V) = -\frac{q_0 N_{eff}}{\epsilon\epsilon_0} W(V) \tag{2.4}$$

at the $p^+ - n$ interface (x=0). A further integration under the boundary condition $\Phi(x = W) = 0$ leads to a parabolically function for the potential:

$$\Phi(x) = -\frac{1}{2}\frac{q_0 N_{eff}}{\epsilon\epsilon_0}(x - W)^2 \qquad \begin{array}{l}\text{for} \quad 0 \le x \le W \\ \text{and} \quad W \le d\,.\end{array} \tag{2.5}$$

The corresponding electron potential energy $(-q_0\Phi)$ is schematically displayed in Fig. 2.7 c). There it is also indicated that the applied reverse bias V is equal to the difference between the Fermi levels in the p^+ and n region, E_{Fp} and E_{Fn}, which, of course, in the case of thermal equilibrium have to be the same as the overall electrochemical potential. With the condition $\Phi(x = 0) = -V_{bi} - V$ one obtains an expression for the depletion depth:

$$W(V) = \sqrt{\frac{2\epsilon\epsilon_0}{q_0|N_{eff}|}(V + V_{bi})} \quad \text{for} \quad W \le d. \tag{2.6}$$

With increasing reverse bias the field zone expands until the back contact is reached (W=d). The corresponding voltage, needed to fully deplete the diode, is called *depletion voltage* V_{dep} and connected with the effective doping concentration N_{eff} by:

$$V_{dep} + V_{bi} = \frac{q_0}{2\epsilon\epsilon_0}|N_{eff}|d^2 \tag{2.7}$$

Very often the built-in voltage V_{bi} is neglected since the depletion voltage is in most cases more than one order of magnitude higher. However, if one wants to obtain an even more exact expression for the depletion voltage also the *Debye-tail* of the carrier distribution at the edges of the depleted zone has to be taken into account. In such a case the depletion approximation is no more valid and V_{bi} has to be replaced by $V_{bi} + k_B T/q_0$ in the equations above [Sze81].

2.3.2 Capacitance

The dynamic junction capacitance is defined as $C = dQ/dV$, where dQ is the incremental change in depletion layer charge for an incremental change in the applied voltage dV. The space charge Q is given by $Q = q_0 N_{eff} A W$ with A being the area of the diode. Therefore, the differential dQ is given by $q_0 N_{eff} A\, dW$ and with the help of

$$C = \frac{dQ}{dV} = \frac{dQ}{dW}\frac{dW}{dV} \tag{2.8}$$

and the first derivative of Eq. 2.6 with respect to V one gets the following expression for the junction capacitance:

$$C(V) = \epsilon\epsilon_0 \frac{A}{W(V)} = A\sqrt{\frac{\epsilon\epsilon_0\, q_0\, |N_{eff}|}{2\,(V + V_{bi})}} \qquad \begin{array}{l}\text{for} \quad W \le d, \\ (\text{resp.} \quad V \le V_{dep}).\end{array} \tag{2.9}$$

With increasing voltage the capacitance decreases with $C \propto 1/\sqrt{V}$ and reaches with full depletion ($V = V_{dep}$; $W = d$) a final value of

$$C_{geo} = \frac{\epsilon\epsilon_0 A}{d}. \tag{2.10}$$

This capacitance is called the *geometrical capacitance* since it only depends on the geometrical size of the diode. Applying voltages higher than the depletion voltage does not change the depletion depth any more. Therefore also the capacitance should stay constant. However, in practice one observes, especially with floating guard ring, very often a slight decrease of the capacitance for voltages higher than the depletion voltage. This is due to lateral extension of the field zone.

2.3.3 Forward current

Although the radiation damage induced change in the forward current characteristics was not investigated in this work (for such experiments see e.g. [Cro96, McP97]), the mechanism of forward current generation is very important for the understanding of the DLTS and TSC methods described in Secs. 4.4 and 4.5, respectively.
The ideal forward current characteristics of a p^+-n junction for $V \geq 3k_BT/q_0$ can be described by [Sze85]

$$\begin{aligned} I &= I_{rec} + I_{diff} \\ &= q_0 A \frac{W n_i}{2\tau_r} \exp\left(\frac{q_0 V}{2k_B T}\right) + q_0 A \sqrt{\frac{D_p}{\tau_p}} \frac{n_i^2}{N_D} \exp\left(\frac{q_0 V}{k_B T}\right). \end{aligned} \tag{2.11}$$

Here I_{rec} denotes the recombination current caused by traps in a diode with area A and a depleted region of thickness W. If the recombination lifetime τ_r is dominated by only one defect of concentration N_t, it can be described as $\tau_r = 1/(\sigma v_{th} N_t)$ where σ denotes the capture cross section of the defect (for details see Sec. 3.4). n_i is the intrinsic carrier concentration (see Sec. 3.4.1.2). The second term in Eq. 2.11 describes the diffusion current of holes from the p^+ region into the bulk with a donor density of N_D. D_p is the diffusivity of holes and τ_p the hole life time which are related with the diffusion length of holes by $L_p = \sqrt{D_p \tau_p}$. Experimental results are often represented by

$$I(V) \propto \exp\left(\frac{q_0 V}{\eta k_B T}\right) \tag{2.12}$$

with η being the so-called *ideality factor*. When the ideal diffusion current dominates, η equals 1; whereas when the recombination current dominates, η equals 2. When both currents are comparable, η has a value of between 1 and 2.

The forward diode characteristic of a Schottky diode is governed by the thermoionic-field emission current of electrons from the bulk into the metal contact. This is the reason why, in contrast to $p^+ - n$–junctions, minority carrier traps can not be filled in

DLTS measurements by switching the diode to forward bias. The forward current can be described by[13]

$$I_{Schottky}(V) = AA^{**}T^2 \exp\left(-\frac{q_0\phi_B}{k_BT}\right)\left(\exp\left(\frac{q_0V}{k_BT}\right) - 1\right). \tag{2.13}$$

Here A^{**} denotes the effective Richardson constant and ϕ_B the barrier heights. The experimental values for the devices produced according to the Hamburg group process with a gold front contact (see page 18) are of the order of $100\,\mathrm{AK^{-2}cm^{-2}}$ for A^{**} and about 0.92 eV for ϕ_B [Als93].
It has to be noted that in case of high currents the voltage drop due to the bulk (series) resistivity has to be taken into account in Eqs. 2.11, 2.12 and 2.13 by replacing V with $V - I_{forward} \times R_{bulk}$.

2.3.4 Leakage current

The current of a reverse biased diode is called *leakage current* or *reverse current*. While the reverse current of an ideal diode consists only of a diffusion current (*saturation current* I_S) in reality impurities, contaminations and process induced defects in the silicon, Si/SiO_2 interface states and further edge and interface effects contribute to the current making it difficult to produce detectors with leakage currents lower than $1\,\mathrm{nA/cm^2}$.
However, the radiation induced leakage current can be divided into two basic components. The first one, the *bulk generation current* (I_{bulk}), arises from electron-hole pair generation at radiation induced defects in the silicon bulk that are energetically located close to the middle of the band gap, while the second one, the *surface generation current*[14], is due to radiation induced SiO_2–Si interface states. Depending on the kind of radiation and the structure of the diode the one or the other component dominates. Since the oxide charge and interface states are introduced by ionizing radiation (photons or charged particles) the surface current is of no major concern for the neutron irradiations performed in this work. However, for the proton damage studies it had to be taken into account and for the gamma-irradiations it was a serious problem to distinguish between surface and bulk current. More information about surface current and its radiation induced generation can be found in [Nic82].
The investigations in this work were concentrated on the bulk generation current. Because only defects located in the space charge region contribute to the bulk generation current, it depends on the voltage in the same way as the width W of the depleted zone (Eq. 2.6)

$$I_{bulk} \propto W \propto \sqrt{V} \qquad \text{for } V \leq V_{dep} \tag{2.14}$$

[13] For restrictions see [Rho88] and [Sch90].

[14] Contributing to the leakage current for voltages higher than the flat-band voltage (see e.g. [Wun92]).

and saturates when the applied voltage reaches the depletion voltage. The bulk generation current is often described by the *generation life time* τ_g (compare Sec. 3.7)

$$I_{bulk} \propto \frac{W}{\tau_g} \tag{2.15}$$

A further important feature of the bulk generation current is the strong temperature dependence. In this work all current measurements performed at "room temperature" have been scaled to a reference temperature of $T_R = 20°\mathrm{C}$ by [Sze85]:

$$I(T_R) = I(T) \cdot R(T) \quad \text{mit} \quad R(T) = \left(\frac{T_R}{T}\right)^2 \exp\left(-\frac{E_g}{2\,k_B}\left[\frac{1}{T_R} - \frac{1}{T}\right]\right). \tag{2.16}$$

For the band gap E_g a value of 1.12 eV was used. As an example one has to subtract 15% from the measured current at 22°C to scale it to the reference temperature T_R of 20°C (R(22°C) = 0.85).

2.4 Operation of silicon detectors

This section can only give the basic features of the operation of silicon detectors. For further details the reader is referred to [Hal94, Kno89] and [Ber68].

2.4.1 Basic principle of detector operation

A silicon detector is a diode operated under reverse bias with the depleted zone acting as a *solid state ionization chamber*. If the incident particle is stopped in the detector the particle energy can be measured (spectroscopy), if the particle is traversing the detector it is only possible to state whether or not a particle has passed (tracking). The latter case is the main application of silicon detectors in high energy physics.
A minimum ionizing particle (mip) traversing a silicon layer of $d = 300\,\mu$m thickness deposits most probable an energy of ≈ 90 keV. Although the energy gap in silicon is about 1.12 eV at room temperature the required average energy to produce an electron-hole pair is $\approx 3.6\,$eV. Thus most probable about 25000 electron-hole pairs (≈ 4 fC) are created by a mip (about 85 e-h pairs per μm) [Cas98a]. If the detector is fully depleted all generated electrons and holes are drifting in the applied field with their drift velocities $v_{dr,n}$ and $v_{dr,p}$ in direction of the anode and cathode, respectively (see Fig. 2.8 on page 30). The current influenced by a single charge carrier can be described by Ramo's theorem:

$$I = q_0 \frac{v_{dr,n,p}}{d} \quad \text{with} \quad v_{dr,n,p} = \mu_{n,p}(E(x)) \times E(x). \tag{2.17}$$

The mobility $\mu_{n,p}$ is depending on the field strength E and the field strength itself is depending on the depth x in the detector (see Fig. 2.7).
The resulting current pulse signal of a few 10 ns is sunk into the high frequency branch of a electrical circuit consisting of a coupling capacitor and a charge amplifier. The output is proportional to the overall generated charge in the detector if the detector is fully depleted.

Property	Si	Ge	GaAs	Diamond
Atomic number (Z)	14	32	31/33	6
Atomic weight (A)	28.1	72.6	144.6	12.0
Density [g cm^{-3}]	2.33	5.32	5.32	3.51
Atoms 10^{22} cm^{-3}	4.96	4.41	4.43	17.7
Crystal structure	diamond	diamond	zincblende	diamond
Lattice constant [Å]	5.43	5.64	5.63	3.57
Thermal conductivity [$W cm^{-1} K^{-1}$]	1.5	1.05	0.45	10–20
Dielectric constant (ϵ)	11.9	16.0	13.1	5.7
Band gap [eV]	1.12	0.66	1.42	5.47
	indirect	indirect	direct	indirect
Energy to create e–h pair [eV]	3.6	2.9	4.3	13
Radiation length [cm]	9.4	2.3	2.3	18.8
Average minimum ionizing energy loss [MeV $g^{-1} cm^2$]	1.66	1.37	1.45	1.75
Average signal [e-h/μm]	110	260	130	36
Electron mobility [$cm^2 V^{-1} s^{-1}$]	1450	3900	8500	1800
Hole mobility [$cm^2 V^{-1} s^{-1}$]	450	1900	400	1200
Intrinsic carrier density (n_i) [cm^{-3}]	1.1×10^{10}	2.4×10^{13}	1.8×10^6	$< 10^3$
Intrinsic resistivity [Ωcm]	3.1×10^5	47	10^8	$> 10^{11}$
Saturation field [V cm^{-1}]	2×10^4	8×10^3	3×10^3	2×10^4
Saturation velocity (e) [10^6 cm s^{-1}]	10.5	5.5	8.0	22

Table 2.3: Basic properties of Silicon, Germanium, Gallium Arsenide and Diamond at room temperature (300 K) [Hal94, Sze85, Mad89, Fri98, Ber68, Can71, Gre90].

2.4.2 Why silicon?

Before trying to improve the radiation hardness of silicon in order to allow for operation in very intense radiation environments, one should look for an alternative material that could do the job. However, as a comparison with other detector materials shows, silicon is still the best choice of material for tracking purposes and is worth to be developed for more radiation hardness.
In Tab. 2.3 the basic silicon properties are compared to some further detector materials (Germanium, Gallium Arsenide and Diamond). Silicon crystals have a diamond lattice structure[15] with a lattice constant a of 5.43 Å. The indirect bandgap is about

[15] A diamond lattice is consisting of two interpenetrating face-centered cubic (fcc) sublattices with one sublattice displaced from the other by one quarter of the distance along a diagonal of the cube (displacement of $a\sqrt{3}/4$).

1.12 eV at room temperature. Besides the good physical properties with respect to the application as detector material one should keep in mind the huge advantage coming from the exploitation of silicon by the microelectronics technology that already lead to the very high developed processing technology of silicon.

Germanium offers excellent properties for gamma ray spectroscopy. However, due to its small band gap it has to be operated cryogenically (normally 77 K) and is therefore not very attractive for tracking purposes.

Gallium Arsenide with a direct bandgap of 1.42 eV can easily be operated at room temperature. The electrical properties, especially the internal electrical field strength distribution, of semi-insulating (high resistivity) GaAs are dominated by the presence of the arsenic antisite defect EL2, which has two donor levels (double donor) close to the middle of the band gap. Since this defect is present in the material in high concentrations (typical in the order of some $10^{16}\,\mathrm{cm}^{-3}$) it can compensate the shallow acceptors and make the material so-called *semi-insulating*. This defect is also the reason why there is no "depletion voltage" in GaAs and even after very high radiation fluences a moderate voltage can be used to "fully activate"(saturate) the charge collection. Unlike silicon the radiation damage does not show any annealing effects and the noise is believed to be not seriously influenced by radiation damage [Rog97a]. However, recently it has been shown that gallium arsenide is not, as believed for a long time, radiation harder than silicon. With increasing high energy particle fluence – particularly for charged hadrons – a dramatical degradation of charge collection efficiency (CCE) was observed [Rog97a, Rog97b, Chi97]. It is, for example, expected that the CCE after 10 years of operation in the ATLAS inner detector[16] ($\Phi_{eq,GaAs} = 1.1 \times 10^{15}\,\mathrm{cm}^{-3}$)[17] would lie in the order of only 25% ($\approx 6500\,e^-$; $d = 200\,\mu$m; 200 V) with a signal to noise ratio of only 5.4 for the envisaged detector system [Rog97a].

Diamond for detector purposes is usually chemical vapour deposited (CVD) diamond which grows in a polycrystalline columnar structure. With a band gap of 5.5 eV diamond is an insulator with only a very small carrier concentration ($< 10^3\,\mathrm{cm}^{-3}$) and a very high resistivity ($10^{11}\,\Omega$cm) at room temperature. Consequently diamond has not to be "depleted" and there is no need for a diode structure to build a detector. Metal layers (e.g. Cr-Au or Ti-Pt-Au) are sufficient for the contacts. Furthermore it shows an excellent radiation hardness; no significant decrease in charge collection distance[18] was e.g. observed up to 5×10^{14} neutrons/cm^2 and 1.8×10^{15} pions/cm^2 (300 MeV/c) [Fri98]. However, the high energy needed to produce an e-h pair (13 eV) and the polycrystalline structure, leading to the fact that the collection distance is al-

[16] GaAs wheel in inner detector system at $R = 30$ cm.

[17] The corresponding value for silicon is $\Phi_{eq,Si} = 1.4 \times 10^{14}\,\mathrm{cm}^{-2}$. 1MeV neutron displacement damage for GaAs and Si: D_{GaAs}(1 MeV n) = 70 MeVmb [Oug90], D_{Si}(1MeV n) = 95 MeVmb (compare Sec. 3.2). Hardness factors for GaAs: e.g. κ_{GaAs}(23 GeV protons)$\approx$ 7, κ_{GaAs}(192 MeV π^+)$\approx$ 9 (for more details see [Rog97a]).

[18] The charge collection distance is defined as $\delta = (\mu_e \tau_e + \mu_h \tau_h)E$ where $\tau_{e,h}$ is the lifetime and $\mu_{e,h}$ the mobility of the charge carrier.

ways smaller than the detector thickness, results in a relatively small signal compared to silicon. Furthermore the inhomogeneity of the material leads to an non-uniformity of charge collection efficiency over the detector area which might limit the achievable resolution of position sensitive devices [Beh98]. Currently a lot of work is under way to improve the diamond properties for the application of diamond in future tracking detectors [R42].

2.4.3 Signal to noise ratio

The signal to noise ratio is a key design specification of detectors since with an electronic noise level reaching the signal level no reliable operation is possible any more. Sources for the noise are the detector capacitance and the leakage current. The capacitance of a detector at depletion voltage does not change significantly due to radiation induced changes in the bulk material. However, ionizing radiation can produce charges in the silicon oxide and lead to additional noise by increasing e.g. the interstrip capacitance of microstrip detectors. Far more problematic is the strong radiation induced leakage current increase (see Sec. 5.1). To avoid a strong rise of noise (and an increase in power consumption and heat dissipation) the detector has to be cooled if operated in harsh radiation fields (compare Eq. 2.16). This also offers the further advantage of a suppressed reverse annealing (see Sec. 5.3.3).
However, since the leakage current problem can be solved by cooling the main problem of radiation damage arises not from the increase in noise but from the decrease in signal. Charge (signal) loss by trapping in radiation induced defects (see Sec. 3.7) and, more seriously, the radiation induced change of the depletion voltage are responsible for the degradation. The latter effect is of importance if the depletion voltage becomes larger than the operation voltage and the detector has to be operated in partial depletion. In such a case the charge generated in the undepleted volume does not contribute to the signal any more. Furthermore, the capacitance of an undepleted device is increased (compare Eq. 2.9) leading to additional noise. This is the reason why the major efforts of investigations on radiation damage in silicon are focused on the radiation induced changes in the effective space charge.

2.4.4 Microstrip and pixel detectors

The design of detectors used for tracking purposes is by far more complicated than the one of the test devices presented in Sec. 2.2.2. This is the reason why systematic radiation damage studies have to be performed on simple understandable structures and the results of the investigations have to be proved on "real" devices like microstrip and pixel detectors.
The most widely used semiconductor device for particle tracking is the silicon microstrip detector (Fig. 2.8). In its simplest form it is structured as a row of diodes on a single silicon wafer. Typical dimensions are 8-15 μm wide diodes with 25-50 μm pitch (distance from middle of one strip to middle of the next strip). The maximum length of such detectors is determined by the diameter of the used wafers (current standard

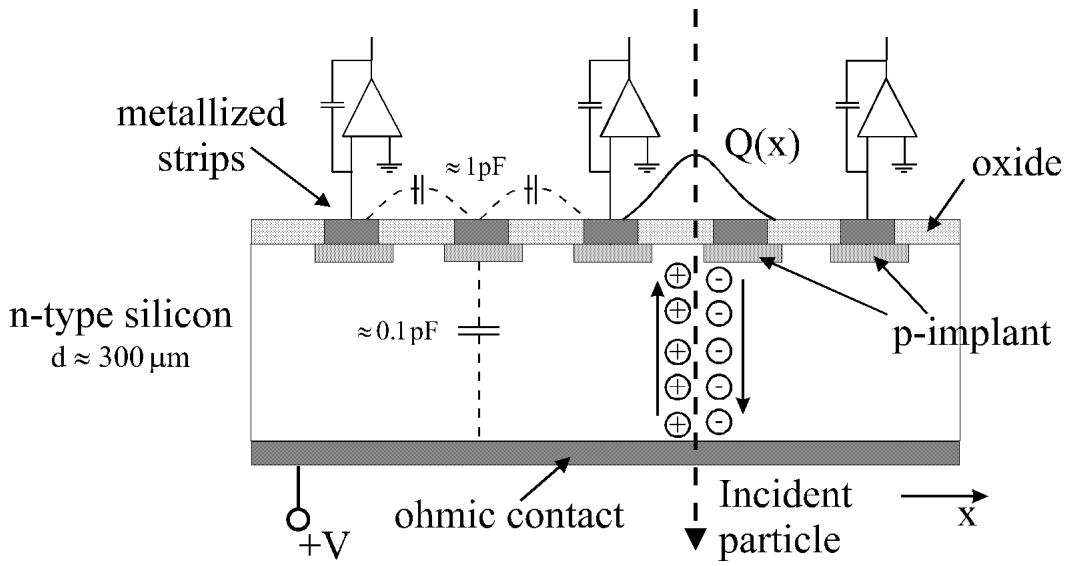

Figure 2.8: Schematic cross section of a silicon microstrip detector. Diffusion distributes the collected charge over multiple strips and capacitive charge division between the readout amplifiers allows position interpolation (after [Hal94]).

is 4"); longer detectors are constructed by bonding together shorter units. To operate diodes as a detector, either a low input resistance amplifier (*DC-coupled*) or a capacitively coupled amplifier with a large bias resistor (*AC-coupled*) is required. For more details see [Hal94]. Meanwhile the spatial resolution has reached values in the order of some μm. A further improvement is reached by using pixel detectors. They offer the possibility of a 2 dimensional localization of particle tracks without ambiguities like in double sided strip detectors. As an example the pixels in the ATLAS pixel detector will have a size of $50 \times 300\,\mu\mathrm{m}^2$ [ATL97].

Chapter 3

Radiation damage – Defects in silicon

Radiation damage in silicon detectors can roughly be divided in surface and bulk damage. The subject of this work is the bulk damage which is the limiting factor for the use of silicon detectors in the intense radiation fields close to the interaction point of high energy physics (HEP) experiments.

This chapter starts with the description of the basic radiation damage mechanisms initiated by the interaction of high energy particles (hadrons, leptons, photons) with the silicon crystal and resulting in the formation of point defects and defect clusters. It is shown how the radiation damage produced by different particles with different energies can be scaled under the assumption of the so-called *Non Ionizing Energy Loss (NIEL) hypothesis*. This leads to the hardness–factor concept enabling e.g. an intercomparison between different radiation sources and the calculation of the expected radiation damage in the mixed radiation fields of high energy physics (HEP) detectors. Subsequently the defects produced in the silicon lattice are classified by their electrical properties and the theory of defect occupation under various equilibrium and non-equilibrium conditions is described. A short review of identified defects relevant for this work – thermal donors and radiation induced defects – is given and finally the impact of defects on the electrical properties of silicon detectors is summarized.

3.1 Damage mechanism

The bulk damage produced in silicon particle detectors by hadrons (neutrons, protons, pions and others) or higher energetic leptons is caused primarily by displacing a *primary knock on atom* (PKA) out of its lattice site resulting in a silicon interstitial and a left over vacancy (Frenkel pair). Both can migrate through the lattice and may finally form point defects with impurity atoms being resident in the silicon. However, the primary recoil atom can only be displaced if the imparted energy is higher than the displacement threshold energy E_d of approximately 25 eV [Lin80]. The energy of a recoil PKA or any other residual atom resulting from a nuclear reaction can of course be

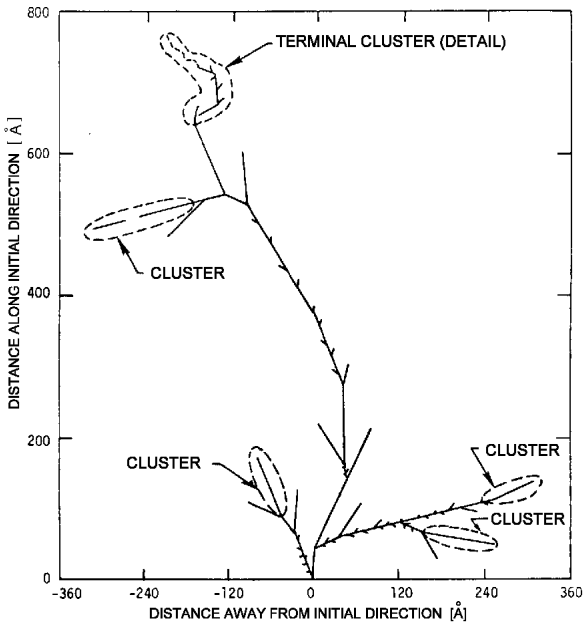

Figure 3.1: Monte Carlo simulation of a recoil-atom track with a primary energy E_R of 50 keV [Lin80].
The primary recoil energy of 50 keV has been chosen because it is approximately the average kinetic energy that a 1 MeV neutron imparts on a PKA. The PKA releases its energy over a distance of about 1000 Å to the silicon lattice. Approximately 37% of the recoil energy will go into ionization effects and the rest can displace further lattice atoms. In average 3 terminal clusters are produced with a typical diameter of about 50 Å [Laz87, Mue82].

much higher. Along the paths of these recoils the energy loss consists of two competing contributions, one being due to ionization and the other caused by further displacements. At the end of any heavy recoil range the nonionizing interactions are prevailing and a dense agglomeration of defects (*disordered regions* or *clusters*) is formed as displayed in Fig. 3.1. Both, point defects along the particle paths and the clusters at the end of their range, are responsible for the various damage effects in the bulk of the silicon detector. However, ionization losses will not lead to any relevant changes in the silicon lattice.
It is very instructive to calculate the maximum energy $E_{R,max}$ that can be imparted by a particle of mass m_P and kinetic energy E_P to the recoil atom by elastic scattering (nonrelativistic approach):

$$E_{R,max} = 4E_P \frac{m_P m_{Si}}{(m_P + m_{Si})^2} . \tag{3.1}$$

Taking into account the displacement threshold of $E_d \approx 25\,\text{eV}$ and a threshold energy of ≈ 5 keV for the production of clusters [Lin80] one can deduce that neutrons need a kinetic energy of ≈ 185 eV for the production of a Frenkel pair and more than ≈ 35 keV to produce a cluster. Electrons, however, need a kinetic energy E_e of about 255 keV to produce a Frenkel pair and more than ≈ 8 MeV to produce a cluster, if one takes into account the approximate relativistic relation $E_{R,max} = 2E_e(E_e + 2m_0c^2)/(m_{Si}c^2)$. Therefore the ^{60}Co gamma-irradiations, that have been performed within this work, can only produce Frenkel pairs. The ^{60}Co-photons with 1.17 and 1.33 MeV produce secondary electrons in the silicon chiefly by the Compton effect. The maximum energy transfered to the Compton electrons is about $E_{e,max} = 2E_\gamma^2/(1 + 2E_\gamma)$ [Cah59]. Thus the electrons produced by the ^{60}Co-photons have a a maximum energy of about 1 MeV which is not sufficient to create clusters.

With the displacement of a big number of silicon atoms from their lattice sites the dam-

age process has not ended. Interstitials and vacancies are very mobile in the silicon lattice at temperatures above 150 K. Therefore a part of the Frenkel pairs produced at room temperature annihilate and no damage remains. Simulations have shown that this is the case for about 60% of the overall produced Frenkel pairs and can reach in the disordered regions between 75% and 95% [Shi90].

The remaining vacancies and interstitials migrate through the silicon lattice and perform numerous reaction with each other and the impurity atoms existent in the silicon (for further details see Sec. 3.6). The defects produced by such reactions (point defects) and the defects within the clusters are the real damage of the silicon bulk material since their electrical properties are the reason for the macroscopic deterioration of the detector properties (for details see Secs. 3.4 and 3.7).

3.2 The NIEL scaling hypothesis

Charged hadrons interact with silicon primarily by the coulomb interaction at lower energies. Thus a big part of the particle energy is lost due to ionization of lattice atoms which is fully reversible in silicon. Neutrons, however, interact only with the nucleus. The main reactions are elastic scattering and above 1.8 MeV also nuclear reactions [Lin80]. Hence the question arises how the radiation damage produced not only by different kind of particles but also, depending on the particle energy, by different kind of interactions can be scaled with respect to the radiation induced changes observed in the material. The answer is found in the so-called *Non Ionizing Energy Loss (NIEL) hypotheses* which is explained in the following.

3.2.1 Displacement damage cross sections

The basic assumption of the NIEL hypothesis is that any displacement–damage induced change in the material scales linearly with the amount of energy imparted in displacing collisions, irrespective of the spatial distribution of the introduced displacement defects in one PKA cascade, and irrespective of the various annealing sequences taking place after the initial damage event.
In each interaction leading to displacement damage a PKA with a specific recoil energy E_R is produced. The portion of recoil energy that is deposited in form of displacement damage is depending on the recoil energy itself and can analytically be calculated by the so-called *Lindhard partition function* $P(E_R)$ [Laz87]. With the help of the partition function the NIEL can be calculated and is expressed by the *displacement damage cross section*[1]

$$D(E) := \sum_{\nu} \sigma_{\nu}(E) \cdot \int_0^{E_R^{max}} f_{\nu}(E, E_R)\, P(E_R)\, dE_R. \tag{3.2}$$

[1]Also called *damage function* and related to the NIEL by $D(E) = \frac{A}{N_A} \frac{dE}{dx}(E)\Big|_{\text{non ionizing}}$. The NIEL value can also be referred to as the displacement-*KERMA* (Kinetic Energy Released to MAtter). For silicon: $100\,\text{MeVmb} = 2.144\,\text{keVcm}^2/\text{g}$.

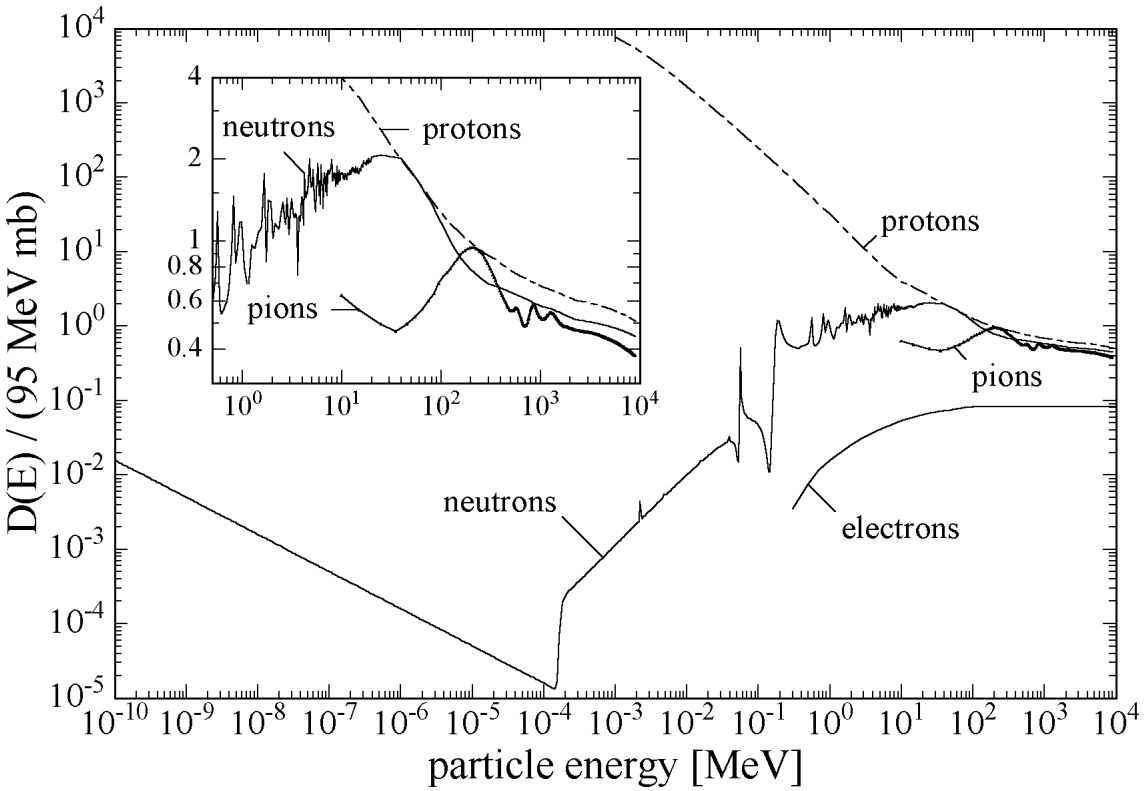

Figure 3.2: Displacement damage functions $D(E)$ normalized to 95 MeVmb for neutrons (10^{-10} to 20 MeV [Gri96], 20 to 400 MeV [Kon92], 805 MeV to 9 GeV [Huh93b]), protons [Huh93b, Sum93, Huh93a], pions [Huh93b] and electrons [Sum93]. Due to the normalization to 95 MeVmb the ordinate represents the damage equivalent to 1 MeV neutrons (see text). The insert displays a zoomed part of the figure.

Here the index ν indicates all possible interactions between the incoming particle with energy E and the silicon atoms in the crystal leading to displacements in the lattice. σ_ν is the cross section corresponding to the reaction with index ν and $f_\nu(E, E_R)$ gives the probability for the generation of a PKA with recoil energy E_R by a particle with energy E undergoing the indicated reaction ν. The integration is done over all possible recoil energies E_R and below the displacement threshold the partition function is set to zero $P(E_R < E_d) = 0$. Fig. 3.2 shows the displacement damage cross sections for neutrons, protons, pions and electrons in an energy range from 10 GeV down to some meV for the thermal neutrons as recommended in [ROS97]. A thorough discussion of these functions can be found in [Vas97a, Huh93b]. A few details should however be mentioned. As described in the last section the minimum neutron kinetic energy needed to transfer enough energy for displacements by elastic scattering is $\approx$ 185 eV. Yet, as displayed in Fig. 3.2 the damage cross section rises below that value with decreasing energy. This is entirely due to neutron capture, for which the

emitted gamma rays result in a recoil energy of about 1 keV, much higher than the displacement threshold energy of $\approx 25\,\mathrm{eV}$ (see Sec. 3.1). Therefore this part of the displacement damage cross section, misleadingly described as the *disappearance part* in [Laz87], can by no means be neglected in general. For spectra to be expected in the inner detector of the LHC experiments it does however not play a significant role. For neutrons with energies in the MeV range an increasing number of nuclear reactions opens up adding to the displacement function. Up to about 20 MeV an accurate and almost complete data basis does exist which was used as a reliable source for damage calculations [Gri96]. At higher energies theoretical approaches had to be used [Kon92]. The proton damage function is on the other hand dominated by Coulomb interaction at lower energies and is therefore much larger than that for neutrons [Sum93]. For very high energies in the GeV range both damage function approach almost a common value. Here the Coulomb contribution becomes very small and the nuclear reactions are practically the same for neutrons and protons (see insert of Fig. 3.2). Pion interaction is largely influenced by the delta resonance around a few hundred MeV but in the high energy limit the damage function tends to be about 2/3 (quark weighting factor) that of protons [Huh93b]. Finally it should be mentioned that the damage function for protons, as given in Fig. 3.2, is now undoubtedly confirmed even at high energies where the displacement damage cross section (hardness factor) for 24 GeV/c protons is experimentally measured in this work as being 0.51 in good agreement with the calculations in [Huh93b] (see Sec. 5.2).

3.2.2 Hardness factors

With the help of the displacement damage cross section $D(E)$ it is possible to define a hardness factor κ allowing to compare the damage efficiency of different radiation sources with different particles and individual energy spectra $\phi(E)$. It is common practice to define the *hardness factor* κ in such a way that it compares the damage produced by a specific irradiation to the damage which would have been produced by monoenergetic neutrons of 1 MeV and the same fluence:

$$\kappa = \frac{\int D(E)\,\phi(E)\,dE}{D(E_n = 1MeV)\cdot\int \phi(E)\,dE}. \tag{3.3}$$

Here $D(E_n = 1\,\mathrm{MeV})$ is set to 95 MeVmb [AST93] to assure the independence of different calculations from the used binning of the spectra. The equivalent 1 MeV neutron fluence Φ_{eq} can be calculated by

$$\Phi_{eq} = \kappa\,\Phi = \kappa\int \phi(E)\,dE. \tag{3.4}$$

The hardness factors of irradiation sources that have been used in this work can be found in Tab. 5.4 on page 108. Furthermore, a very accurate method for experimental determination of the hardness factors will be presented in Sec. 5.2.

3.3 Classification of defects

As already mentioned in Sec. 3.1 two basically different kinds of defects are formed in silicon by high energy hadron irradiation, namely clusters and point defects.

3.3.1 Clusters

The cluster model was first proposed by Gossick in 1959 [Gos59] in order to explain the very high minority carrier recombination rate observed after irradiation with heavy particles compared to the one observed after gamma or electron irradiation. However, up to now there are only a few experimental data that give more detailed information about the topology of clusters. Neither the exact nature of the defects inside a cluster (besides their composition of vacancies and interstitials) is known nor their electrical properties within the space charge region or in thermal equilibrium. Only recently some models have been presented attributing the measurement of *disturbed* point defect levels in heavy particle or fast hadron irradiated material to defects located inside or close to the cluster regions. The suppression of the DLTS-signal of the double charged divacancy (for details see Chapter 6) was attributed to strain fields arising from the close conglomeration of defects inside the clusters [Sve91]. Furthermore the high leakage current observed in silicon detectors after fast hadron irradiation was attributed to the interaction between divacancies located close together within the clusters (intercenter charge transfer model [Wat96, Gil97]). Finally indications for the introduction of negative space charge by the clusters will be given in this work (Sec. 5.3.4).

3.3.2 Point defects

The main classifications of point defects with respect to their electrical properties are shown in Fig. 3.3 and will be discussed in the following:

- **Acceptors, donors and amphoteric defects**
  Defects with levels in the forbidden band gap can capture and emit electrons and holes. In Fig. 3.3 the defect levels E_t for the different kind of defects are indicated by the short solid lines. The ionization energy ΔE_t needed to e.g. emit an electron into the conduction band corresponds to the distance between the conduction band edge E_C and the defect level position ($\Delta E_t = E_C - E_t$). *Acceptors* are defects that are negatively charged when occupied with an electron while *donors* are defects that are neutral when occupied with an electron. In thermal equilibrium the charge state of defects is ruled by the *Fermi level* (see Sec. 3.4). If the Fermi level is located above the defect level, acceptors are negatively charged and donors are neutral; if it is below the defect level, acceptors are neutral and donors are positively charged. This is indicated by the $(-/\circ/+)$–signs in the figure. Some defects have more than one level in the band gap. As an example the levels of the thermal double donor (TDD) and the *amphoteric* divacancy (VV) are shown. An amphoteric defect is a defect with acceptor and donor level.

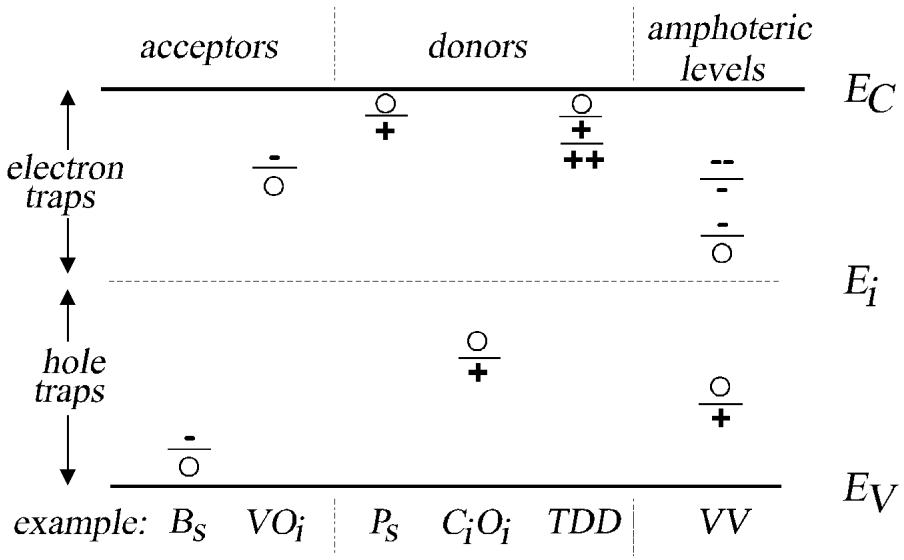

Figure 3.3: Schematic representation of the possible charge states of acceptors, donors and amphoteric levels in the forbidden band gap.

In the space charge region the occupation with charge carriers is ruled by the emission coefficients of the defects. Therefore, usually levels in the upper half of the band gap are not occupied by an electron while the levels in the lower half are occupied with electrons (see Sec. 3.4). This means for example that the defects VO_i (acceptor in upper half of band gap) and C_iO_i (donor in lower half) have no influence on the depletion voltage of a detector since they are neutral in the space charge region. However, B_S (acceptor in lower half) and P_S (donor in upper half) are ionized and therefore introduce negative, respectively positive, space charge.

- **Shallow and deep levels**
  There is no exact definition for the terms of shallow and deep levels. Very often acceptors and donors are called shallow if they are ionized at room temperature. However, the charge state of a defect level is ruled in thermal equilibrium by the Fermi level position and is thus depending on the conduction type and doping concentration of the material. This leads to the fact that the same defect would have to be called shallow in the one and deep in the other material. Furthermore in the space charge region nearly any donor located in the upper half of the band gap would have to be called shallow. In this work the term shallow will be used for defect levels lying closer than about 70 meV to the valence or conduction band and are therefore no more detectable with C-DLTS.

- **Electron and hole traps**
  Every defect can capture (trap) electrons and holes. Thus the names *electron* and *hole trap* might be misleading. They originate from the characterization methods used for the determination of the electrical defect properties which are mostly based on the junction space–charge technique (DLTS, TSC, etc.). A defect

level in the upper half of the band gap but below the Fermi level of a n-type semiconductor is occupied with an electron in thermal equilibrium. By applying a voltage to the junction a space charge region is established and the electrons trapped in the defects are emitted. The observation of the emission time constant as function of temperature can be used to determine the characteristic defect properties ionization energy and capture cross section (see e.g. DLTS–technique Sec. 4.4). However, it is not straight forward to tell whether the electron was emitted from an acceptor or a donor. Thus the defect is called an electron trap.

A short review of identified radiation induced point defects and thermal donors is given in Sec. 3.6.

3.4 Electrical properties of point defects

In this section the occupation of defects with charge carriers under various equilibrium and non equilibrium conditions is described. This serves to understand the impact of defects on detector properties presented in the last section of this chapter and facilitates the understanding of the defect measurement techniques explained in Chapter 4.

3.4.1 Occupation statistics for traps in thermal equilibrium

3.4.1.1 Free carrier concentration

In thermal equilibrium the probability that an electronic state with energy E is occupied by an electron is given by the Fermi-Dirac distribution function

$$F(E) = \frac{1}{1 + \exp\left(\frac{E-E_F}{k_B T}\right)} \tag{3.5}$$

where k_B is the Boltzmann constant, T the absolute Temperature and E_F the electrochemical potential for electrons, usually called the *Fermi level*. Note that the Fermi level is the energy at which the probability of occupation by an electron is exactly one half. If the Fermi level is known, the density n of free electrons in the conduction band and the density p of free holes in the valence band can be calculated by

$$n = \int_{E_C}^{E_{top}} dE \quad g_C(E) \quad \frac{1}{1 + \exp\left(\frac{E-E_F}{k_B T}\right)} \qquad \text{and} \tag{3.6}$$

$$p = \int_{E_{bottom}}^{E_V} dE \quad g_V(E) \quad \frac{1}{1 + \exp\left(\frac{E_F-E}{k_B T}\right)}. \tag{3.7}$$

Here $g_{C,V}(E)$ is the energy density of levels in the conduction and valence band, respectively. E_C and E_V are the band edge energies and E_{top} and E_{bottom} are the top of the conduction band and the bottom of the valence band, respectively. Eqs. 3.6 and 3.7

are valid not only for pure (intrinsic) materials, but also in the presence of defects and impurities which affect the values of n and p solely through an appropriately changed value of E_F. Under the assumption of $|E_{C,V} - E_F| > 3k_BT$ the density of states in the conduction and valence band can be approximated [Sze81] and the integrals 3.6 and 3.7 lead to :

$$n, p = N_{C,V} \exp\left(\pm \frac{E_F - E_{C,V}}{k_B T}\right). \tag{3.8}$$

The *effective densities of states* in the conduction and valence bands, N_C and N_V, are given by

$$N_{C,V} = 2\left(\frac{2\pi m^*_{dC,dV} k_B T}{h^2}\right)^{3/2} \tag{3.9}$$

where m^*_{dC} and m^*_{dV} denote the *density-of-states effective masses* in the conduction and valence bands, respectively. Silicon has six equivalent conduction-band minima forming ellipsoidal constant energy surfaces in the phase space. The corresponding effective mass is [Gre90]

$$m^*_{dC} = 6^{2/3}\left(m^{*2}_t m^*_l\right)^{1/3} \tag{3.10}$$

where m^*_t and m^*_l are the transverse and longitudinal effective masses associated with the ellipsoidal constant energy surfaces. The structure of the valence-band maximum consists of doubly degenerate *light* and *heavy* hole bands plus a *split-off* hole band. Assuming these bands are isotropic and parabolic, the effective mass corresponding to the valence-band density-of-states is given by

$$m^*_{dV} = \left(m^{*3/2}_{lh} + m^{*3/2}_{hh} + \left[m^*_{so}\exp\left(-\Delta/k_BT\right)\right]^{3/2}\right)^{2/3}. \tag{3.11}$$

Here m^*_{lh}, m^*_{hh} and m^*_{so} denote the effective masses of the bands as suggested by the subscripts and Δ is the energy difference between the energy maximum of the *split-off* band and the other two bands (0.0441 eV at 1.8 K).
In this work the effective masses as given in a review article by M.A.Green [Gre90] have been used[2] for the calculation of macroscopic detector parameters. A detailed description of the temperature dependent parameterization can be found in Appendix A.2 on page 216.

3.4.1.2 Calculation of the Fermi level

In the case of intrinsic silicon the concentrations of free electrons and holes are equal ($n = p$) and the Fermi level, which is then called the *intrinsic Fermi level* E_i, can be

[2]Note that the absolute values of m^*_{dC} and m^*_{dV} differ significantly from the older but often used temperature independent ones $1.084\,m_0$ and $0.549\,m_0$ given in [Sze81]. According to [Gre90] the effective masses at 300 K are $1.091\,m_0$ and $1.153\,m_0$, respectively.

calculated from Eqs. 3.8 and 3.9:

$$E_i = \frac{E_C + E_V}{2} + \frac{k_B T}{2} \ln\left(\frac{N_V}{N_C}\right) = \frac{E_C + E_V}{2} + \frac{3}{4} k_B T \ln\left(\frac{m^*_{dC}}{m^*_{dV}}\right). \tag{3.12}$$

The corresponding intrinsic carrier concentration n_i is given by

$$n_i = \sqrt{N_C N_V} \exp\left(-\frac{E_g}{2k_B T}\right) \tag{3.13}$$

where $E_g = E_C - E_V$ stands for the band gap energy. The notation relative to the intrinsic Fermi level E_i is a common praxis since in this case many expressions are simplified. For instance, by using Eq. 3.12 the free carrier concentrations (Eq. 3.8) can be written as

$$n, p = n_i \exp\left(\pm\frac{E_F - E_i}{k_B T}\right) \tag{3.14}$$

and the so-called *mass action law* $n_i^2 = np$, which holds also for the case of extrinsic silicon in thermal equilibrium, is easily obtained.
If the Fermi level E_F is known, the occupation of traps in the band gap by electrons or holes can be calculated. For a defect with concentration N_t and an energy level at E_t the fraction occupied by electrons n_t, respectively holes p_t, is given by

$$\begin{aligned} n_t &= N_t \frac{1}{1 + \exp\left(+\frac{E_t - E_F}{k_B T}\right)} = N_t F(E_t) \\ p_t &= N_t \frac{1}{1 + \exp\left(-\frac{E_t - E_F}{k_B T}\right)} = N_t (1 - F(E_t)) \end{aligned} \tag{3.15}$$

fulfilling the totality condition

$$N_t = n_t + p_t. \tag{3.16}$$

Please note that according to the definition of n_t and p_t a defect level not occupied by an electron is regarded as being occupied by a hole and vice versa a level not occupied by a hole is occupied by an electron[3]. Furthermore, one should keep in mind that an acceptor occupied by an electron is negatively charged while a donor is neutral. On the other hand an acceptor occupied by a hole is neutral while a donor is positively charged. Thus the effective concentration of charge carriers stored in the defects N_{eff} is given by

$$N_{eff} = \sum_{donors} p_t - \sum_{acceptors} n_t \tag{3.17}$$

[3]In literature the occupation of a defect level by a hole is often not defined and the two states of a level are described as occupied and not occupied by an electron only. Instead of n_t and p_t the terms $N_t F(E_t)$ and $N_t(1 - F(E_t))$ are used (compare Eq. 3.15).

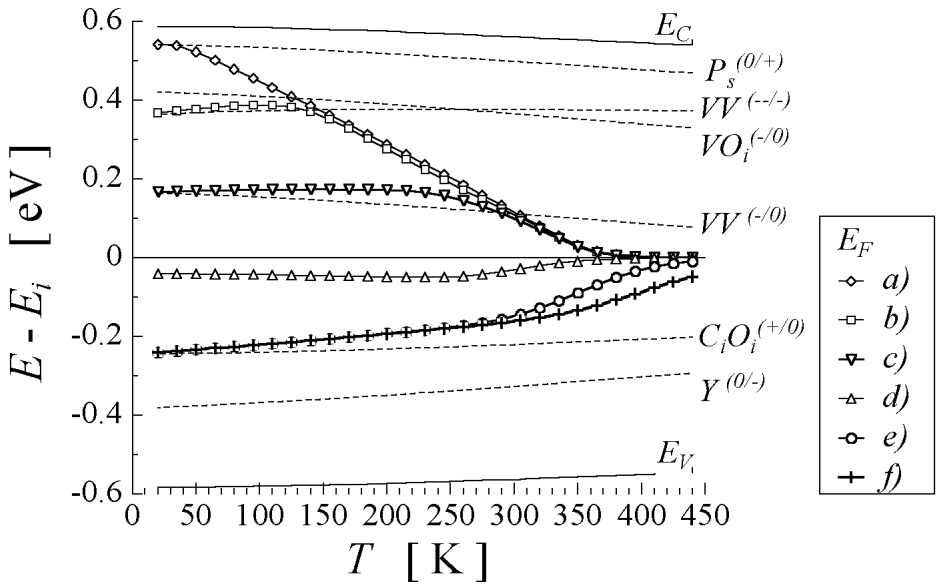

Figure 3.4: Fermi level as function of temperature and defect concentrations [Fei97a]. The calculations have been made with a fixed phosphorus concentration of $[P_s] = 1 \times 10^{12}\,\mathrm{cm}^{-3}$ and various concentrations of VV, VO_i, C_iO_i, and an acceptor level Y placed at $E_V + 0.2eV$. The concentrations have been: [VV] = [VO] = [CO] = a)10^{11} b) 5×10^{11} c) 10^{12} d) 10^{13} e) 10^{14} f) 10^{15} cm^{-3} and in all cases [Y] =0.1× [e.g. VV].

and denoted *effective doping concentration* in the following. In thermal equilibrium the overall charge has to be zero and taking into account the free charge carriers one gets

$$0 = p - n + N_{eff}. \tag{3.18}$$

From Eq. 3.8 and Eq. 3.9 together with Eqs. 3.15 and 3.17 the Fermi level in the case of extrinsic silicon can be calculated for any temperature. As an example the temperature dependence of the Fermi level is shown in Fig. 3.4 for various defect concentrations.

3.4.1.3 Enthalpy and Gibbs free Energy

In the preceding sections the term energy E has only been used in an abstract way. However, according to its thermodynamical definition it should be denoted as *Gibbs free energy* E. The change in Gibbs free energy during a carrier emission from a defect level can be described as $\Delta E = \Delta H - T\Delta S$ where ΔH denotes the change in enthalpy and ΔS that in entropy. The measurements of defect levels in this work have been done with the electrical techniques DLTS and TSC. With such methods not only the change of Gibbs free energy but also the change in enthalpy (ΔH) during the emission of carriers can be determined (see Sec. 4.4.2). Therefore also the change of entropy has to be taken into account in the further discussion of trap level positions in the band gap. This is done by introducing the entropy factors $X_{n,p} = \exp\left(\Delta S_{n,p}/k_B T\right)$ for hole

and electron emissions

$$E_C - E_t = \Delta H_n - k_B T \ln(X_n) \tag{3.19}$$

$$E_t - E_V = \Delta H_p - k_B T \ln(X_p)\,. \tag{3.20}$$

A detailed discussion about defect entropy factors and their dependence on temperature and defect properties can be found in [Vec76].

3.4.1.4 Shockley-Read-Hall statistics

The occupation of traps in the band gap by electrons or holes, respectively, is determined by the interaction of the defect level with the conduction and the valence band. According to the work of W.Shockley, W.T.Read [Sho52] and R.N.Hall [Hal52] this can be described as a statistical process. As indicated in Fig. 3.5 four competing reactions

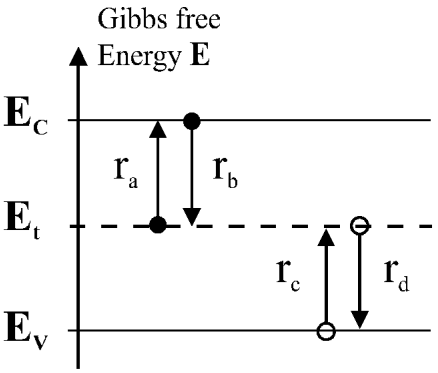

Figure 3.5: Emission and capture rates of an energy level E_t.

a) emission of electrons into the conduction band
$$r_a = e_n\, n_t$$

b) capture of electrons into non occupied states
$$r_b = c_n\, n\, p_t$$

c) capture of holes into states occupied by electrons (equivalent to emission of electrons into valence band)
$$r_c = c_p\, p\, n_t$$

d) emission of holes into the valence band (equivalent to capture of electrons from valence band)
$$r_d = e_p\, p_t$$

take place. The corresponding reaction rates are also given in the Figure. The rate of electrons (holes) emitted into the conduction (valence) band r_a (r_d) is proportional to the fraction of defect states occupied by electrons n_t (holes p_t). The capture rate of electrons (holes) from the conduction (valence) band r_b (r_c) is proportional to the fraction of defect states occupied by holes p_t (electrons n_t) and the concentration of free electrons n (holes p) in the conduction (valence) band. The proportionality factors are the *emission rate* e_n (e_p) and the *capture coefficient* c_n (c_p). Taking into account all four reactions one gets the following differential equation for n_t:

$$\begin{aligned} \frac{dn_t}{dt} &= -r_a + r_b - r_c + r_d \\ &= -e_n\, n_t + c_n\, n\, p_t - c_p\, p\, n_t + e_p\, p_t \end{aligned} \tag{3.21}$$

According to the *principle of detailed balance* the concentrations of free electrons in the conduction band and free holes in the valence band have to be constant. Therefore the interactions with the conduction band (r_a and r_b) as well as the interactions with the valence band (r_c and r_d) have to operate at the same rate. Together with Eqs. 3.8, 3.14 and 3.15 this leads to

$$e_{n,p} = c_{n,p}\, n_i \, \exp\left(\pm\frac{E_t - E_i}{k_B T}\right) \tag{3.22}$$

$$= c_{n,p}\, N_{C,V} \, \exp\left(\pm\frac{E_t - E_{C,V}}{k_B T}\right) \tag{3.23}$$

$$= c_{n,p}\, N_{C,V}\, X_{n,p} \, \exp\left(-\frac{\Delta H_{n,p}}{k_B T}\right) \tag{3.24}$$

where for the last formula the definitions of entropy factors (Eqs. 3.19 and 3.20) have been used.
However, it is still common practice (see e.g. [Sze85]) to define a cross section $\sigma_{n,p}$ by setting

$$X_{n,p} c_{n,p} = \sigma_{n,p} v_{th,n,p} \tag{3.25}$$

in the above equations. Here the parameter $v_{th,n,p}$ is the so-called *thermal velocity*[4] which is given by:

$$v_{th,n,p} = \sqrt{\frac{3\, k_B\, T}{m^*_{dC,V}}}. \tag{3.26}$$

Thus Eq. 3.24 becomes

$$\begin{aligned} e_{n,p} &= \sigma_{n,p}\, v_{th,n,p}\, N_{C,V} \exp\left(-\frac{\Delta H'_{n,p}}{k_B\, T}\right) \\ &= \sigma_{n,p}\, B\, \left(m^*_{dC,V}/m_0\right)\, T^2 \exp\left(-\frac{\Delta H'_{n,p}}{k_B\, T}\right) \end{aligned} \tag{3.27}$$

where B is a constant given by

$$B = 2\sqrt{3}\, k_B^2\, m_0\, \left(2\pi/h^2\right)^{3/2} = 3.256 \times 10^{21}\, \mathrm{K^{-2} cm^{-2} s^{-1}}. \tag{3.28}$$

ΔH has been replaced by $\Delta H'$ in order to indicate that the enthalpy was obtained under the assumption of a constant capture cross section (change of entropy is neglected). In this work $\Delta H'$ will also be called the *activation energy*.

[4]Note that the parameter $v_{th,n,p}$ has not to be confused with the real thermal velocities of free carriers in the valence and conduction band (see [Gre90]).

3.4.2 Basic semiconductor equations

For further calculations of non thermal equilibrium conditions it is very instructive to write down the basic differential equations for semiconductors with an arbitrary number of defects [Sze85].

- The *Poisson equation*

$$\frac{\partial E}{\partial x} = \frac{q_0}{\epsilon\epsilon_0}(n + p + N_{eff}) \tag{3.29}$$

  In contrast to Eq. 2.3 on page 22 the free carriers in the conduction and valence band are not neglected.

- The *continuity equations*

$$\begin{aligned} \frac{\partial n}{\partial t} &= G_{ext} + \sum_{\text{traps}} e_n n_t - n \sum_{\text{traps}} c_n p_t + \frac{1}{q_0}\frac{\partial j_n}{\partial x} \\ \frac{\partial p}{\partial t} &= G_{ext} + \sum_{\text{traps}} e_p p_t - p \sum_{\text{traps}} c_p n_t - \frac{1}{q_0}\frac{\partial j_p}{\partial x} \end{aligned} \tag{3.30}$$

  Here j_n and j_p denote the total electron and hole current densities and G_{ext} describes the direct electron-hole pair generation (e.g. by laser illumination).

- The *total current densities*

$$\begin{aligned} j_n &= q_0\,\mu_n\,n\,E + q_0 D_n \frac{\partial n}{\partial x} \\ j_p &= q_0\,\mu_p\,p\,E - q_0 D_p \frac{\partial p}{\partial x} \end{aligned} \tag{3.31}$$

  When an electric field E is present in addition to a concentration gradient $\frac{\partial n}{\partial x}$, respectively $\frac{\partial p}{\partial x}$, the total current densities for electrons and holes are given as the sum of drift and diffusion currents. Here μ_n and μ_p denote the electron and hole mobility, respectively. The diffusivity $D_{n,p}$ is connected with the mobility via the *Einstein relation*: $D_{n,p} = (k_B T/q_0)\,\mu_{n,p}$. The total current density is given as the sum of the conduction current density $(j_n + j_p)$ and the displacement current density arising from temporal changes in the electrical field strength:

$$j_{total} = j_n + j_p + \epsilon\epsilon_0 \frac{\partial E}{\partial t} \tag{3.32}$$

$$\text{with} \qquad \frac{\partial j_{total}}{\partial x} = 0. \tag{3.33}$$

3.4.3 Occupation of traps in the space charge region

Applying a reverse bias on a diode leads to the formation of a space charge region (SCR, see Sec. 2.3.1). In such a non-equilibrium condition Eq. 3.15 can no longer be used to calculate the occupation of traps. However, due to the electric field it can be assumed that the free carrier concentration is negligibly small in the SCR ($n \approx p \approx 0$). Therefore no capture of free carriers occurs and Eq. 3.21 reduces to

$$\frac{dn_t}{dt} = -e_n\, n_t + e_p\, p_t. \tag{3.34}$$

In steady state the occupation of traps is then given by

$$n_t = N_t \frac{e_p}{e_n + e_p} \quad \text{and} \quad p_t = N_t \frac{e_n}{e_n + e_p}, \tag{3.35}$$

or, by using Eq. 3.22,

$$n_t, p_t = \frac{N_t}{1 + \left(\frac{c_n}{c_p}\right)^{\pm 1} \exp\left(\pm 2 \frac{E_t - E_i}{k_B T}\right)}. \tag{3.36}$$

Now the *effective doping concentration* N_{eff}[5], can be calculated by summing up over all donors occupied by holes and all acceptors occupied by electrons in the space charge region:

$$N_{eff} = \sum_{\substack{\text{donors} \\ \text{in SCR}}} p_t + \sum_{\substack{\text{acceptors} \\ \text{in SCR}}} n_t \tag{3.37}$$

Furthermore the generation rate of electron-hole pairs G_t for a trap in the space charge region is given by:

$$\begin{aligned} G_t &= e_n n_t = e_p p_t \\ &= N_t n_i \frac{c_n c_p}{c_n \exp\left(\frac{E_t - E_i}{k_B T}\right) + c_p \exp\left(-\frac{E_t - E_i}{k_B T}\right)}. \end{aligned} \tag{3.38}$$

As can be seen, only defect centers whose energy levels E_t are close to the intrinsic Fermi level E_i contribute significantly to the generation rate. Often only one capture coefficient (c_n or c_p) is determined by the microscopic defect measurement methods (see Chapter 6). In such cases it is common practice to assume $c_n = c_p$ and Eq. 3.38 simplifies to

$$G_t = \frac{N_t n_i c_n}{2 \cosh\left(\frac{E_t - E_i}{k_B T}\right)} \qquad (\text{ with } c_n \equiv c_p). \tag{3.39}$$

[5]Note that the total effective charge stored in the traps strongly depends on the bias condition of the diode. In thermal equilibrium the occupation of traps has to be calculated with Eq. 3.15 while in the SCR Eq. 3.35 has to be applied. However, if not mentioned otherwise N_{eff} refers in this work to the latter case and thus $q_0 N_{eff}$ gives the *effective space charge density*.

Finally the bulk generation current density is given by

$$j_{BGC} = \sum_{\text{traps}} q_0 G_t \tag{3.40}$$

and determines the leakage current of irradiated silicon diodes.

3.4.4 Occupation of traps under forward bias

For the microscopic DLTS (Sec. 4.4) and TSC (Sec. 4.5) techniques the filling of the defect levels is often achieved by injection of charge carriers by applying forward bias. Thus, it is very important to understand the trap occupation under such a condition. When a high number of free electrons and holes are injected into the silicon bulk and the emission rates are small compared to the capture rates ($c_n n \gg e_n$ and $c_p p \gg e_p$) the occupation of a defect level (Eq. 3.21) is governed by the capture rates. Therefore the steady state occupation by electrons and holes is given by

$$n_t = N_t \times \frac{1}{1 + \dfrac{c_p\, p}{c_n\, n}} \quad \text{and} \quad p_t = N_t \times \frac{1}{1 + \dfrac{c_n\, n}{c_p\, p}}, \quad \text{respectively.} \tag{3.41}$$

Thus an electron (hole) trap is only filled in the case that $c_p p$ is smaller (larger) than $c_n n$ at the filling temperature. Due to the high resistivity of the samples used for this work, the concentration of free carriers can easily reach the doping level. This situation is known as the high-level injection case [Sze85]. Furthermore injection of holes from the p^+ contact as well as injection of electrons from the n^+ contact may occur, which has been described in terms of a double injection p-i-n diode in the literature [Sze85]. Both mechanisms imply that $p = n$, a condition being clearly desirable for the experimenter, since Eq. 3.41 is greatly simplified. If it is however not possible to inject a sufficient amount of free carriers to reach the high injection case, it is necessary to take into consideration the charges trapped in the defects. These charges have to be absorbed in the difference of the concentrations of free electrons and holes in order to maintain the approximate space charge neutrality [Lam62]. Such a situation ($n \neq p$) may easily happen unless the filling current is very large. Therefore, one major shortcoming of this filling mode is that the value of p/n is not easily controlled. In addition, this ratio may vary with distance and consequently the filling of defects becomes inhomogeneous. It is noted here that this problem may best be overcome by generating free carriers by illumination with above band gap light.

3.4.5 Occupation of traps under high leakage current

The following calculations can be used to roughly estimate the occupation of traps in devices with high leakage currents and have already been used in [Mat95] to formulate the so-called *deep-acceptor model*. In this model the leakage current is responsible for the steady state occupation in the space charge region of an acceptor level close to midgap. The occupation of this *deep defect* then determines the negative space charge

responsible for some of the observed macroscopic damage (*stable acceptor generation*, see Sec. 5.3.4). However, one should keep in mind that this formulation is only a rough estimate and that only by numerical modeling the spatial distribution of free carriers in the presence of defects can be calculated (e.g. with the KURATA–[Mat95], HFIELDS–[Pas98] or Lutz– [Lut96] program).

After severe radiation damage the leakage current increases and the assumption of $n \approx p \approx 0$ is no longer valid. Therefore the capture of free carriers in the space charge region has to be taken into account. In such a case the steady state occupation of the defect levels by electrons can be calculated from Eq. 3.21 and Eq. 3.22:

$$\begin{aligned} n_t &= N_t \frac{c_n n + e_p}{e_n + c_p p + c_n n + e_p} \\ &= N_t \frac{c_n n + n_i c_p \exp\left(-\frac{E_t - E_i}{k_B T}\right)}{c_n \left(n + n_i \exp\left(\frac{E_t - E_i}{k_B T}\right)\right) + c_p \left(p + n_i \exp\left(-\frac{E_t - E_i}{k_B T}\right)\right)} \end{aligned} \quad . \tag{3.42}$$

However, the carrier concentrations in the depleted silicon bulk are still very small (e.g. in the order of some $10^8 cm^{-3}$ after $\Phi_{eq} = 3 \times 10^{13} n/cm^2$ [Mat95]) and therefore the diffusion component of the current density equation 3.31 can be neglected, resulting in

$$\begin{aligned} j_n &= q_0 \, \mu_n \, n \, E \\ j_p &= q_0 \, \mu_p \, p \, E. \end{aligned} \tag{3.43}$$

Under steady state conditions $\left(\frac{\partial E}{\partial t} = 0\right)$ from Eqs. 3.32 and 3.33 it can be deduced that

$$\left| \frac{\partial j_n}{\partial x} \right| = \left| \frac{\partial j_p}{\partial x} \right| \tag{3.44}$$

and therefore

$$\mu_n \, n = \mu_p \, p. \tag{3.45}$$

Furthermore the continuity equation (3.30) for electrons becomes

$$0 = G_{ext} + \sum_{\text{traps}} e_n n_t + \frac{1}{q_0} \frac{\partial j_n}{\partial x} \tag{3.46}$$

and can be written by substituting j_n with Eq. 3.43 as

$$G_{ext} + \sum_{\text{traps}} e_n n_t = -\frac{\partial}{\partial x} \left(n \mu_n E \right). \tag{3.47}$$

Now, under the assumption of a constant free electron concentration and a constant electron mobility, the Poisson equation 3.29 can be used to get:

$$\underbrace{G_{ext} + \sum_{\text{traps}} e_n n_t}_{1/(2q_0) \times \text{ leakage current density}} = \frac{n \, \mu_n}{\epsilon \, \epsilon_0} \underbrace{q_0 \, (-n + p + N_{eff})}_{\text{effective space charge}} . \tag{3.48}$$

The sum of the charge stored in the defects ($q_0\, N_{eff}$) and in the free carriers $q_0\,(-n+p)$ corresponds to the macroscopically measured effective space charge which is proportional to the depletion voltage of the sample. The left hand side of the formula corresponds to half of the leakage current density since the current is composed of electron and hole current. The external generation rate of electrons (G_{ext}) can be used to artificially add a leakage current of unknown origin into the calculations. This has been done within the *deep acceptor model* [Mat95, Mac96b] for neutron irradiated silicon diodes where a very high leakage current is observed that cannot be explained by standard Shockley-Read-Hall statistics [Gil97]. However, one should always keep in mind that under such an assumption the mechanism that produces the leakage current is supposed to have no influence on the space charge at the same time.
Finally, with all the assumptions mentioned above, it is possible to find defect level parameters for a deep acceptor that could explain the increase of negative space charge after neutron irradiation. Since the defect concentration the capture cross sections and the level position are free parameters, the solution is not unique. Consequently one should check such calculations by experiments. The easiest way to do this would be to perform measurements of the effective space charge at different temperatures since the leakage current is strongly depending on temperature.

3.5 Defect annealing

Defects cannot only be characterized by their electrical properties ($\Delta H, \sigma$) but also by their annealing behavior. Very often the decisive hint for the identification of a defect by data available in the literature comes from annealing experiments. Parallel investigations on the evolution of microscopic defects and macroscopic detector properties offer a powerful tool to understand more about the relation between specific defects and their impact on macroscopic detector properties. Furthermore, systematic annealing studies of macroscopic detector parameters give important hints for the underlying microscopic processes (compare e.g. the reverse annealing effect described in Sec. 5.3.3).

3.5.1 Annealing mechanisms

The mechanisms leading to annealing of defects can roughly be divided in migration, formation and dissociation processes:

- **Migration and complex formation.**
  The defects become mobile at a certain temperature. They migrate through the silicon lattice until they are gettered at sinks (surface, dislocations, etc.), recombine with their counterparts (e.g. $V + (Si)_i \rightarrow (Si)_s$) or form new defects by association with identical or other types of defects (or impurities) (e.g. $V + V \rightarrow V_2$ or $C_i + C_s \rightarrow C_iC_s$).

- **Dissociation**
  A complex (defect composed of more than one constituent) dissociates into its

components if the lattice vibrational energy is sufficient to overcome the binding energy. At least one of the constituents migrates through the lattice until it forms another defect or disappears into a sink (e.g. $C_iC_s \overset{T\approx 250^{\circ}C}{\longrightarrow} C_i + C_s$).

As shown in Fig. 3.6 each of the processes, i.e. migration, complex formation and complex dissociation, is characterized by an activation energy (E_m, E_f, E_d). Since it is often difficult to tell from experimental results which of these processes is underlying the observed changes in the silicon properties the term *activation energy* E_A will by used for the mathematical formulation of all three cases.

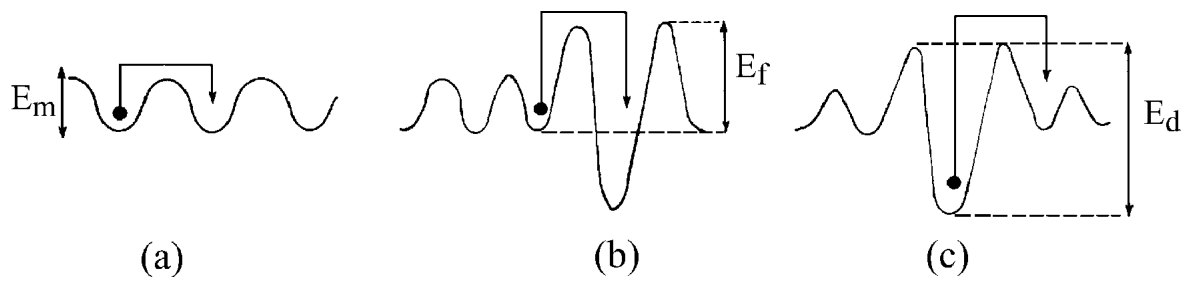

Figure 3.6: Schematic representation of the mechanism of defect migration (a), complex formation (b), and complex dissociation (c) showing the corresponding activation energies involved in the process (after [Bou83]).

3.5.2 Rate of reaction

The migration of defects into sinks (defects and sinks randomly distributed) and the dissociation of defects can easily be described by a first order process. The number of defects disappearing into sinks or dissociating per unit time is proportional to the number of defects present at that time and can thus be written as

$$-\frac{dN_X}{dt} = kN_X \tag{3.49}$$

where N_X denotes the defect concentration and k the so-called *rate constant*. The temperature dependence of the rate constant is given by an *Arrhenius relation*

$$k = k_0 \exp\left(-\frac{E_A}{k_B T}\right) \tag{3.50}$$

where k_0 denotes the *frequency factor* and E_A the activation energy for dissociation or migration (see Fig. 3.6). The frequency factor is related to the attempt-to-escape frequency that can be estimated by the most abundant phonon frequency ($\approx k_BT/h$ $= 2.1 \cdot 10^{10} \times T[K]$ s^{-1} [Cor66]). By using

$$k_0 = \delta \cdot \frac{k_B T}{h} \tag{3.51}$$

the factor δ can give an indication whether the observed reaction was due to a dissociation of a defect ($\delta \approx 1$; single jump process) or due to a long range migration of a defect ($\delta \ll 1$) with $1/\delta$ giving an approximation of the number of jumps necessary to remove the defect. However, the later interpretation holds only in the case of *diffusion limited processes* for which the activation energy E_m for migration is smaller than the activation energy E_f for association or removal into sinks (compare Fig. 3.6).

Diffusion limited reactions between two different kind of homogeneously distributed defects X and Y with concentration N_X and N_Y can be described by the differential equation

$$-\frac{d}{dt}N_X = -\frac{d}{dt}N_Y = 4\pi\, R(X,Y)\, D\, N_X N_Y \tag{3.52}$$

with D being the *diffusion coefficient* (or *diffusivity*) and R(X,Y) the *capture radius* for the reaction $X + Y \rightarrow XY$ [Wai57]. The diffusion coefficient is the sum of the diffusion coefficients of the defects X and Y which is, however, most often dominated by one of the defects (the faster diffusing[6]one). Thus the temperature dependence of the diffusion constant can be described by an Arrhenius relation with a single activation energy

$$D = D_0 \exp\left(-\frac{E_A}{k_B T}\right). \tag{3.53}$$

The *diffusion constant* D_0 can be approximated by $D_0 = \alpha a^2 \nu$ where α gives the number of possible next jump places, a is the lattice constant of silicon and ν the jump frequency ($\approx$ most abundant phonon frequency). The capture radius is a measure for the distance to which the reaction partners have to be brought together in order to form a complex. For neutral defects this is about a single jump distance and for Coulomb interaction it may be approximated by

$$R = \frac{q_X q_Y}{\epsilon\epsilon_0 k_B T}. \tag{3.54}$$

Taking a reaction where one reaction partner has a much higher concentration than the other (e.g. $N_Y \gg N_X$) and thus can be assumed to be a constant ($N_Y \approx N_{Y,0}$) results in an expression for the reaction which is very similar to Eq. 3.49. In such a case the rate constant k equals $4\pi RDN_Y$ and δ in Eq. 3.51 is given by $\delta \approx 4\pi R\alpha a^2 N_Y$.

A more common expression for reaction kinetics is given by

$$-\frac{dN_X}{dt} = k_\gamma N_X^\gamma \tag{3.55}$$

where γ denotes the order of reaction. A second order reaction ($\gamma = 2$) is given for bimolecular reactions where both reaction partners are of about the same concentration

[6]Usually the term *diffusion* is used for processes driven by a concentration gradient. However, in defect kinetics it is often used as a synonym for *migration*.

(compare Eq. 3.52 for $N_X \approx N_Y$) while for $\gamma = 1$ the equation results in Eq. 3.49. However, the order of reaction has not to be an integer number. The solutions of Eq. 3.55 for $\gamma = 1$ and 2 are given by

$$\gamma = 1 \quad : \quad N_X(t) = N_{X,0} \exp\left(-k_1 \left(t - t_0\right)\right) \tag{3.56}$$

$$\gamma = 2 \quad : \quad N_X(t) = N_{X,0} \frac{1}{1 + k_2 N_{X0}(t - t_0)} \tag{3.57}$$

with $N_{X,0}$ being the initial defect concentration at $t = t_0$. The main difference between these reactions is displayed in the half life periods ($\tau_{1/2}$: $N_X(\tau_{1/2}) = N_{X,0}/2$)

$$\gamma = 1 \quad : \quad \tau_{1/2} = \frac{\ln 2}{k} \tag{3.58}$$

$$\gamma = 2 \quad : \quad \tau_{1/2} = \frac{1}{k N_{X0}}. \tag{3.59}$$

For a first order process the annealing is independent of the defect concentration. Thus also the half life period for $\gamma = 1$ is independent of the defect concentration. However, the speed of reaction for a second order process is determined by the momentary defect concentration $N_X(t)$ and therefore for higher initial defect concentration $N_{X,0}$ a lower half life period is found.

3.5.3 Annealing temperature

There is no exact specification for the *annealing temperature* (T_{ann}). However, commonly it is defined as the temperature at which the defect concentration drops below the (1/e)-th part of the initial concentration in a certain time interval Δt usually chosen to be in the order of 20 min. For a dissociation process the annealing temperature can be calculated from Eq. 3.56 with $N_X(\Delta t, T_{ann}) = N_{X,0}/e$ and the help of Eq. 3.50

$$1/e = \exp\left(-k(T_{ann}) \cdot \Delta t\right) \quad \Rightarrow \quad T_{ann} = \frac{E_A}{k_B \ln\left(k_0 \Delta t\right)} \tag{3.60}$$

with k_0 depending linearly on the temperature (Eq. 3.51). However, for all reactions except dissociation, the annealing temperature is material dependent:

- For bimolecular reactions it depends strongly on the concentration of the reaction partners (see Eq. 3.52).
- Different impurity or defect concentrations can give rise to new reaction channels changing the overall annealing kinetics (compare e.g. $(Si)_i$–annealing hierarchy in Fig. 3.8 for materials with different [O], [C] and [B] concentration).
- The charge state of a defect (Fermi level position) can play an important role (e.g. charge state dependent annealing of VP, see Tab. B.1).

Finally it has to be noted that for 2nd order reactions the definition of an annealing temperature is not very useful since it would depend on the initial defect concentration (see Eq. 3.59). Thus care has to be taken if annealing temperatures measured for the same defect in different materials are compared with each other.

3.6 Review of point defects

In this section a short review of point defects relevant for this work – mainly radiation induced defects but also thermal donors – is given. The basic properties of the defects (level position, capture cross section, annealing behavior, etc. and the corresponding references) are assembled in the tables of Appendix B. Furthermore a set of defect reactions taking place in high resistivity detector silicon is displayed in the framework of a defect kinetics model in Sec. 7.2.2.

3.6.1 Radiation induced defects

In Sec. 3.1 the production of the primary radiation induced defects, silicon self-interstitial ($(Si)_i$ or I), vacancy (V), divacancy (V_2) and the so-called clusters, has been described. However, with the production of these defects the damage process has not ended. Since interstitials and vacancies are very mobile at room temperature they migrate through the silicon lattice and are almost completely trapped at impurities and defects. This process gives rise to further defects and defect reactions that are described in the following.

3.6.1.1 Vacancy related defects

Although the vacancy is one of the two basic defects less is known about its electrical properties than for many other defects. It is believed that the vacancy has five different charge states ($--/-/\circ/+/++$). However, the exact level positions for the acceptor levels $V^{(--/-)}$ and $V^{(-/0)}$ could up to now not be determined although the existence of the V^- and V^{--} has been proved directly, respectively indirectly, by the EPR (Electron Paramagnetic Resonance) method [Wat92]. Another problem occurs for the observation of the donor levels due to their so-called *negative-U* behavior [Wat80]. The double donor level $V^{(++/+)}$ is located deeper in the bandgap (+0.13 eV) than the single donor level $V^{(+/0)}$ ($\approx$ +0.05 eV). This means that by thermal activation only the emission of two holes from the V^{++} state can be observed

$$V^{++} \quad \stackrel{0.13\,\mathrm{eV}}{\longrightarrow} \quad V^{+} + h \quad \stackrel{\approx 0.05\,\mathrm{eV}}{\longrightarrow} \quad V^{\circ} + 2h$$

since the energy needed to emit the first hole is higher than the one for the second hole. The thermally activated migration of the vacancy depends strongly on its charge state with activation energies of 0.45 eV for V^0, 0.32 eV for V^{++} and 0.18 eV for V^{--}. This is displayed in Fig. 3.7 where the non-annealed fraction of the defect concentration after a 20 min isothermal heat treatment is plotted versus the annealing temperature. However, if a high concentration of charge carriers is present (generated e.g. by ionizing radiation or illumination), the vacancy becomes mobile even at 20 K by means of *recombination enhanced diffusion* [Wat92]. This diffusion is driven by the energy released when electrons and holes recombine at the migrating defect.

The migrating vacancies form pairs with acceptors (B, Al, Ga), donors (P, As, Sb) or other impurities (Ge, Sn, H, etc.) present in the silicon. Furthermore the vacancies

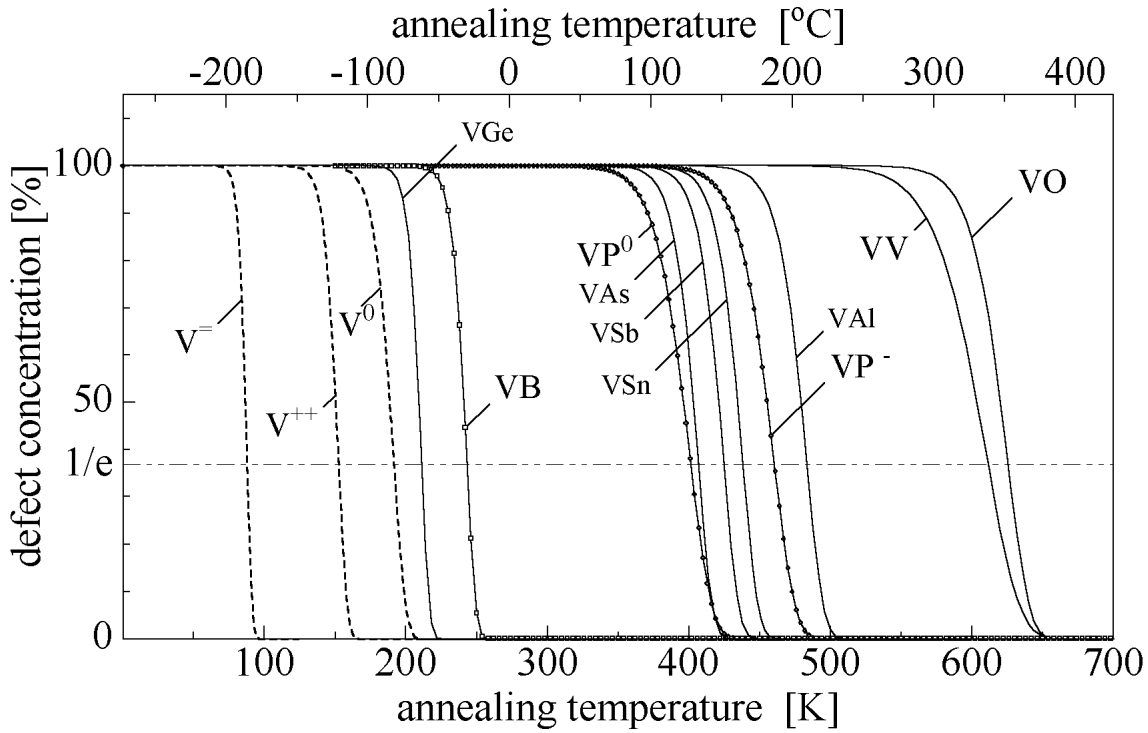

Figure 3.7: Schematic representation of vacancy and vacancy-defect pair annealing. The ordinate indicates the fraction of defects remaining after a 20 min isothermal heat treatment at the annealing temperature T_a. All curves were calculated with the individual annealing parameters of the defects given in Tab. B.1 in Appendix B. Note that the annealing of vacancies (diffusion limited process) is strongly depending on the concentration of sinks ([O], [P], etc.).

can combine with each other and form divacancies (V_2). The V_2 is an amphoteric level with four different charge states in the band gap ($--/-/\circ/+$) and next to the VO it is one of the most abundant vacancy-related defects in irradiated high resistivity silicon (see Chapter 6). The annealing behavior of vacancy-related complexes is shown in Fig. 3.7. Their respective energy levels and annealing parameters are given in Tab. B.1 in Appendix B.

Higher order vacancy defects like $V_3, V_4, etc.$ in various configurations are very likely important structural components of clusters but have up to now only been investigated in a few experiments (see e.g. [Lee73] for V_4 and V_5). Molecular-dynamics simulations predict that one gains energy by forming an aggregate of n vacancies out of an isolated vacancy plus an aggregate of $(n-1)$ vacancies [Has97]. Thus there is the tendency to form higher order vacancy aggregates by capture of migrating monovacancies. The gain of energy has a pronounced maximum for $n = 6$. The six vacancies of the V_6 form a planar hexagonal ring in the lattice which is very stable. The activation energy for annealing is bigger than 3.7 eV while e.g. for the processes $V_7 \rightarrow V_6 + V$ only about 1.3 eV is needed. However, in contrast to the predictions for V, V_2, V_3, V_4, V_5 and V_7

no levels are predicted within the band gap making it impossible to prove the existence of such a defect by electrical techniques like DLTS. Additionally V_6 is expected to be invisible to the optical methods like Photo Luminescence (PL) and infrared absorption (IR). Thus it was suggested that V_6 could be the so far unknown electrical inactive defect remaining in silicon after neutron irradiation[7] and high temperature annealing ($\approx 850°C$) becoming only visible in diffusion experiments where it acts as sink (for details see [Has97]). During irradiation vacancies and interstitials are formed in equal numbers. Thus one would expect to detect more interstitial-related defects than vacancy-related defects if the V_6 is formed unless, of course, similar *undetectable* interstitial clusters exist.

3.6.1.2 Interstitial related defects

Less is know about the silicon self-interstitial ($(Si)_i$ or I) than about the vacancy. In p-type silicon the self-interstitial was observed to be mobile even at 4.2 K (recombination enhanced diffusion) while in n-type it does not migrate until about 150 K [Wat79]. However, at room temperature it is highly mobile in n- and p-type silicon and can react with impurities or defects. By the so-called *Watkins replacement mechanism* it can eject impurities (e.g. C_s, B_s or Al_s) from their substitutional lattice sites and take over their position leading to a perfect silicon lattice, e.g.

$$(S_i)_i + C_s \rightarrow (S_i)_s + C_i \quad .$$

The impurities are left on interstitial sites (e.g. C_i, B_i or Al_i), are electrically active and mobile at room temperature. The forming of B_i and C_i is schematically displayed in Fig. 3.8. As shown in the figure, $(Si)_i$ can also combine with oxygen. However, this complex is not stable at room temperature and the interstitial is released again very fast. Furthermore the interstitial can react with radiation induced defects (not shown in the figure). Thus it is e.g. possible to recombine with vacancy-related defects (e.g. $VO_i + I \rightarrow O_i$ or $VV + I \rightarrow V$).

Since the boron concentration is very low in high resistivity silicon the boron reactions in Fig. 3.8 are not very likely to be observed[8] in such material and substitutional carbon is usually the main sink for migrating self-interstitials. The resulting carbon interstitials are mobile at room temperature and produce further complexes like C_iO_i and C_iC_s which are the most abundant interstitial-related defects in detector silicon. The production of C_iP_s is very unlikely[8]due to the small phosphorus concentration in high resistivity silicon (usually $[P_s] \ll [C_s] < [O_i]$). The time constant for the annealing of C_i, respectively the formation of C_iO_i and C_iC_s, is strongly depending on the oxygen and carbon concentrations. In high resistivity FZ silicon at room temperature it lies in the order of some days (compare Chapter 6). The annealing and level parameters are displayed in Tab. B.1 in Appendix B.

[7] Irradiation in reactors for Neutron Transmutation Doping (see page 11).

[8] Although these reactions are not very likely to be observed in microscopic defect investigations they can have an impact on macroscopic detector properties (compare *acceptor* and *donor removal* in Sec. 3.7).

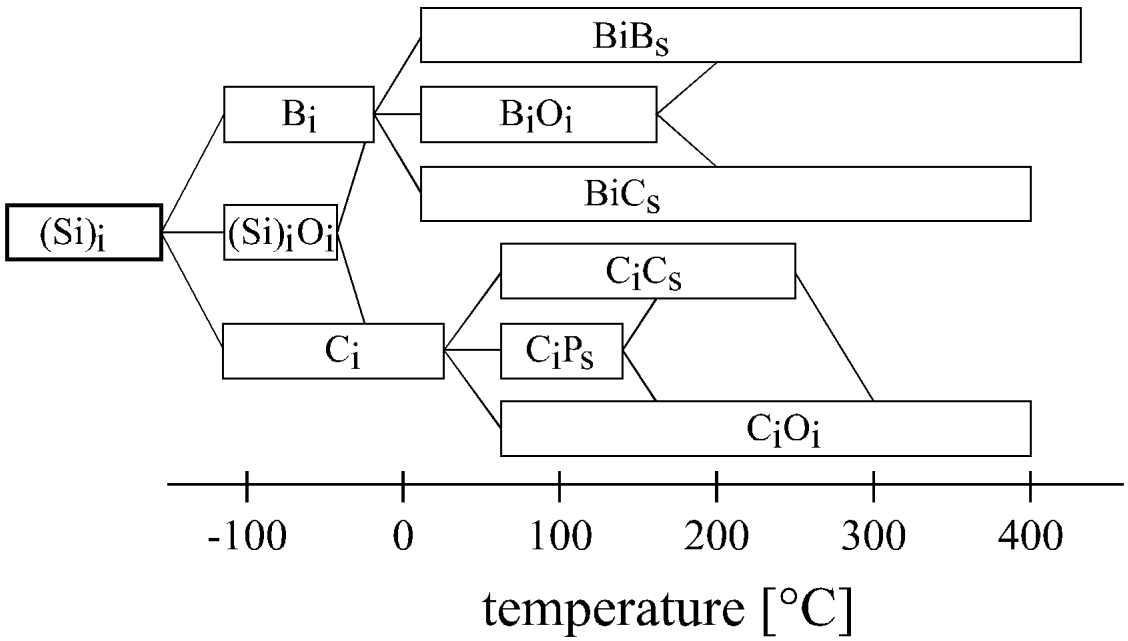

Figure 3.8: Hierarchy and stability of self-interstitial related defects as function of temperature. For annealing parameters and references see Tab. B.1.

Another important feature of some defects is their *metastability*. Depending on the temperature and the charge state different configurations of a defect can have the lowest total energy. A well–known example is the *bistability* of the C_iC_s [Son90b]. The configurational co-ordinate diagram and the structural change in the bonding is shown in Fig. 3.9. Since this bistability has an important impact on the microscopic measurements performed in this work (see Sec. 6.3) it has to be explained here in more detail.
The difference between the two configurations, named A and B, is based on a molecular bond-switching as shown in the lower half of Fig. 3.9. In both configurations C_iC_s is an amphoteric defect with acceptor states at $E_C - 0.17\,\mathrm{eV}$ (A) and $E_C - 0.11\,\mathrm{eV}$ (B) and donor states at $E_V + 0.09\,\mathrm{eV}$ (A) and $E_V + 0.05\,\mathrm{eV}$ (B). As can be seen from the configurational co-ordinate diagram, configuration A has the lowest total energy in the negatively or positively charged state while configuration B is the one with the lowest energy in the neutral charge state. Thus there is the tendency to change the configuration if the charge state of the defect is altered. However, for each configurational change an energetic barrier has to be overcome. For example about $0.145\,\mathrm{eV}$ is needed to transfer the negatively charged $C_iC_s^-$(B) into the negatively charged $C_iC_s^-$(A). The corresponding time constant can be expressed by [Son90b]

$$B^- \rightarrow A^- : \qquad 1/\tau_{(B^- \rightarrow A^-)} = 1.4 \times 10^{12}\,\mathrm{s}^{-1} \exp\left(-\frac{1.45\,\mathrm{eV}}{k_B\,T}\right)$$

with a frequency factor in the order of the most abundant phonon frequency and thus matching very well to a single jump process (compare Sec. 3.5). The activation energies and frequency factors for the transitions $B^0 \rightarrow A^0$ and $A^+ \rightarrow B^+$ are given in Tab. B.1.

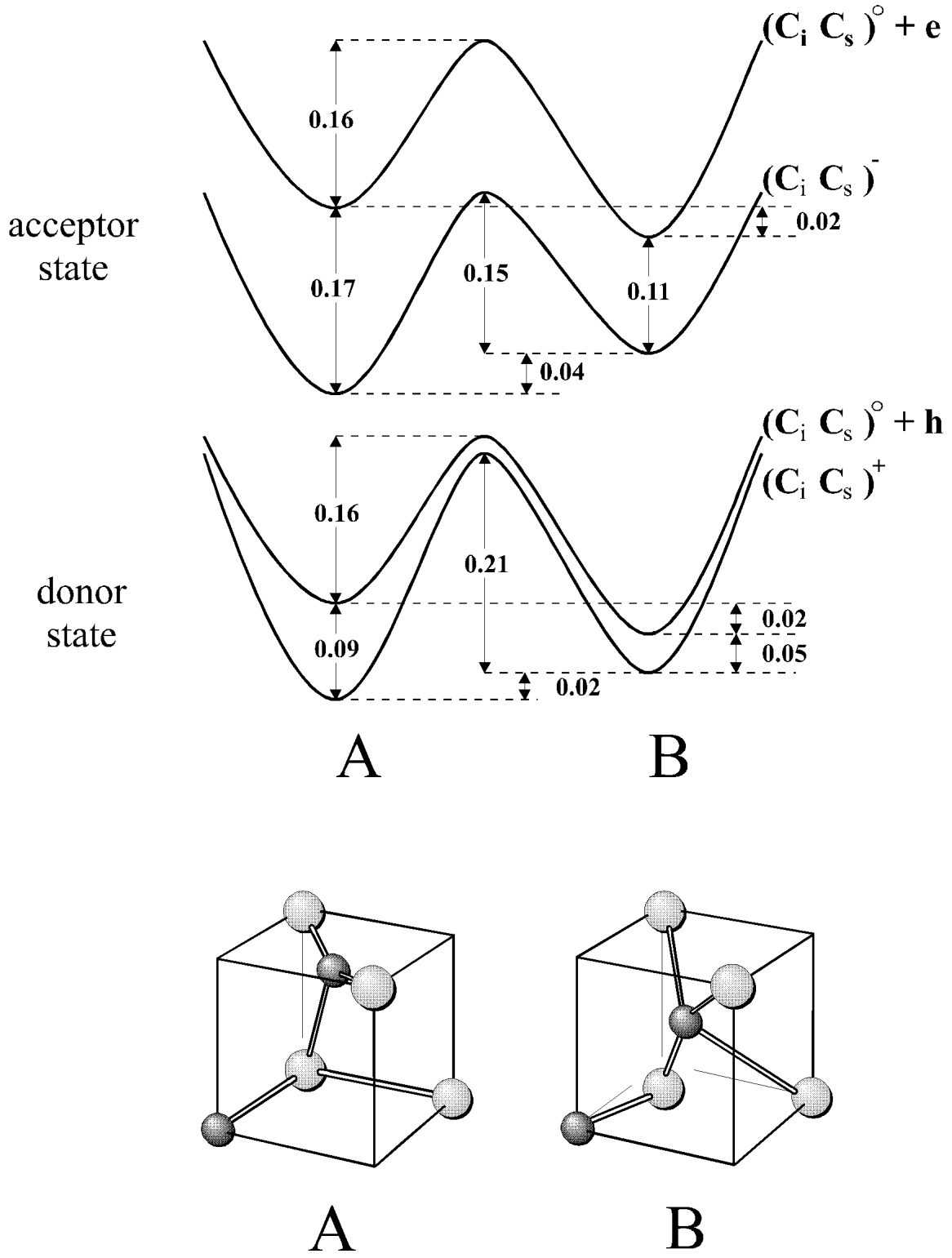

Figure 3.9: Configurational co-ordinate diagram for the C_iC_s complex and a structural model after [Son90b]. The dark spheres indicate the carbon atoms.

Finally it should be mentioned that for the C_iP_s an even more complicated multistability has been reported [Zha93]. As much as five different configurations were observed (see Tab. B.1).

3.6.2 Thermal donors

In silicon with a high oxygen concentration the formation of thermal donors due to heat treatments can seriously change the effective doping concentration. Consequently the temperature steps during the processing of a silicon detector using highly oxygenated material can have an influence on the final depletion voltage of the device (compare Tab. 4.1). In order to avoid, respectively control, the thermal donor generation it is necessary to understand their formation kinetics.
Oxygen in silicon is usually on interstitial lattice sites and electrically inactive. Otherwise the production of high resistivity floatzone silicon with an effective doping concentration in the order of $10^{12}\,\mathrm{cm}^{-3}$ would not be possible since the typical oxygen concentration lies in the order of some $10^{15}\,\mathrm{cm}^{-3}$. Even Cz silicon with a typical oxygen concentration of about $1\times10^{18}\,\mathrm{cm}^{-3}$ is used for the production of integrated circuits without influencing the electrical performance of the devices. However, in 1954 Fuller et al. [Ful54] discovered the formation of electrical active centers upon heat treatment of Cz silicon in the temperature range of 350–550°C. Later it was discovered that these centers are donors [Kai58] and because of their generation under thermal treatment were called *Thermal Donors* (TD's) [Mic94]. Meanwhile it was found that the thermal donors consist of two separate families, double donors (TDD's) and single donors with more shallow levels than the ground state of the TDD's. The latter ones have been named *Shallow Thermal Donors* (STD's) [Åbe98]. Above 650°C further oxygen related donors, so-called *New Donors* (ND), form.
The important factors that control the formation of the thermal donors are the annealing temperature and the annealing time. This is displayed in Fig. 3.10(a) where the TDD concentration for Cz silicon with $[O_i] = 7.7\times10^{17}\,\mathrm{cm}^{-3}$ as function of inverse annealing temperature is shown for various heat treatment times. Below 450°C the formation rate is decreased and the saturation concentration is less than for a 450°C treatment. Above 450°C the saturation concentration of TDD's decreases with increasing temperate. These experimental data have been obtained from resistivity measurements which are not sensitive for the type of thermal donor. However, IR measurements revealed that the TDD family consists of up to 16 different electrically active defects (TDD1–TDD16) which form in a seemingly sequential way [Göt92]. They are assumed to have a common electrical core with added oxygen atoms which gradually shift the donor states towards the conduction band edge (E_C). The overall formation rate and the maximum concentration of thermal donors at 450°C were found to depend on fourth and third powers of the oxygen concentration, respectively [Mic94]:

$$\frac{d}{dt}[\mathrm{TDD}] \propto [O_i]^4 \qquad \text{and} \qquad [\mathrm{TDD}]_{max} \propto [O_i]^3.$$

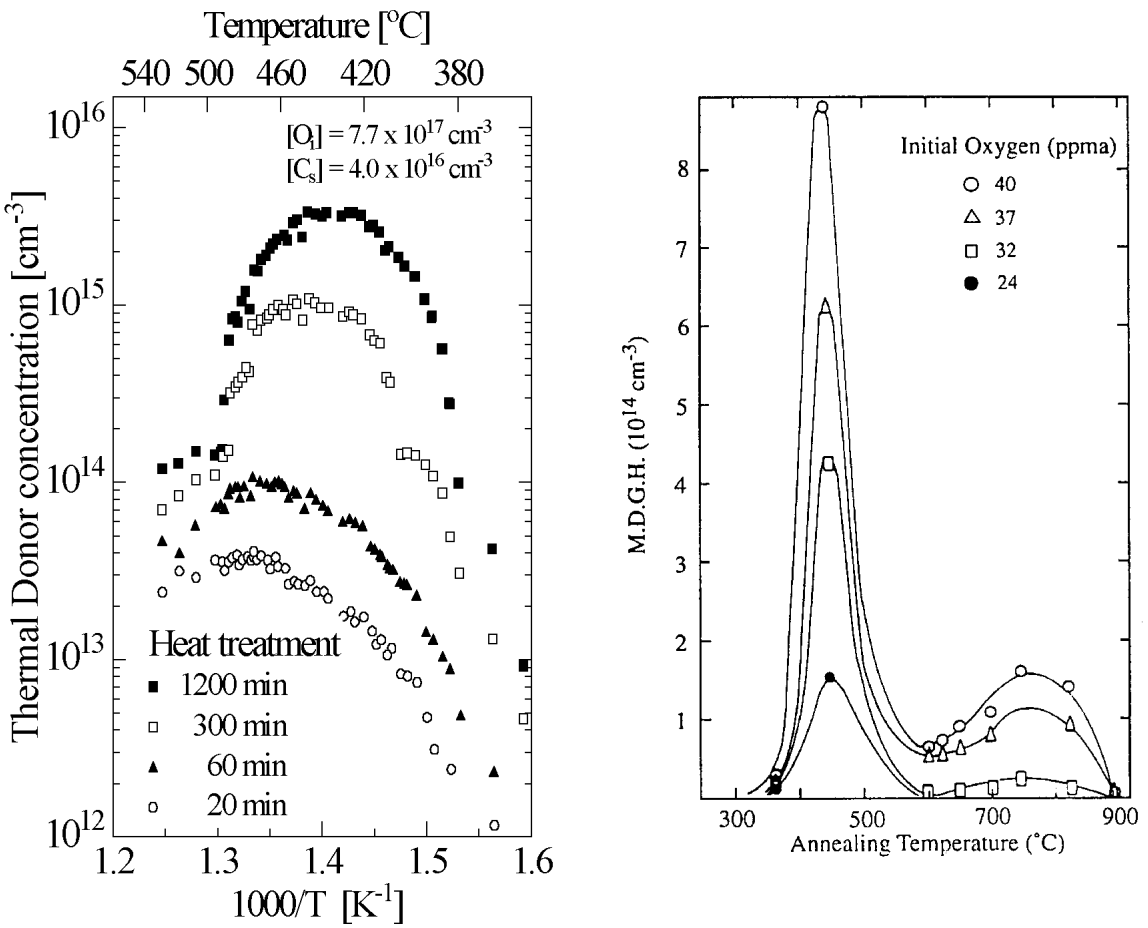

Figure 3.10: (a) Thermal Donor concentration as function of inverse annealing temperature for various heat treatment times.(b) Maximum donor generation per hour (M.D.G.H.) of annealing at given temperature in a nitrogen ambience (1ppma = $4.96\times10^{16}\,\mathrm{cm}^{-3}$). Both figures taken from [Mic94].

The diffusivity of O_i ($\approx 6 \times 10^{-19} cm^2 s^{-1}$ at 450°C; see Tab. B.1) is however not sufficient to explain the generation of TDD's. The diffusivity extracted from the TDD formation rate is in the order of $10^{-16}\,\mathrm{cm}^2\mathrm{s}^{-1}$ [Mic94]. Based on this discrepancy the existence of a fast diffusing molecular oxygen (O_2) was proposed [Gös82] and recently experimental evidence for its existence was given [Mur98]. Furthermore a kinetic study of this *oxygen dimer* in the temperature range from 350 to 420°C has been performed and its role in the formation kinetics of TDD's has been partly revealed. Based on the experimental data a set of differential equations was achieved allowing a first modeling of the TDD1 and TDD2 formation kinetics [Åbe98]. Combining the experimental data and the model predictions the most probable formation process of TDD1 is the association of two oxygen dimers $O_2 + O_2 \rightarrow$ TDD1. This process can be described by a second order reaction (compare Sec. 3.5)

$$\frac{d[\mathrm{TDD1}]}{dt} = -\frac{1}{2}\frac{d[O_2]}{dt} = 4\pi\, R\, D_{O_2}\, [O_2]^2. \tag{3.61}$$

However, in practice the description of the formation process is far more complicated since e.g. at the same temperature TDD1 is transformed into TDD2 (and higher order TDD's) and also a few new dimers are generated by diffusing O_i. In Ref. [Åbe98] it is predicted that TDD2 consist also of 4 oxygen atoms but in another configuration while TDD3 is generated by the capture of a third dimer and thus consists of 6 oxygen atoms.
Two defect states $E_C - 0.07\,\text{eV}$ and $-0.15\,\text{eV}$ due to thermal donors have been identified by DLTS [Ben83]. They appear during 450°C annealing and disappear during annealing above 550°C. The ionization energy of the states decreases with the applied field strength according to the Poole-Frenkel mechanism, confirming the shallow donor nature of the center (compare with experimental data in Sec. 6.5).

The second family of thermal donors, the Shallow Thermal Donors (STD's), can be formed by annealing nitrogen rich Cz-silicon at around 650°C. They have ionization energies from 0.0347 eV to 0.0374 eV which is much shallower than the single donor levels of the TDD's at 0.0530 to 0.0693 eV [Ewe97]. However, their structure is not exactly known and besides complexes of N-O also C-H complexes or Al atoms were suggested to be possible candidates to build the defect core of STD's (for details see [Ewe97] and references therein).

Finally another group of donors, generated however at higher temperatures, has to be mentioned. In Fig. 3.10(b) the maximum thermal donor generation per hour (M.D.G.H) of annealing at the given temperature is shown. As can be seen heat treatments between 650°C and 800°C – temperatures at which the TDD's generated between 350°C and 550°C are no more stable – can lead to the production of further donors, so-called *New Donors* (ND). However, little is known about their structure. It was suggested that they are related to Si_yO_x clusters of a few hundred atoms of oxygen acting as nucleation centers for oxygen precipitation. Furthermore their generation depends strongly on the annealing history of the material and is influenced by further impurities in the material like carbon [Mic94].

For further details see Refs. [Shi94, Åbe98, Ewe97] from which most of the information given here has been taken.

As a conclusion for the practical detector process technology of oxygen rich silicon temperature steps around 450°C at the end of the process – as e.g. often used for the annealing of the aluminum layers – have to be avoided (see Sec. 2.2.2.2).

3.7 Impact of defects on detector properties.

The electrical properties of defects and their occupation under various bias conditions have been described in Sec. 3.4. Thus the relation between the defects and the macroscopic detector properties has implicitly already been explained. However, in this section the impact on specific detector properties (depletion voltage, leakage current, charge collection efficiency, resistivity, etc.) will be reviewed. This serves on the one

hand to clarify the role of the defects and on the other hand to aid the discussion of the experimental results presented in Chapter 7. One should keep in mind that there is no comprehensive model about the electrical properties of clusters. They can not be described by standard Shockley–Read–Hall statistics and thus the following descriptions are mainly aimed on isolated defect levels. Whenever possible, a comment about the influence of clusters is given.

- **Generation lifetime** ($\longrightarrow$ Leakage current)
  Defects close to the middle of the band gap are efficient electron-hole pair generation centers (Sec. 3.4.3) and thus responsible for the leakage current. The bulk generation current (leakage current) I_{bulk} is often described by the so-called *generation lifetime* τ_g

$$I_{bulk} = A\, d\, q_0\, \frac{n_i}{\tau_g} \tag{3.62}$$

  where A is the area and d the thickness of the totally depleted detector and n_i the intrinsic carrier density. One should keep in mind that different kinds of defects contribute to the leakage current and thus a summation over all kinds of defects with individual concentration N_t has to be performed (compare Eq. 3.38):

$$\tau_g = \left(\sum_t \frac{1}{\tau_{g,t}}\right)^{-1} = n_i \left(\sum_t G_t\right)^{-1} = n_i \left(\sum_t N_t \frac{e_{n,t} e_{p,t}}{e_{n,t} + e_{p,t}}\right)^{-1}. \tag{3.63}$$

  Thus the electron and hole emission coefficients (e_n, e_p) of the defects (Eq. 3.22 for point defects) determine the overall electron-hole pair generation rate $G = \sum_t G_t$, respectively the leakage current.
  Recently the high leakage current observed after fast hadron irradiation was attributed to the interaction between divacancies located close together within the clusters and thus making a so-called intercenter charge transfer mechanism possible that effectively decreases the generation lifetime [Wat96, Gil97].

- **Space charge density** ($\longrightarrow$ Depletion voltage)
  Only some of the defects contribute to the space charge density N_{eff} of a depleted detector and hence influence the depletion voltage ($V_{dep} \propto |N_{eff}|$, Eq. 2.7). Ionized donors (donors occupied with holes) contribute positive space charge and ionized acceptors (acceptors occupied with electrons) negative space charge (Eqs. 3.35 and 3.37):

$$N_{eff} = \sum_{donors} p_t - \sum_{acceptors} n_t = \sum_{donors} N_t \frac{e_{n,t}}{e_{n,t} + e_{p,t}} - \sum_{acceptors} N_t \frac{e_{p,t}}{e_{n,t} + e_{p,t}}$$

  Usually donors in the upper half (e.g. P_s) and acceptors in the lower half (e.g. B_s) of the band gap are ionized in the space charge region at room temperature while donors in the lower half (e.g. C_iO_i) and acceptors in the upper half (e.g. VO_i, C_iC_s and VV) are not ionized. Therefore the latter ones usually do

not change the depletion voltage at room temperature.
Note that a very high leakage current (free carriers in the space charge region) can have an influence on the occupation of defects. Recently a so-called *deep-acceptor model* was suggested attributing an increase of negative space charge observed after fast hadron irradiation to the generation of a deep acceptor [Mat95, Mac96b]. According to this model the acceptor is partially occupied with electrons due to the high leakage current produced by clusters (for further details see Sec. 3.4.5).

- **Donor and acceptor removal** ($\longrightarrow$ Depletion voltage)
  Phosphorus and boron are usually the shallow defects that determine the effective doping concentration of an unirradiated silicon detector. During irradiation mobile defects are generated in the lattice that can react with the dopants by forming complexes or by removing them from their lattice site (e.g. $V + P_s \rightarrow VP_s$ or $I + B_s \rightarrow B_i$, see Sec. 3.6.1 for details). The formed defects (e.g. VP_s, B_i) are not ionized in the space charge region. Thus the effective doping concentration has changed or, in other words, shallow donors or acceptors have been *removed.*

- **Free carrier concentration** ($\longrightarrow$ Resistivity)
  The resistivity ρ is given by

$$\rho = \frac{1}{\sigma} = \frac{1}{q_0 \left(\mu_n n + \mu_p p\right)} \tag{3.64}$$

  where σ is the conductivity, n and p are the electron and hole densities in thermal equilibrium and μ_n and μ_p are the low field electron and hole mobilities. If the free carrier concentration is dominated by the shallow dopants (unirradiated, no deep defects, $|N_{eff}| \gg n_i$) the resistivity can be related to the effective doping concentration N_{eff} by $\rho = 1/(q_0 \mu_{n,p} |N_{eff}|)$ with $N_{eff} = N_{Donor} - N_{Acceptor}$ and μ_n or μ_p according to the conduction type. However, if the deep defect concentration reaches the order of the shallow doping concentration, this relation does not hold any more and resistivity and space charge can not easily be related to each other. The resistivity is related to the series resistance of the undepleted bulk by $R_S = \rho\,(d - W)/A$ with A and (d-W) being the area and the thickness of the undepleted (neutral) zone.

- **Trapping** ($\longrightarrow$ Charge collection deficiency)
  Electrons and holes generated by an ionizing particle in the silicon bulk drift to the electrodes due to the applied field (charge collection). Some of the drifting charge carriers are captured (*trapped*) by deep defects. If it takes longer than the shaping time of the electronic readout to re-emit the charge carrier the trapping results in a charge collection deficiency. The trapping probability of electrons by a certain kind of defect is proportional to the electron capture coefficient of this kind of defect, its concentration and the fraction not occupied with electrons (Eq. 3.35). Thus the overall trapping time constants $\tau_{T,n,p}$ for electrons and holes

are given by:

$$\frac{1}{\tau_{T,n}} = \sum_{traps} c_{n,t}\, N_t\, \frac{e_{n,t}}{e_{p,t} + e_{n,t}} \quad \text{and} \quad \frac{1}{\tau_{T,p}} = \sum_{traps} c_{p,t}\, N_t\, \frac{e_{p,t}}{e_{p,t} + e_{n,t}}. \tag{3.65}$$

- **Carrier freeze out, compensation** ($\longrightarrow$ Depletion voltage, *Lazarus effect*)
  With decreasing temperature the Fermi level usually moves closer to one of the band edges (E_C for n-type and E_V for p-type silicon, compare also Fig. 3.4). This represents the fact that with decreasing temperature more and more defects are not able any more to re-emit the captured carriers back into the bands. The carriers are *frozen* in the defects and *compensate* the shallow doping. The free carrier concentration decreases and, if a voltage is applied, the observed absolute space charge density ($\propto$ depletion voltage) is smaller than at higher temperatures. For high resistivity n-type silicon with $N_{eff,0}$ in the order of $10^{12}\,\mathrm{cm}^{-3}$ this has strong implications on the microscopic measurement methods. Already after a fluence in the order of $\Phi_{eq} \approx 10^{12}\,\mathrm{cm}^{-2}$ the divacancy concentration (deep acceptor in upper half of band gap) is high enough to *fully compensate* the silicon. No free electrons are available at temperatures below about 200 K for trap filling and e.g. the DLTS method can not be applied any more. For even higher fluences the deep defects completely rule the electrical behavior of the detector. Cooled to a cryogenic temperature (e.g. 77 K) the concentration of electron and hole traps is always high enough to capture all free carriers. Consequently there is also no *undepleted bulk* any more and applying a voltage results in an electric field reaching through the whole detector. Thus the charge collection efficiency is increased compared to the high temperature operation of a not fully depleted detector. This effect has most recently been named the *Lazarus effect* [R39] and the cryogenic operability of silicon detectors has been demonstrated after a fluence of $2 \times 10^{15}\,\mathrm{cm}^{-3}$ [Pal98].
  In this temperature range most of the trapped carriers are not emitted again. Thus it is possible that after the capture of an electron a hole is captured at the same defect. In such a case the *trapping process* could also be described as *"recombination"*.

Chapter 4

Experimental Methods and Experimental Equipment

In this chapter the experimental techniques and the experimental setup are presented. The chapter starts with a survey about the used materials and devices followed by a description of the irradiation facilities at which samples have been irradiated. Subsequently the setup for the measurement of current and capacitance as function of reverse bias (I/V and C/V characteristics) and the evaluation methods used for determination of the generation current and the depletion voltage are described. In the second part of the chapter the Deep Level Transient Spectroscopy (DLTS) and Thermally Stimulated Current (TSC) techniques, used for the investigation of radiation induced defect levels in the forbidden bandgap, are explained in more detail. The chapter ends with a short description of the experimental setup for these microscopic methods.

4.1 Materials and devices

A detailed description of the production techniques for the different materials and test structures used in this work has already been given in Chapter 2. Therefore the main purpose of this section is the classification and labelling of the materials and devices. Tab. 4.1 summarizes the main properties which will be discussed in more detail in the following.

Labelling of the materials and devices

In the last column of Tab. 4.1 the labelling of the different materials and devices is given. The first letter of the acronym stands for the producer of the material and the second one for the manufacturer of the diode. The companies and institutes corresponding to the letters are given at the bottom of the table. Further details about the devices can be found in Sec. 2.2.2 and Tab. 2.2 on page 20. The values following the letters indicate the resistivity and p-type material is additionally marked with a "P". More accurate values for the resistivity (ρ) are also given in the table. These values were determined from the averaged effective doping concentration of the samples (N_{eff}).

Material properties						Device properties		
Type	Producer of crystal	$[O_i]$ $\left[\frac{10^{16}}{\mathrm{cm}^{-3}}\right]$	$[C]$ $\left[\frac{10^{16}}{\mathrm{cm}^{-3}}\right]$	$[P]$ $\left[\frac{10^{12}}{\mathrm{cm}^{-3}}\right]$	$[B]$ $\left[\frac{10^{12}}{\mathrm{cm}^{-3}}\right]$	N_{eff} $\left[\frac{10^{12}}{\mathrm{cm}^{-3}}\right]$	ρ [kΩcm]	Acronym of diode
n-type with *"low"* oxygen concentration								
n-FZ	Wacker	< 0.02	< 3	0.3	0.04	1.0	4.3	WH-4k
						1.1	3.9	WI-4k
n-type with *"standard"* oxygen concentration								
n-FZ	Wacker	< 5	< 0.5			0.17	25	WE-25k
n-FZ	Wacker	< 5	< 0.5			0.38	11.4	WE-11k
n-FZ	Wacker	< 5	< 0.5			0.64	6.7	WE-7k
n-FZ	Topsil	< 5	< 0.5			0.65	6.6	TS-7k
n-FZ	Wacker	< 5	< 0.5	0.80	0.05	1.4	3.2	WM2-3k
n-FZ	Wacker	< 5	< 0.5			1.6	2.6	WM3-3k
n-FZ	Polovodice	< 5	≤ 1	0.5	0.07	1.9	2.2	PI-2k
n-FZ	Wacker	< 5	< 2	6.44	0.21	10	0.41	WI-400
n-FZ	ITME	< 5	2	40	1	37	0.12	II-120
						33	0.13	IH-130
n-FZ	Wacker					48	0.090	WH-90
n-FZ	Wacker					770	0.006	WH-6
n-type with *"high"* oxygen concentration								
n-FZ	Wacker	15	< 1			1.6	2.7	WS-3k
n-FZ	ITME	21	1.0	2	0.05	3.6	1.2	II-1k
n-FZ	ITME	17	< 2	2.27	0.09	5.5	0.78	II-800
n-type with *"very high"* oxygen concentration								
n-Cz	Polovodice	90	0.5	40	8	31	0.14	PH-140
						39	0.11	PH-110
						103	0.04	PI-40
p-type								
p-MCz	Komatsu	50	≤ 0.5	9	4	4.0	3.5	KIP-4k
p-Cz	MEMC	73	≤ 0.5	50	50	21	0.65	MIP-650
p-EPI	ITME	$4-20$	$1-2$			32	0.44	IDP-400
p-EPI	ITME	$3-20$	$1-2$			7.8	1.8	IDP-2k
p-EPI	ITME	$4-60$	$1-2$			3.2	4.4	IDP-4k

Material Producers (first letter in acronym)			Device Producers (second letter in acronym)		
Komatsu	San Jose, USA	[KOM]	**D**iotec	Radošina, Slovakia	[DIO]
ITME	Warsaw, Poland	[ITM]	**E**lma	Moscow, Russia	[ELM]
MEMC	Novara, Italy	[MEM]	**H**amburg	Schottky diodes (own lab)	
Polovodice	Prague, Czech Republic	[POL]	**I**TE	Warsaw, Poland	[ITE]
Topsil	Frederikssund, Denmark	[TOP]	**M**PI	München, Germany	[MPI]
Wacker	Burkhausen, Germany	[WAC]	**S**intef	Oslo, Norway	[SIN]

Table 4.1: Properties and labelling of the used materials (see text).

Changes in material properties due to diode processing

The columns of Tab. 4.1 are divided in two parts describing on the left side the material and on the right side the device parameters. This division is necessary since the material properties – especially the effective doping concentration N_{eff} – can be changed by the device processing. This is most obvious for the Cz materials with the very high oxygen concentration. Although the different type of diodes (PH and PI) were produced on wafers originating from the same ingot the measured effective doping concentration differs strongly. This is due to the formation of thermal donors (see Sec. 3.6.2). The Schottky diodes[1] PH-110Ωcm were produced on not oxidized wafers while the Schottky diodes PH-140Ωcm were produced from oxidized wafers. DLTS measurements showed that the thermal donor concentration was reduced during the oxidation procedure, leading to the change in resistivity from 110 Ωcm to 140 Ωcm. The change in resistivity due to the processing is even more pronounced for the devices of type PI-40Ωcm. The reason for this dramatic change in resistivity from 140 Ωcm to 40 Ωcm is found in the last processing step of the diodes in which the aluminium layers are annealed at 450°C (the full process is described in Sec. 2.2.2.2). This temperature is by chance also the temperature with the maximum generation rate for thermal donors (compare Fig. 3.10 on page 58). In consequence the diode production process for highly oxygenated material has been modified in such a way that the last heat treatment is a high temperature step well above 450°C. As demonstrated by the existence of the highly oxygenated high resistivity p-type materials KIP-4kΩcm and MIP-650Ωcm the formation of thermal donors can be avoided (details about the process are given in Sec. 2.2.2.2).

Impurity and dopant concentrations

The oxygen and carbon concentrations given in Tab. 4.1 were measured by *Secondary Ion Emission* (SIMS) [EVA, FTE, Dez97] and/or *infrared absorption* (IR) [Cla97, Dez97]. As indicated in the table some of theses values are below the detection limits of the used methods. Nevertheless the n-type samples were divided in four categories regarding their oxygen concentration[2] $[O_i]$:

- **low** $[\mathbf{O_i}]$: FZ silicon with $[O_i]$ below $2 \times 10^{14}\,\mathrm{cm}^{-3}$ (IR-measurement [Cla97]),
- **standard** $[\mathbf{O_i}]$: FZ silicon purchased from industrial manufacturers without any predefined oxygen concentration; $[O_i]$ lies below the detection limit of the performed SIMS measurements but is expected to be in the order of $5 \times 10^{15}\,\mathrm{cm}^{-3}$,

[1] For the formation of Schottky-contacts no high temperature step is needed and thus also no influence of the diode production process on the material properties is expected (see Sec. 2.2.2.3).

[2] With the IR method the interstitial oxygen concentration $[O_i]$ and with the SIMS method the overall oxygen concentration $[O]$ is detected. If not mentioned otherwise the given data refer to the interstitial oxygen concentration. In many cases the oxygen concentration was measured with the SIMS method and found to be below the detection limit. Since always $[O_i] \leq [O]$ this detection limit is also the upper limit for the $[O_i]$ concentration.

- **high** [$\mathbf{O_i}$]: oxygenated FZ silicon with $[O_i] \approx 2 \times 10^{17}\,\mathrm{cm}^{-3}$,
- **very high** [$\mathbf{O_i}$]: Cz silicon with $[O_i] = 9 \times 10^{17}\,\mathrm{cm}^{-3}$.

All given carbon concentrations were measured by the SIMS method. The broad range of [O] and [C] in the epitaxial p-type material produced by ITME reflects the inhomogeneous distribution of oxygen and carbon derived from depth profile SIMS measurements [Dez97].

The given phosphorus and boron concentrations were determined from Photo Luminescence (PL) measurements by G. Davies from King's College London [Dav98]. Although the measured phosphorus and boron concentrations do not reproduce the measured effective doping concentration they give a clear indication that in most of the used materials the boron concentration is well below the phosphorus concentration. Thus there is no strong compensation between phosphorus and boron in the investigated n-type materials. However, the two p-type materials MIP-650Ωcm and KIP-4kΩcm are compensated. The influence of this compensation on radiation damage effects will be discussed in Chapter 8.
In two of the materials investigated with the PL method, namely the WI/WH-4k and KIP-4k, dislocations have been detected. The first material (FZ from Wacker; low oxygen content; WI/WH-4k) was produced in 1967 and thus may be dislocated due to the former production technology. To the second material (MCZ from Komatsu; high oxygen content; KIP-4k) a *thermal donor killing process* ($\approx$ 1000°C for 5 h) has been applied in our laboratory. This heat treatment has not only reduced the thermal donor concentration – the resistivity changed from about 15 Ωcm n-type to 4 kΩcm p-type (the value specified by the producer) – but most probably also introduced the dislocations.

4.2 Irradiation facilities

4.2.1 The Be(d,n) source at the PTB–Braunschweig

Most of the data presented in this work were obtained on samples irradiated at the neutron source of the *Physikalisch–Technische Bundesanstalt* (PTB) in Braunschweig [PTB]. Since this source is used as a reference for the calibration of fluence by the so-called α value (Sec. 5.2) it is described in more detail and with special interest in the fluence determination.
The source is a 2 mm thick beryllium target which is bombarded with deuterons of about 13.5 MeV energy. The reaction $^9Be(d,n)^{10}B$ provides a neutron field with a mean energy of 5.2 MeV. The target is surrounded by a collimator consisting of a multilayer structure containing Fe, polyethylene with boron carbide, Pb and W. It assures an adequate beam for neutron therapy, a possible application for this source, and shields the experimental area from neutron contamination. For the detector irradiation experiments a part of the collimator was removed. At the beginning of each beam time at the PTB the flux was measured with a ionization chamber as function

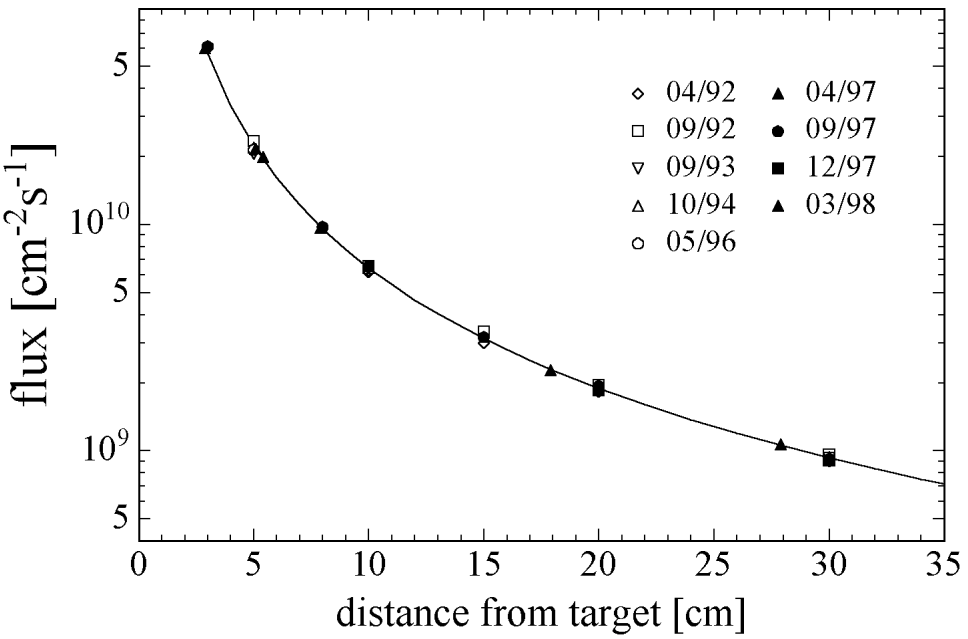

Figure 4.1: Neutron flux as function of distance from target measured during several beam times and normalized to a deuteron beam current of 30 μA. Note that the displayed flux is not normalized to the 1 MeV neutron equivalent flux ϕ_{eq}. In order to get ϕ_{eq} the given data have to be multiplied with the (r-dependent) hardness factor presented in Fig. 4.2.
(The fit is given by $\phi(r) = I_{target} \times k_\phi \times f(r)$ with $I_{target} = 30\,\mu$A describing the beam current and $k_\phi = 1.05 \times 10^{18}\,\mathrm{C}^{-1}\mathrm{cm}^{-2}$ being a calibration factor that takes into account the specific properties of the used ionization chamber. The function $f(r)$ describes the ratio between the charge measured in the ionization chamber and the charge deposited by the deuteron beam on the target. $f(r)$ is given by $\log(f(r)) = -1.8463 - 1.8994r + 0.0566r^2$ with the distance from the target r expressed in [cm].)

of distance from the target. Fig. 4.1 shows the corresponding results for several beam times normalized to the typically used beam current of 30 μA on the target. The neutron flux scales linear with the deuteron beam current and with increasing distance r from the target it decreases almost with an $1/r^2$-dependence. For the maximum beam current of about 32 μA the flux reaches the value of about $9 \times 10^9\,\mathrm{cm}^{-2}s^{-1}$ at 10 cm distance from the target. The error in the flux strongly depends on the distance from the target and was estimated to be about 9% at 5 cm and 3% at 30 cm [Bre97a]. The temperature during all irradiations was 18 ± 1°C.
Due to the interaction of the primary neutrons with the collimator material the energy spectrum changes slightly with the distance from the target. This was taken into account for the calculation of the hardness factor. The spectrum was measured without collimator by the time-of-flight method with very high accuracy [Bre86]. This spectrum was then used as an input for Monte Carlo simulations calculating the influence of the collimator and resulting in a set of spectra for various distances from the target [Bre97b]. In collaboration with A. Vasilescu from the INPE Bucharest the hardness factors were determined for the different distances [Vas98]. The corresponding values

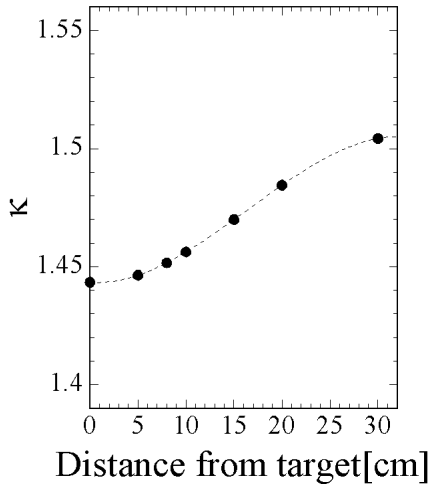

Figure 4.2: Dependence of κ on the distance from the target for the Be(d,n) irradiation source at the PTB. (The dashed line corresponds to a polynomial fit with $\kappa(r) = -4.02 \times 10^{-6} r^3 + 1.98 \times 10^{-4} r^2 - 3.03 \times 10^{-4} r + 1.4434$ with r in units of [cm].)

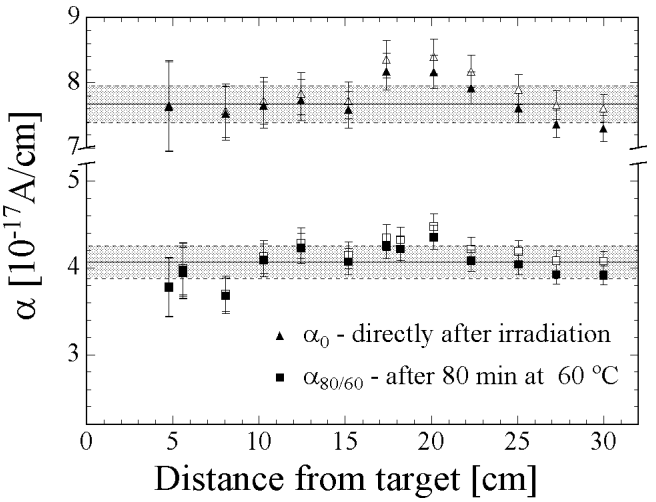

Figure 4.3: Dependence of α on the distance from the target measured directly after irradiation and after a heat treatment for 80 min at 60°C. The filled symbols indicate the data calculated with the κ-values as displayed in Fig. 4.2 and the open symbols the values calculated with a constant κ of 1.44.

are displayed in Fig. 4.2 in which the κ–value of 1.44 at the target corresponds to the undisturbed spectrum.

In order to check the r-dependence of the flux measured by the ionization chamber and the r-dependence predicted for the hardness factor by the simulations, a set of detectors (type WE-11k, see Tab. 2.2) was irradiated at different distances from the target. The samples were irradiated in several runs in order to achieve about the same nominal fluence for the individual samples. However, a deviation in the fluences could not be avoided and the nominal fluence ranged from $\Phi = (7 \text{ to } 18) \times 10^{11}\,\text{cm}^{-2}$. According to the experimental data presented in Sec. 5.2 this is not problematic if the α value ($= \Delta I/(V\Phi)$) is used as damage parameter for checking the r-dependence. This parameter is displayed in Fig. 4.3 as function of distance from the target. The shown α values were measured directly after irradiation[3] (α_0) and after a heat treatment of the samples for 80 min at 60°C ($\alpha_{80/60}$). Two sets of data are displayed for each annealing state. The open symbols correspond to the data achieved under the assumption that the hardness factor is not depending on the distance from the target while the filled symbols correspond to data that take into account an r-dependent κ–value (Fig. 4.2). Within the measurement error no difference is observed regarding the variation of α

[3]Approximately 15 min after irradiation the samples were dropped into liquid nitrogen in order to avoid any further annealing. Then the samples were transported within the nitrogen to our laboratory where they were taken one after another from the nitrogen for the leakage current measurement.

with distance from the target:

$\alpha_0 = (7.89 \pm 0.08)\,10^{-17}$ A/cm and $\alpha_{80/60} = (4.18 \pm 0.04)\,10^{-17}$ A/cm (with $\kappa = 1.44$)
$\alpha_0 = (7.67 \pm 0.08)\,10^{-17}$ A/cm and $\alpha_{80/60} = (4.06 \pm 0.04)\,10^{-17}$ A/cm (with $\kappa = \kappa(r)$)

The difference between the two sets of data is not very significant. Even comparing the χ^2 values does not give a clearer picture. They differ only by below 10%. For the measurement after 80 min at 60°C the r-dependent κ displays the smaller χ^2 and for the measurement directly after irradiation the data with the constant κ. However, the data obtained after the heat treatment are regarded as more reliable since for the ones obtained after irradiation small deviations in the annealing time are unavoidable. In conclusion the r-dependent kappa values are used within this work since, first, the more reliable values measured after the heat treatment display the smaller χ^2 and, second, the r-dependence is predicted by the simulations.

4.2.2 Further neutron sources

Besides the neutron source at the PTB some other irradiation facilities have been used for this work. They are described only very briefly in the following. For further informations the reader is referred to the given references. The hardness factors calculated from the individual spectra will be discussed in more detail in Sec. 5.2. There they are compared to the ones experimentally determined from the increase in leakage current (α value) of diodes irradiated at the corresponding sources.

University Hospital Hamburg (UKE) (14.1 MeV monoenergetic neutrons)
Here a rotating tritium-titanium target is bombarded with 500 keV deuterons. In a $^3H(d,n)^4He$ reaction monoenergetic neutrons with 14.1 ± 0.2 MeV are produced. The average flux for the irradiations presented in this work was about 1×10^8 n/cm^{2}s. Further details about the source can be found in [Sch78].

National Center for Scientific Research (NCSR) Demokritos (reactor)
At the open-pool 5 MW research reactor at the NCSR Demokritos, Greece [DEM] the samples are brought in a pneumatic transfer system close to the reactor core. This allows short irradiations and a very fast access. The samples as well as the gold foils for fluence determination by activation method were wrapped in cadmium foil in order to shield them from thermal neutrons. Different magnitudes in irradiation fluences were obtained by changing the reactor power. At the irradiation position the flux differed between $\approx 3 \times 10^8$ n cm^{-2}s^{-1} at 7.5 kW to $\approx 2 \times 10^{11}$ n cm^{-2}s^{-1} at 5 MW. Thus it was possible to irradiate a set of samples for the same time (100 s) but with different reactor powers in order to investigate the flux dependence of the radiation damage.

Jožef Stefan Institute, Ljubljana, Slovenia (reactor)
The 250 kW TRIGA Mark II research reactor at the Jožef Stefan Institute [LJU] is a light water reactor with solid fuel elements. As for the Demokritos reactor the reactor power was changed in order to reach the different orders of magnitude in fluence. Here, depending on the reactor power, a flux ranging from 2×10^9 n cm$^{-2}s^{-1}$ to

$2 \times 10^{12}\,\mathrm{n\,cm^{-2}s^{-1}}$ can be reached. The energy distribution of reactor neutrons covers a wide range of energies. Therefore the spectrum was determined with a set of activation foils made from different materials in order to calculate the hardness factor [Žon99] (compare Sec. 5.2). For the individual samples the fluence was determined by gold foil activation and later on also by the *α-value* method described in Sec. 5.2.

4.2.3 Proton and gamma sources

CERN Proton Synchrotron (PS) (24 GeV/c protons)

The used proton beam has a momentum of 24 GeV/c. It was extracted from the accelerator one to three times per 14.4 s lasting cycle depending on the beam sharing with other experiments. Per extraction a spill of about 2×10^{11} protons, defocused in vertical direction over a length of $\approx 3\,\mathrm{cm}$, was swept horizontally (2.5 cm) in a constant rate within the 400 ms crossing time. The resulting average proton flux with one spill per cycle is $\approx 2 \times 10^{9}\,\mathrm{cm^{-2}s^{-1}}$. The fluence was measured by activation of aluminium foils ($^{27}\mathrm{Al(p,3pn)}^{24}\mathrm{Na}$) using the gamma emission (1.37 and 2.75 MeV) of ^{24}Na ($\tau_{1/2} = 14.96$ h) [Leó95]. For further details see [Dez97, Cas98b].

Brookhaven National Laboratory (BNL) (^{60}Co–gamma irradiations)

The ^{60}Co–gamma irradiations at BNL were carried out with a dose rate of 1.5 kGy (150 krad) per hour. During all irradiations the temperature was kept below 30°C [BNL]. $^{60}_{27}Co$ has a half-life of 5.27 years. In a β^- decay (99%) it decays to $^{60}_{28}Ni$ and two γ–photons (1.17 MeV and 1.33 MeV) are emitted. The received photon fluence can be calculated from the dose by using a conversion factor of 1 Mrad = 10 kGy = $1.90 \times 10^{15}\,\gamma\mathrm{cm^{-2}}$ [Hol94].

4.3 Diode characteristics

The used test diodes are quite small ($\approx 0.25\,\mathrm{cm^2}$) and have - contrary to the microstrip detectors used for tracking - a simple pad structure with one or a few guard rings surrounding the central electrode. Such structures are fabricated by various manufacturers in addition to prototype strip or pixel detectors on the same wafer or exclusively for test purposes (compare Sec. 2.2.2). It has become obvious during this work, that for all measurements the proper use of the guard ring is essential, since only in this way the depleted volume is precisely defined by the geometrical area of the pad electrode and lateral effects contributing to both the capacitance and the leakage current are practically excluded. Although that is of course true for the as processed p^+-n diodes with the pad and guard ring structure on the p^+ side and the electric field starting below that electrode, it is even more relevant for diodes after high irradiation levels, when the original n-type bulk material had effectively changed to p-type[4]. In this case the junction side is switched to the rear electrode and the electric field starts to grow

[4]The term *type inversion* is explained in Sec. 5.3.1.

from there[5]. Normally the rear electrode is completely metallized all over the total area and hence the volume of the depleted zone is much larger. Only when the electric field extends completely to the front electrode, one gets a homogeneous field distribution across both the pad and guard ring extension and hence the guard ring will act again as such, defining the active volume exclusively. The resulting effect can be clearly seen in Fig. 4.4, where for the same situations capacitance versus voltage (C/V) and current versus voltage (I/V) measurements are compared with floating and connected guard ring.

Current voltage characteristics (I/V)

In Fig. 4.4 I/V characteristics of three type inverted detectors are shown. As can be seen it is necessary to connect the guard ring of the diodes in order to extract reproducible and reliable damage parameters from standard I/V characteristics. While for the measurements with connected guard ring the current reaches a saturation value for measurements without connected guard ring no such value can be achieved. Thus it is not possible to determine the generation current density since on the one hand the depleted volume and on the other hand the amount of surface current (e.g. from the cutting edge) are unknown. All current related data presented in this work were achieved with a connected guard ring with exception - of course - for the diodes that did not have a guard ring (see Tab. 2.2). For all evaluations the saturation value of the leakage current reached well above depletion was used (indicated by the horizontal lines in the figure) and not the current value at the voltage corresponding to the depletion voltage as determined from C/V characteristics (indicated by vertical lines in the figure). It has to be emphasized that most deviations between the results presented in this work and the ones of previous publications result from the different techniques with respect to the use of the guard ring.

Capacitance voltage characteristics (C/V)

With a capacitance bridge the admittance Y, respectively the impedance $Z = Y^{-1}$, of a device is measured. Only by assuming that the measured sample can be regarded as an equivalent parallel circuit of a resistor R_p and a capacitance C_p the imaginary part of the admittance divided by ω gives the (*parallel*) capacitance of the device:

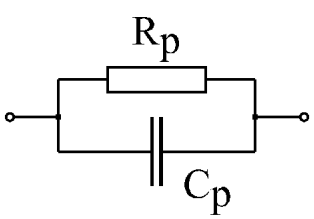

$$Y = \frac{1}{R_p} + j\omega C_p. \tag{4.1}$$

[5]To be more precise it has to be mentioned that after type inversion not only on the n^+ side but also on the p^+ side a growing depletion zone is observed with the one on the n^+ side to be the dominating one. This so-called *double junction* was proposed in 1992 [Wun92, Li 92] and has meanwhile been confirmed in many measurements (e.g. [Cas98b, Bea98b]).

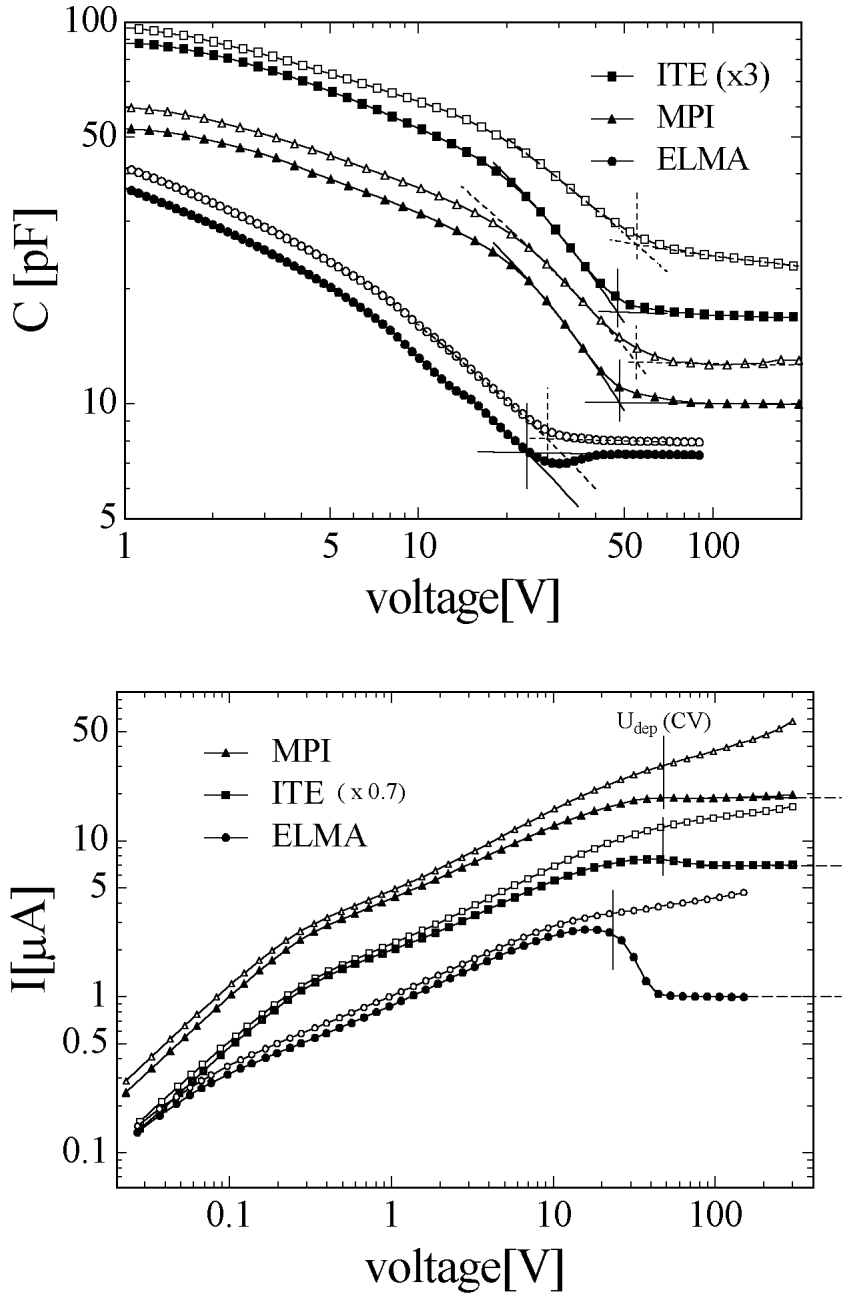

Figure 4.4: Examples of C/V and I/V characteristics for three type inverted diodes from different manufacturers (see Sec. 2.2.2). The filled symbols indicate the measurements with and the open ones those without connected guard ring. The vertical lines denote the depletion voltage as extracted from C/V measurements (connected guard: solid line; floating guard: dashed line). The horizontal lines in the lower figure indicate the extracted leakage current saturation value for further evaluation. The data for the sample ITE are scaled by 0.7 (I/V) and 3 (C/V) for better visibility.

(Fluences and annealing times for the three shown examples: MPI: $4 \times 10^{13}\,\mathrm{cm}^{-2}$, directly after irradiation; ITE: $4 \times 10^{13}\,\mathrm{cm}^{-2}$, 80 min at 60°C; ELMA: $6.5 \times 10^{12}\,\mathrm{cm}^{-2}$, 5120 min at 60°C).

Here $\omega/2\pi$ is the frequency of the used AC-signal. However, if it is assumed that the device is best described by a serial circuit of a resistor R_s and a capacitance C_s the *(serial)* capacitance of the device can be calculated from the imaginary part of the impedance:

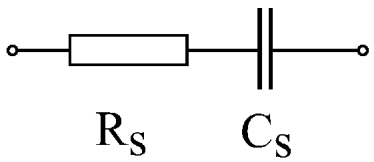

$$Z = R_s - j\frac{1}{\omega C_s}. \tag{4.2}$$

Since the two equivalent circuits are different representations of the same measured data they can be converted from one to another. If for example the parallel mode of the bridge is chosen the measured capacitance C_p and conductance $G_p = R_p^{-1}$ can be transformed into the serial values R_s and C_s by

$$C_s = \frac{1+\omega^2 R_p^2 C_p^2}{\omega^2 R_p^2 C_p} \quad \text{and} \quad R_s = \frac{R_p}{1+\omega^2 R_p^2 C_p^2}. \tag{4.3}$$

In practice the parallel circuit is a good description for unirradiated diodes because the undepleted bulk can be neglected due to its high conductivity. Furthermore the leakage current of the device, represented by the parallel resistor, is very small which means that also the conductivity is very small and the measured admittance represents almost only the capacitance. However, for a highly irradiated diode no such clear figure exists. Due to radiation damage the resistivity of the undepleted bulk and the leakage current increase (see [Big97] and Chapter 5). Thus neither the parallel nor the serial circuit can represent the detector (see e.g. [Li 94]). The high leakage current demands a small parallel resistor R_p (resp. high G_p) in the circuit while the high resistivity of the undepleted bulk demands a serial resistor R_s. Furthermore the presence of a high concentration of deep defects adds an additional frequency dependent contribution to the signal (see e.g. [Dab89]). Finally there is a strong evidence that the depletion zone of type inverted detectors is growing from both, the p^+ and the n^+, junctions (e.g. [Bea98b, Cas98b]). For such a situation up to now no model exists that describes how the capacitance measurement is influenced. In conclusion the C/V characteristics (*serial* or *parallel*) of a type inverted detector are by far not understood. Consequently it is also not clear how the depletion voltage should be extracted from the C/V characteristics of highly irradiated detectors.

In this work the capacitance voltage characteristics were measured at room temperature with a capacitance bridge in parallel mode and a frequency of 10kHz if not mentioned otherwise. The depletion voltage V_{dep} was extracted from a plot of *parallel* capacitance against $1/\sqrt{V}$ by determining the intercept of two straight lines fitted to the data before and after the kink in the plot (compare Eq. 2.9). The corresponding effective doping concentration was calculated by using Eq. 2.7:

$$|N_{eff}| = \frac{2\epsilon\epsilon_0}{q_0}\frac{V_{dep}}{d^2} \tag{4.4}$$

For the unirradiated low resistivity materials ($\rho < 200\,\Omega$cm) the depletion voltages where higher than the maximum available voltage of 1000 V. Therefore the effective

doping concentration was determined from the slope in a plot of $1/C^2$ versus voltage. The transformation of Eq. 2.9 results in

$$\frac{d}{dV}\left(\frac{1}{C^2}\right) = \frac{2}{A^2\,\epsilon\epsilon_0\,q_0\,N_{eff}} \tag{4.5}$$

and, if solved for the effective doping concentration, in

$$N_{eff} = \frac{2}{A^2\,\epsilon\epsilon_0\,q_0}\left(\frac{d\,(1/C^2)}{dV}\right)^{-1}. \tag{4.6}$$

This method was also used for determination of the effective doping concentration during the measurements of the DLTS spectra (see Sec. 4.4) since the maximum voltage of the DLTS system was limited to 20 V.

Setup for measurement of diode characteristics

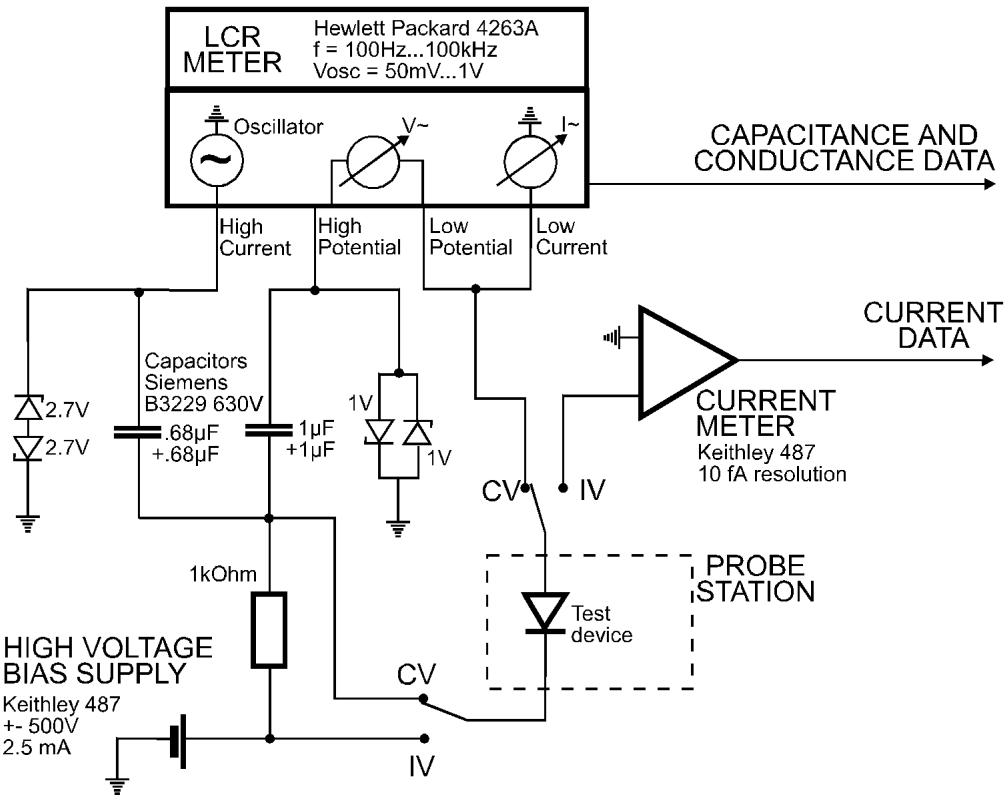

Figure 4.5: Electrical setup for C/V and I/V measurements (taken from [Fei97a]).

In Fig. 4.5 the electrical setup for C/V and I/V measurements is shown. For the C/V and I/V measurements the samples were mounted on a Suss probe station. The front contact was connected to the low potential and the guard ring to ground. A Keithley 487 (500 V, 2.5 mA) and later on a Keithley 6517A (1000 V, 1 mA) was

used as bias source. These two instruments were also used for the leakage current measurements. The capacitance was measured with a Hewlett Packard 4263A LCR meter in parallel mode. This capacitance bridge provides fixed frequencies of 0.1, 0.12, 1, 10, and 100 kHz and fixed amplitudes in the range from 50 mV to 1 V. Typically a frequency of 10 kHz and an amplitude of 100 mV or 500 mV were used. Since the operation of the bridge is limited to voltages below 20 V, a special adapter (see Fig. 4.5) was linked into the circuit to allow the application of higher voltage (up to 1000 V). The temperature in the probe station was monitored with a Pt100 platinum resistor in connection with a Keithley 195A multimeter.
I/V and C/V measurements were controlled by a computer over a standard GPIB (IEEE) bus. For the C/V measurements the capacitance and the conductance values as function of voltage were always stored in the data file.

4.4 Deep Level Transient Spectroscopy (DLTS)

Deep level transient spectroscopy (DLTS) is a widely used spectroscopic method to characterize deep level defects in semiconductor materials and devices by determining their concentration, their thermal activation energy and their capture cross sections. DLTS uses capacitance, voltage or current transient signals resulting from relaxation processes following an abrupt change of the bias voltage or light applied to the investigated sample. These measurement modes are called capacitance (C-) DLTS, constant capacitance (CC-) DLTS and current (I-) DLTS, respectively. Detailed descriptions of these methods can be found in [Brä79, Mil77] (C-DLTS and CC-DLTS) and [Mei92] (I-DLTS).
In this work the C-DLTS method, originally proposed by D. V. Lang [Lan74], has been used. After a short description of the C-DLTS principle of operation, it will be shown how the defect parameters activation energy, capture cross sections and concentration were determined from the measured capacitance transients. The DLTS setup is described in Sec. 4.6.

4.4.1 Principle of operation

Because states in the space charge region have no possibility of being filled by capture processes due to the lack of free charge carriers (see Sec. 3.4.3), emission processes can only be observed following the forced introduction of carriers which are to be captured. This is most conveniently done by pulsing of the junction bias as shown in Fig. 4.6. In order to explain the principle of operation it is assumed that only one kind of defect is present in an n-type semiconductor. On the left hand side of the figure the defect under investigation is assumed to be an electron trap in the upper half of the band gap. Initially the junction is under reverse bias (V_R) and the states are not occupied by electrons (1). A bias pulse towards a smaller voltage (V_P) or even zero bias will momentarily reduce the space charge region, making majority carriers – in this case electrons – available for capture in the region that was formerly the space

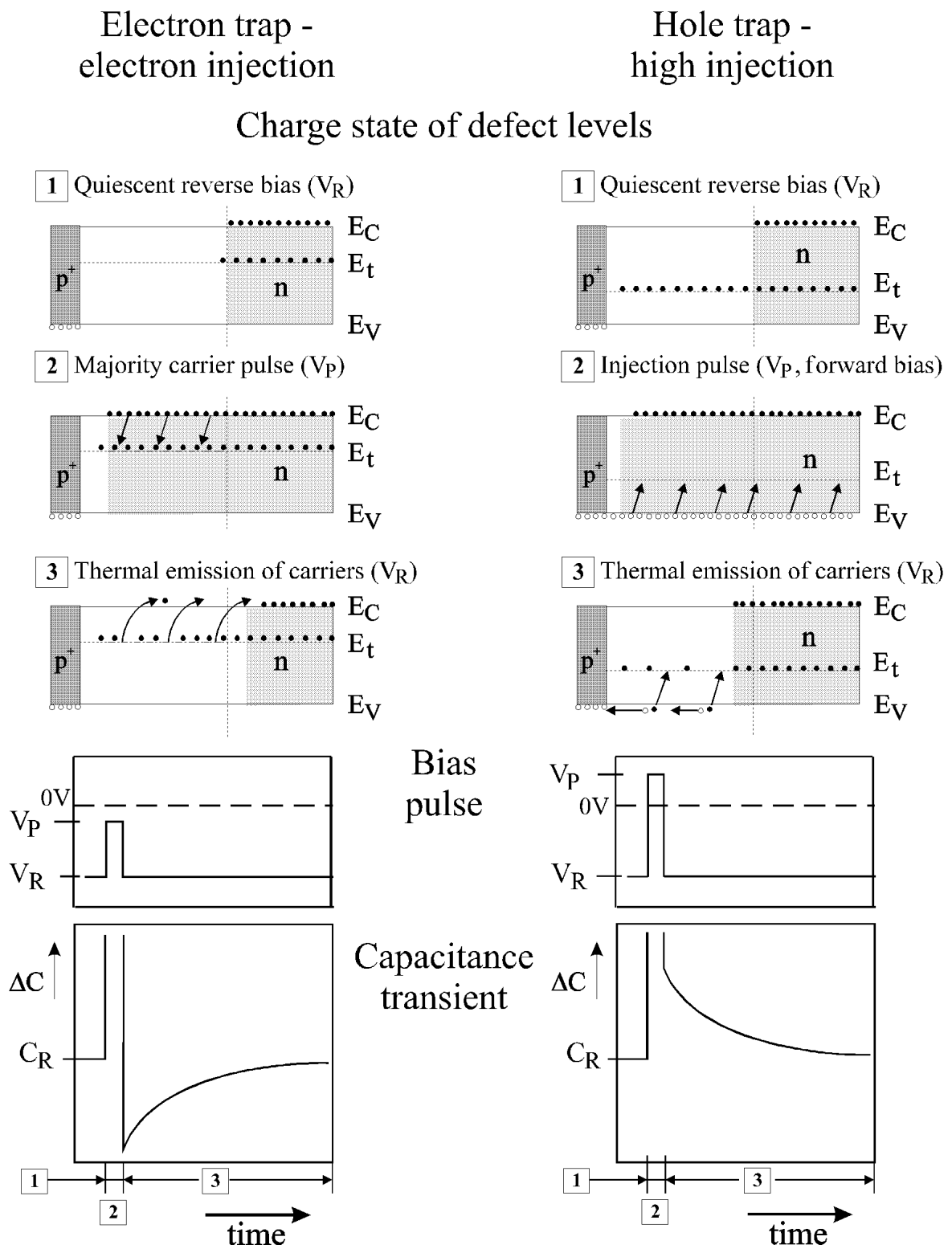

Figure 4.6: Principle of C-DLTS operation by a reduced reverse bias pulse for majority carrier injection (left) and by a forward bias pulse for high injection ($n \approx p$) (right). The charge state of defects, the bias pulsing and the time dependence of the capacitance during the measurement are schematically shown.

charge region. Since the defect states are now below the Fermi level they will be filled with electrons (2). When the pulse is turned off and V_R is reestablished, the junction capacitance is reduced because compensating negative charge has been trapped in the space charge region. This charge is subsequently emitted into the conduction band if sufficient thermal excitation energy is present and swept away from the space charge region by the applied junction potential (3). The process of carrier emission can be followed as a junction capacitance transient, as shown in the lower part of Fig. 4.6. Since the level of compensation is becoming smaller during the emission of electrons the space charge region width is decreasing and therefore the capacitance is increasing. The characteristic time constant of this transient is given by the reciprocal emission rate e_n of the defect level.
As shown on the right hand side of Fig. 4.6, a pulse into forward bias can be used to introduce both, minority and majority carriers, into the semiconductor bulk. This makes possible minority-carrier capture, but one should take into account that the steady-state occupation of the levels corresponds to a balance between majority- and minority-carrier capture. Under conditions of high injection ($n \approx p$) the occupation of traps with holes is given by the ratio of electron to hole capture coefficients ($p_t = (1 + \frac{c_n}{c_p})^{-1}$, see Sec. 3.4.4). Therefore the assumed hole trap in the figure must have the feature of $c_p \gg c_n$ to be filled with holes during the injection pulse. In order to detect also hole traps with electron capture coefficients higher than their hole capture coefficient ($c_n > c_p$) other filling methods, like e.g. optical filling with a short-wave-length laser from the back electrode, have to be used that solely inject holes into the space charge region during the filling pulse. After the injection pulse the defect states are filled with holes and the effective space charge is higher than before the pulse. Therefore the width of the space charge region is smaller than before the pulse and consequently the capacitance is higher. With emission of the trapped holes the capacitance becomes smaller and relaxes into its initial value C_R.
Therefore C-DLTS offers, in contrast to current based transient methods like I-DLTS, the possibility to discriminate between electron and hole traps by the sign of the observed capacitance transient $\Delta C(t)$. As later on will be shown the signals arising from electron and hole traps in n-type semiconductors correspond to positive and negative peaks[6] in the C-DLTS spectra, respectively.

4.4.2 Determination of defect parameters

4.4.2.1 Defect concentration

In order to estimate a relation between the defect concentration and the measured capacitance transient it is necessary to discuss the band-diagram of an asymmetric junction in the presence of a defect in more detail. For the discussion it is considered that the semiconductor is of n-type with a shallow donor concentration N_D and contains a deep acceptor in the upper half of the bandgap (negatively charged when occupied

[6]In this work the peaks corresponding to majority carrier traps have been defined as positive although the amplitudes of the transients have a negative sign (compare left-hand side of Fig. 4.6).

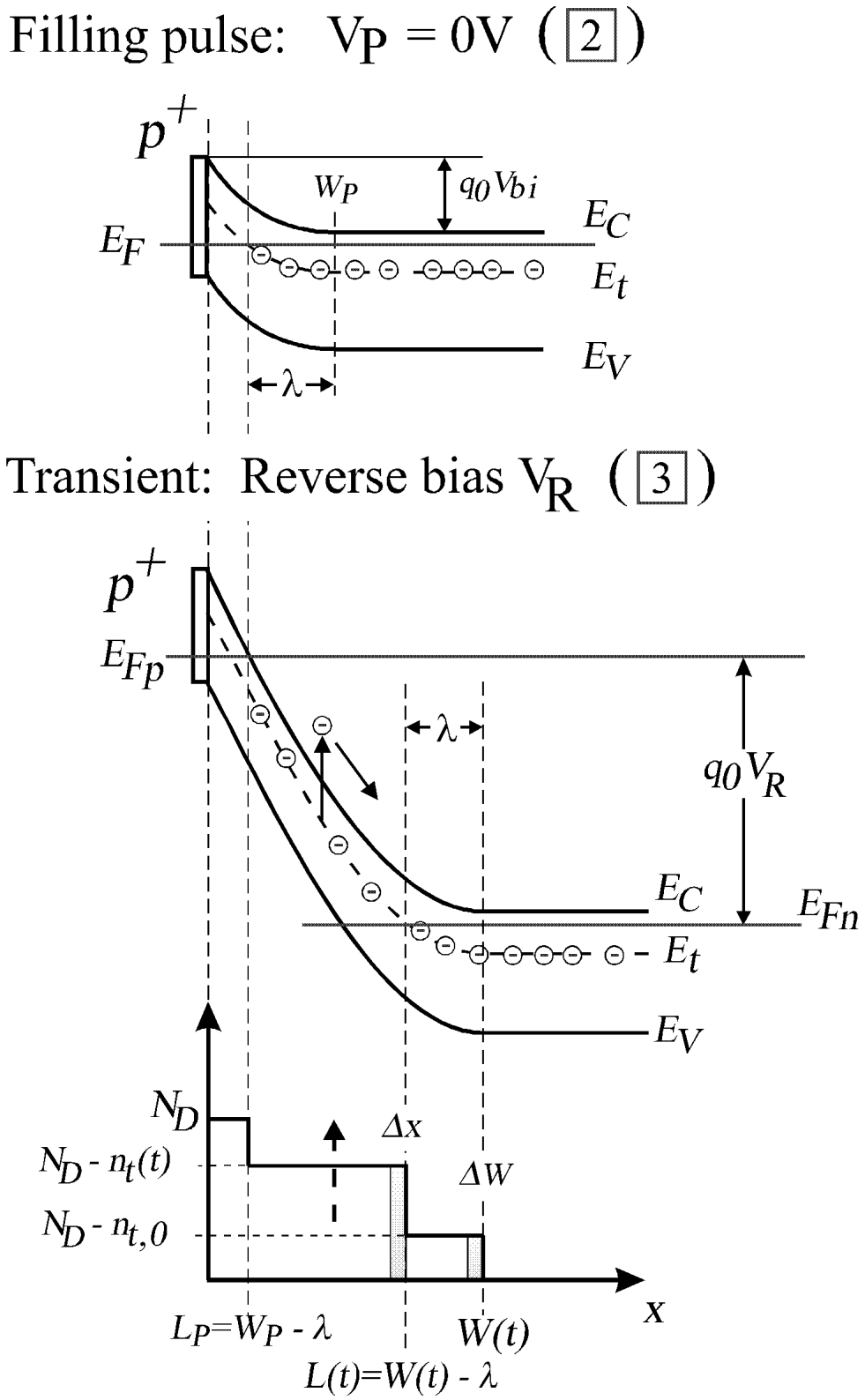

Figure 4.7: Band bending diagrams for a p^+n step junction during (2) and shortly after (3) a majority carrier filling pulse. The diagram at the bottom displays the space charge distribution corresponding to the lower band bending diagram (see text).

with an electron) of concentration N_t. In Fig. 4.7 the band-bending diagrams for a filling pulse with zero bias and the subsequent emission process of electrons with applied reverse bias V_R are shown (The situations correspond to 2 and 3 in the left hand side of Fig. 4.6, respectively.) As shown in Fig. 4.7 there are two different parts of the space charge region. At the outer edge of the region there is a transition between the neutral bulk and the central part of the space charge region which is essentially depleted of free carriers. For a particular defect with an energy level at E_t this gives rise to the so-called *edge* or *transition region* of thickness λ, defined by the point where the trap level crosses the quasi-Fermi level E_{Fn}. The quasi-Fermi level is assumed to be constant throughout the transition region (see Fig. 4.7) and set to the Fermi level E_F in the neutral bulk. From Poisson's equation it can readily be shown that

$$\lambda = \sqrt{\frac{2\epsilon\epsilon_0 \left(E_F - E_t\right)}{q_0^2 \, N_D}}. \tag{4.7}$$

However, this holds only under the assumption of $N_t \ll N_D$, or if the defect level is a donor. If the acceptor concentration reaches the order of the doping concentration, N_D in the denominator has to be replaced for an acceptor level by $N_D - N_t$ due to the compensation of space charge in the transition region (see Fig. 4.7). Note that λ is independent of bias voltage.
The filling pulse leads to an occupation with electrons of all defects in the region $x > L_P = W_P - \lambda$. During the subsequent emission process the electrons are emitted in the region $L_P < x < L(t)$ where $L(t)$ is defined as $L(t) = W(t) - \lambda$. The corresponding change in the capacitance signal $\Delta C(t) = C(t) - C_R$ can be calculated from the Poisson equation (for details see Appendix A.3 on page 217). These calculations show that the amplitude of the capacitance transient $\Delta C_0 = C(t = 0) - C_R$ is proportional to the defect concentration N_t:

$$N_t = -2N_D \, \frac{\Delta C_0}{C_R} \, \frac{W_R^2}{L_R^2 - L_P^2}. \tag{4.8}$$

For the experimental application it is more convenient to express the given length values with their corresponding capacitance values

$$N_t = -2N_D \, \frac{\Delta C_0}{C_R} \left[1 - \left(\frac{C_R}{C_P} \right)^2 - \frac{2\lambda C_R}{\epsilon\epsilon_0 A} \left(1 - \frac{C_R}{C_P} \right) \right]^{-1}. \tag{4.9}$$

Therefore with the knowledge of $(E_F - E_t)$ and the measurement of C_R, C_P, ΔC_0 and N_D the exact trap concentration can be determined. However, the transition region is often neglected (see e.g. [Mil77]) and the equation results in the well known simple form

$$N_t \approx 2N_D \, \frac{|\Delta C_0|}{C_R}. \tag{4.10}$$

In this approximation the knowledge of the level position in the band gap and the capacitance during the filling pulse C_P has not to be determined.

4.4.2.2 Activation energy $\Delta H'$ and cross section $\sigma_{n,p}$

In the case of $N_t \ll N_D$ the capacitance transient follows the emission of carriers

$$\Delta C(t) \propto n_t(t) = N_t \exp(-e_n t). \tag{4.11}$$

Thus the characteristic time constant of the transient τ_e is the reciprocal emission coefficient ($\tau_e^{-1} = e_n$). With the help of Eq. 3.24 the measured temperature dependence of τ_e can be used to establish an Arrhenius plot

$$\ln(\tau_e c_{n,p} N_{C,V} X_{n,p}) = \frac{\Delta H}{k_B T}. \tag{4.12}$$

However, the entropy factor $X_{n,p}$ and the temperature dependence of the capture coefficient $c_{n,p}(T)$ are often not known. In such cases $X_{n,p}$ is set to 1 and the capture coefficient to $c_{n,p} = \sigma_{n,p} v_{th,n,p}$ with a temperature independent cross section $\sigma_{n,p}$. The Arrhenius plot is then given by (compare Eq. 3.27 and e.g. right hand side of Fig. 4.11)

$$\ln(\tau_e v_{th,n,p} N_{C,V}) = -\ln(\sigma_{n,p}) + \frac{\Delta H'}{k_B T}. \tag{4.13}$$

The cross section $\sigma_{n,p}$ can be deduced from the intercept with the ordinate and the activation energy $\Delta H'_{n,p}$ from the slope. Note that the parameters on the left hand side in Eq. 4.13 have a T^2-dependence resulting from the temperature dependence of the density of states ($\propto T^{3/2}$) and the thermal velocity ($\propto T^{1/2}$).
However, in order to determine the exact enthalpy $\Delta H_{n,p}$ and the entropy factor $X_{n,p}$ the capture coefficient $c_{n,p}$ has to be determined as function of temperature.

4.4.2.3 Enthalpy ΔH and entropy factor $X_{n,p}$

A majority carrier capture measurement is done by varying the filling pulse duration t_p and monitoring the amplitude $\Delta C(t_p)$ of the emission transient at a constant temperature. If the capture dominates over the emission and the trap concentration is small compared to the doping concentration the following proportionality is obtained for an electron trap in n-type material

$$\Delta C_0(t_p) \propto n_t(t_p) = N_t \times (1 - \exp(-c_n n t_p)). \tag{4.14}$$

With knowledge of the free carrier concentration the majority carrier capture coefficient can be determined from the time constant τ_c of the capture transient ($c_n n = 1/\tau_c$). Comparing the capture coefficient measured in this way with the one obtained from the Arrhenius plot (Eq. 4.13; $c_n = v_{th,n}\sigma_n$) yields the entropy factor X_n.
The measurement of the capture coefficient at different temperatures can be used to produce a parameterization $c_n(T)$. The knowledge of $c_n(T)$ allows then to establish an Arrhenius plot with the temperature dependent capture coefficients (Eq. 4.12). In such a case on the left hand side of the Arrhenius equation not only the T^2 dependence resulting from the thermal velocity and the density of states but also the temperature dependence of the capture cross section has to be taken into account. Instead of the activation energy $\Delta H'$ the enthalpy ΔH is obtained.

4.4.3 Transient analysis

As shown in the last section the characteristic time constants and amplitudes of the capacitance transients are used for the evaluation of the defect parameters. In this section it will be shown how these parameters have been obtained from the measured transients and how the DLTS-spectra are generated. In the following an exponential behavior

$$C(t) = \Delta C_0 \times \exp\left(-\frac{t+t_0}{\tau_e}\right) + C_R \tag{4.15}$$

for the capacitance transient is assumed with a definition of the time axis as displayed in Fig. 4.8. Since the capacitance bridge needs some time to give the correct capacitance after end of the filling pulse (pulse overload recovery) a delay period t_0 has to be included before the transient is recorded.

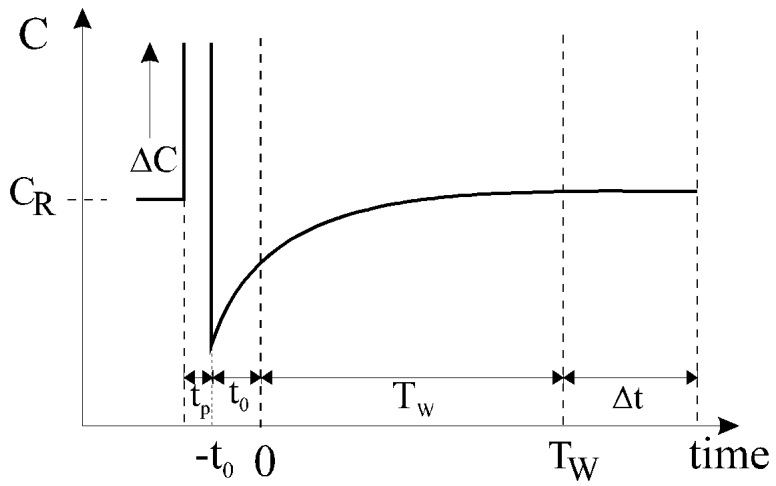

Figure 4.8: Time axis used for analysis of capacitance transients. A delay period t_0 has to be included due to the pulse overload recovery of the capacitance bridge.

4.4.3.1 Double boxcar method

The initial DLTS system presented by Lang in 1974 [Lan74] used a dual gate boxcar averager to define a time window $t_W = \{t_1 < t < t_2\}$, as illustrated in Fig. 4.9. The double boxcar method consists of taking the difference between $C(t_1)$ and $C(t_2)$ at two precise moments after the filling pulse. The difference $\Delta C_{1,2} = C(t_1) - C(t_2)$ plotted versus the temperature results in a DLTS spectrum. The DLTS signal will be zero at low temperatures where the emission process is too slow to be measured and also zero at high temperatures where the emission process is too fast to be observed within the chosen time window t_W. However, the DLTS signal will reach a maximum at a temperature T_{max} where the corresponding emission time constant $\tau_e(T_{max})$ fits to the chosen time window t_w depending on the installation of t_1 and t_2. The emission time constant $\tau_e(T_{max})$, corresponding to the peak maximum temperature in the DLTS

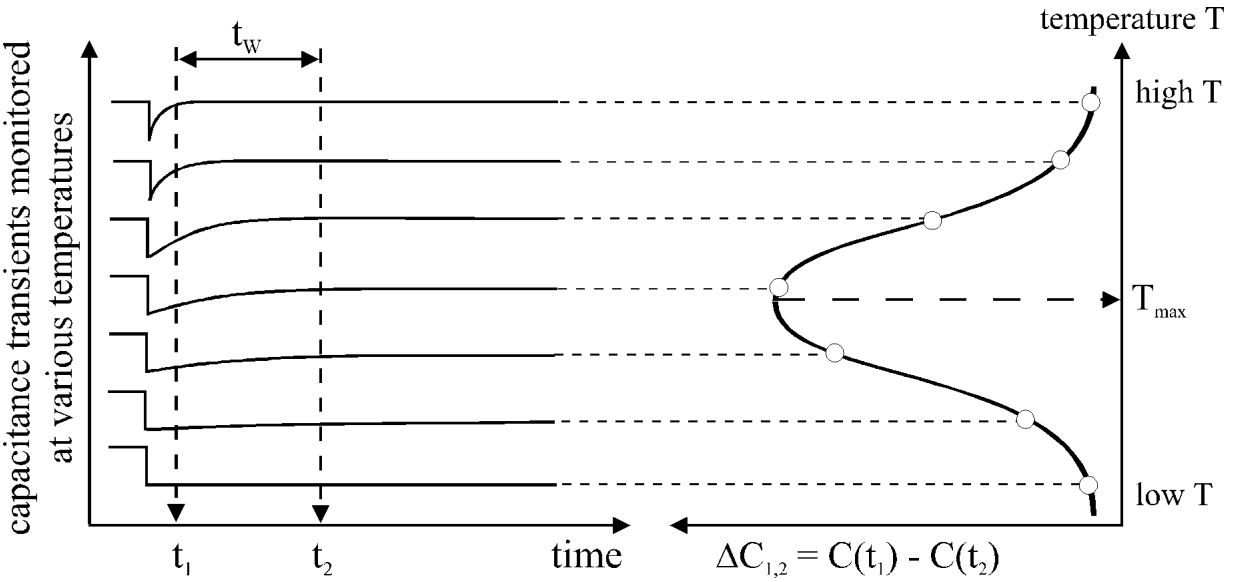

Figure 4.9: The left-hand side shows capacitance transients at various temperatures, while the right-hand side shows the corresponding DLTS signal resulting from using the double boxcar to display the difference between the capacitance at time t_1 and the capacitance at time t_2 as a function of temperature (after [Lan74]).

spectrum, is for a boxcar analysis given by

$$\tau_e(T_{max}) = \frac{t_1 - t_2}{\ln\left(\frac{t_1}{t_2}\right)}. \tag{4.16}$$

Performing several temperature scans with different time windows T_W, respectively applying several time windows on each transient, results in a set of data $(T_{max,i}, \tau_e(T_{max,i}))$ that can be used to construct an Arrhenius-plot.
An important drawback of the use of a double boxcar integrator for analysing the incoming transient signal is the fact that the outcoming signal is fully influenced by the accidental behavior of the signal at the sampling points and will not depend on the signal outside these time points. To improve the signal/noise ratio other weighting operations for signal processing have been applied: lock-in, correlator functions, [Mil77], Fourier-transformation [Oku83, Ike83] and Laplace-transformation [Dob94].
In this work the transients, recorded with a transient recorder, have been analyzed with a computer program by S.Weiss [DLT] that offers the use of several correlator functions or a so-called discrete Fourier analysis (DLTFS[7]). Both possibilities will be described shortly in the following. For details see [Wei88] and [Wei91].

4.4.3.2 Correlator functions

In contrast to the double boxcar method the complete transient is used for further analysis by folding the measured transient with a correlator function, e.g. a sine. The

[7]DLTFS = Deep Level Transient Fourier Spectroscopy

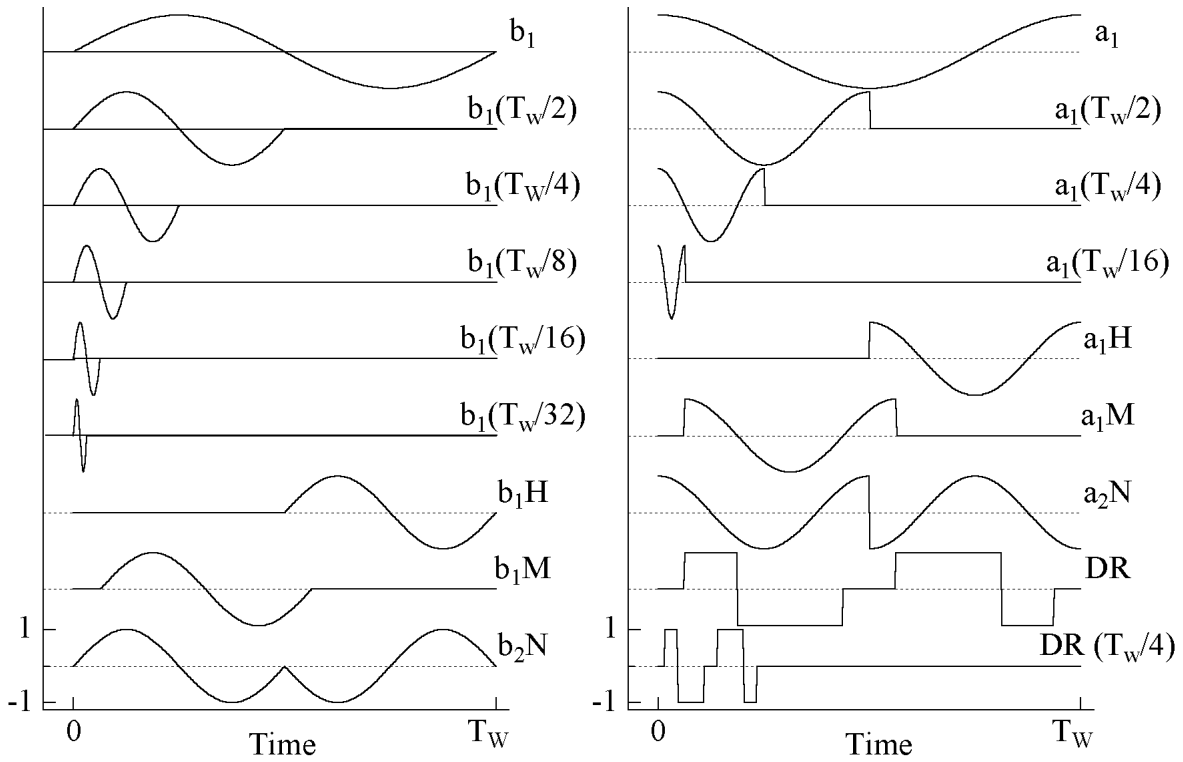

Figure 4.10: The 18 correlator functions used for the *maximum evaluation*.

result is a correlator

$$b_1 = \frac{2\,\Delta C_0}{T_W} \int_0^{T_W} \exp\left(-\frac{t+t_0}{\tau_e}\right) \sin\left(\frac{2\pi}{T_W} t\right) dt \tag{4.17}$$

with T_W being the time window. As $\Delta C_{1,2}$ in the double boxcar method (compare Fig. 4.9) also the correlator b_1 depends on the temperature and a peak will occur if b_1 is plotted versus temperature (DLTS spectrum). However, in this case the relation between the peak maximum temperature T_{max} and the corresponding emission time constant $\tau_e(T_{max})$ can only be calculated numerically [Wei91]. For the b_1 correlator it is given by[8]

$$\tau_e(T_{max}) = 0.43 \times T_W. \tag{4.18}$$

In total 18 different correlator functions, as displayed in Fig. 4.10, were used. Thus for each time window T_W 18 pairs $(T_{max,i}, \tau_e(T_{max,i}))$ are obtained and can be used to produce an Arrhenius plot. Fig. 4.11 shows an example for such an analysis. The DLTS signals corresponding to 9 different correlators and an Arrhenius plot are displayed for the transition $VV^{(-/0)}$ of the divacancy as measured on a ^{60}Co-gamma irradiated sample (see Sec. 6.6). This method will be called *maxima evaluation* hereafter. Usually three different time windows T_W of 20, 200 and 2000 ms have been used in this work during one temperature scan.

[8]Since the transient is a continuous signal and the folding is a numerical procedure, the value depends on the time binning. The given value of 0.43 corresponds to a transient of 512 bins.

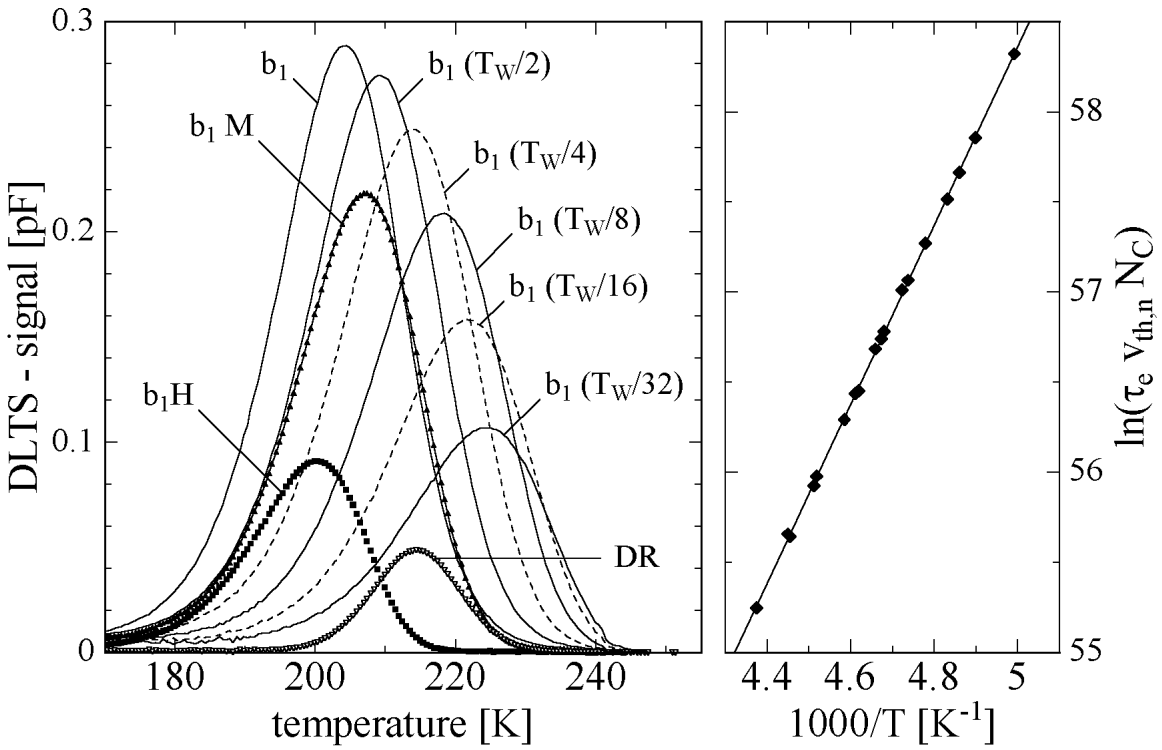

Figure 4.11: DLTS spectra obtained with various different correlators (see Fig. 4.10). For better visibility not all of the 18 used correlators are shown. However, the Arrhenius plot on the right-hand contains the data obtained with all 18 correlators. (transition: $VV^{(-/0)}$, sample M21009, $V_R = -10\,\mathrm{V}$, $V_P = 0\,\mathrm{V}$, $T_W = 200\,\mathrm{ms}$, $t_0 = 6\,\mathrm{ms}$, ^{60}Co-γ-irradiated: 107 kGy)

4.4.3.3 Fourier transformation

A periodical signal $f(t)$ with a frequency $\omega = \frac{2\pi}{T_W}$ can be written as an infinite sum of harmonic functions (Fourier series)

$$f(t) = \frac{a_0}{2} + \sum_{n=1}^{\infty} a_n \cos(n\omega t) + \sum_{n=1}^{\infty} b_n \sin(n\omega t) \tag{4.19}$$

with the so-called Fourier coefficients ($n \geq 1$)

$$a_n = \frac{2}{T_W} \int_0^{T_W} f(t) \cdot \cos(n\omega t)\, dt \tag{4.20}$$

$$b_n = \frac{2}{T_W} \int_0^{T_W} f(t) \cdot \sin(n\omega t)\, dt. \tag{4.21}$$

Since the recording of the transient does not start directly after the pulse one has to include either a phase shift in the harmonic functions of the Fourier transformation or move the time zero to the beginning of the recording. Here the latter possibility has been chosen (see Fig. 4.8). The Fourier coefficients for the capacitance transient

(Eq. 4.15) are

$$a_0 = \frac{2\,\Delta C_0}{T_W}\,\exp\left(-t_0/\tau_e\right)\left[1-\exp\left(-T_W/\tau_e\right)\right]\tau_e + 2C_R, \tag{4.22}$$

$$a_n = \frac{2\,\Delta C_0}{T_W}\,\exp\left(-t_0/\tau_e\right)\left[1-\exp\left(-T_W/\tau_e\right)\right]\frac{1/\tau_e}{1/\tau_e^2+n^2\omega^2}, \tag{4.23}$$

$$b_n = \frac{2\,\Delta C_0}{T_W}\,\exp\left(-t_0/\tau_e\right)\left[1-\exp\left(-T_W/\tau_e\right)\right]\frac{n\omega}{1/\tau_e^2+n^2\omega^2}. \tag{4.24}$$

From the Fourier coefficients the time constant τ_e can be calculated in three different ways:

$$\tau_e\left(a_n,a_k\right) = \frac{1}{\omega}\sqrt{\frac{a_n-a_k}{k^2a_k-n^2a_n}}, \tag{4.25}$$

$$\tau_e\left(b_n,b_k\right) = \frac{1}{\omega}\sqrt{\frac{kb_n-nb_k}{k^2nb_k-n^2kb_n}}, \tag{4.26}$$

$$\tau_e\left(a_n,b_n\right) = \frac{1}{n\omega}\frac{b_n}{a_n}. \tag{4.27}$$

It is of advantage that Eqs. 4.25–4.27 use only ratios of coefficients and neither amplitude (ΔC_0) nor the offset (C_R). Hence the temperature dependence of the amplitude does not present a source of error. The amplitude of the transient can be calculated from each coefficient in Eqs. 4.23 and 4.24, e.g.:

$$\Delta C_0 = b_n\,\frac{T_W}{2}\,\frac{\exp\left(t_0/\tau_e\right)}{1-\exp\left(-T_W/\tau_e\right)}\,\frac{1/\tau_e^2+n^2\omega^2}{n\omega}. \tag{4.28}$$

Thus in contrast to the correlator method the emission time constant and the amplitude can be calculated from each transient. Therefore each transient gives a point in the Arrhenius plot. This is displayed in Fig. 4.12 where the same experimental data are analysed as displayed in Fig. 4.11 for the maxima evaluation method. Furthermore this method, that will be called *direct evaluation* method hereafter, offers the possibility to check whether the transient is exponential or not. For an exponential transient the following relations hold for the coefficients:

$$\begin{aligned} &(a) \quad a_2 < a_1 < 4a_2, \\ &(b) \quad b_2/2 < b_1 < 2b_2, \\ &(c) \quad \frac{b_1\,a_2}{a_1\,b_2} = \frac{1}{2} \end{aligned} \tag{4.29}$$

Thus it is possible to reject transients that show no exponential behavior for some reasons.

The third and most sophisticated method of analysis that was used is the so-called *variable time window* method. Here the time window is changed with temperature in such a way that the ratio between the emission time constant τ_e and the time window

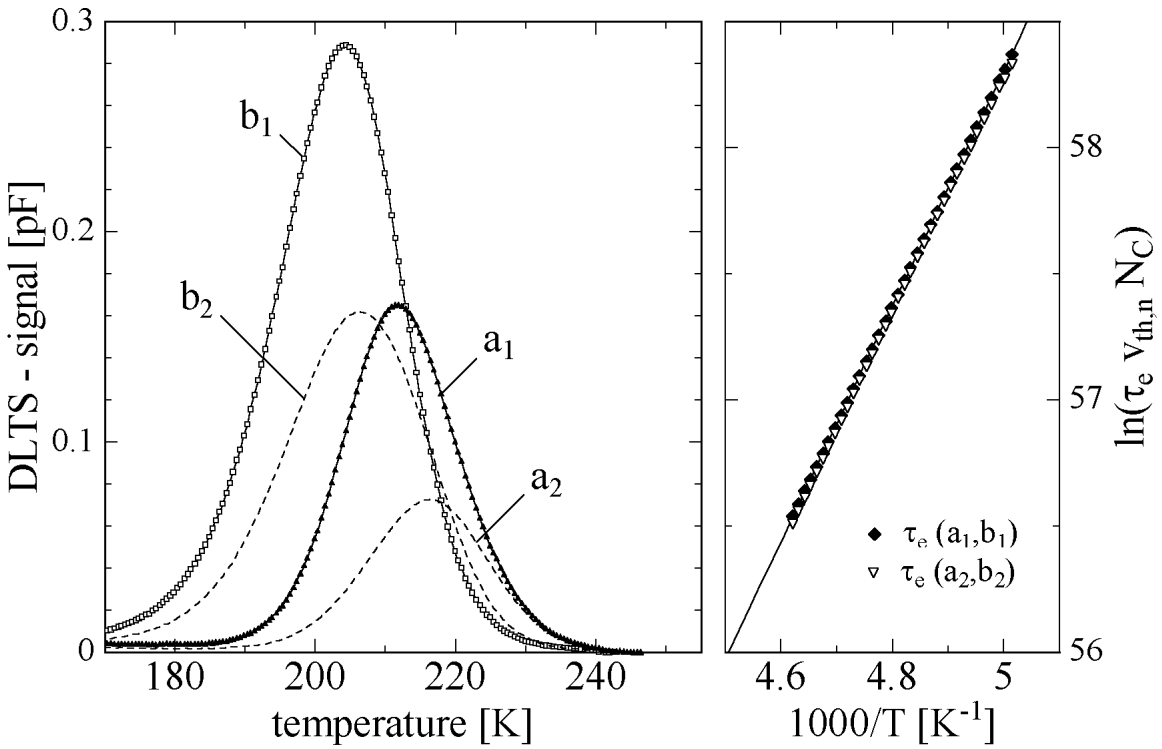

Figure 4.12: DLTS spectra obtained with the sine and cosine correlators a_1, b_1, a_2 and b_2. (same measurement as shown in Fig. 4.11)

T_W is kept at a constant value that results in an optimum signal for evaluation of the transient parameters ($\tau_e/T_W \approx 0.2$; for details see [Wei91]). The measurement starts at deep temperatures with a large initial time window (e.g. 20 s) or at high temperatures with a small initial time window (e.g. 5 ms). The DLTS signal is measured and analyzed and then the temperature is increased resp. decreased for the next measurement. As soon as a signal with a sufficient signal to noise ratio is detected the emission time constant is calculated from the sine and cosine correlators (see above). After the determination of a a view time constants as function of temperature the program automatically produces an Arrhenius plot that allows the calculation of the optimal time window for the next temperature. An example of such a measurement is shown in Fig. 4.13. The advantages of this method are the online data analysis and the large temperature range for the Arrhenius plot resulting in very accurate defect parameters. However, by using multiple time windows for the maxima and direct evaluation the temperature range for those methods can also be extended. The disadvantage of the variable time window method becomes obvious when the transients display a non exponential behavior. In such a case the transients are rejected (see above) and no data are obtained. Both other methods at least produce a spectrum that can be used for further analysis.

Finally the defect parameters obtained with the three different methods for the shown

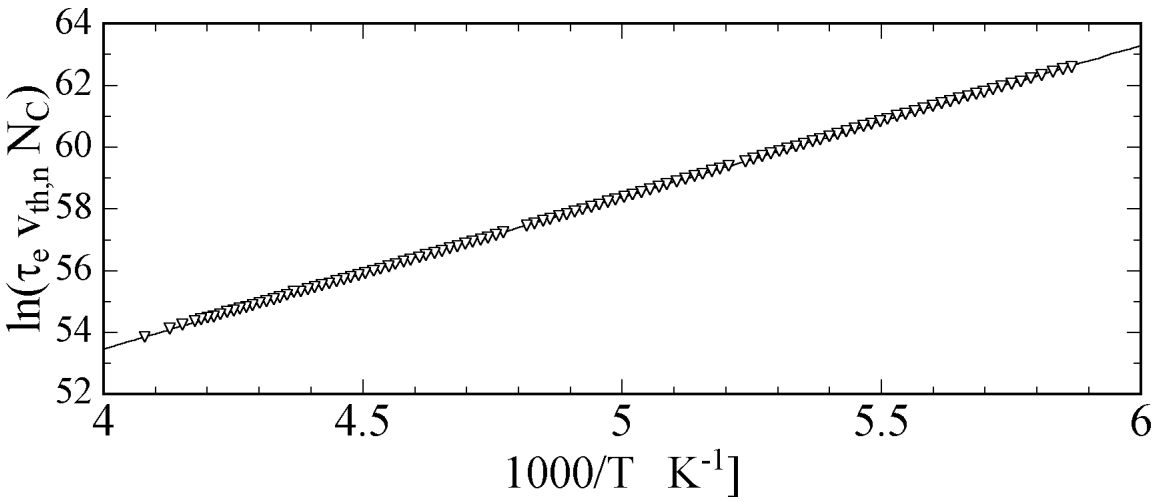

Figure 4.13: Arrhenius plot obtained with the variable time window method. Note the large temperature range from 170 to 245 K corresponding to emission time constants reaching from 20 s to 2 ms. (same sample and defect as shown in Figs. 4.11 and 4.12)

example, the transition $V_2^{(-/0)}$ for a ^{60}Co-gamma irradiated sample, shall be compared:

0.427 eV	and	$\sigma_n = 2.6 \times 10^{-15}\,\mathrm{cm}^2$	for	maxima evaluation with 3 T_W
0.420 eV	and	$\sigma_n = 1.7 \times 10^{-15}\,\mathrm{cm}^2$	for	direct evaluation with 3 T_W
0.424 eV	and	$\sigma_n = 2.2 \times 10^{-15}\,\mathrm{cm}^2$	for	variable time window method.

The parameters for the maxima and direct evaluation were obtained with 3 time windows $T_W = 40, 200$ and 2000 ms.
The direct evaluation, that was not used in this work, displays the strongest deviation from the variable time window method. This is due to the fact that with this evaluation method also transients are analysed for the evaluation of the emission time constant that are not optimal with respect to the time window ($\tau_e \gg T_W$ or $\tau_e \ll T_W$) and lead to a higher error in the obtained emission time constant.
However, compared to the most accurate method, the variable time window method, the maxima evaluation method displays only a very small difference. This becomes obvious when the emission time constants are recalculated with the obtained defect parameters:

temperature	180 K	200 K	230 K
τ_e – maxima evaluation	3.05 s	157 ms	4.70 ms
τ_e – direct evaluation	2.97 s	160 ms	5.05 ms
τ_e – variable T_W	2.97 s	156 ms	4.77 ms

The maximum deviation between the maxima and the variable time window methods is about 3%. One should keep in mind that in the investigated temperature range

(180K–230 K) a deviation of 0.2 K already results in larger deviations between the measured emission time constants. A more quantitative discussion about the influence of inaccurate temperature measurements on the obtained defect parameters can be found in [Deh95, Sch96a].

In conclusion the agreement within the two evaluation methods used in this work, *variable time window* and *maxima method*, is very good. However the errors in the defect parameters presented in Chapter 6 display not the errors obtained from a single Arrhenius plot but the statistical error obtained by averaging the Arrhenius plots measured on different samples. Although the accuracy for a particular defect parameter ($\Delta H'$ or σ) is smaller, it makes sense to display the activation energy with 3 digits and the capture cross section with 1 digit behind the point. This has to be done in order to accurately reproduce the emission time constant, that is a function of both parameters, over a wide temperature range.

4.5 Thermally Stimulated Current (TSC)

In 1968 Weisberg and Schade [Wei68] applied the TSC technique, that before had only been used on insulators or semiinsulators, also on low resistivity semiconductors by making use of the depletion region created by a p-n junction or a Schottky barrier. Since that time the theoretical description and the experimental techniques to determine the deep level properties with the TSC technique in diodes have been much improved [For71, Bue72, Bal92, Li 95b, Fei97d]. In contrast to the DLTS technique that is limited for high resistivity silicon to rather small defect concentrations by the requirement of $N_t \ll N_{\text{doping}}$ (see Sec. 4.4) the TSC technique can be applied independent of the effective doping concentration. Thus TSC is a powerful tool to investigate defects in irradiated silicon detectors even after very high fluences [Hei76, Big94, Fei97a].
In this section the principle of TSC operation will be described, the basic equations for analysis of the spectra will be given and finally various experimental methods for evaluation of the defect level properties will be presented.

4.5.1 Principle of operation

A schematic representation and an example of a TSC measurement are given in Figs. 4.14 and 4.15, respectively. The measurement process can be divided in three different steps.

a) **Cooling:** The sample is cooled to a low temperature at which the traps will be filled with electrons or holes. If the sample is cooled down under reverse bias the steady state generation current can be monitored and the traps will not be filled with carriers during the cooling. However, cooling under zero bias leads to filling with majority carriers (electrons in n-type and holes in p-type silicon). As long as the majority carrier concentration is higher than the majority carrier trap concentration all majority carrier traps will be filled. Otherwise only the majority carrier traps nearest to midgap are filled.

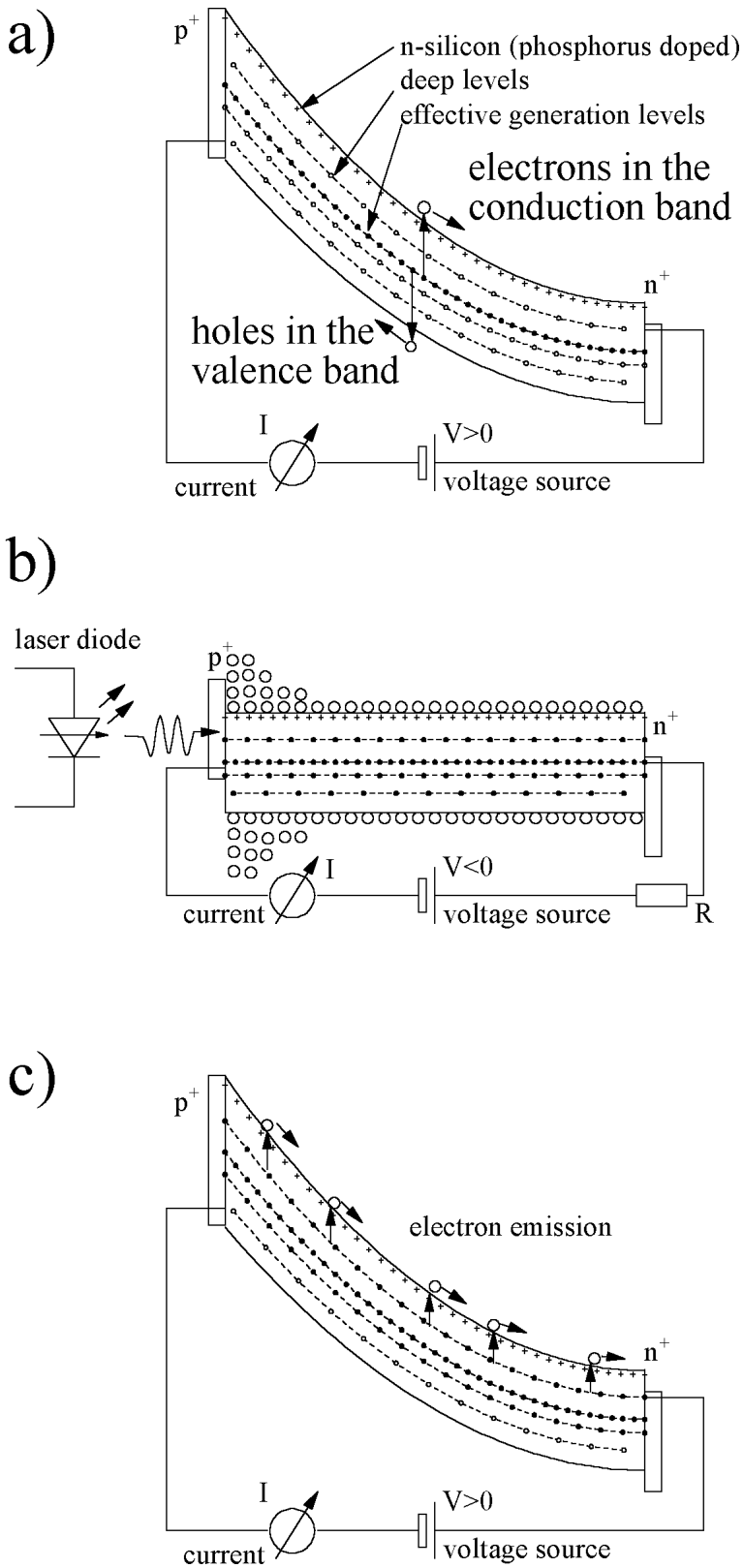

Figure 4.14: Schematic representation of the TSC measurement [Fei97a].

a) Cooling
Cooling down under reverse bias. The current measured is due to the steady state generation at the close to midgap levels.

b) Injection
Injection of free carriers at a low temperature. The diode is forward biased and the injection current is limited by the series resistor R. Injection is also possible by optical generation of free carriers.

c) Recording
Recording of the TSC spectrum. The sample is reverse biased and heated at a constant rate. At a specific temperature the trapped charges are emitted giving rise to a unique current peak signal.

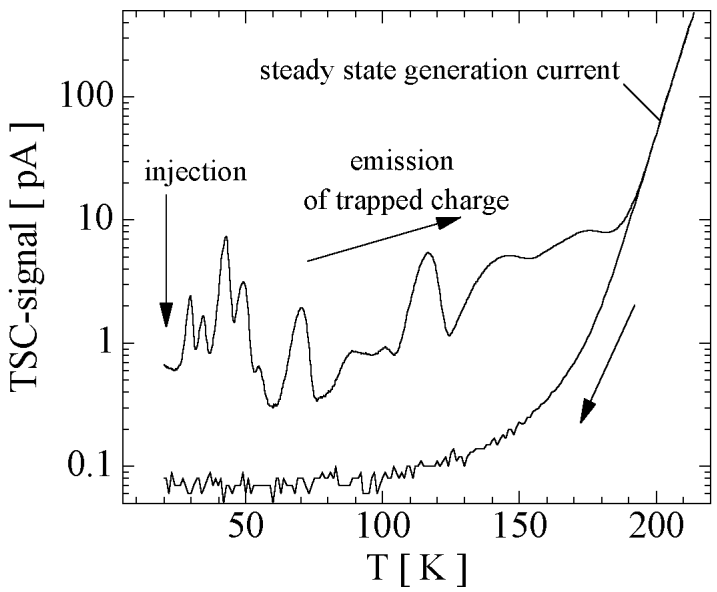

Figure 4.15: Typical TSC spectrum of a detector irradiated with $\Phi_{eq} = 1{\times}10^{13}\,\mathrm{cm}^{-2}$. (sample M20713; $\beta = 0.183\,\mathrm{K/s}$; 30 s injection at 20 K (1.7 mA); 100 V; after 100 min annealing at room temperature)

b) **Filling:** Besides the cooling under zero bias various further techniques can be used to fill the traps at low temperatures. Current injection (applying forward bias) or illumination with band gap light produce both, holes and electrons, in the bulk. In such a case the occupation of the traps is determined by their individual ratio between electron and hole capture coefficient (see Sec. 3.4.4). Switching to zero bias leads to filling with majority carriers (in contrast to cooling down under zero bias also shallow levels are filled if the free majority carrier concentration is smaller than the majority carrier trap concentration). Finally illumination with short wave length light of the n^+ junction side or the p^+ junction side of the sample can be used to fill only electron respectively hole traps. However, illumination of the non-junction side of the diode will only lead to a filling if the applied bias is sufficient to fully deplete the sample respectively if the diffusion length of the free charge carriers is sufficient to reach the depleted zone.

c) **Recording:** After the filling process the sample is heated under reverse bias and at a specific temperature the trapped charges are emitted giving rise to a unique current peak signal for each kind of defect level.

4.5.2 Determination of defect parameters

4.5.2.1 Defect concentration

The total current measured during a TSC scan is given by [For71]

$$I_{TSC}(t) = q_0 A \int_0^{W(t)} \sum_{\text{all defects}} \frac{e_n(t) n_t(t) + e_p(t) p_t(t)}{2} dx \qquad (4.30)$$

where W(t) denotes the depletion depth. Since the temperature is increased during the TSC scan with a heating rate $\beta(t) = dT/dt$ the emission rates e_n and e_p are also time dependent.
For further calculations only one electron trap is assumed that was filled with electrons during a filling process at temperature T_0. Furthermore it is assumed that the applied reverse bias is sufficient to keep the device depleted during the whole TSC scan ($W(t) = d$). In such a case the corresponding TSC current is given by

$$I_{TSC}(t) = \frac{q_0 A d}{2} e_n(t) n_t(t) \tag{4.31}$$

where $n_t(t)$ is given by

$$n_t(t) = n_{t,0} \exp\left(-\int_0^t e_n(t')dt'\right) \tag{4.32}$$

and $n_{t,0}$ denotes the absolute fraction of traps occupied with electrons during the filling process. Substituting t by $T = T_0 + \beta(t)t$ one gets

$$I_{TSC}(T) = \frac{q_0 A d}{2} e_n(T) N_t \exp\left(-\int_{T_0}^{T} \frac{1}{\beta(T')} e_n(T')dT'\right) \tag{4.33}$$

An integration over the observed TSC peak $Q_t = \int dt I_{TSC}(t)$ can therefore be used to determine the concentration $n_{t,0}$

$$n_{t,0} = 2\frac{Q_t}{q_0 A W} \tag{4.34}$$

which corresponds to the total defect concentration if the defect was completely filled with electrons during the filling process. Under the assumption of a constant heating rate β the concentration can also be calculated from the peak heights I_{max} [Sim71, Fei97a]

$$n_{t,0} = \frac{2}{q_0}\frac{I_{max}}{AW}\frac{k_B T_{max}^2}{\beta \Delta H_t'} \exp\left(\frac{\Delta H_t'}{\Delta H_t' + k_B T_{max}}\right). \tag{4.35}$$

The peak maximum temperature T_{max} can be calculated from the following formula [Bue72]

$$T_{max} = \frac{\Delta H_{n,p}'/k_B}{\ln\left(\frac{T_{max}^4}{\beta}\frac{B\,\sigma_{n,p}\,\left(m_{dC,V}^*/m_0\right)}{\left(\Delta H_{n,p}'/k_B\right) + 2T_{max}}\right)} \tag{4.36}$$

where B is a constant given by Eq. 3.28.

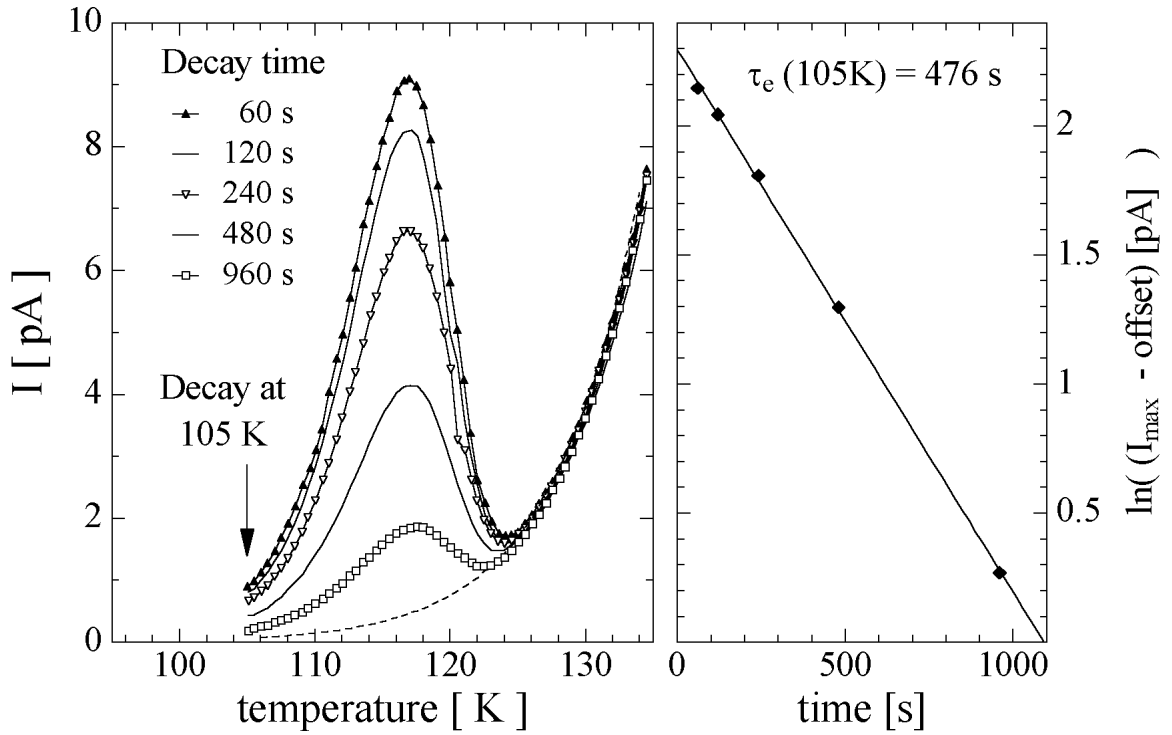

Figure 4.16: Delayed heating at 105 K. (sample M20713 of type WM2-3kΩcm; transition: $C_i^{(+/0)}$; $\Phi_{eq} = 1\times10^{13}\,\mathrm{cm}^{-2}$; $V = 100$V; after 850 min annealing at room temperature; filling: 1.7 mA for 30 s at 105 K)

4.5.2.2 Energy level parameters $\Delta H'$ and σ

There are various methods to obtain the defect level parameters from the measured TSC spectra. The one that has been used in this work for most of the parameter evaluations is the so-called *delayed heating method*. For completeness also two other methods will be described in this section.

Delayed heating method [Mul74]

This method has been introduced by Muller et al. in 1974 [Mul74]. The TSC-peak is measured several times from the same starting temperature T_0 with different delay times between the end of filling and the start of heating. With increasing delay time more and more charge carriers are already emitted at the temperature T_0 ($e_n \propto \exp(-\Delta H'/(k_B T_0))$) and therefore do not contribute to the TSC-signal any more. Thus the TSC-peak is decreasing with increasing delay time. An example is shown in Fig. 4.16. There the trap filling was performed at 105 K by forward biasing. Thereafter the sample was kept at reverse bias at 105 K for the indicated delay time in the figure. The subsequent heating is then performed with the same heating rate for all measurements. On the right hand side of the figure the natural logarithm of the peak amplitude is plotted against the delay time. Note that a small offset in the signal

due to the next TSC–peak at higher temperatures (indicated by the dashed line in the figure) had to be subtracted. The slope in the right-hand side figure gives the emission time constant at 105 K. Repeating such delay measurements at different temperatures can therefore be used to establish an Arrhenius plot in order to determine the activation energy $\Delta H'_{n,p}$ and the cross section $\sigma_{n,p}$ of the defect.

Method of variable heating rate [Bue72]

With increasing heating rate β the peak maximum temperature T_{max} shifts to higher temperatures. From Eq. 4.36 the following expression can be obtained

$$\ln\left(\frac{T_{max}^4}{\beta}\right) = \ln\left(\frac{\Delta H'_{n,p} + 2k_B T_{max}}{B\, k_B\, \sigma_{n,p}\, \left(m^*_{dC,V}/m_0\right)}\right) + \frac{\Delta H'_{n,p}}{k_B T_{max}}. \tag{4.37}$$

Since $2k_BT_{max} \ll \Delta H'_{n,p}$ (e.g. for $T_{max}=100K$: $2k_BT_{max}=17meV$) a plot of $\ln\left(T_{max}^4/\beta\right)$ versus $1/k_BT_{max}$ can be used to determine the activation energy of the defect from the slope and the cross section from the intercept.

Deconvolution method [Bru95, Hey96]

After high irradiation levels the TSC spectra become very complex (see e.g. Fig. 4.15). The signals from the different defects strongly overlap and the individual peaks are not clearly resolved inside the TSC spectrum. In such a situation it is very difficult to obtain the level parameters from the methods described before. However, a numerical least squares fit to the whole spectrum (deconvolution of the spectrum) can be used to obtain defect parameters. Let m be the total number of defects and $(\Delta H'_\ell, \sigma_\ell, n_{\ell,0})$ the activation energy, the cross section and the initial absolute concentration of occupied defects of type ℓ. Then the TSC-current is given by the superposition of all defect signals

$$I_{TSC}(T) = \frac{q_0 A d}{2} \sum_{\ell=1}^{m} e_\ell(T, \sigma_\ell, \Delta H'_\ell)\; n_{\ell,0}\; \exp\left(-\int_{T_0}^{T} \frac{1}{\beta}\; e_\ell(T', \sigma_\ell, \Delta H'_\ell)\; dT'\right). \tag{4.38}$$

One of the major problems is the number of levels. The minimum number can be obtained by counting the peaks visible in the spectrum. But the number of smaller peaks that are hidden in the spectrum can only be guessed. Therefore such numerical calculations have to be proved with spectra obtained under different conditions (e.g. different heating rates, start temperatures and filling conditions) and should not rely on a single spectrum only. Very often it turns out that the level parameters obtained from a single spectrum cannot be reproduced under slightly different experimental conditions [Hey96]. In the specific case of very high defect concentrations after irradiation also the change in the depletion depth has to be taken into account [Fei97d]. For the numerical model this leads to a further increase in the complexity of the fit especially when electron and hole traps have been filled.

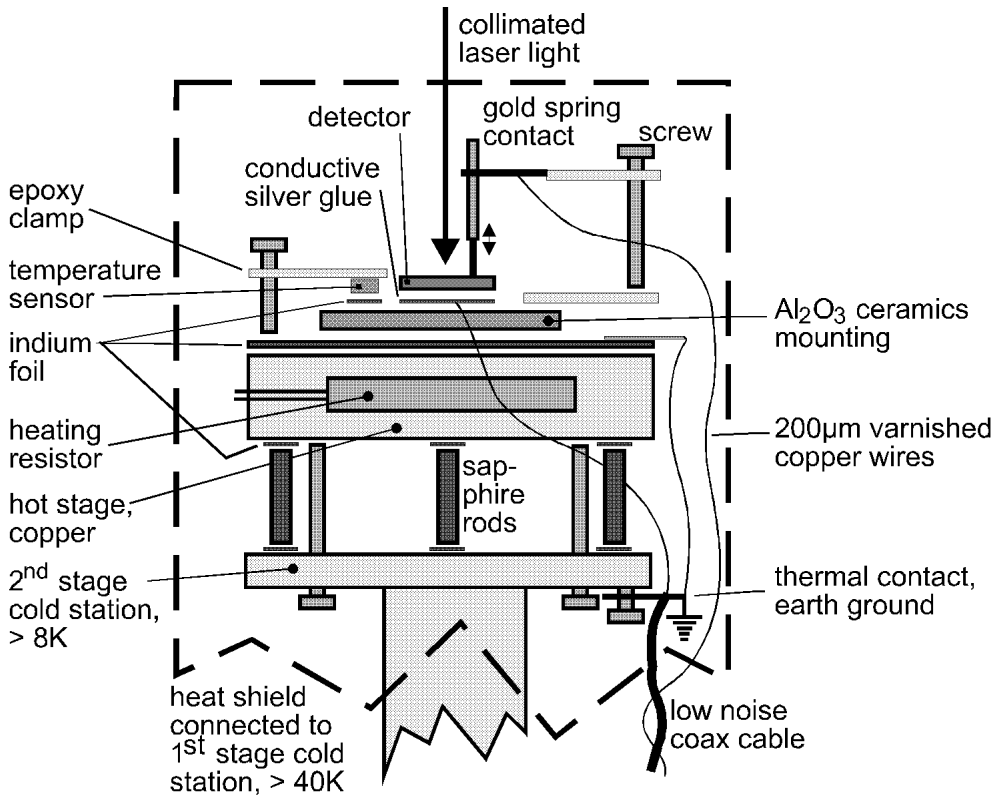

Figure 4.17: Schematic view of the second-stage cold station (taken from [Fei97a], modified).

4.6 DLTS and TSC setup

The cryostat

A closed cycle two-stage helium refrigerator from CTI-Cryogenics (Model 22C, operated at 50 Hz) was used for the DLTS and TSC measurements. A schematic view of the second-stage cold station is shown in in Fig. 4.17. It is located inside an evacuated cryostat chamber and protected by a cylindrical aluminum shield (indicated by the dashed lines in the figure) against thermal radiation. The heat shield itself is connected with the first-stage cold station ($T \geq 40$ K). On top of the second-stage cold station a so-called hot stage has been mounted on sapphire rods. It consists of a copper plate in which a heating resistor (30 W) is embedded allowing for heating rates of up to 1 K/s. The samples were glued with silver glue to aluminum ceramic supports (2×2.5 cm^2). These supports were clamped very tightly to the hot stage. An indium foil between the hot stage and the ceramics assured a good thermal contact. Also the silicon diode used for the temperature measurement was clamped, on top of an indium foil, to the ceramics (see figure). The temperature accuracy of the diode (Lake Shore DT-470-SD-12) was $\pm$ 0.5 K for $T < 100$ K and $\pm$ 1.0 K for $T < 300$ K. The minimum measured sample temperature on the ceramics was about 12 K. The temperature sensor and the heating resistor were connected to a temperature controller DRC 91 CA from Lake Shore. As

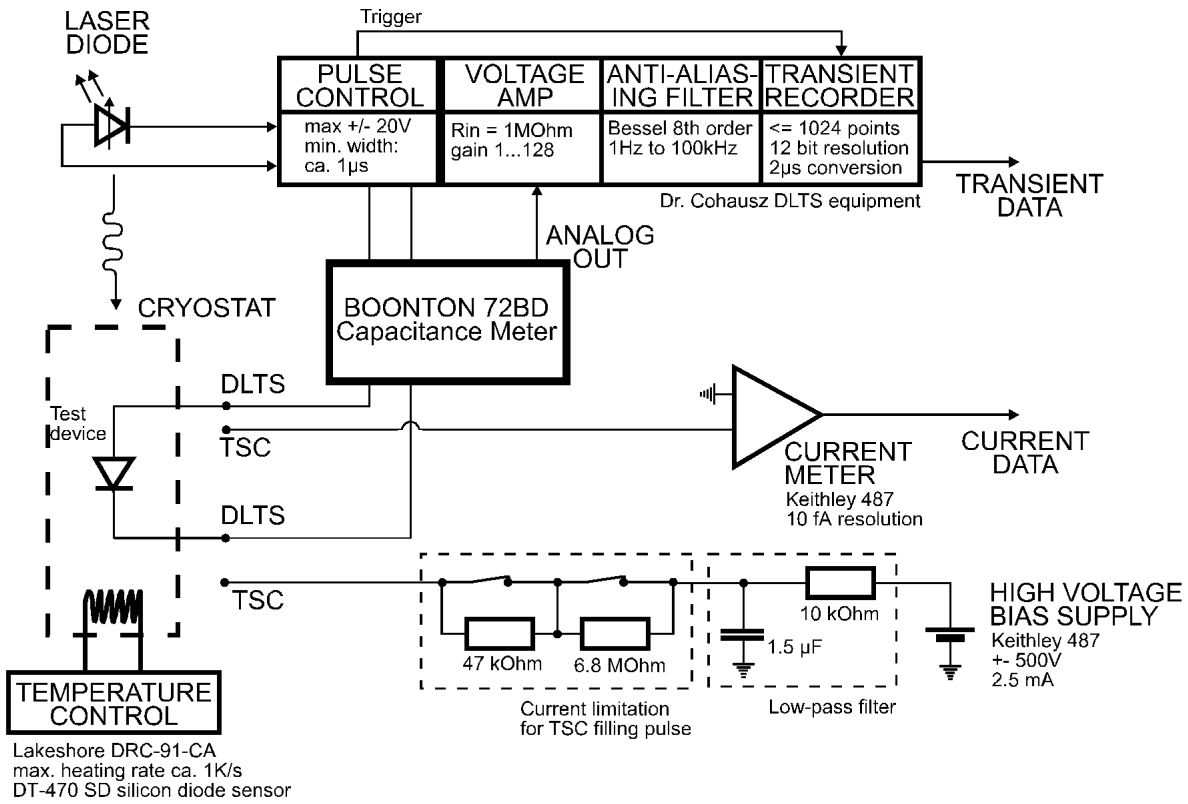

Figure 4.18: Schematic representation of the electrical setup for DLTS and TSC measurements.

indicated in the figure a laser, mounted outside the cryostat chamber, could be used to generate electron - hole pairs in the sample. A more detailed description of the setup within the cryostat chamber can be found in [Fei97a].

DLTS setup

In Fig. 4.18 a schematic drawing of the electrical setup of the DLTS and TSC measurements is shown. Besides the cryostat and temperature controller described above the DLTS-System consists of a capacitance meter, a digital data acquisition system and a software package to control and analyze the measurements. The latter two components were made by the Dr. Ludwig Cohausz Halbleitermesstechnik GmbH in Moosburg. The capacitance meter was a Boonton 72B working with a 15 mV (r.m.s) 1 MHz signal. Within the capacitance meter a set of switchable compensation capacitances was installed enabling the compensation of the steady state sample capacitance. Therefore it was possible to measure the DLTS signal in the lowest capacitance range of the meter, the 1 pF range with a nominal resolution of 5 fF and an accuracy of about 10 fF. However, with multiple averaging of the analog output signal a resolution of about 100 aF was reached. The maximum voltage supplied by the system was $\pm$ 20 V and the minimum pulse width 1 μs. The capacitance meter analog voltage output

signal was fed into a variable gain amplifier and then filtered by an anti-aliasing filter (eighth-order Bessel [Wei91]). Finally the signal was digitized (12 bit ADC) and stored by a transient-recorder at up to 1024 points. The time binning of the data points could be chosen between 20 μs and 3 s length. Repeatedly recording of the transients was used for averaging. The transient analysis (folding with correlator functions, compare Sec. 4.4) was done by the computer. A more detailed description of the hardware and software can be found in [Boc88, Wei91].

TSC setup

A schematic representation of the TSC setup is given in Fig. 4.18. Besides the cryostat and temperature controller it consists of an electrometer and a simple RC low pass filter (see figure). For the current measurement a Keithley 487 with 10 fA resolution was used. The injection of charge carriers was either achieved by laser illumination or by applying a forward bias of about 100 V to the sample. In the latter case a resistor was switched into the circuit (see Fig. 4.18) in order to limit (control) the injection current. The measurement and data recording was controlled by a computer. The typical heating rate was $\beta = 0.183$ K/s (220 K in 20 min).

Chapter 5

Change of Detector Properties

The essential radiation induced changes in macroscopic detector properties due to bulk damage are an increase in leakage current, a degradation in charge collection efficiency and a change in the effective doping concentration. The latter effect is corresponding to a change in the depletion voltage and has the most detrimental impact on the detector operability since the leakage current can efficiently be suppressed by cooling and the charge loss due to trapping is no major problem as long as the detector can be fully depleted.
In this chapter experimental findings on the leakage current and effective doping concentration are presented. The experimental data are parameterized in order to allow for better comparison with data in the literature and - of course - damage projections for HEP experiments. These parameterizations will be combined in Chapter 7 with the microscopic findings of Chapter 6 in order to relieve the discussion about the relation between microscopic defects and macroscopic damage. Additionally a very accurate fluence normalization method based on the experimental findings on leakage current and developed during this work is presented. This method is now widely used for the fluence monitoring of hadron fields in various irradiation facilities. Finally a short review is given about the radiation induced changes in charge collection efficiency.
The first paragraphs of the sections about leakage current and effective doping concentration give an introduction about the experimental findings and their parameterization. In the subsequent paragraphs the fluence dependence, the annealing behavior and the material dependence is discussed in more detail. Since most of the data in this work have been obtained after fast neutron irradiation and only a few after ^{60}Co–gamma and 24 GeV/c proton irradiations also experimental data published by other groups will be taken into account in order to describe the particle dependence of radiation damage in silicon. Here, special interest is taken in recent results of the ROSE–collaboration on the effective doping concentration of material with high carbon or oxygen concentration and irradiated with charged hadrons.

5.1 Leakage current

5.1.1 Introduction

In this section it will be demonstrated that the radiation induced increase of leakage current after irradiation with fast hadrons is proportional to fluence and independent of the used material (high or low resistivity, n- or p-type, high or low concentration of the impurities carbon and oxygen). Furthermore a universal annealing behavior for all materials is observed.

However, before starting to discuss the details two experimental conditions have to be mentioned that must be fulfilled in order to obtain reliable leakage current data, namely the *temperature correction* to a certain reference temperature and the use of a guard ring. Most of the differences between published data and the ones presented in this work result from not taking into account these two conditions.
The first one is due to the strong temperature dependence of the leakage current (compare Sec. 2.3.4). Assuming the generation centers are located close to the middle of the band gap Eq. 2.16 on page 26 can be used to scale the leakage current to a certain reference temperature. In this work all leakage current data measured at *room temperature* have been normalized to 20°C.
The second condition for reliable data is the use of a guard ring. Measurements without a connected guard ring lead to drastically wrong generation current density values due to the indeterminate active volume of the device, especially after type inversion[1] when the field zone starts from the rear side of the detector (for details see Sec. 4.3). All presented data corresponding to the leakage current were obtained with connected guard ring unless – of course – the used device had no guard ring (see Tab. 2.2).

5.1.2 Fluence dependence

The radiation induced increase of the leakage current ΔI is given by the difference between the currents measured after and before irradiation. The reverse current of a typical test structure ($0.25\,\mathrm{cm}^2$, $300\,\mu\mathrm{m}$) measured before irradiation is usually below one nA and already after irradiations with fluences of about $1 \times 10^{12}\,\mathrm{cm}^{-2}$ some hundred nA are additionally generated by the radiation damage. Thus the current before irradiation is normally negligible compared to ΔI, but was nevertheless always taken into account. In Fig. 5.1 the fluence dependence of the increase in leakage current normalized to volume $\Delta I/V$ is shown. Each point corresponds to an individual detector irradiated with fast neutrons in a single exposure to the given fluence. Directly after irradiation the samples were put into liquid nitrogen in order to suppress any further annealing. Subsequently the samples were taken out of the nitrogen one after another and annealed[2] for 80 min at 60°C. The I/V characteristic was measured at room temperature and the extracted leakage current saturation value corrected to 20°C (compare

[1] *Type inversion* is explained in Sec. 5.3.1

[2] The annealing state reached after 80 min at 60°C corresponds to the minimum in the change of effective doping concentration (ΔN_{eff}) after irradiation (compare Fig. 5.9).

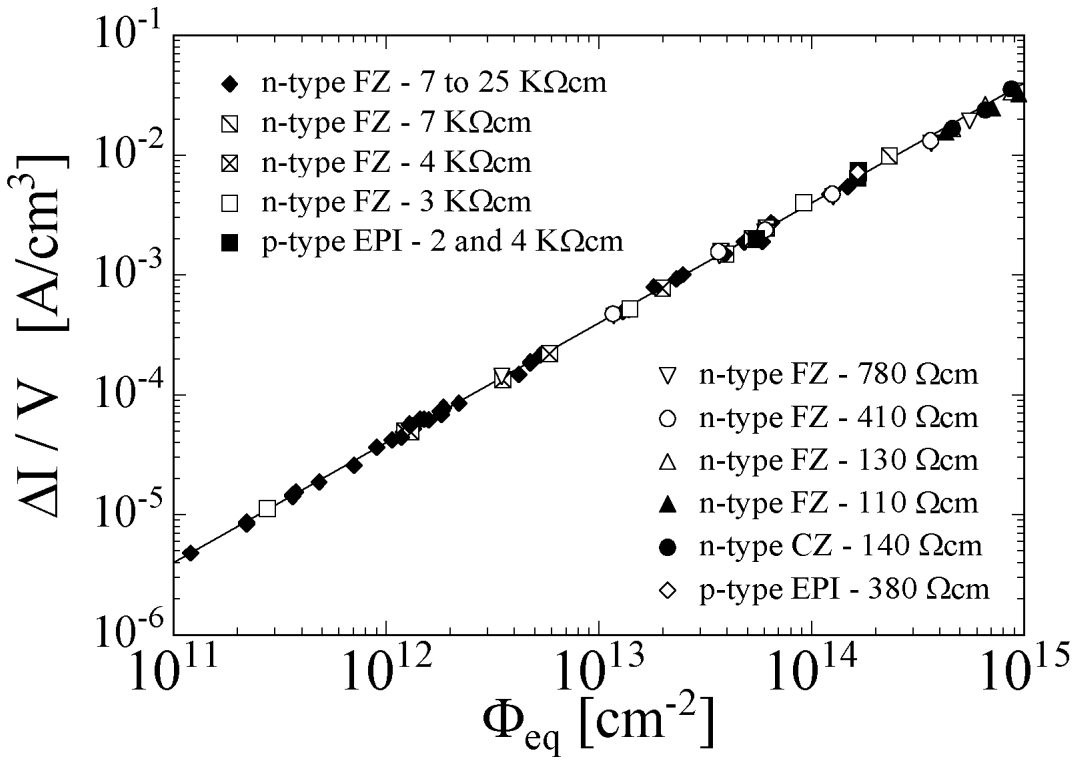

Figure 5.1: Fluence dependence of leakage current for silicon detectors produced by various process technologies from different silicon materials. The current was measured after a heat treatment for 80 min at 60°C $\{\alpha(80\,\text{min}, 60°\text{C}) = (3.99 \pm 0.03) \times 10^{-17}\text{A/cm}$; for details see Fig. 5.6$\}$.

Sec. 4.3). The measured increase in current was observed to be proportional to fluence and can thus be described by

$$\Delta I = \alpha\, \Phi_{eq}\, V \tag{5.1}$$

where the proportionality factor α is called *current related damage rate*. A fluence range from 1×10^{11} cm^{-2} to 1×10^{15} cm^{-2} is covered by the displayed data and therefore some of the samples are type inverted and some are not depending on the initial effective doping concentration. However, in contrast to previous investigations which did not use guard rings [Wun92, Sch96a] no difference in the current related damage rate between type inverted and not type inverted diodes is observed.

5.1.3 Annealing

The annealing behavior of the current related damage rate α after irradiation is displayed in Fig. 5.2 for various temperatures. The α value, respectively the leakage

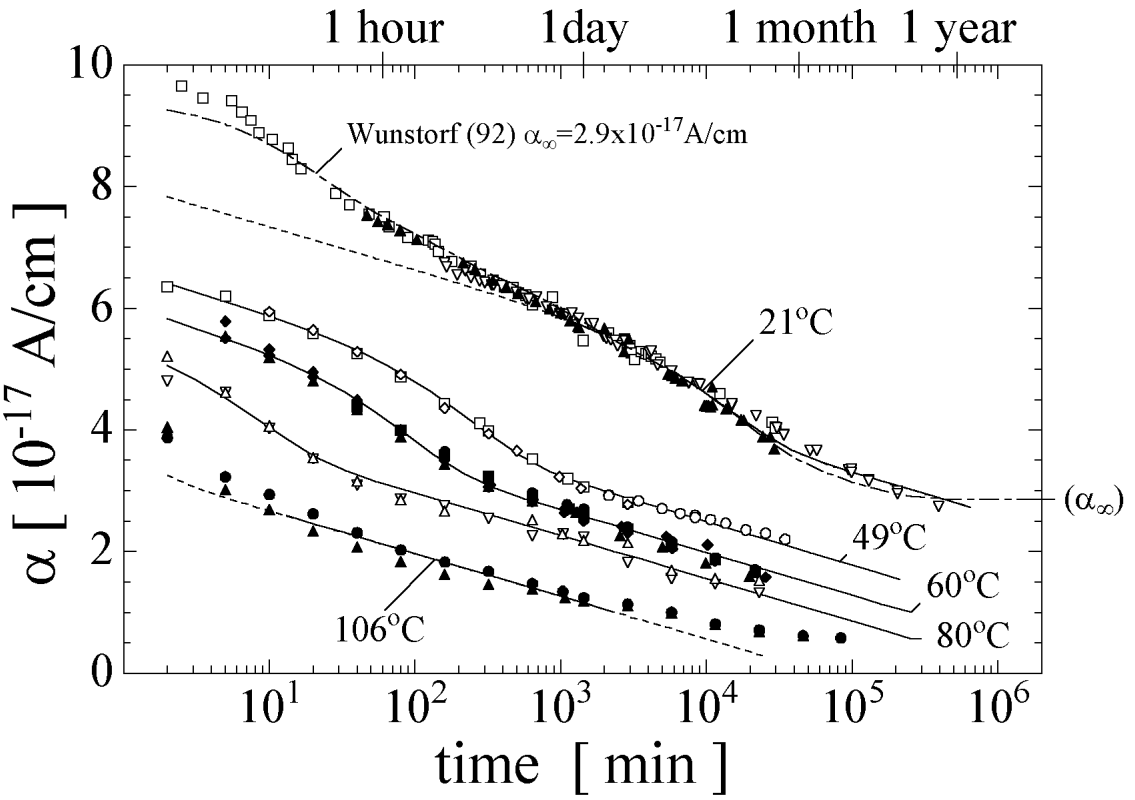

Figure 5.2: Current related damage rate α as function of cumulated annealing time at different temperatures. For each temperature at least one type inverted and one not type inverted sample has been used. The dashed–dotted line represents a simulation according to Eq. 5.3 with parameters as given in Tab. 5.1 and α_∞ as displayed in the figure. The solid lines are fits according to Eq. 5.4. (Samples of type WE-7kΩcm and WE-25kΩcm; see Tab. 4.1)

current, is continuously decreasing and only for the highest temperature, after a 2 months lasting annealing at 106°C, a saturation is indicated at a value of about 6×10^{-18} A/cm. The annealing curves are usually fitted to a sum of exponentials [Wun92, Gil92]

$$\Delta I(t) = \Delta I(t=0) \times \sum_i b_i \exp\left(-\frac{t}{\tau_i}\right) \tag{5.2}$$

with the sum over all relative amplitudes b_i being one ($\sum_i b_i = 1$). The parameter $\Delta I(t=0)$ describes the leakage current at the end of the irradiation, but is not easily determined since the current has to be corrected for selfannealing during the irradiation process [Wun92]. This parameterization can be interpreted in such a way that different defects contribute to the leakage current and anneal out with individual time constants τ_i in a first order process (compare Sec. 3.5). Most often it was reported that after several months at room temperature a saturation value α_∞ is reached and no further

term	$i=1$	$i=2$	$i=3$	$i=4$	$i=5$	$i=\infty$
τ_i [min]	1.78×10^1	1.19×10^2	1.09×10^3	1.48×10^4	8.92×10^4	∞
b_i	0.156	0.116	0.131	0.201	0.093	0.303

Table 5.1: Parameters of leakage current annealing at room temperature as determined in [Wun92] for not type inverted detectors.

annealing takes place [Wun92, Sch96a, Chi95, Fei97a]. Thus the overall annealing of the current related damage rate α has been described by

$$\alpha(t,T_a) = \frac{\Delta I(t,T_a)}{\Phi_{eq}\, V} = \alpha_\infty \sum_i \frac{b_i}{b_\infty} \exp\left(-\frac{t}{\tau_i(T_a)}\right) \tag{5.3}$$

where the relative amplitude b_i with the highest index is named b_∞ and corresponds to the stable fraction of the leakage current ($\Delta I(t=\infty)\,/\,\Delta I(t=0)$). The indicated temperature T_a is the annealing temperature and not the temperature at which the current has been measured (compare comment in Sec. 5.1.1). In Fig. 5.2 a simulation for the annealing at 21°C according to Eq. 5.3 with $\alpha_\infty = 2.9 \times 10^{-17}$ A/cm as given in [Chi95] is shown. The corresponding b_i have been taken from [Wun92] and are displayed in Tab. 5.1. The overall agreement with the annealing data measured in this work is good. However, it has to be mentioned that in [Wun92] two sets of coefficients b_i for type inverted and not type inverted detectors have been published. Here the set for not type inverted detectors has been used. Although for each temperature at least one type inverted and one not type inverted detector has been used for the experiment displayed in Fig. 5.2, no difference is seen in the annealing functions. Thus it is suggested here to use the set of data given in [Wun92] for not type inverted detectors (Tab. 5.1) in order to describe the leakage current short term annealing at room temperature for both, inverted and not inverted, detectors. The difference between the data for inverted and not inverted detectors in the older experiments is obviously caused by the lack of a guard ring.

However, the parameterization described above does not represent the long term annealing data at room temperature for t >1 year. This is most obviously seen in the figure from the annealing at higher temperatures where no saturation value α_∞ can be seen. Instead, in the long term annealing the α-value seems to follow a logarithmic function in time. Thus the long term annealing at room temperature and the annealing at higher temperatures was chosen to be described by one exponential and a logarithmic term:

$$\alpha(t) = \alpha_I \cdot exp\left(-\frac{t}{\tau_I}\right) + \alpha_0 - \beta \cdot ln\,(t/t_0)\,. \tag{5.4}$$

For each temperature the data were fitted according to Eq. 5.4 with t_0 set to 1 min. The corresponding parameters are displayed in Tab. 5.2. For the exponential term the

T_a [°C]	α_I 10^{-17} A/cm	τ_I [min]	α_0 10^{-17} A/cm	β 10^{-18} A/cm	t_0 [min]
21	1.23	1.4×10^4	7.07	3.29	1
49	1.28	260	5.36	3.11	1
60	1.26	94	4.87	3.16	1
80	1.13	9	4.23	2.83	1
106	–	–	3.38	2.97	1

Table 5.2: Fit parameters of current annealing at different annealing temperatures T_a according to Eq. 5.4. For the fit the parameter t_0 was set to 1 min. The corresponding fit functions are displayed in Fig. 5.2 as solid lines.

weighted average value for the amplitude α_I was found to be

$$\alpha_I = (1.23 \pm 0.06) \times 10^{-17}\,\mathrm{A/cm}$$

and the Arrhenius plot of the time constant τ_I displayed in Fig. 5.3 revealed

$$\frac{1}{\tau_I} = k_{0I} \times \exp\left(-\frac{E_I}{k_B T_a}\right) \qquad \text{with} \qquad \begin{array}{l} k_{0I} = 1.2^{+5.3}_{-1.0} \times 10^{13}\,\mathrm{s}^{-1} \\ E_I = (1.11 \pm 0.05)\ \mathrm{eV}. \end{array}$$

Thus, with a first order kinetics and a frequency factor k_{0I} close to the most abundant phonon frequency, it is very likely that a dissociation of a defect is responsible for the exponential part of the leakage current annealing (compare Sec. 3.5).
The interpretation of the logarithmic part of Eq. 5.4 is far more complicated and it is noted here that the presented parameterization does not claim to be based on a physical model. The average value of the parameter β is given by

$$\beta = (3.07 \pm 0.18) \times 10^{-18}\,\mathrm{A/cm},$$

whereas the parameter α_0 clearly displays a temperature dependence. In Fig. 5.4 α_0 is plotted versus the reciprocal annealing temperature and can be described by[3]

$$\alpha_0 = -(8.9 \pm 1.3) \times 10^{-17}\mathrm{A/cm} + (4.6 \pm 0.4) \times 10^{-14}\mathrm{AK/cm} \times \frac{1}{T_a}\,. \qquad (5.5)$$

It has to be noted that the given parameterization only holds for the time and temperature range indicated in Fig. 5.2. It is neither valid for annealing times shorter than 1 min nor for annealing times and temperatures resulting in values of α above 6×10^{-17}A/cm or below 1×10^{-17}A/cm. For values above 6×10^{-17}A/cm further short term annealing components have to be taken into account while for values below 1×10^{-17}A/cm the annealing comes close to saturation (compare Fig. 5.2).
As mentioned above, there is no clear physical interpretation of the logarithmic annealing behavior. However, a similar time dependence is observed for the annealing of

[3]The $1/T_a$ dependence was chosen since it displayed a smaller χ^2 compared to a linear dependence and for another reason that will be explained at the end of this section.

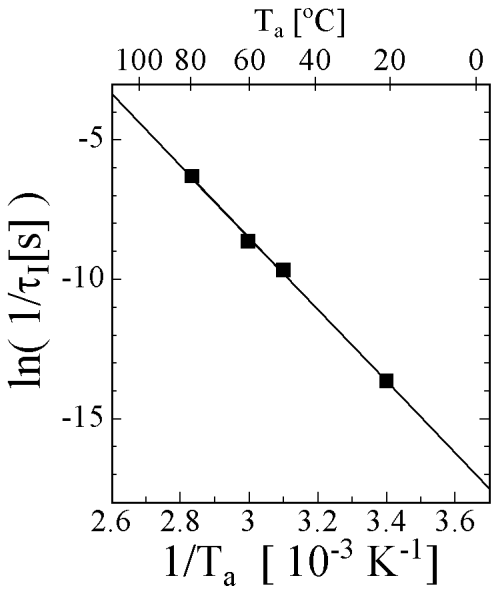

Figure 5.3: Arrhenius plot for the time constant τ_I. The line corresponds to a fit with $ln\,(1/\,(\tau_I[\mathrm{s}])) = (30.1 \pm 1.7) - (12.9 \pm 0.5) \times 10^3\, 1/T_a[\mathrm{K}]$.

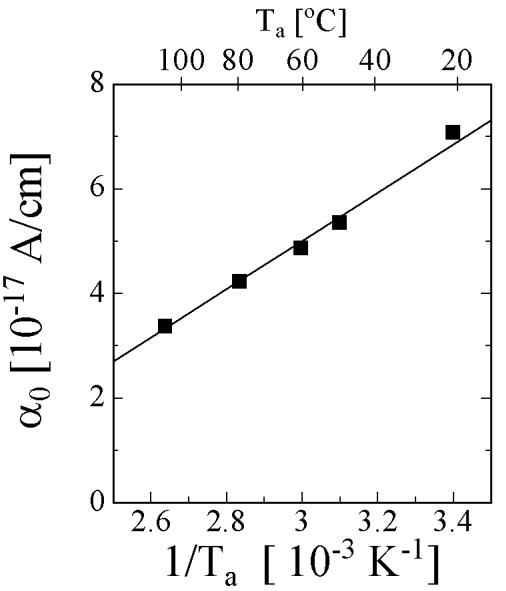

Figure 5.4: Parameter α_0 plotted versus the inverse annealing temperature T_a. The line corresponds to a fit with $\alpha_0 = -\,(8.9 \pm 1.3) \times 10^{-17}\mathrm{A/cm} + (4.6 \pm 0.4) \times 10^{-14}\mathrm{AK/cm} \times 1/T_a$.

trapped oxide charge induced in thermally grown SiO_2 passivation layers by ionizing irradiation [McW90a]. Here the logarithmic annealing behavior is attributed to a distribution of activation energies for the emission (annealing) of trapped oxide charges. It can be shown that a uniform occupation of oxide states which are also uniformly distributed in emission (annealing) activation energy leads to a logarithmic time dependence of the overall trapped oxide charge [McW90b].
Since the leakage current is independent of material type (e.g. FZ or Cz, n- or p-type) and impurity concentration, it is most likely due to radiation induced clusters (see next section). Thus, in comparison with the oxide charge annealing, one could think of a more or less uniform distribution of annealing activation energies for the clusters. This is not unlikely since the clusters have, according to simulations, a certain distribution in size and also their physical structure differs from cluster to cluster. However, one should keep in mind that the leakage current may not scale linearly with the concentration of defects that are responsible for the current generation. In such a case also the observed annealing function of the leakage current will not scale linearly with the annealing of the defects. In other words the *real* annealing function of the defects may be *hidden* by the up to now not understood current generation mechanism. An example for such a non linear relation is the *intercenter-charge-transfer model* [Wat96, Gil97]. In this model the leakage current is explained by the interaction of defects located close together in a cluster. Therefore the current depends on the size of the cluster and the local density of defects inside it. Consequently a non linear relation between

the concentration of the defects in the clusters and the current generated by them can be expected.
Thus it may be allowed to assume for a moment a first order process and introduce the temperature dependence in Eq. 5.4 by a scaling factor for the time axis[4]

$$\Theta(T_a) = \exp\left(-\frac{E_I^*}{k_B}\left(\frac{1}{T_a} - \frac{1}{T_{ref}}\right)\right)$$

instead of a temperature dependent α_0. This scales the time axis relative to a certain reference temperature T_{ref} and changes the logarithmic part of the annealing function to $\alpha_0^* - \beta \cdot ln\left(\Theta(T_a)\, t/t_0\right)$ with a temperature independent α_0^*. It is straight forward to show that such a formulation is equivalent to the parameterization according to Eq. 5.4. The activation energy E_I^* is given by $E_I^* = k_B b_0^*/\beta$ with b_0^* being the slope of the fit in Fig. 5.4. The resulting value is $(1.30 \pm 0.14)\,\mathrm{eV}$ which is close to the activation energy obtained for the reverse annealing of the radiation induced change of effective doping concentration (see Sec. 5.3.3).
However, in the end it has to be noted again that the annealing mechanism may be parameterized in the one or other formulation but it's physical background still remains far from being understood.

5.1.4 Material dependence

For numerous detectors fabricated from different materials the isothermal annealing of the leakage current at $T_a = 60°\mathrm{C}$ has been measured. The extracted α values as function of cumulated annealing time are plotted in Fig. 5.5 for devices irradiated in a fluence range between $2.5 \times 10^{11}\,\mathrm{cm}^{-2}$ and $1.7 \times 10^{14}\,\mathrm{cm}^{-2}$. Neither a dependence on the fluence (as expected from the results of the last sections) nor any material dependence is seen. In order to compare the different materials and the fluence dependence in more detail several α values measured after 80 min at 60°C are plotted in Fig. 5.6 as function of fluence and are summarized in Tab. 5.3. It is very striking that the current related damage rate α does not depend on the material properties of the silicon, although the oxygen concentration is variing by about 4 orders of magnitude ($10^{14}\,\mathrm{cm}^{-3} < [O_i] < 10^{18}\,\mathrm{cm}^{-3}$) and the resistivity is ranging from about 400 Ωcm to 4 kΩcm in p-type and from about 100 Ωcm to 25 kΩcm in n-type materials. Since such strong variations in impurity content have an influence on the defect kinetics of migrating vacancies and interstitials it is concluded here, that after irradiation with high energetic hadrons mainly intrinsic defects composed of vacancies and interstitials inside or close to the clusters are responsible for the increase of the generation current but not impurity related defects.
Taking a closer look on Fig. 5.6 it can be seen that for fluences larger than $1 \times 10^{14}\,\mathrm{cm}^{-2}$ α seems to decrease slightly. A possible explanation could be that for such high fluences the concentration of the defects (clusters) responsible for the leakage current are in the

[4]This method has e.g. been used in [Chi95] to describe the short term annealing of leakage current at temperatures below room temperature.

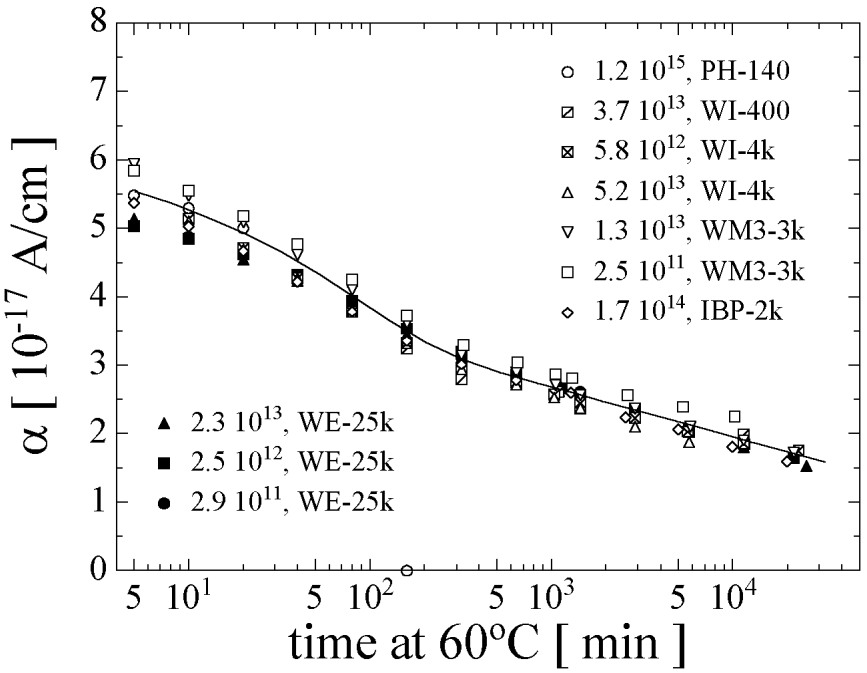

Figure 5.5: α values as function of cumulated annealing time at 60°C for some diodes. The legend gives the 1 MeV equivalent neutron fluence in [cm^{-2}] and the type of diode.

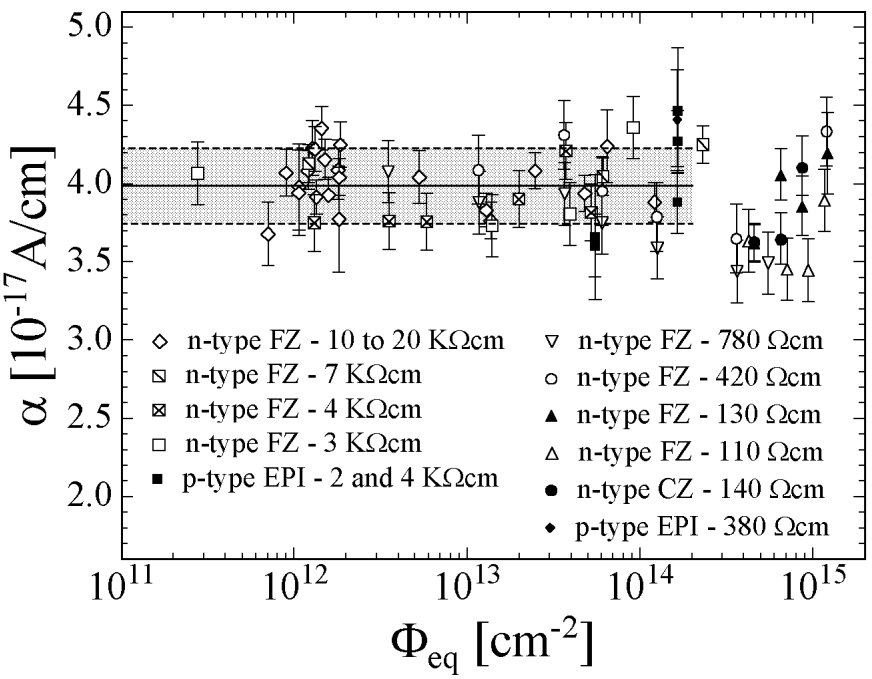

Figure 5.6: α values measured after 80 min at 60°C for several kind of materials (see Tab. 5.3). The solid line represents the mean value of $(3.99 \pm 0.03) \times 10^{-17}$ A/cm in the fluence range of up to $2 \times 10^{14}\,cm^{-2}$ while the dashed lines indicate the one sigma level of 0.24×10^{-17} A/cm. Structures without a guard ring are indicated by filled symbols.

Acronym	Type	Producer		Guard-	ρ	$[O]$	$[C]$	$\alpha_{(80/60)}$
		Crystal	Diode	ring	[kΩcm]	$\left[\frac{10^{16}}{\text{cm}^{-3}}\right]$	$\left[\frac{10^{16}}{\text{cm}^{-3}}\right]$	$\left[\frac{10^{-17}}{\text{Acm}^{-1}}\right]$
WM-3k	n-FZ	Wacker	MPI	yes	2.7	< 5	< 0.5	3.99±0.14
WE-7k-25k	n-FZ	Wacker	ELMA	yes	6.7 - 25	< 5	< 0.5	4.01±0.04
WI-4k	n-FZ	Wacker	ITE	yes	4.0	< 0.02	< 3	3.87±0.07
WI-400	n-FZ	Wacker	ITE	yes	0.42	< 5	< 2	4.02±0.11
TS-7k	n-FZ	Topsil	Sintef	yes	6.6	< 5	< 0.5	4.14±0.06
II-800	n-FZ	ITME	ITE	yes	0.78	17	< 2	3.79±0.08
II-120	n-FZ	ITME	ITE	yes	0.12	< 5	2	3.61±0.11
IH-130	n-FZ	ITME	HH	no	0.13	< 5	2	3.93±0.13
CZ-140	n-CZ	Polovodice	HH	no	0.14	90	0.5	3.94±0.18
ID-400	p-EPI	ITME	DIOTEC	no	0.4	$4 - 20$	$1 - 2$	4.41
ID-2k	p-EPI	ITME	DIOTEC	no	1.6	$3 - 20$	$1 - 2$	3.92±0.19
ID-4k	p-EPI	ITME	DIOTEC	no	3.9	$4 - 60$	$1 - 2$	4.06±0.40

Table 5.3: α values measured after 80 min at 60°C for various materials. Further details about the materials and the type of diodes can be found in Tab. 4.1 and Tab. 2.2, respectively.

order of the impurity concentrations and, therefore, are influenced by the migrating interstitials and vacancies produced by the irradiation. Another possibility is that the overall concentration of defects is high enough to sufficiently lower the leakage current by recombination processes. The validity of such speculations, however, can only be checked by further experiments.

In conclusion it has been shown that the leakage current is proportional to fluence and independent of the used material. These properties will be used in the next section to demonstrate that the leakage current is a very good monitor for the hadron fluence a diode has been exposed to.

5.2 Experimental determination of hardness factors

The samples irradiated with neutrons at the PTB Braunschweig were put into liquid nitrogen directly after the end of irradiation in order to avoid any further annealing. This was not possible for the samples irradiated at e.g. the CERN PS (24 GeV/c protons) or the reactors in Ljubljana and Demokritos (for details about the facilities see Sec. 4.2). Thus the samples were kept for about one to three days at room temperature before they could be handled in the laboratory. Additionally they were exposed to an unknown temperature history if sent by express mail. Therefore a heat treatment had to be applied to the samples in order to achieve a comparable annealing state independent of their individual annealing history at room temperature. In this work a temperature of 60°C was chosen. As shown in the last section a heat treatment of

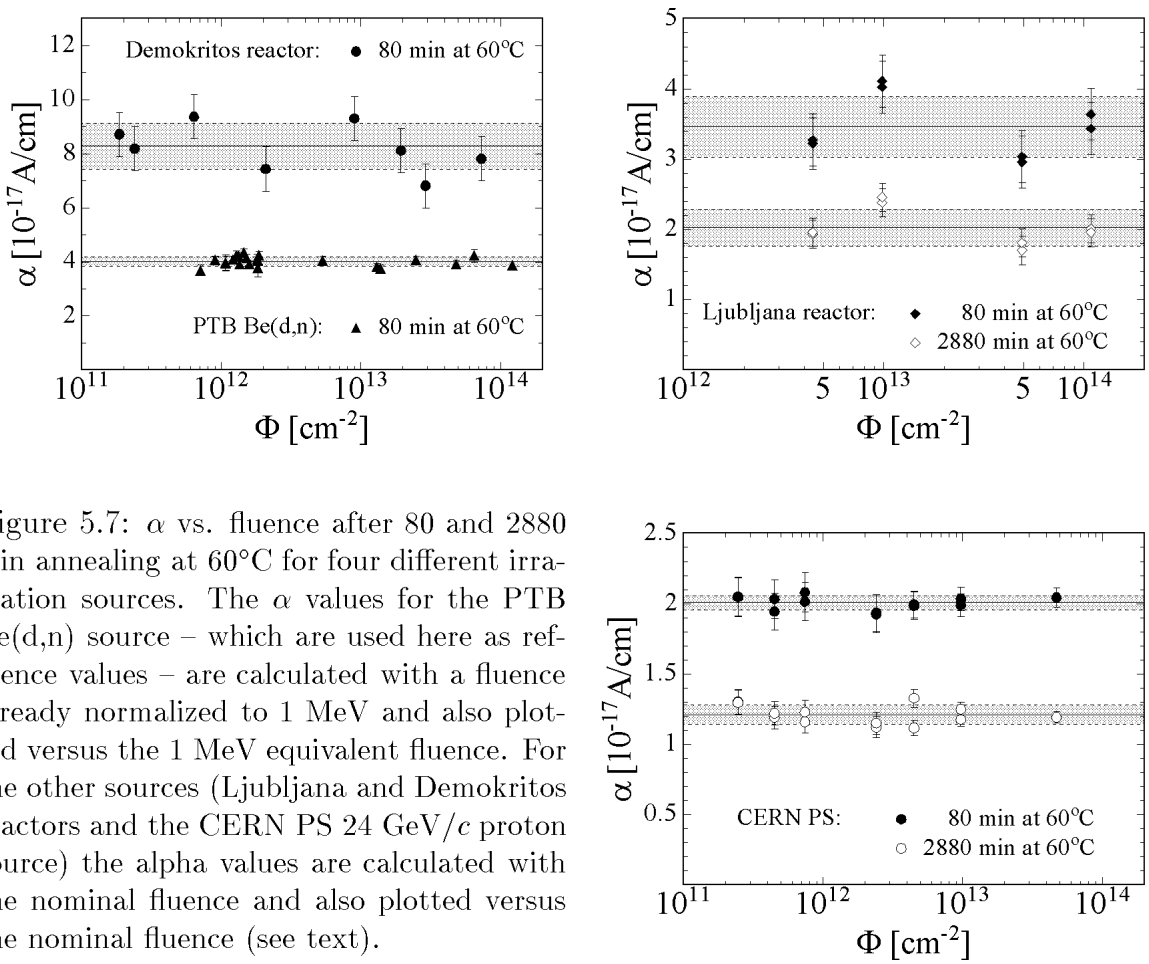

Figure 5.7: α vs. fluence after 80 and 2880 min annealing at 60°C for four different irradiation sources. The α values for the PTB Be(d,n) source – which are used here as reference values – are calculated with a fluence already normalized to 1 MeV and also plotted versus the 1 MeV equivalent fluence. For the other sources (Ljubljana and Demokritos reactors and the CERN PS 24 GeV/c proton source) the alpha values are calculated with the nominal fluence and also plotted versus the nominal fluence (see text).

80 min at 60°C has the same annealing effect on the leakage current as a storage for about 20 days at room temperature and an annealing for 2880 min at 60°C already corresponds to some years at room temperature (compare Fig. 5.2). Thus, after such an annealing procedure, the samples irradiated at different facilities can be regarded as being in the same annealing state.

The α values for samples irradiated at different sources and measured after 80 and 2880 min at 60°C are displayed in Tab. 5.4 and Fig. 5.7. As shown in the previous section the α value for a specific annealing state is independent of material and fluence. Thus, taking the NIEL hypothesis presented in Sec. 3.2 strict, α is a very good damage parameter for the measurement of hardness factors of high energetic particles or radiation fields. In Tab. 5.4 the hardness factors κ calculated from the individual spectra of the different sources are compared to the hardness factors obtained from α values. Since the spectrum – and thus also the hardness factor – for the neutron source at the PTB is very well known (see Sec. 4.2.1) the results obtained on α at the PTB have been chosen as a reference for the κ values.

Compared to α measured on identical samples after neutron irradiation at the PTB

irradiation source	diode type	$\alpha_{80/60}$ [10^{-17} A/cm]	$\alpha_{2880/60}$ [10^{-17} A/cm]	κ α value	κ spectrum	(*)
PTB Be(d,n) $<E_n>=$ 5.2 MeV	(1)	4.01 ± 0.04	2.38 ± 0.02	(reference)	1.44 - 1.51	(a)
	(2)	3.79 ± 0.08	2.25 ± 0.07			
CERN PS 24 GeV/c protons	(1)	2.01 ± 0.03	1.20 ± 0.02	0.51 ± 0.01	≤ 0.51	(b)
Ljubljana reactor neutrons	(2)	3.46 ± 0.15	2.03 ± 0.09	0.90 ± 0.05	0.91 ± 0.05	(c)
Demokritos reactor neutrons	(1)	8.29 ± 0.29	–	2.07 ± 0.08	–	–
UKE $^3H(d,n)$ 14.1 MeV neutrons	(3)	$\alpha(14400\,\mathrm{min}\,/\,80°\mathrm{C}) = 2.41$		≈ 1.66	1.80	(d)
BNL ^{60}Co-gamma	(3)	$\alpha = (1.4 \pm 0.2) \times 10^{-11}$ A/cm^{3}Gy $= (7.4 \pm 1.1) \times 10^{-23}$ A/cmγ		$\approx 1.9 \times 10^{-6}$	6.4×10^{-3}	(e)

Type of diode:
(1) WE-7kΩcm and WE-25kΩcm (2) II-800Ωcm (3) WM2-3kΩcm
Comments about κ determined from α value:
(d) Based on one sample only !
(e) Measured after 2 years at room temperature (see text).
Comments about κ determined from spectrum:
(a) Details can be found in Sec. 4.2.1.
(b) $D(E)$ for protons is only calculated up to 9 GeV (κ (9 GeV) = 0.51, see Fig. 3.2).
(c) The hardness factor of 0.91 [Cin98] supercedes the one of 0.88 given in [Žon99].
(d) Taken from [Gri96] for monoergetic neutrons with 14.1 MeV.
(e) Taken from [Sum93], displacement threshold $E_d = 21$ eV.

Table 5.4: Determination of hardness factors κ from α values for various sources (see text).

the hardness factor for the 24 GeV/c protons was determined to be 0.51 ± 0.01 and the one of the TRIGA reactor in Ljubljana to be 0.90 ± 0.05. Please keep in mind that the given errors are of statistical nature. This means they describe the reproducibility under the same experimental conditions only. Systematic errors regarding the fluence determination are not taken into account. The measured hardness factor for the protons is in good agreement with the experimental value of 0.58 ± 0.03 given in [Fei97a] and fits to the theoretical value predicted by Huhtinen (about 0.5, see[Huh93b]) while there is no accordance with the older value of 0.93 given by van Ginneken [Gin89]. For the TRIGA research reactor a hardness factor of 0.91 ± 0.05 has currently been calculated from the measured spectrum [Cin98]. The agreement with the experimental hardness factor given here is very good.

However, looking at the results for the other irradiation sources some discrepancies become visible. The spectrum at the Demokritos reactor was not measured in very detail and the nominal fluence was only roughly estimated by activation of gold foils. From the α value a hardness factor of about 2 was obtained. As can be seen from the neutron damage function diplayed in Fig. 3.2 on page 34 the highest possible hardness

α [10^{-11} A/cm^{3}Gy]	reference
1.4±0.2	this work
2.1	[Mac96a]
3.3	[Li 96]
3.9±1.5	[Fei97a] (no guard ring)
1.4	[Fre98]

Table 5.5: α values obtained on "standard" material after ^{60}Co-gamma irradiation.

factor for neutons is 2.07 and reached for neutrons with about 25 MeV kinetic energy. Thus it is obvious that the very high hardness factor is due to an incorrect fluence determination. By comparison with the results obtained at the Ljubljana reactor it can be assumed that the estimated nominal fluence was to small by about a factor of two.

The difference between the hardness factors for the UKE source should not be taken to strict since only one sample could be used to calculate the hardness factor from the α value. Thus, without a sufficient statistics, no conclusion can be drawn. Unfortunately the irradiation facility was closed before further irradiation experiments could be performed.

It is very difficult to determine the bulk generation current after irradiation with ^{60}Co-gammas since also radiation induced surface states contribute to the measured leakage current. However, by using devices with connected guard ring and without an overlap of the metallization onto the oxide (MOS-structure) it is possible to isolate the bulk generation current [Fre98]. It has been shown that there is no leakage current annealing at room temperature for ^{60}Co-gamma irradiated detectors [Fei97a]. Thus it is possible to compare the measured data with data from the literature without special attention to the annealing time at room temperature of the irradiated samples. Taking into account the above mentioned problems the value of 1.4×10^{-11} A/cm^{3}Gy determined in this work is in good agreement with the data given in the literature (see Tab. 5.5). However, by comparing the hardness factor determined from the α value to the one expected by the calculation of the NIEL (see Tab. 5.4), an obvious discrepancy arises. The values differ by almost 3 orders of magnitude. Therefore, the ^{60}Co-gamma irradiation is a very good example that one has to be careful in applying the NIEL-hypothesis to detector damage parameters. In this case the leakage current does not scale with the NIEL in the same way as was observed for the hadron damage. From the conclusions drawn in the last section – leakage current after hadron irradiation is mostly due to clusters – it is obvious that for the gamma irradiations a completely different mechanism is responsible for the current generation since gamma irradiation does not produce clusters (see Sec. 3.1). The bulk generation current after gamma irradiation is due to point defects only. Since the reaction kinetics of point defect is influenced by the impurities in the material (see Chapter 6) a material dependence is expected for the bulk generation current. This was very recently also observed [Fre98]. With increasing oxygen concentration the bulk generation current decreases. Thus, in contrast to the observations after hadron irradiations, the α value obtained after gamma irradiations

is by no means a good measure for the NIEL.

However, α is regarded here to scale very well with the NIEL if the bulk generation current is dominated by the contribution of the clusters and not the point defects. This is the case after high energetic hadron irradiations. Besides the hadron sources used in this work the NIEL scaling of the α value has recently been confirmed for 192 MeV pions (π^+) and 27 MeV protons [Fre99]. So far no discrepancy between the predicted and the measured hardness factor (determined from α) has been reported for hadron irradiations. In consequence it can be assumed that the 1 MeV neutron equivalent fluence for any hadron irradiation can be obtained by measuring the bulk generation current of an exposed diode in a well defined annealing state (e.g. 80 min 60°C). This method is most often more convenient than the determination of the full spectrum with e.g. activation foils. In the Ljubljana reactor for example, the reactor core configuration has to be changed from time to time. Since not for every irradiation a full set of activation foils can be used to determine the spectrum, systematic deviations of about 10% can be expected for irradiations that are monitored with a reduced set of activation foils only [Cin98]. This clarifies the need for a standardized and easy to use method for hardness factor determination of different sources or different source configurations (like the one presented in this work) in order to get a basis for comparing radiation damage experiments.

5.3 Effective doping concentration

5.3.1 Introduction

The observed change in the absolute effective doping concentration $|N_{eff}|$ of the bulk material as measured immediately after irradiation[5] is displayed in Fig. 5.8. For the starting n-type material it is obvious, that at lower fluences N_{eff} is reduced by an apparent *donor removal* and on top acceptor like states are being generated leading finally to inversion of the sign of the space charge from positive to negative and a further fluence proportional increase of $|N_{eff}|$.
In contrast to what was seen for the damage rate α the time dependence of the irradiation effect in N_{eff} is not only subject to a beneficial annealing but also to an adverse effect, called *anti-annealing* or *reverse annealing*. An example of the whole complex behavior is given in Fig. 5.9. Here ΔN_{eff} is the irradiation induced change in the effective doping concentration with respect to its initial value before irradiation:

$$\Delta N_{eff}\left(\Phi_{eq}, t(T_a)\right) = N_{eff,0} - N_{eff}\left(\Phi_{eq}, t(T_a)\right). \tag{5.6}$$

As function of time and fluence ΔN_{eff} can be described as:

$$\Delta N_{eff}\left(\Phi_{eq}, t(T_a)\right) = N_A\left(\Phi_{eq}, t(T_a)\right) + N_C\left(\Phi_{eq}, t(T_a)\right) + N_Y\left(\Phi_{eq}, t(T_a)\right). \tag{5.7}$$

Here it has been explicitly denoted that the time dependence is in itself subject to the annealing temperature T_a. As indicated in Fig. 5.9 and obvious from Eq. 5.7

[5]The displayed data are corrected for self-annealing during the irradiation (see [Wun92]).

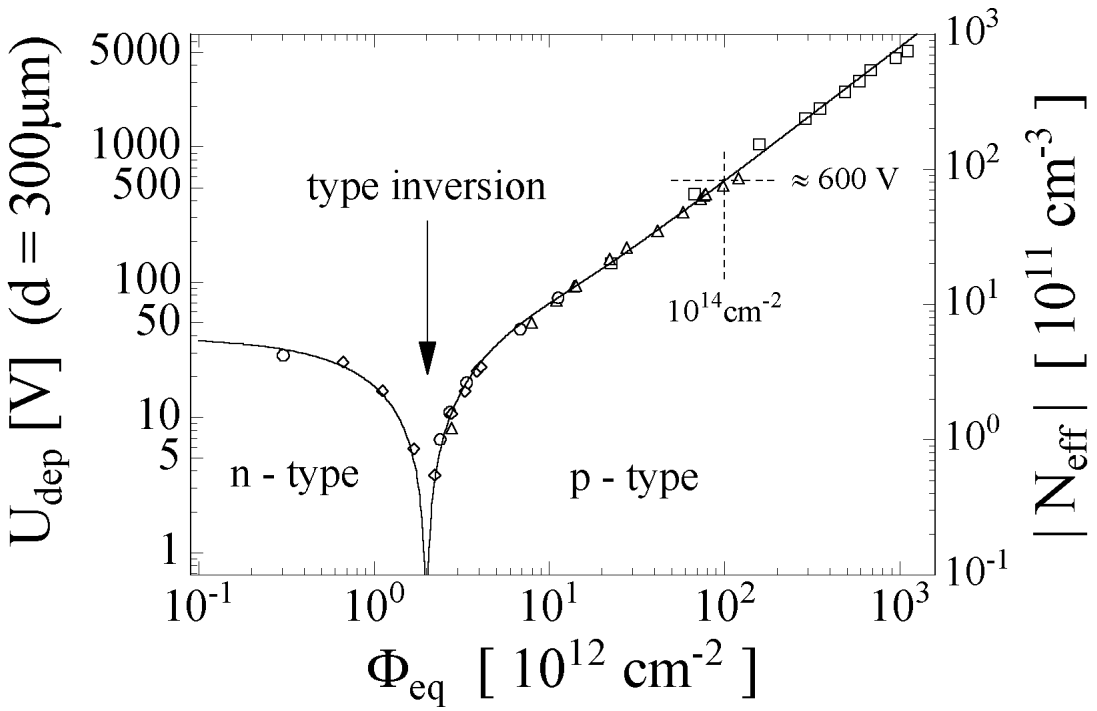

Figure 5.8: Change in the depletion voltage respectively the absolute effective doping concentration as measured immediately after irradiation [Wun92].

ΔN_{eff} has been divided in three components, namely N_A, N_C and N_Y. N_A is a *short term annealing* component which may be represented by a sum of several exponentials. However, in Fig. 5.9 the annealing at 60°C is presented and in contrast to the annealing at room temperature only the component with the largest time constant can be seen. N_C is not depending on annealing and therefore called the *stable damage* part. It consists of a so-called *incomplete donor removal*, depending exponentially on the fluence with a final value of N_{C0}, and in addition a fluence proportional introduction of *stable acceptors*:

$$N_C = N_{C0}\,(1 - \exp\,(-c\Phi_{eq})) + g_c\Phi_{eq}. \tag{5.8}$$

Finally, N_Y is the so-called *reverse annealing* as its behavior is opposite to the beneficial annealing. N_Y starts from zero for $t = 0$ and saturates to a fluence proportional value $N_{Y,\infty}$ for very large times with a time constant of about 500 days at room temperature.

In the following sections these three components will be described in more detail. The presented experimental data were obtained by fitting the annealing curves of ΔN_{eff} for various materials after irradiation with different fluences and annealed at different

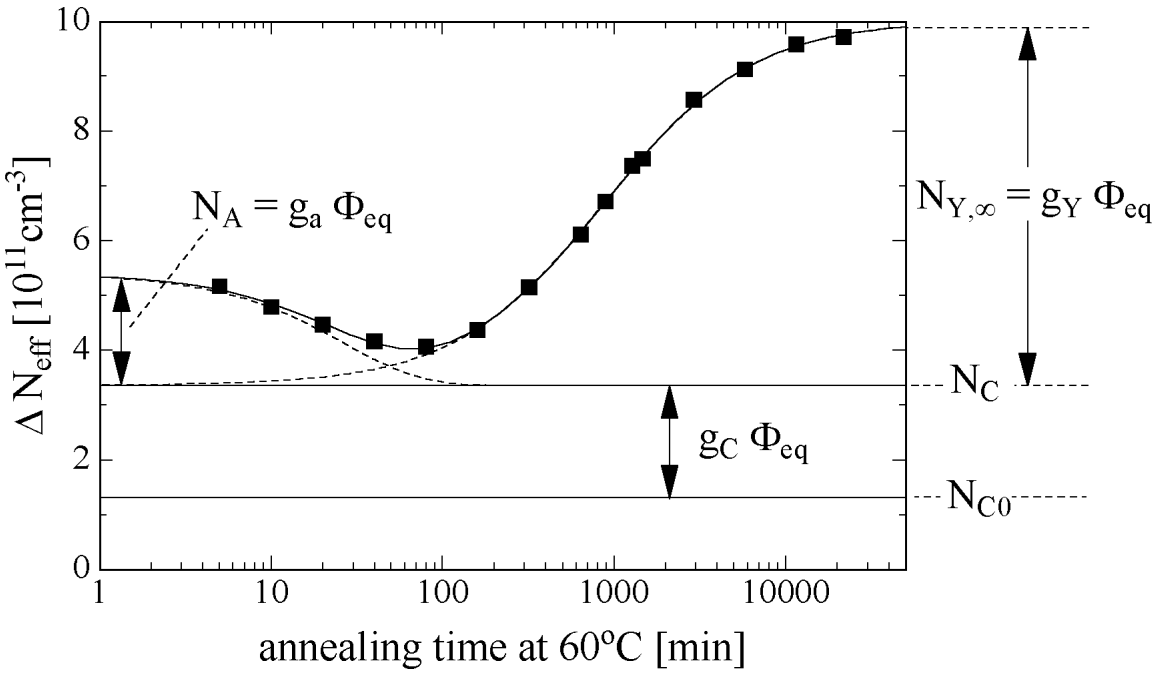

Figure 5.9: Annealing behavior of the radiation induced change in the effective doping concentration ΔN_{eff} at 60°C. The shown example is a sample of type WE-25kΩcm irradiated with a fluence of $1.4 \times 10^{13}\,\mathrm{cm}^{-2}$.

temperatures to Eq. 5.7. One should keep in mind that the resulting parameters for the damage components N_C, N_A and N_Y are not independent. Changing e.g. the parameterization for the reverse annealing component N_Y would also result in a different set of parameters for the two other components (compare Sec. 5.3.3). Therefore one has to be very careful in comparing results obtained with different parameterizations.

5.3.2 Short term annealing

Directly after irradiation a variation in full depletion voltage V_{dep} is observed. For type inverted detectors the depletion voltage decreases – this is the reason why this annealing component is also called *beneficial annealing* – while for not type inverted detectors the depletion voltage increases. Both cases can be interpreted in the same way, namely that the effective doping concentration N_{eff} is increasing. In other words: For type inverted detectors N_{eff} is negative and becoming less negative, while for not type inverted detectors N_{eff} is positive and becoming more positive. Usually this

Acronym	$N_{eff,0}$ [$10^{12}\,\mathrm{cm}^{-3}$]	g_a [$10^{-2}\,\mathrm{cm}^{-1}$]	$\tau_a(60°\mathrm{C})$ [min]	g_Y [$10^{-2}\,\mathrm{cm}^{-1}$]	$\tau_Y(60°\mathrm{C})$ [min]
WM3-3kΩcm	1.63±0.01	1.67±0.62	15.4±7.8	5.29±0.32	1160±370
WE-25kΩcm	0.17±0.02	1.59±0.16	24.6±2.9	4.84±0.14	880±180
WI-4kΩcm	1.10±0.02	2.01±0.46	24.1±3.6	4.92	1010
WI-400Ωcm	10.4±0.1	2.13±0.55	11.2±8.0	4.17	550
II-800Ωcm	5.53±0.07	1.68±0.39	12.2±5.5	4.58	960
II-120Ωcm	37.2±0.6	1.33±0.13	16.2±4.1	4.45	1560
PH-140Ωcm (Cz)	30.6±0.1	2.01±0.44	30.9±10.2	2.53±0.38	804
IDP- 2-4kΩcm	-7.8 to -3.2	1.95±0.35	23.0±3.5	5.63±0.54	1090±210
IDP-400Ωcm	-31.9±1.5	1.87±0.34	23.7±5.2	2.24	2200
weighted average:		1.81±0.14	24.1±2.3	(5.16±0.09)†	1060±110

† Average for high resistivity (2 kΩcm to 25 kΩcm) n-type material (see Fig. 5.15 and text).

Table 5.6: *Beneficial annealing* and *reverse annealing* parameters for different materials (see Tab. 4.1) obtained from fits according to Eq. 5.7 to isothermal annealing curves of ΔN_{eff} at 60°C (compare Fig. 5.9).

behavior is attributed to an annealing of acceptors[6]. However, one should keep in mind that in principle also the generation of donors[6]could lead to the same experimental effects. This first-order approach corresponds to a mathematical representation of the annealing curve by a sum of exponential terms

$$N_A = \Phi_{eq} \sum_i g_{a,i} \exp\left(-\frac{t}{\tau_{a,i}}\right). \tag{5.9}$$

As annealing time constants of minutes and hours are not relevant for the operation of silicon detectors in high-energy physics experiments, only the longest decay time constant has been considered in this work. Therefore Eq. 5.9 reduces to a single exponential term with a time constant τ_a and an amplitude $N_A = g_a \phi_{eq}$. Further details about the components with shorter time constants can e.g. be found in [Wun92]. The fluence dependence of N_A is displayed in Fig. 5.10 for various different materials and the corresponding introduction rates are presented in Tab. 5.6. Within the fluctuations of the data points no material dependence is seen for g_a although the oxygen concentration is ranging from below $2 \times 10^{14}\,\mathrm{cm}^{-3}$ to about $1 \times 10^{18}\,\mathrm{cm}^{-3}$ (see Tab. 4.1 on page 64). The average introduction rate g_a is given by

$$g_a = (1.81 \pm 0.14) \times 10^{-2}\mathrm{cm}^{-1}.$$

[6]Here types of acceptor or donors are meant that introduce negative, respectively positive, space charge (for details see Sec. 3.7).

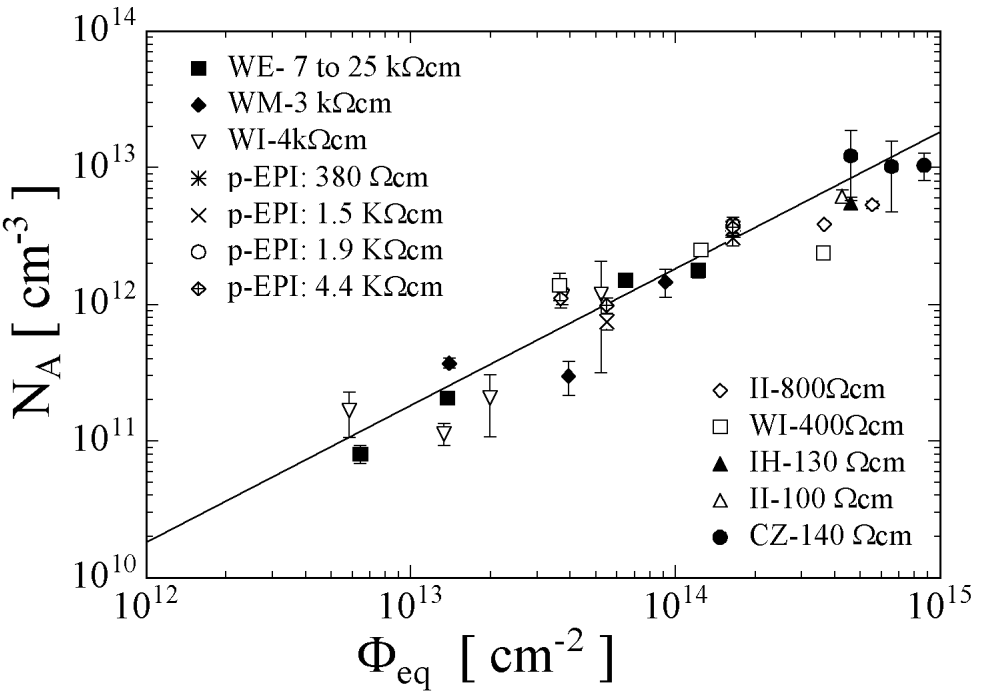

Figure 5.10: Fluence dependence of the short term annealing amplitude N_A.

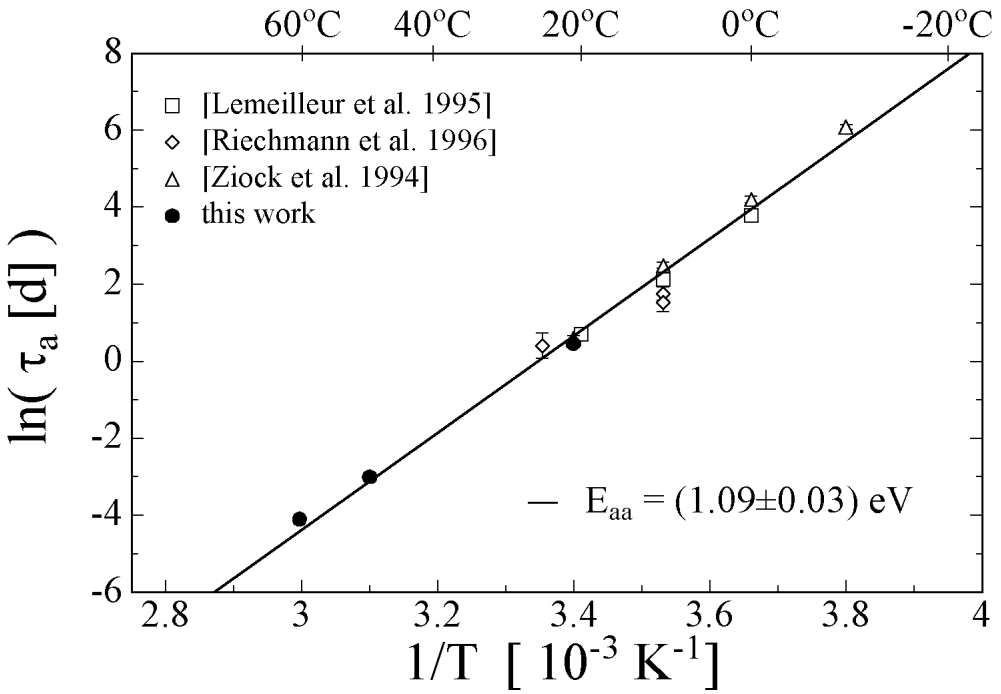

Figure 5.11: Arrhenius Plot of the time constant τ_a. The external data cited in the caption [Zio94, Lem95, Rie96] are taken from a compilation in Ref. [Fei98a].

temperature (T_a)	-10°C	-7°C	0°C	10°C	20°C	40°C	60°C	80°C
time constant(τ_a)	306 d	180 d	53 d	10 d	55 h	4 h	19 min	2 min
acceleration factor	1/134	1/78	1/23	1/5	1	16	174	1490

Table 5.7: Temperature dependence of the time constant τ_a calculated with the annealing parameters extracted from the Arrhenius plot (see text). The last row gives the acceleration factor for the *beneficial annealing* with respect to 20°C.

The temperature dependence of the time constant τ_a can be expressed by a standard Arrhenius relation (Eq. 3.50)

$$\frac{1}{\tau_a} = k_a = k_{0a} \exp\left(-\frac{E_{aa}}{k_B T_a}\right). \tag{5.10}$$

Since in this work the time constant was only measured for 21, 49 and 60°C the Arrhenius Plot displayed in Fig. 5.11 was complemented with data from the literature. The resulting activation energy E_{aa} and frequency factor k_{0a} are

$$E_{aa} = (1.09 \pm 0.03)\,\text{eV} \qquad \text{and} \qquad k_{0a} = 2.4^{+1.2}_{-0.8} \times 10^{13}\,\text{s}^{-1}.$$

With a frequency factor in the order of the most abundant phonon frequency $k_B T/h \approx 10^{13}\,\text{s}^{-1}$, it is very likely that the annealing of the microscopic defects underlying the beneficial annealing is due to a single jump (dissociation or reorientation) process rather than a long range migration (compare Sec. 3.5). Furthermore it has to be noted that the parameters given above are very close to the values found for the exponential decay of the leakage current presented in Sec. 5.1.3 ($E_I = (1.11 \pm 0.05)$ eV and $k_{0I} = 1.2^{6.5}_{0.2} \times 10^{13}\,\text{s}^{-1}$). This suggests that both phenomena, the short term annealing of the leakage current and the short term annealing of the effective doping concentration, are due to the annealing of the same microscopic defects. This topic will be discussed in more detail in Sec. 7.2.1.
In Tab. 5.7 some time constants τ_a calculated with the parameters obtained from the Arrhenius plot are displayed as function of temperature. As can be seen from the data the annealing is strongly suppressed at temperatures below room temperature. Thus the operation of detectors at low temperatures (e.g. the envisaged operating temperature for the ATLAS SCT is -7°C [ATL97]) will not only suppress the leakage current during detector operation but also *freeze* the beneficial annealing. Therefore short periods at room temperature, as needed for the detector maintenance, do not only have the negative effect of *reverse annealing* (see next section) but also the positive effect of *beneficial annealing*.

5.3.3 Reverse annealing

In the long term the space charge is becoming more negative (the depletion voltage of type inverted detectors is increasing). This is most often interpreted as a build up of an acceptor. However, as mentioned before for the *beneficial annealing*, one should

keep in mind that also the annealing of a donor leads to the same experimental effect. So far the latter possibility can not be ruled out although in Sec. 7.2.3 an indication for the build up of an acceptor during the reverse annealing will be given.

5.3.3.1 First or second order process ?

There has been a long lasting discussion whether the *reverse annealing* should be described as a first order [Zio94, Li 95a] or a second order [Fre94, Sch94, Sch96a] process. In this section it will be shown that the reaction kinetics underlying the reverse annealing is best described as a first order process. However, the best fit to the individual annealing curves was found to be the one with the second order approach. Therefore in this work a pragmatic compromise between both approaches is used for the parameterization of the data (Eq. 5.15, see below).

As described in Sec. 3.5 the first and second order reaction kinetics lead to the following equations for the evolution of the defect concentration $N_Y(t)$

$$N_Y(t) = N_{Y,\infty}\left(1 - \exp\left(-k_{1Y}\, t\right)\right) \quad (\gamma = 1, \text{ first order}) \tag{5.11}$$

$$N_Y(t) = N_{Y,\infty}\left(1 - \frac{1}{1 + k_{2Y}\, N_{Y,\infty} t}\right) \quad (\gamma = 2, \text{ second order}) \tag{5.12}$$

with $N_{Y,\infty}$ being the reverse annealing amplitude. In Fig. 5.12 the experimental data

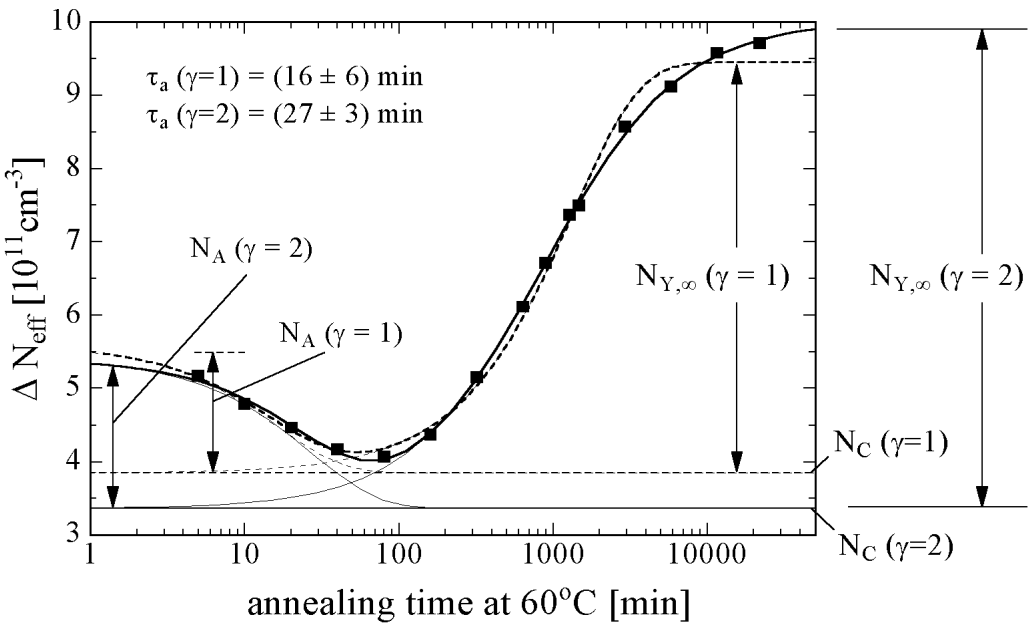

Figure 5.12: Comparison between first order (γ=1, dashed line) and second order (γ=2, solid line) approach to the reverse annealing. Fits according to Eq. 5.7 with Eq. 5.11 (γ=1) and Eq. 5.12 ($\gamma = 2$) for the reverse annealing, respectively (same data as displayed in Fig. 5.9).

are fitted according to the overall annealing function of ΔN_{eff} (Eq. 5.7) by either using the first (dashed line) or the second order (solid line) approach to the reverse annealing. As clearly can be seen the second order approach enables a far better least squares fit to the data. Furthermore it is shown in the figure that the different approaches to the reverse annealing have an influence on the fit parameters obtained for the beneficial annealing (N_a and τ_a) and the stable damage (N_C). Using e.g. the first order parameterization for the reverse annealing instead of the second order one leads to a bigger N_C and a smaller N_A, τ_a and $N_{Y,\infty}$. Thus one should always keep in mind that the three damage components *reverse annealing*, *beneficial annealing* and *stable damage* cannot be determined independently from each other.

Although the second order approach gives the best fit to the data, it cannot describe the physics underlying the reverse annealing process. This is best understood by looking at the half life periods for the different orders of reaction:

$$\tau_{(1/2)} = \ln 2 \times \frac{1}{k_{1Y}} \quad (\gamma = 1, \text{ first order}) \tag{5.13}$$

$$\tau_{(1/2)} = \frac{1}{N_{Y,\infty}} \times \frac{1}{k_{2Y}} \quad (\gamma = 2, \text{ second order}). \tag{5.14}$$

While for a first order process the half life period is independent of the defect concentration for the second order process it is. In a second order process two reaction partners (defects) have to meet each other in order to perform the reaction (see Sec. 3.5). Thus with increasing defect concentration the probability for a reaction is higher, meaning in our case that the generation of negative space charge per unit time is increasing with the reverse annealing defect concentration $N_{Y,\infty}$. Since $N_{Y,\infty} \propto \Phi_{eq}$ (see below), the half life period for the reverse annealing should become smaller with increasing particle fluence. This is by no means seen in the experimental data. In Fig. 5.13 the reverse annealing $N_Y(t)$ is shown for four samples irradiated with different fluences. The data are normalized to the individual reverse annealing amplitudes $N_{Y,\infty}$ for better visibility. The expected time dependence according to the second order parameterization (Eq. 5.12) with the parameters given in [Chi95] are displayed as dashed lines. In contrast to the theoretical prediction for a second order process no fluence dependence of the half life periods is observed. This contradiction to the second order approach is also displayed in Fig. 5.14. Here the second order rate constant k_{2Y} obtained in isothermal annealing procedures at 60°C is plotted against the reverse annealing amplitude $N_{Y,\infty}$ for various materials. Unlike expected for a second order process k_{2Y} is not independent of the reverse annealing amplitude $N_{Y,\infty}$ but shows a reciprocal dependence on $N_{Y,\infty}$ ($1/(N_{Y,\infty} \times k_{2Y}) = (1.1 \pm 0.1) \times 10^3$ min).

Consequently a first order process has to be assumed for the defect reactions underlying the *reverse annealing*. Since the macroscopic behavior is still best fitted by Eq. 5.12 ($\gamma = 2$) a pragmatic parameterization was chosen for the reverse annealing by replacing $(N_{Y,\infty} \times k_{2Y})^{-1}$ with a time constant τ_Y in Eq. 5.12:

$$N_Y(t) = N_{Y,\infty}\left(1 - \frac{1}{1 + t/\tau_Y}\right) \tag{5.15}$$

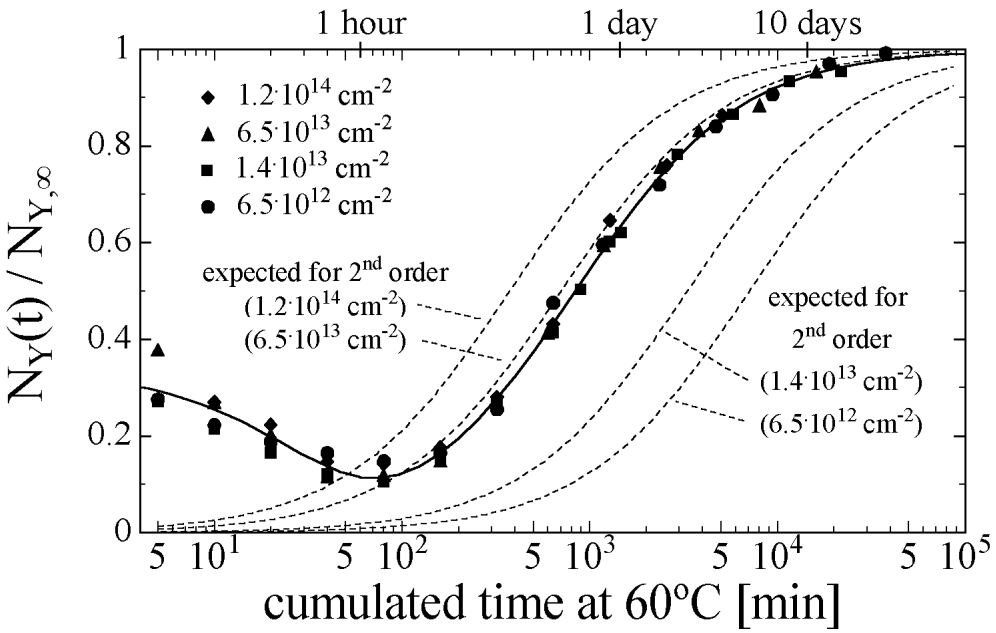

Figure 5.13: Reverse annealing at 60°C for samples irradiated with different fluences as given in the legend. The line matching the data points represents a least squares fit under the assumption of a second order annealing kinetics. The 4 dashed lines indicate the expected fluence dependence for a *"real"* second order process (see text). The theory predicts a fluence dependent half life period which is not seen in the experiment (Samples: WE-25kΩcm from same wafer, irradiated with neutrons).

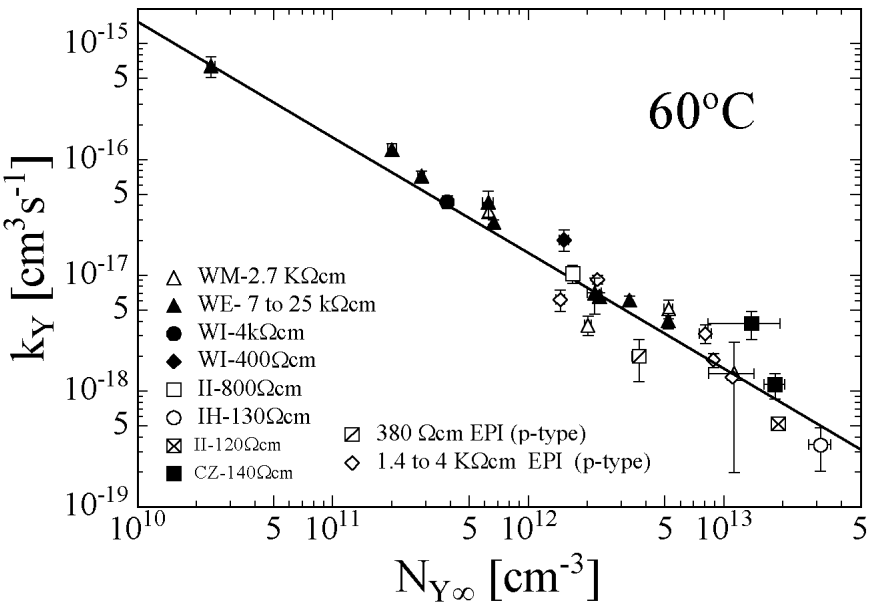

Figure 5.14: Fluence dependence of the 2^{nd}-order rate constant k_{2Y} obtained from isothermal annealing experiments at 60°C for various materials. The solid line represents a fit to the data with $(N_{Y,\infty} \times k_{2Y})^{-1} = (1.1 \pm 0.1) \times 10^3$ min.

with $N_{Y,\infty} = g_Y \cdot \Phi_{eq}$ being the amplitude of the reverse annealing. It is noted that for short reverse annealing times ($t \ll \tau_Y$) Eq. 5.15 gives the same result as a first order parameterization with a time constant τ_Y:

$$1 - \frac{1}{1 + t/\tau_Y} \approx 1 - (1 - t/\tau_Y) = t/\tau_Y \qquad (t \ll \tau_Y) \tag{5.16}$$

$$1 - \exp(-t/\tau_Y) \approx 1 - (1 - t/\tau_Y) = t/\tau_Y \qquad (t \ll \tau_Y). \tag{5.17}$$

One can think of two possible reasons for the insufficient description of the reverse annealing by a simple first order model.

First, there might be systematic errors in the determination of the depletion voltage (effective doping concentration) from the C/V characteristics. The interpretation of where the kink in the C/V characteristics is indicating the full depletion voltage does depend on the individual interpretation of the person analyzing the data. Since the shape of the C/V characteristics (and their frequency dependence) is strongly changing during the reverse annealing process [Mol95a] there is a source for systematic errors. Furthermore, the shape of the C/V characteristics depends on the mode of the capacitance bridge (serial or parallel, see Sec. 4.3), whether or not a guard ring is used and – of course – on the chosen plot for analyses (e.g. log(C) vs. log(V), C vs. $1/\sqrt{V}$, etc.; compare Sec. 4.3). Very recently it was demonstrated that the capacitance measured in serial mode and plotted in a log(C) vs. log(V) diagram may lead to individual annealing curves of ΔN_{eff} rather to be interpreted as first than second order [Lin99a].

The second possibility is that the C/V characteristics have been interpreted correctly in this work and the reverse annealing is more complicated than a simple first order process. One could think e.g. of a superposition of two processes. In this context the observation of a *bistable defect* generated and activated in neutron irradiated samples by heat treatments in the temperature range between 50 and 120°C and described in more detail in [Mol95b, Fei97b] has to be mentioned. Although after each heat treatment lasting longer than 320 min the detectors were stored for at least one day at room temperature in the dark in order to allow the *bistable defect* to decay (first order decay with a time constant of 500 min at room temperature, for further details see [Mol95b]) a contribution of this defect to the negative space charge cannot be ruled out. Therefore one could think e.g. of a sum of two exponential terms as suggested in [Li 95a] or a sum of an exponential term and another function in order to fit the reverse annealing. This, however, also increases the number of fit parameters substantially leading to further uncertainties depending on the number of data points.

In conclusion it is assumed here that the *reverse annealing* is dominated by a first order process that is superimposed by another annealing process. Since this second process can up to now not be isolated from the reverse annealing Eq. 5.15 was chosen as a parameterization. In the following the parameters obtained with this parameterization will be discussed.

5.3.3.2 Fluence and temperature dependence of the reverse annealing

The fluence dependence of the reverse annealing amplitude $N_{Y,\infty}$ is shown in Fig. 5.15 for various materials. The solid line represents the average introduction rate

$$g_Y = (5.16 \pm 0.09) \times 10^{-2}\,\mathrm{cm}^{-1}$$

for the high resistivity n-type material (2 kΩcm to 25 kΩcm; 57 samples). The introduction rates g_Y for the other materials are given in Tab. 5.6 on page 113. Apart from the low resistivity epitaxial p-type (IDP-400Ωcm, one sample only) and the low resistivity n-type Czochralski silicon (PH-140Ωcm, three samples) all results are close to the average value. While for the epitaxial p-type material the very thin epitaxial layer (105 μm) and the type of diode (MESA, see comment in Sec. 2.2.2.4) may be sources for systematic errors, the result for the Cz material is far more significant. For all three investigated samples a reduced reverse annealing amplitude was observed. However, a definite evidence for a correlation between the very high oxygen concentration in the Cz silicon ($[O] = 9 \times 10^{17}\,\mathrm{cm}^{-3}$) and the observed effect cannot be given. On the one hand the material with the second highest oxygen concentration (II-800Ωcm, $[O] = 1.7 \times 10^{17}\,\mathrm{cm}^{-3}$) does not show a significant reduction (compare Tab. 5.6) and on the other hand the reverse annealing of samples with a lower oxygen concentration has not been investigated in the same fluence range ($\Phi_{eq} = 6$ to $9 \times 10^{14}\,\mathrm{cm}^2$). Therefore, a direct comparison between the Cz silicon and material with *standard* oxygen concentration is still missing. The data obtained on the CZ material have so far been interpreted as a reduction of the reverse annealing introduction rate g_y (indicated by the dashed line in Fig. 5.15). However, a saturation of the reverse annealing amplitude at fluences above about $5 \times 10^{14}\,\mathrm{cm}^{-2}$ is not ruled out by the observed data. In this case the dashed line in Fig. 5.15 would be misleading (compare with results presented in Sec. 8.1).
In this context it has to be mentioned that very recently a further hint for an impact of the oxygen concentration on the reverse annealing was given by A.Ruzin et al. [Ruz99c]. They showed that after irradiation with charged hadrons (192 MeV π^+ and 23 GeV protons) the reverse annealing amplitude in oxygen enriched FZ silicon ($[O] \approx 2 \times 10^{17}\,\mathrm{cm}^{-3}$) is suppressed by a factor of about 1.5 compared to *standard* FZ silicon.
In conclusion some indications for a beneficial influence of a very high oxygen concentration on the reverse annealing process after neutron irradiation have been presented. However, a clear evidence can only be given by further experiments.

As discussed in the last section, a first order reaction kinetics is assumed for the reverse annealing. Thus the time constant τ_Y (half life period) can be expressed by a standard Arrhenius relation (Eq. 3.50)

$$\frac{1}{\tau_Y} = k_Y = k_{0Y} \exp\left(-\frac{E_Y}{k_B T_a}\right). \tag{5.18}$$

The corresponding Arrhenius plot for annealing temperatures ranging from 21 to 106°C is shown in Fig. 5.16. The resulting activation energy E_Y and the frequency

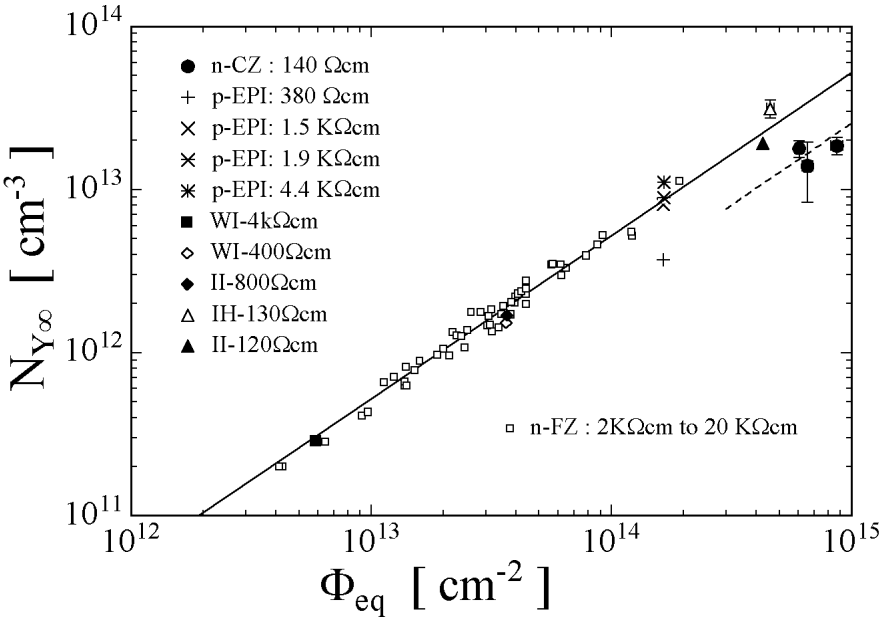

Figure 5.15: Reverse annealing amplitude $N_{Y,\infty}$ versus fluence for various silicon materials. Each point corresponds to an individual detector annealed in an isothermal heat treatment. The solid line represents the average introduction rate $g_Y = (5.16 \pm 0.09) \times 10^{-2}\,\mathrm{cm}^{-1}$ for the high resistivity n-type FZ silicon and the dashed one the introduction rate of $(2.53 \pm 0.38) \times 10^{-2}\,\mathrm{cm}^{-1}$ for the Cz silicon (see text).

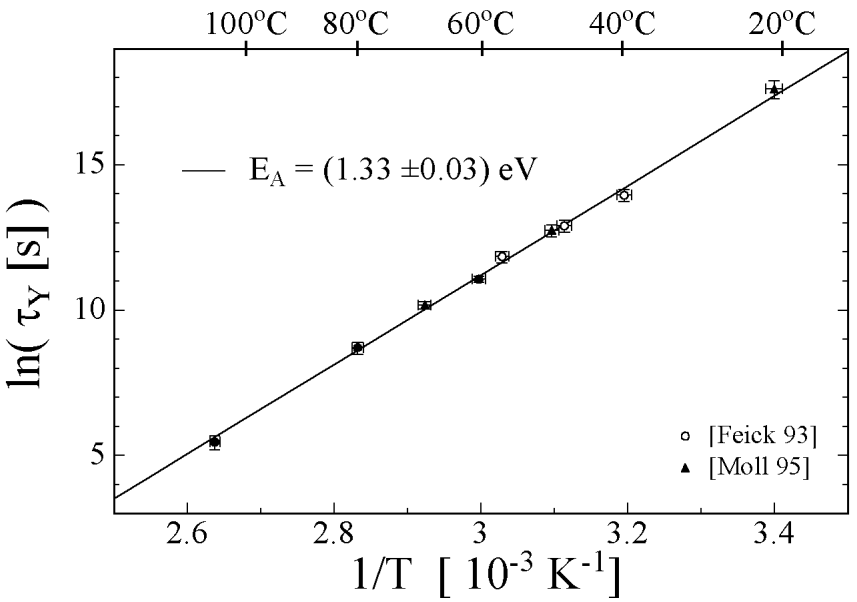

Figure 5.16: Arrhenius Plot for the reverse annealing time constant τ_Y. The line represents the least squares fit with the fit parameters $ln(\tau_Y[\mathrm{s}]) = -(34.93 \pm 1.19) + (1.325 \pm 0.034)\,\mathrm{eV}/(k_B T)$. Some of the data points have been calculated from annealing studies presented in [Fei93] and [Mol95a].

factor[7] k_{0Y} are

$$E_Y = (1.33 \pm 0.03)\,\mathrm{eV} \qquad \text{and} \qquad k_{0Y} = 1.5^{+3.4}_{-1.1} \times 10^{15}\,\mathrm{s}^{-1}.$$

The frequency factor is higher than the expected value for a single jump process (most abundant phonon frequency $k_B T/h \approx 10^{13}\,\mathrm{s}^{-1}$, compare Sec. 3.5). This may be taken as a further indication for the insufficient description of the reverse annealing by a single first order process.
Although there is a lack in understanding of the microscopic defect kinetics as deduced from the macroscopic parameterization, the parameterization itself can - of course - very well be used for temperature and fluence dependent *damage projections*. As an example the expected time constant τ_Y as function of annealing temperature is given in Tab. 5.8.

temperature (T_a)	-10°C	0°C	10°C	20°C	40°C	60°C	80°C	100°C
time constant(τ_Y)	516y	61y	8y	475d	17d	1260min	92min	9min
acceleration factor	1/396	1/47	1/6	1	29	544	7430	76650

Table 5.8: Temperature dependence of the time constant τ_Y calculated with the annealing parameters extracted from the Arrhenius plot (see text). The last row gives the acceleration factor for the reverse annealing with respect to 20°C.

5.3.4 Stable damage – Material dependence

It has to be emphasized that the *stable damage* is the most important damage component regarding the operability of silicon detectors in intense radiation fields. Taking the LHC applications as an example the short term annealing component $N_A(t)$ with a time constant of about two days at room temperature ($\tau_a(20°\mathrm{C}) = 55$ h) will completely anneal during the maintenance periods of two weeks. Furthermore the *reverse annealing* will be frozen during the operation of the detector at -7°C and only a small contribution of negative space charge will arise during the two weeks of maintenance at room temperature ($\tau_Y(20°\mathrm{C}) = 475$ d). Therefore, the main problem remains the *stable damage* that cannot be influenced by the operational temperature. In this section it will be shown that the *stable damage* generated by neutron irradiations can be reduced by using oxygen rich material. Investigations after charged hadron irradiations will be presented and discussed in Secs. 5.3.5 and 8.1.

Fig. 5.17 displays the fluence dependence of the effective doping concentration N_{eff} for the low resistivity float zone and Czochralski silicon measured after a heat treatment at 60°C for 80 min. In this state of annealing the change in the effective doping concentration ΔN_{eff} has reached its minimum as can be seen in Fig. 5.9. The short term annealing has nearly ended whereas the reverse annealing is just beginning. Therefore the plotted data are almost exclusively governed by the stable damage component.

[7] To be strict, the definition of the frequency factor should be given by $k_{0Y} \times \ln 2$, since τ_Y is the half life period and not the first order time constant of the reverse annealing (compare Eq. 5.13).

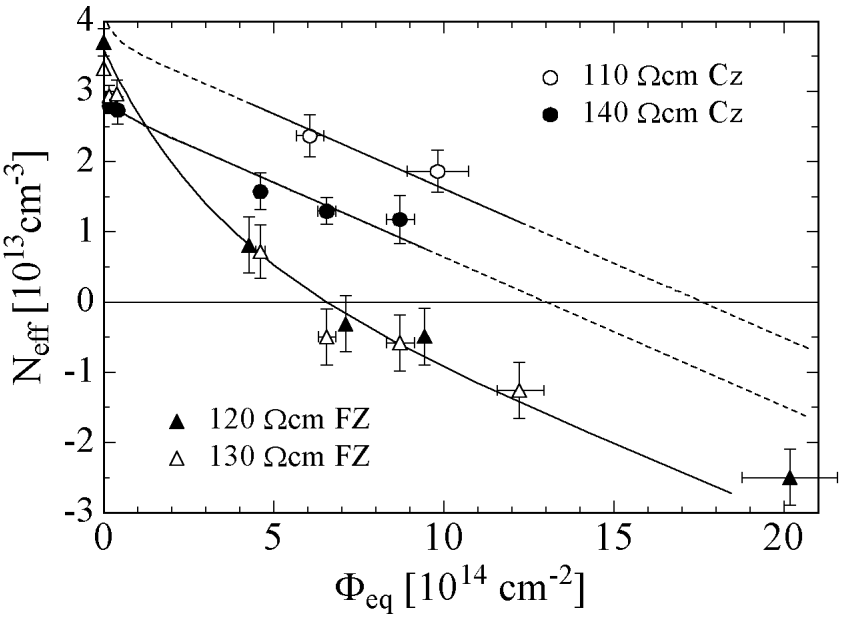

Figure 5.17: Fluence dependence of the effective doping concentration N_{eff} for low resistivity FZ and Cz silicon (see Tab. 4.1) measured after 80 min at 60°C.

Already from this figure it can be seen that the Czochralski silicon is radiation harder. The float zone devices with the low oxygen concentration are type inverted after a fluence of about $6 \times 10^{14}\,\mathrm{cm}^{-2}$ whereas the Czochralski silicon diodes with nearly the same initial resistivity but a higher oxygen concentration are still n-type. From the extrapolations in the plot (dashed lines) it is expected that the type inversion fluences are higher than $12 \times 10^{14}\,\mathrm{cm}^{-2}$.
To gain a better understanding of these findings several samples produced from different materials as displayed in Tab. 4.1 have been irradiated and exposed to a heating and measurement procedure at 60°C. Afterwards the sets of annealing data, ΔN_{eff} vs. time at 60°C, were fitted for each sample with a least squares fit according to Eq. 5.7 with the stable damage component given by

$$N_C = N_{C0}\,(1 - \exp\,(-c\Phi_{eq})) + g_c\Phi_{eq} \qquad \text{(Eq. 5.8)}.$$

In Fig. 5.18 the stable damage parameter N_C is displayed for all investigated materials as a function of fluence. The solid lines in the figures are the fits according to Eq. 5.8. The corresponding fit parameters are displayed in Tab. 5.9.
With exception of the 420 Ωcm float zone silicon from Wacker (WI-400Ωcm) all materials exhibit nearly the same introduction rate of stable acceptors with a weighted average value of

$$g_c = (1.49 \pm 0.04) \times 10^{-2}\mathrm{cm}^{-1}.$$

The reason for the reduced introduction rate of $(0.61 \pm 0.07) \times 10^{-2}\mathrm{cm}^{-1}$ for the 420 Ωcm Wacker silicon is up to now unknown. There are basically two possibil-

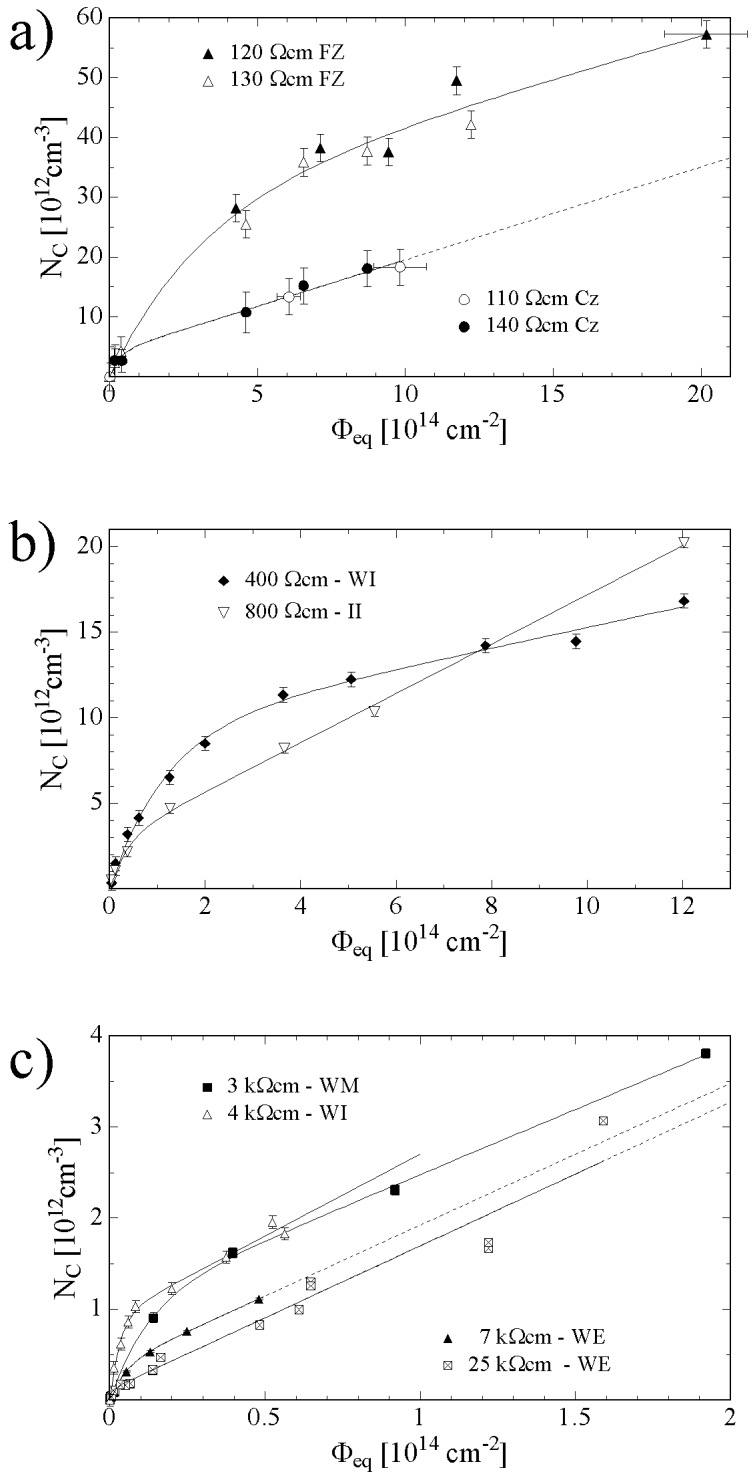

Figure 5.18: Damage parameter N_C plotted against the fluence. Each point represents one sample of a) low resistivity material ($\approx 100\,\Omega$cm) b) medium resistivity material ($400\,\Omega$cm to $800\,\Omega$cm) and c) high resistivity material (3 kΩcm to 25 kΩcm). The solid lines are fits to the data points according to Eq. 5.8. The corresponding fit parameters N_{C0}, c and g_c are displayed in Tab. 5.9.

Acronym	$N_{eff,0}$ $[10^{12}\,\mathrm{cm}^{-3}]$	N_{C0} $[10^{12}\,\mathrm{cm}^{-3}]$	c $[10^{-14}\,\mathrm{cm}^{2}]$	g_c $[10^{-2}\,\mathrm{cm}^{-1}]$	$\frac{N_{C0}}{N_{eff,0}}$	$N_{C0} \times c$ $[10^{-2}\,\mathrm{cm}^{-1}]$
WM-3kΩcm	1.63 ± 0.01	1.05 ± 0.08	$\approx (8 \pm 2)$	1.43±0.06	0.64±0.05	≈ (9±2)
WE-7kΩcm	0.64 ± 0.01	0.36 ± 0.02	19.3 ± 1.9	1.56±0.05	0.56±0.04	6.9±0.8
WE-25kΩcm	0.17 ± 0.02	0.11 ± 0.07	75 ± 17	1.58±0.09	0.65±0.49	8.3±5.6
WI-4kΩcm	1.10 ± 0.02	0.90 ± 0.08	31 ± 7	1.80±0.20	0.83±0.09	27.9±6.8
WI-400Ωcm	10.4 ± 0.1	9.22 ± 0.65	0.86 ± 0.11	0.61±0.07	0.89±0.07	7.9±1.2
II-800Ωcm	5.53 ± 0.07	2.78 ± 0.27	2.82 ± 0.80	1.44±0.04	0.50±0.06	7.8±2.4
II-120Ωcm	37.2 ± 0.6	28.5 ± 0.6	0.31 ± 0.13	1.43±0.38	0.77±0.03	8.8±3.7
IH-130Ωcm	33.3 ± 0.4				0.86±0.03	
CZ-110Ωcm	39.4 ± 0.5	4.02 ± 0.15	$\approx (3 \pm 2)$	1.55±0.21	0.10±0.01	≈ (12±9)
CZ-140Ωcm	30.6 ± 0.5				0.13±0.01	

Table 5.9: Damage parameters for different n-type materials (see text). The data for II-120Ωcm and IH-130Ωcm as well as the data for CZ-110Ωcm and CZ-140Ωcm have been fitted together.

ities. Firstly, the introduction of the stable acceptors is really suppressed or, secondly, an additional donor is created with a rate of about $0.9 \times 10^{-2}\,\mathrm{cm}^{-1}$ thus lowering the effective introduction rate of negative space charge from $1.5 \times 10^{-2}\,\mathrm{cm}^{-1}$ to $0.6 \times 10^{-2}\,\mathrm{cm}^{-1}$. Because the microscopic defects underlying the introduction of negative space charge are not known - only a few experimental and theoretical indications exist [Fre97, Mat95, Gil97] - there is no hint which of the possibilities is more likely. Since such a reduced introduction rate would be very helpful in terms of radiation hardness, because it corresponds to a 120 V smaller depletion voltage after a fluence of $2 \times 10^{14}\,\mathrm{cm}^{-2}$ for a 300 μm thick detector, this effect is subject to intense further investigations.

However, a further promising way to improve the radiation hardness with respect to neutron irradiations lies in the variation of the oxygen concentration and is manifested in the damage parameter N_{C0}. Looking at Eq. 5.8 it is obvious that N_{C0} can be interpreted as a *removable donor concentration*. Since $N_{eff,0}$ is the effective doping concentration measured before irradiation, $N_{C0}/N_{eff,0}$ displays the fraction of initial donor concentration that is removed after high fluences ($\Phi_{eq} > 1/c$, see Tab. 5.9). The corresponding data are displayed in Tab. 5.9 and plotted in Fig. 5.19 against the oxygen concentration of the materials. For most of the FZ samples the oxygen concentration lies below the detection limit of the performed SIMS measurements (see Tab. 4.1). Therefore a value of $[O_i] = 5 \times 10^{15}\,\mathrm{cm}^{-3}$ has been assumed as measured by IR on similar standard FZ silicon [ROS97]. Furthermore materials with resistivities higher than 5 kΩcm have been neglected in the figure since the amount of compensation between initial donors (P) and acceptors (B) is unknown. It can be seen that the removed fraction becomes smaller with increasing oxygen concentration. For material with interstitial oxygen concentration $[O_i] < 5 \times 10^{16}\,\mathrm{cm}^{-3}$ between 60% and 90%, for material with $[O_i] = 2 \times 10^{17}\,\mathrm{cm}^{-3}$ about 50% and for material with $[O_i] = 9 \times 10^{17}\,\mathrm{cm}^{-3}$

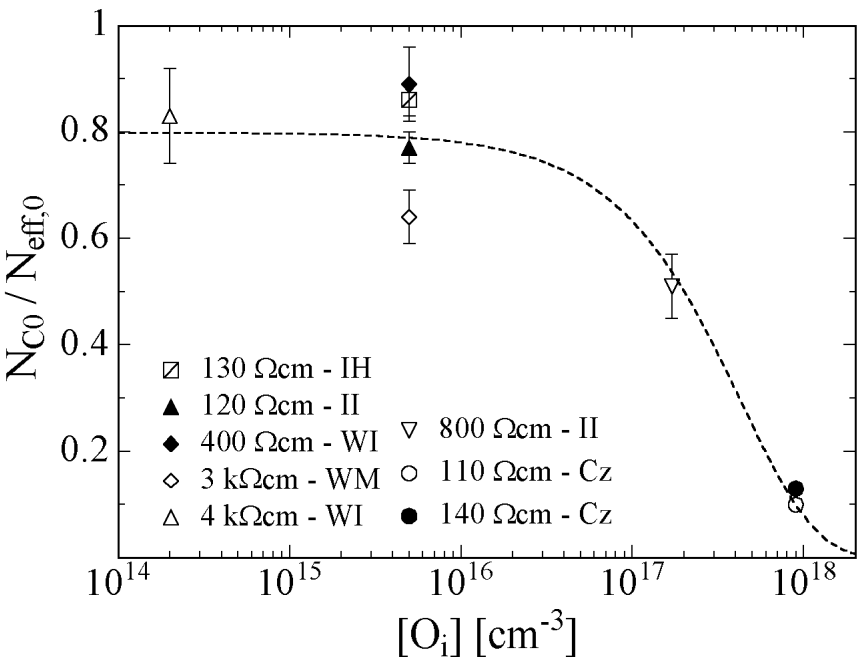

Figure 5.19: Fraction of initial effective doping concentration $N_{eff,0}$ that is removed after high fluences (see text). The dashed line is plotted only to guide the eye and corresponds to a exponential fit to the data points ($0.8 \times \exp(-[O_i]/(4.3 \times 10^{17}\,\mathrm{cm}^{-3}))$).

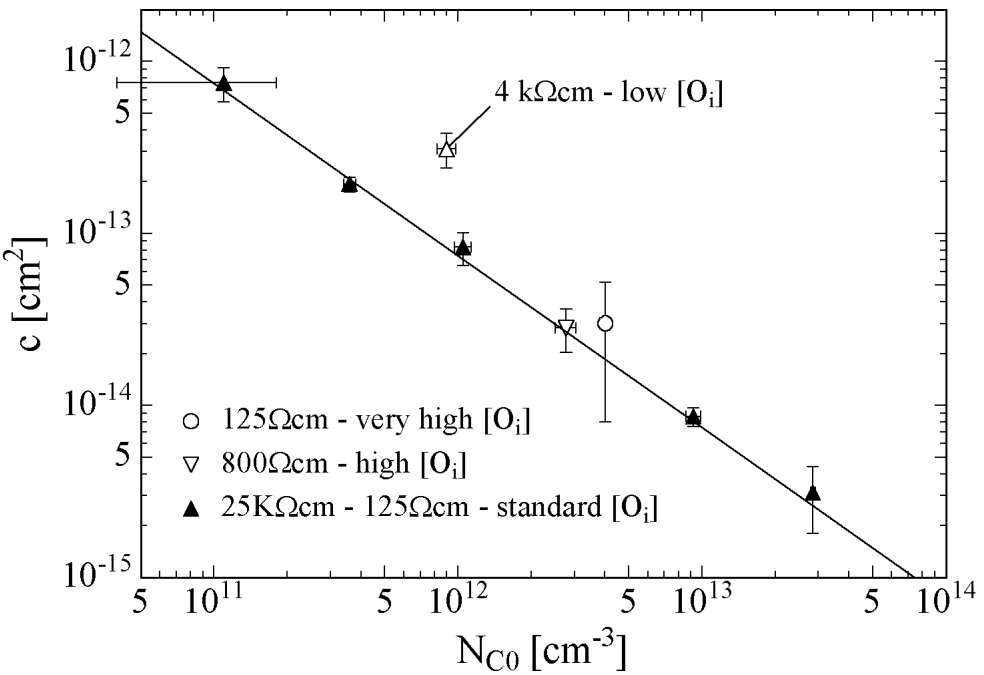

Figure 5.20: Donor removal constant c plotted versus removed donor concentration after high fluence irradiation $\Phi_{eq} > 1/c$ (N_{C0}). (A corresponding figure of c vs. $N_{eff,0}$ can be found on page 195.)

only about 10% of the initial doping concentration is removed after exposure to high fluences. The non removed fraction stays electrically active (positive space charge) in the material and compensates a fraction of the radiation induced negative space charge. The impact on the radiation hardness is easily clarified. For a 1 kΩcm starting material with a thickness of 300 μm the initial depletion voltage is about 300 V. Therefore after a high fluence (e.g. some $10^{14}\,\mathrm{cm}^{-2}$) the concentration of active donors in the highly oxygenated material is higher by about $0.7 \times N_{eff,0}$ than in the standard material corresponding to a 200 V lower depletion voltage.

In Fig. 5.20 the removal constant c is plotted versus the removable initial donor concentration N_{C0}. The experimental data clearly display the reciprocal dependence on the donor concentration, correspondingly $c \times N_{C0}$ is a constant (see Tab. 5.9). The weighted average of the data of the FZ material with the standard oxygen concentration (filled triangles) gives

$$N_{C0} \times c = (7.5 \pm 0.6) \times 10^{-2}\,\mathrm{cm}^{-1}.$$

This value has also a physical meaning. It denotes the *initial donor removal rate*[8] and will be discussed under special attention to the microscopic defect kinetics in Sec. 7.2.2. For completeness it is mentioned here that the weighted average of $N_{eff,0} \times c$ is given by

$$N_{eff,0} \times c = (10.9 \pm 0.8) \times 10^{-2}\,\mathrm{cm}^{-1}.$$

The corresponding data are presented in Fig. 7.2 on page 195.

5.3.5 Particle dependence

Detectors of type WE-25kΩcm ("*standard*" high resistivity FZ, see Tab. 4.1 on page 64) were irradiated with neutrons at the PTB Braunschweig (<5.2 MeV>) and at the reactor in Demokritos. Furthermore, identical samples were irradiated with 23 GeV protons at the CERN PS (see Sec. 4.2 for the irradiation facilities).
Subsequently all samples were exposed to an isothermal heat treatment at 60°C and measured in the same way as described in the previous sections. The obtained damage parameters g_Y and g_C are displayed in Tab. 5.10. As can be seen, no significant difference was observed. Therefore the parameters g_C and g_Y scale in the same way with the particle (hadron) fluence as the α value since this value has been used in Sec. 5.2 to calculate the individual hardness factors for the hadrons, respectively hadron fields. These findings are in agreement with the data presented in [Fei97a] where it has been shown that the ratio between the alpha value obtained after a long annealing time at room temperature (α_∞, see Sec. 5.1) and the damage parameter g_C, respectively g_Y, is almost the same for <5.2 MeV> neutrons (PTB), 23 GeV protons (CERN PS) and 236 MeV pions (PSI).

Therefore it is very astonishing that the ROSE collaboration has very recently pub-

[8]Not to be confused with the donor removal constant (c).

particle	facility	g_Y [cm^{-1}]	g_C [cm^{-1}]	max ϕ_{eq} [cm^{-2}]
<5.2 MeV> neutrons	PTB Be(d,n)	4.6±0.2	1.51±0.11	1.2×10^{14}
reactor neutrons	Demokritos	5.0±0.3	1.57±0.10	1.6×10^{14}
23 GeV protons	CERN PS	5.4±0.3	1.66±0.35	0.3×10^{14}

Table 5.10: Damage parameters g_Y and g_C obtained with samples of type WE-25kΩcm after proton and neutron irradiations. The hardness factors determined from the α value (see Tab. 5.4) were used for the calculation of the 1 MeV neutron equivalent fluence Φ_{eq}. The last column gives the maximum Φ_{eq} for the fit of the g_C parameter.

lished data showing that for oxygen rich materials the radiation induced changes in N_{eff} do not scale in the same way with the 1 MeV neutron equivalent fluence for neutrons and charged hadrons [ROS98a, Ruz99c]. Since such results might be misinterpreted as being in contradiction with the findings presented in this work they will be shortly discussed here.

In Fig. 5.21 the radiation induced changes in the depletion voltage as measured on *standard* and *oxygen enriched* FZ silicon after irradiation with 192 MeV pions (π^+), 23 GeV protons or reactor neutrons are compared to each other. The oxygen concentration in the oxygen rich samples was $\approx 2\times10^{17}\,\mathrm{cm}^{-3}$ while the concentration in the standard material was below the SIMS detection limit of $5\times10^{16}\,\mathrm{cm}^{-3}$ (for details see [Cas99, Ruz99c]). It has to be noted that the data were obtained in a different experimental procedure compared to the one used in this work. Only one sample is used which is irradiated in several steps. In between the irradiation steps the sample is heated for 4 min at 80°C in order to accelerate the short term annealing. Then the depletion voltage is measured and the sample is irradiated again. Hence, the abscissa in Fig. 5.21 gives the cumulated fluence[9].

The open symbols in Fig. 5.21 indicate the results for the standard FZ silicon. As expected from the results presented in this work[10], no difference is observed between the data obtained after pion, proton or neutron irradiation.

Compared to the standard silicon (open symbols) the oxygen enriched silicon (filled symbols) shows an improved radiation hardness after neutron as well as after charged hadron irradiation. However, the improvement after charged hadron irradiation is much more pronounced.

In this section the data for the neutron irradiated material will be compared to the data presented in this work, while the results obtained after charged hadron irradiation will be commented in Chapter 8 where a most recent experiment with a 23 GeV proton irradiated oxygen enriched FZ silicon will be presented.

[9] A heat treatment of 4 min at 80°C was chosen because after such an annealing ΔN_{eff} is almost in its minimum. The minimum is reached after about 6 min at 80°C or after about 60 min at 60°C (compare Fig. 5.9). For the reverse annealing a 4 min heat treatment at 80°C corresponds to an annealing period of about 21 days at 20°C (compare Tab. 5.8). Therefore, such an irradiation and annealing procedure could be interpreted as a rough simulation of the LHC operational scenario.

[10] It was shown for that the damage parameters g_C and g_Y scale with the NIEL for high energetic hadron irradiation of standard material, see Tab. 5.10.

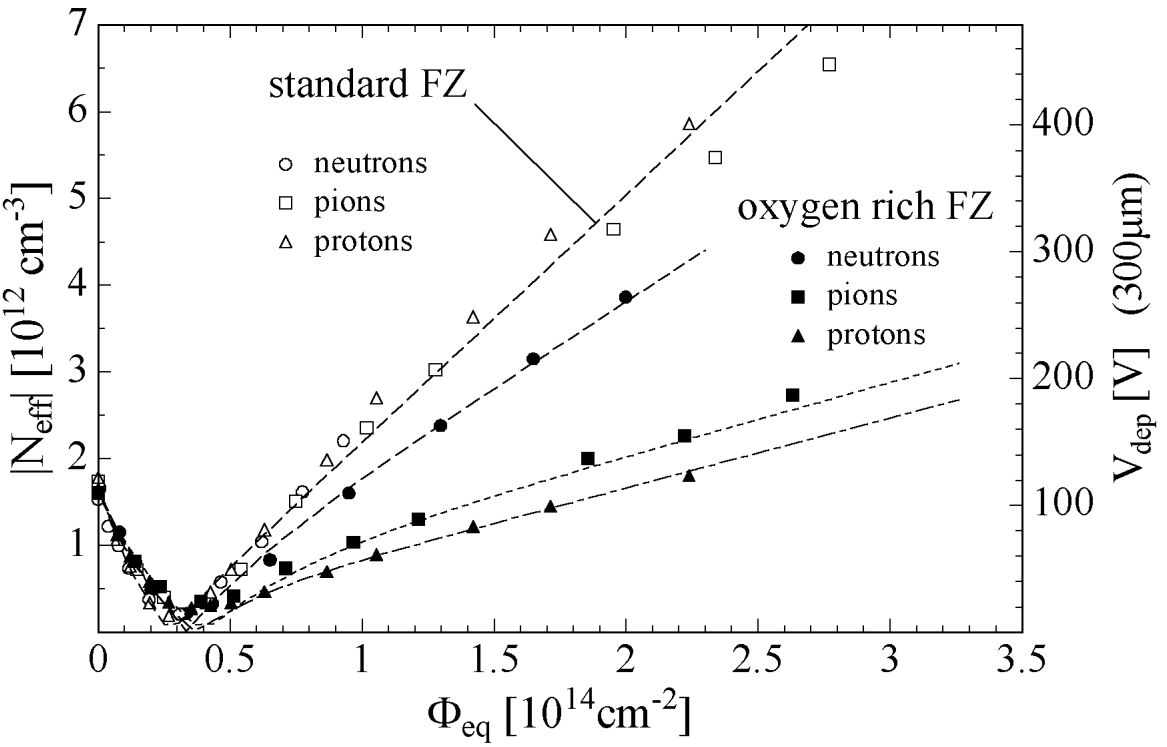

Figure 5.21: Dependence of N_{eff} on the accumulated 1 MeV neutron equivalent fluence Φ_{eq} for *standard* and *oxygen enriched* FZ silicon irradiated with reactor neutrons (Ljubljana), 23 GeV protons (CERN PS) and 192 MeV pions (PSI) (see text). The data were provided by A.Ruzin (CERN) and are published in [Ruz99c] and [Ruz99a].

Using the results described in Sec. 5.3.4 an improved radiation hardness of the oxygen enriched material ($[O] = 2 \times 10^{17}\,\mathrm{cm}^{-3}$) in the high fluence range by $\approx 0.3 \times N_{eff,0} \approx 5 \times 10^{11}\,\mathrm{cm}^{-3} \approx 35\mathrm{V}\,(300\,\mu\mathrm{m})$ is predicted (see Fig. 5.19). An improvement in the order of this value is also observed in Fig. 5.21 (compare open and filled circles). However, the improvement is not a constant value of 35 V as would be expected from the data shown in this work but does depend on the fluence i.e. the slope of the dashed lines in the figure is not the same. The depletion voltage of the device produced on standard material increases faster than the one of the device produced on the oxygenated material. In terms of the parameterization presented in this work this means that the g_c values are different for the two materials. However, in Sec. 5.3.4 it was shown that this parameter does not depend on the oxygen concentration (compare Tab. 5.9). Hence, the data published by the CERN group cannot be described in the framework of the parameterization presented in this work. A possible explanation could be that the different experimental methods – single exposure and isothermal heating in this work and subsequent irradiations with intermediate heating steps used by the CERN group – are leading to different experimental results. This, however, can only be investigated in further experiments.

Nevertheless a common conclusion can be drawn from the experimental data presented

in this work and the ones provided by the CERN group: Oxygen enriched silicon is radiation harder with respect to neutron damage than the up to now used standard silicon. However, a much more pronounced improvement is found after irradiations with charged hadrons. In Chapter 8 a first annealing experiment with 23 GeV proton irradiated diodes produced from oxygen enriched FZ silicon will be presented.

5.4 Charge collection efficiency

Although no investigations on the charge collection efficiency (CCE) have been performed in this work, it shall be shortly reviewed here that the loss in CCE is not the major radiation damage problem for silicon detectors used for tracking.

In addition to the formation of generation/recombination centers, being responsible for the increase of the leakage current and the creation of charged defects leading to the dramatic effects for the depletion voltage, damage induced defects can also act as trapping centers. The trapping would then affect the charge collection efficiency giving rise to an irradiation induced decrease of the signal height. However, for silicon detectors used for tracking this is not nearly as problematic as the other two deterioration causes, given that experimentally an operational voltage could be established which is high enough to guarantee a sufficiently high electric field throughout the detector thickness. The minimum voltage needed is of course the depletion voltage but it proves to be advisable to maintain some overbias, since otherwise the electric field would drop to zero at the end of the depleted zone. Measurements have been performed with minimum ionizing particles, e.g. using an appropriate β-source showing that even after an equivalent fluence of 10^{14}cm^{-2} the mip signal height had dropped only to 90% [Lem95, Bea98a]. Thus even for higher fluences the charge collection deficiency does not really establish any critical problem. Charge collection has also been the subject of more elaborate experiments in which the electron and hole contributions were measured separately using infrared ultrashort laser pulses incident on either side of the detector and thus allowing to observe the respective charge carrier drift by measuring the time resolved current with a Gigahertz digital oscilloscope [Fei97a, Ere96]. These investigations have led to a parameterized description of the electron and hole trapping as function of the equivalent fluence and with this knowledge the overall behavior of the charge collection in the case of mip's had been modeled [Fei97a]. It should be emphasized that these results describe the above mentioned experimental data obtained with minimum ionizing electrons extremely well. Finally, it should be noted that measurements have also be undertaken employing a monoenergetic alpha source. Also in this case the particle range is quite small compared to the detector thickness allowing the above described separate measurements for both charge carriers. In fact, this method was the first to show undoubtedly the type inversion of the original material, switching from n- to p-type at a given fluence (compare Sec. 5.3.1 and Fig. 5.8) [Wun91, Kra93].

Chapter 6

Microscopic Defects

The radiation induced changes of the *macroscopic* silicon detector properties – leakage current, effective doping concentration and charge collection efficiency – are caused by radiation induced electrical active *microscopic* defects. Therefore a more fundamental understanding of the *macroscopic* radiation damage, as described and parameterized in the previous chapter, can only be achieved by studying the *microscopic defects*, their reaction and annealing kinetics, and especially their relation to the macroscopic damage parameters. The results of such investigations can then be used to improve the radiation hardness of the silicon starting material by *defect engineering.* In other words: Based on the knowledge about the defect kinetics and the relation between the defects and the macroscopic parameters the defect kinetics has to be influenced in such a way that less *macroscopic damage* is produced. One possibility of *defect engineering* is the enrichment of the starting material with certain impurities leading to a reduced introduction of defects having a detrimental effect on the detector performance. As was shown in the previous chapter, the enrichment with oxygen leads to a reduced donor removal. This is most probably due to a suppressed formation of VP defects. In highly oxygenated material nearly all vacancies are gettered at the oxygen forming the VO defect which has no negative influence on the *macroscopic* detector properties in the temperature range of interest for HEP detector applications ($T > -20°C$). Another possibility of *defect engineering* is the controlled formation of defects having an influence on the space charge. The controlled introduction of a defect leading to positive space charge could be used to compensate the overall radiation induced negative space charge. Here one could also think of highly boron/phosphorus compensated starting materials in which the boron is removed faster than the phosphorus in order to compensate the radiation induced negative space charge (A first experiment with compensated material will be presented in Chapter 8).
However, all these approaches need a detailed understanding of the electrical active microscopic defects. Since already many defect studies have been performed on the field of high energetic hadron irradiated high resistivity silicon (e.g. [Bor94, Sch96a, Mac96a, Fei97a]) the data presented in this work are regarded as a further step on the way to a more profound understanding of the microscopic defects with the goal of a defect engineered radiation harder silicon.

This chapter starts with a systematic labelling of the defects (Sec. 6.1) which is necessary, since for many of the observed trap levels an assignment to a specific defect was not possible.

Subsequently (Sec. 6.2) it is shown that the defect concentrations obtained with the TSC and DLTS methods are in a good agreement with respect to the measurement of isolated point defects, while in the case of superimposed defect levels e.g. close to or inside of *clusters* the interpretation of the DLTS and TSC data is rather difficult.

The bistable behavior of the C_iC_s defect is used as a concrete example in Sec. 6.3 to demonstrate that the cooling and filling conditions for DLTS and TSC measurements have to be chosen very carefully in order to obtain reproducible data.

Furthermore it is shown in Sec. 6.4 that the capture cross sections can have a strong temperature dependence making it very difficult to extrapolate the defect properties to room temperature at which the macroscopic detector parameters are usually monitored. As an example the capture cross sections of the C_iO_i defect are investigated.

Sec. 6.5 deals with the field strength dependence of charge carrier emission time constants. As an example a thermal double donor is investigated in neutron irradiated CZ silicon.

In Sec. 6.6 DLTS measurements on a set of ^{60}Co-γ irradiated samples are presented and compared in the following section (Sec. 6.7) to measurements obtained on neutron irradiated samples of the same type.

Subsequently investigations on the annealing behavior of the defects at room temperature and during an isochronal annealing study are presented in Sec. 6.8 and Sec. 6.9, respectively.

The chapter closes with a study of the material dependence of the damage observed after neutron irradiation. Four different materials are investigated during isothermal heat treatments at 60°C (Sec. 6.10).

6.1 Labelling of defects

In this work the electrical properties of the defects have been determined with the DLTS and TSC methods (Secs. 4.4 and 4.5). Since these methods give no indication about the specific defect structure (e.g. chemical components) the assignment of defect levels to specific defects used in this work, as e.g. displayed in Tab. 6.1, is based on data published by other groups working with methods that are sensitive to the physical structure of the defects (for details see Appendix B and literature cited there). In cases where no assignment was possible the defects are labelled with an E or H for an electron or hole trap, respectively, followed by the DLTS peak-maximum temperature for the b_1-coefficient as recorded with a time window of $T_W = 200$ ms.
A list of radiation induced defects observed in this work on neutron or proton irradiated samples during annealing studies at room temperature is given in Tab. 6.1. The displayed capture cross sections correspond to the temperature given in the first column. For some of the defects both capture cross sections, for holes and electrons, have been

Label (DLTS)	$\Delta H'$ [eV]		$\sigma_{n,p}$ [cm^2]	Assignment	γ	Annealing at room temperature(21.5°C)	DLTS [K]	TSC [K]
E(35)	0.077		2.09×10^{-13}	–	–	$\uparrow\approx$ 7 h ; $\downarrow\approx$ 91 h	36	30
E(40)	0.079		1.68×10^{-14}	–	no	$\uparrow\approx$ 40 d	40	34
E(60a)	0.114		5.90×10^{-15}	$C_i^{(-/0)}$	–	$\downarrow\approx$ 80 h	59	49
E(60b)	0.110		3.00×10^{-15}	$C_iC_s^{(-/0)}$(B)	yes	$\uparrow\approx$ 60 h	58	48
E(85a)	0.176		1.44×10^{-14}	$VO_i^{(-/0)}$	yes	stable	84	70
E(85b)	0.171		1.44×10^{-14}	$C_iC_s^{(-/0)}$(A)	yes	$\uparrow\approx$ 60 h	83	70
E(120)	0.224		7.00×10^{-16}	$VV^{(=/-)}$	yes	increase $\uparrow\approx$ 36 d	119	100
E(170)	$\approx$ 0.36		$\approx 4 \times 10^{-15}$	–	no	$\downarrow\approx$ 29 d	169	(141)
E(205)	0.42		2×10^{-15}	$VV^{(-/0)}$+?	–	–	202	(168)
E(205a)	0.393		1.30×10^{-15}	–	no	stable	195	(158)
E(205b)	0.424		2.10×10^{-15}	$VV^{(-/0)}$	yes	stable	205	(167)
E(210)	0.456		5.02×10^{-15}	–	no	$\downarrow\approx$ 29 d	210	(174)
H(32)	0.071		3.22×10^{-11}	–	–	–	32	(25)
H(42)	0.084		5.26×10^{-14}	$C_iC_s^{(+/0)}$(A)	–	$\uparrow\approx$ 60h	42	(36)
H(50)	0.090		1.77×10^{-15}	–	–	$\downarrow\approx$ 31 d	(51)	42
H(74)	–		–	–	–	–	74	–
H(108)	0.200	σ_p	8.00×10^{-16}	$VV^{(+/0)}$	–	–	105	89
		σ_n	$> 8 \times 10^{-16}$					
H(140)	0.284	σ_p	4.28×10^{-15}	$C_i^{(+/0)}$	–	$\downarrow\approx$ 80h	141	116
		σ_n	1.11×10^{-15}					
H(180)	0.360	σ_p	2.45×10^{-15}	$C_iO_i^{(+/0)}$	yes	$\uparrow\approx$ 70h	179	147
		σ_n	(2.05×10^{-18})					
H(220)	0.480	σ_p	5.50×10^{-15}	measured in n-type material (γ = no)			221	(186)
		σ_n	$> 6 \times 10^{-16}$					
	0.532		2.92×10^{-14}	measured in p-type material			235	(193)

Table 6.1: Labelling of radiation induced electron and hole traps (Defects observed during annealing studies at room temperature). The given parameters have been measured in this work with the DLTS and/or TSC technique after neutron and/or proton irradiation (see text). The levels observed after ^{60}Co-γ irradiation are displayed in Tab. 6.9 and are indicated in the column labelled γ. A list of radiation induced defects reported in the literature can be found in Appendix B on page 219. The annealing time constants were obtained on a high resistivity FZ sample (see Sec. 6.8). Please note that the time constants for the carbon related defects strongly depend on the carbon and oxygen concentration (see Sec. 6.10).
Note that $\Delta H'$ is the Gibbs free energy and not the enthalpy ΔH (compare Sec. 3.4). Furthermore the capture cross sections were determined with temperature independent *density-of-states effective masses* as given in [Sze81] ($m^*_{dC} = 1.084\, m_0$ and $m^*_{dV} = 0.549\, m_0$, see comment in Sec. 3.4).

measured (Sec. 6.4). Furthermore it is noted that the hole capture cross sections of all given electron traps are expected to be larger than the electron capture cross sections in the temperature range covered by the DLTS method. This results from the fact that these levels are not visible in DLTS measurements after trap filling by forward biasing (see Sec. 4.4.1). From the fact that the hole traps C_i, C_iO_i and H(220) are visible after trap filling by forward biasing the same conclusion can be drawn. For these defects the hole capture cross section is larger than the electron capture cross section.

Levels detected after ^{60}Co-gamma irradiation are indicated in the column labelled γ by a "yes". Since the γ-irradiated samples were already annealed for a longer period at room temperature before the first DLTS measurement some of the levels could not be observed (e.g. the C_i levels were already annealed). Furthermore no experiments with hole injection from the back contact (see Sec. 6.3) were performed on the γ-irradiated n-type material. Thus also some of the hole traps could not be observed although they were expected to be present in the material (e.g. the $V_2^{(+/0)}$ level). In such cases no entry is given in Tab. 6.1.

The room temperature annealing time constants given in the table were obtained on a high resistivity FZ sample. It is noted here that the time constants for the carbon related defects are strongly depending on the carbon and oxygen concentration of the material (see Sec. 6.10).

The temperatures given in the last two columns are the peak maximum temperatures obtained for a DLTS measurement with a time window of 200 ms and a TSC measurement with a heating rate β of 0.183 K/s, respectively. Temperatures in brackets denote that the trap level was not observed with the corresponding measurement method (DLTS or TSC). In such cases the peak maximum temperature was calculated from the defect parameters obtained with the other method (If e.g. the level was only detected with the DLTS method the level parameters were used to calculate the expected peak maximum temperature for a TSC measurement and vice versa by using either Eq. 4.18 or Eq. 4.36).

An uncertainty in the level parameters observed for the deep hole trap H(220) could not be solved within this work. On the one hand investigations on n-type neutron irradiated material (WM2-3kΩcm, see e.g. Fig. 6.7) led to a level position at $E_V + 0.48\,\mathrm{eV}$ and a capture cross section of $\sigma_p = 5.5 \times 10^{-15}\,\mathrm{cm}^2$. On the other hand measurements on neutron irradiated p-type material (IDP-400Ωcm, see Tab. 4.1) led to a much deeper level position at $E_V + 0.53\,\mathrm{eV}$ and a capture cross section of $\sigma_p = 2.9 \times 10^{-14}\,\mathrm{cm}^2$. In Tab. 6.1 both values are given although it is believed that the signals arise from the same defect. After ^{60}Co-gamma irradiation this defect was not observed[1]. Since this level could play an important role for the macroscopic detector properties (see Chapter 7) it is suggested here to treat this defect with special interest in further experiments.

[1] In [Fre97] the authors report about a hole trap with $E_V + 0.54\,\mathrm{eV}$ observed after ^{60}Co-gamma irradiation. The introduction rate was measured to be $g_t = 3 \times 10^5\,\mathrm{cm}^{-3}\mathrm{Gy}^{-1}$ and is thus below the detection limit of the experiments performed within this work on ^{60}Co-gamma irradiated samples.

6.2 Accuracy of defect concentrations

In this section defect concentrations obtained on the same sample by different spectroscopic methods – DLTS (Deep Level Transient Spectroscopy), TSCap (Thermally Stimulated Capacitance) and TSC (Thermally Stimulated Current) – are compared with each other. It is shown that there is a good agreement in the determined defect concentrations between the different methods for isolated point defects while for defects with superimposed defect signals (e.g. located close to or inside of clusters) the obtained defect concentrations have to be treated with care. Furthermore, and especially for the TSC method, it is very important to suppress the lateral extension of the field zone by using a guard ring.
This section is divided into two parts. In the first part the experimental results are presented and discussed in very detail with respect to their systematic errors regarding more technical problems like the use of a guard ring and the data evaluation method. In the second part the results of the first part are briefly summarized, compared with each other and discussed with respect to systematic errors arising from the defect properties themselves. Therefore, readers with less interest in the technical problems may go directly to the second subsection.

6.2.1 Measurement results – DLTS, TSC, TSCap

The sample

The investigated sample of type WM3-3k (see Tabs. 2.2 and 4.1) was irradiated with fast neutrons ($\phi_{eq} = 2.77 \times 10^{11}\,\mathrm{cm}^{-2}$) at the PTB (see Sec. 4.2). After irradiation and before the measurements presented here the sample was annealed for 10200 min at 60°C. It has to be mentioned that the defect concentration was almost too high for a DLTS measurement since with $N_{eff,0} = 1.6 \times 10^{12}\,\mathrm{cm}^{-3}$ and $N_t \approx 8 \times 10^{11}\,\mathrm{cm}^{-3}$ (all electron traps) the DLTS condition $N_t/N_{eff,0} \ll 1$ (compare Sec. 4.4.2) was not fulfilled. Thus the DLTS results are afflicted with a higher error than usual. However, this neutron fluence (defect concentration) was chosen since it offered the possibility of a high resolution TSC measurement and thus enabled the comparison between a current based (TSC) and capacitance based (DLTS, TSCap) methods on a high resistivity neutron irradiated sample.

DLTS - Deep Level Transient Spectroscopy

Fig. 6.1 shows DLTS spectra obtained without (solid line) and with (squares) connected guard ring. The front electrode was set to low potential and the guardring was connected to ground. In the following the two conditions of the guard ring will be called *floating* and *connected*. While no difference is seen between the spectra with floating and connected guard ring the reverse capacitance C_R shows a significant difference due to the different lateral extensions of the field zone. Consequently also the active area of the device differs. Since the active area of the detector is used for the calculation of the effective doping concentration (Eq. 4.6) and the effective doping concentration is used

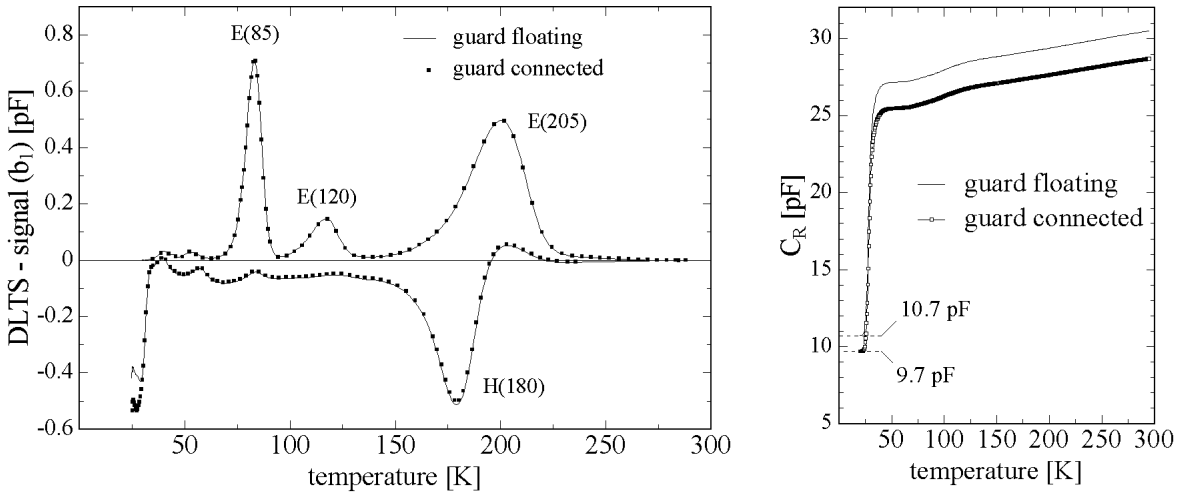

Figure 6.1: Left: DLTS spectra obtained with floating and grounded guard ring. The number of data points for the measurement with grounded guard ring was reduced for better visibility. Right: Corresponding capacitance at $U_R = 10V$. (Sample: M3D103 of type WM3-3k; $\phi_{eq} = 2.77 \times 10^{11}\,\mathrm{cm}^{-2}$; after 10200 min at 60°C; $T_W = 200\,\mathrm{ms}$; $t_p = 100/1\,\mathrm{ms}$; $U_R = 10\,\mathrm{V}$; U_P= 0/-3 V.)

for the calculation of the defect concentration (Eq. 4.9) this difference has a strong impact on the determined defect concentration. The active area of the detector can be calculated from the *geometrical capacitance* C_{geo} (see Eq. 2.10 on page 24) which can either be obtained by measuring the capacitance for voltages higher than the depletion voltage, or – as shown on the right hand side of Fig. 6.1 – also for smaller voltages after the free carrier freeze out at deep temperatures. The corresponding values are displayed in Tab. 6.2. The first column gives the *geometrical capacitance* as calculated from the assumed active areas. In the case of a connected guard ring the active area is expected to be the implanted pad area plus half of the area between the guard and the pad. In the case of a floating guard ring the active area is assumed to be bigger. Here a value determined with a proton micro beam on a very similar structure was used (for details see [Wun96]). The second and third columns in the table give the active areas as calculated from the measured *geometrical capacitances*. As can be seen there are drastic differences between the active areas of a device with floating and connected guard ring. This has to be taken into account in order to calculate the defect concentration with a high accuracy. Tab. 6.3 displays the calculated defect concentrations under various conditions. The first column gives the defect concentration obtained with a connected guard ring and an assumed active area of 0.25 cm^2. For comparison also the defect concentration N_t^* (Eq. 4.10) is given which is obtained if the depletion width during the filling process (W_P) and the transition region λ are neglected (for details see Sec. 4.4). The second column gives the defect concentrations that are obtained if the lateral extension of the field zone is not taken into account and finally the last column shows the data that one gets if the lateral extension of the field zone is taken

			a) $C_{geo}(T <$ freeze out)		b) $C_{geo}(V > V_{dep})$	
guard ring	area measured	C_{geo} calculated	C_{geo} measured	area(C_{geo}) calculated	C_{geo} measured	area(C_{geo}) calculated
connected	$0.251\,\mathrm{cm}^2$	9.4 pF	9.7 pF	$0.259\,\mathrm{cm}^2$	9.8 pF	$0.261\,\mathrm{cm}^2$
floating	$\approx 0.275\,\mathrm{cm}^2$	10.3 pF	10.7 pF	$0.285\,\mathrm{cm}^2$	11.0 pF	$0.293\,\mathrm{cm}^2$

Table 6.2: First column: *Geometrical capacitance* C_{geo} (Eq. 2.10) calculated from the front contact area (connected) and from an active area assumed for the case of a floating guard ring (floating). Second column: Active area calculated from the capacitance measured below the free carrier freeze out temperature (compare Fig. 6.1). Third column: Active area calculated from the capacitance measured at room temperature for $V > V_{dep}$ (The thickness of the device is 281 μm).

	guard connected ($A = 0.25\,\mathrm{cm}^2$)		floating - as measured ($A = 0.25\,\mathrm{cm}^2$)	floating - corrected ($A = 0.275\,\mathrm{cm}^2$)
defect level	N_t $[10^{11}\,\mathrm{cm}^{-3}]$	N_t^* $[10^{11}\,\mathrm{cm}^{-3}]$	N_t $[10^{11}\,\mathrm{cm}^{-3}]$	N_t $[10^{11}\,\mathrm{cm}^{-3}]$
E(85)	2.88 ± 0.35	(2.34 ± 0.28)	3.21 ± 0.48	2.84 ± 0.48
E(120)	0.59 ± 0.06	(0.47 ± 0.04)	0.65 ± 0.06	0.58 ± 0.06
E(205)	2.93 ± 0.15	(2.30 ± 0.12)	3.26 ± 0.20	2.85 ± 0.17

Table 6.3: Defect concentrations as determined from the DLTS spectra shown in Fig. 6.1 for measurements with and without connected guard ring (see text for details).

into account by using an active area of 0.275 cm^2.
As can be seen from the data, a good agreement between the data measured with and without connected guard ring is achieved if the active area is known. However, the lateral extension of the electric field zone is depending on the structure and the resistivity of the used device and is usually not known. Since in many experiments the lateral extension of the field zone is not taken into account the defect concentrations are often overestimated. In this example (5×5 mm^2 area device) the systematic error for not taking into account the lateral field extension would have been about 15%. However, for smaller devices the error can easily become bigger.

TSC - Thermally Stimulated Current

Fig. 6.2 a) shows TSC spectra obtained with connected (left) and floating (right) guard ring obtained on the same sample as used before for the DLTS measurements. The sample was cooled to deep temperatures under zero bias in order to allow majority carrier capture of the traps during the cooling. Since the shallow dopant (phosphorus) concentration is higher than the concentration of the electron traps all electron traps are occupied with this filling method. The heating was performed with various voltages. In Fig. 6.2 a) and b) the emitted charge Q_t, respectively the current at peak

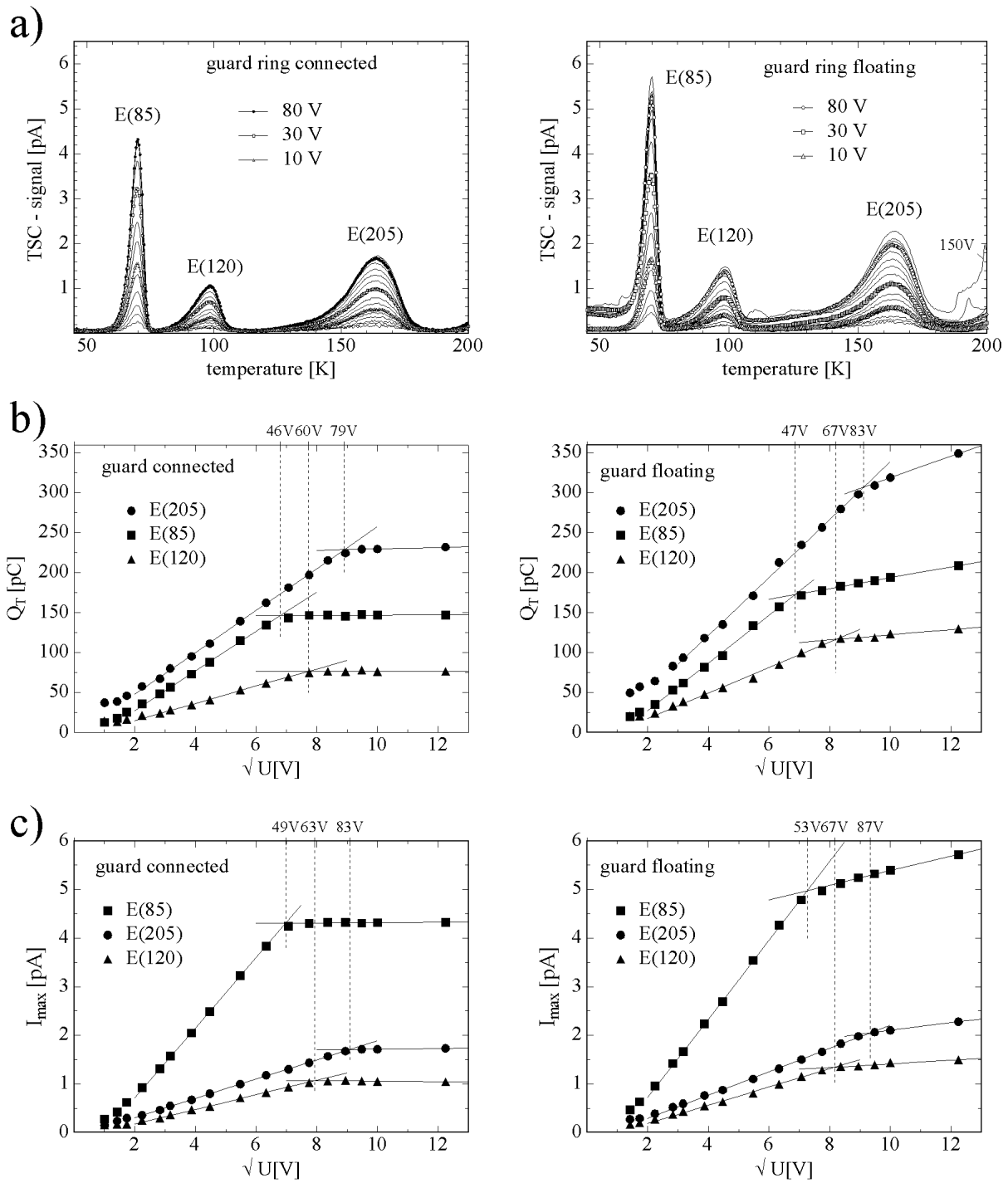

Figure 6.2: Determination of defect concentrations with TSC measurements. The sample was cooled with no bias applied. Therefore only electron traps are observed (see text). (Sample: M3D103; $\phi_{eq} = 2.77 \times 10^{11}\,\mathrm{cm}^{-2}$; after 10200 min at 60°C)

a) TSC-spectra obtained with connected (left) and floating (right) guard ring for different applied voltages U (1-150 V) during the heating.

b) Integrated charge for the three observed peaks plotted against $\sqrt{U}$.

c) Peak heights for the three observed peaks plotted against $\sqrt{U}$.

	guard connected ($A = 0.25\,\mathrm{cm}^2$)		guard floating ($A = 0.275\,\mathrm{cm}^2$)	
method	integration	peak maximum	integration	peak maximum
defect level	N_t $[10^{11}\,\mathrm{cm}^{-3}]$	N_t $[10^{11}\,\mathrm{cm}^{-3}]$	N_t $[10^{11}\,\mathrm{cm}^{-3}]$	N_t $[10^{11}\,\mathrm{cm}^{-3}]$
E(85)	2.60 ± 0.07	2.60 ± 0.07	2.78 ± 0.17	2.72 ± 0.17
E(120)	1.37 ± 0.04	0.99 ± 0.03	1.88 ± 0.11	1.14 ± 0.07
E(205)	4.06 ± 0.11	2.32 ± 0.07	4.96 ± 0.29	2.61 ± 0.16

Table 6.4: Defect concentrations as determined from the TSC spectra shown in Fig. 6.2 for measurements with and without connected guard ring (see text for details).

maximum I_{max}, are plotted versus the square root of the applied voltage. As can be seen for both parameters (Q_t and I_{max}) the measurements with connected guard ring result in much more pronounced kinks in the data curves indicating the voltage of full depletion. Additionally, after the full depletion of the device is reached, no further increase in signal is observed with connected guard ring while with floating guard the signal further increases due to the lateral extension of the field zone. Consequently the data obtained with connected guard ring are regarded as far more reliable than the ones obtained without connected guard ring.
The defect concentrations determined from the peak maxima (Eq. 4.35) and the integrated charge (Eq. 4.34) are given in Tab. 6.4. As theoretically expected, there is no difference between the defect concentrations determined from the peak maximum and the integrated charge for the defect E(85) (superposition of VO_i and C_iC_s(A)). However, for the other peaks (E(120) and E(205)) the defect concentrations determined by the two methods differ strongly. As will be discussed in the next section the reason for this difference is based on the defect properties and not on problems arising from the measurement technique.

TSCap - Thermally Stimulated Capacitance

The third method used to determine the defect concentration was Thermally Stimulated Capacitance (TSCap). In Fig. 6.3 the TSCap spectra obtained with and without connected guard ring are shown. The differences between the measurements with and without connected guard ring are once again due to the different lateral extension of the field zone. Thus, in the following only the data with the connected guard ring will be discussed.
The solid lines show measurements without any filling step. The capacitance was measured at a voltage of 10 V during cooling and heating of the sample. Since no defects are filled in the space charge region during the cooling process under reverse bias no difference is observed between the data obtained during cooling and heating. The triangles indicate the data obtained during the heating with a bias of 10 V after the sample was cooled down with zero bias. Starting from the low temperature the first step in

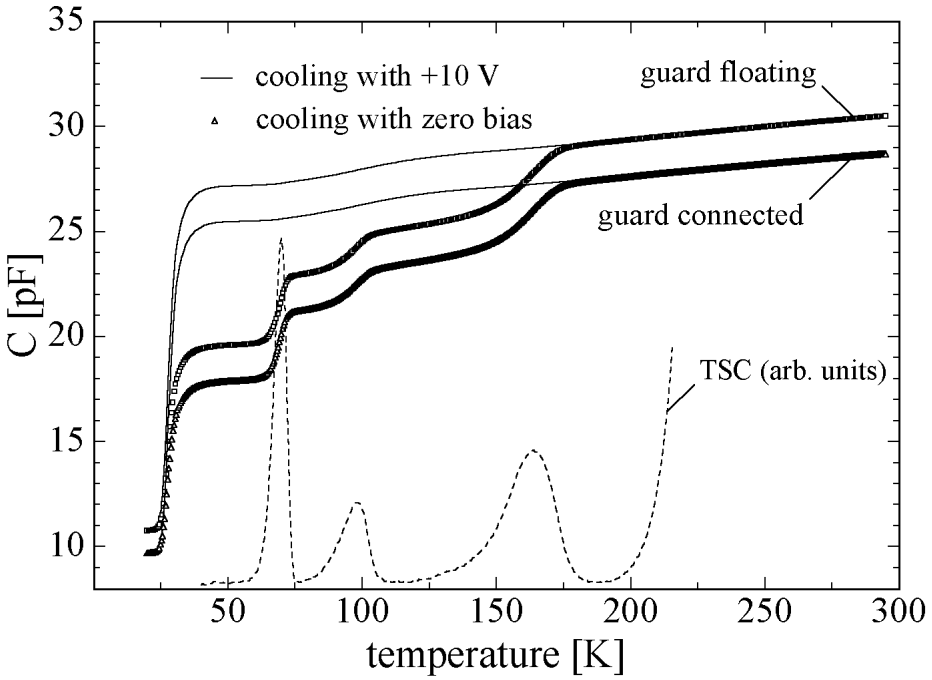

Figure 6.3: TSCap measurements with floating and connected guard ring. The TSC measurement was achieved with the same heating rate (see Fig. 6.3). (Sample: M3D103; $\phi_{eq} = 2.77 \times 10^{11}\,\mathrm{cm}^{-2}$; after 10200 min at 60°C; $U_R = 10\,\mathrm{V}$; $\beta = 0.183$ K/s; 1 MHz.)

the capacitance curve at about 25 K indicates the *freeze out* of the shallow dopants[2] (phosphorus). For temperatures above 25 K the phosphorus atoms are ionized. However, due to the trapped electrons in the defects E(85), E(120) and E(205) a part of the positive space charge due to the phosphorus atoms is compensated by the negative charge of the trapped electrons. Thus the effective space charge is smaller than the effective doping concentration measured at room temperature. Consequently the depth of the depleted zone is bigger and the observed capacitance value is smaller. At about 70 K a further step is observed in the TSCap data. At this temperature the electrons from the defect level E(80) (assigned to a superposition of $VO_i^{(-/0)}$ and $C_iC_s^{(-/0)}(A)$) are emitted (detrapped) which is very well seen by the corresponding TSC spectrum (dashed line) obtained with the same heating rate. Further steps are observed for the levels E(105) and E(205). The resulting defect concentrations are displayed in Tab. 6.5 and will be discussed in the next section.

defect level	N_t $[10^{11}\,\mathrm{cm}^{-3}]$
E(85)	3.21 ± 0.48
E(120)	1.51 ± 0.12
E(205)	3.94 ± 0.23

Table 6.5: Defect concentrations as determined from the TSCap measurement shown in Fig. 6.3 with connected guard ring (see text for details).

[2]In the present case the *carrier freeze out* corresponds to the temperature at which the free carriers induced by the shallow dopants can no longer respond to the 1 MHz signal of the capacitance bridge.

measurement	current		capacitance	
method	TSC peak maximum	TSC integration	DLTS "peak maximum"	TSCap "integration"
defect level	N_t $[10^{11}\,\mathrm{cm}^{-3}]$	N_t $[10^{11}\,\mathrm{cm}^{-3}]$	N_t $[10^{11}\,\mathrm{cm}^{-3}]$	N_t $[10^{11}\,\mathrm{cm}^{-3}]$
E(85)	2.60 ± 0.07	2.60 ± 0.07	2.88 ± 0.35	3.21 ± 0.48
E(120)	0.99 ± 0.03	1.37 ± 0.04	0.59 ± 0.11	1.51 ± 0.12
E(205)	2.32 ± 0.07	4.06 ± 0.11	2.93 ± 0.29	3.94 ± 0.23

Table 6.6: Defect concentrations as determined with the TSC, DLTS and TSCap method with connected guard ring.

6.2.2 Comparison – DLTS, TSC, TSCap

The measurements presented in the last section revealed that a high accuracy in the determined defect concentration can only be achieved if the lateral extension of the field zone (the active area of the device) is known. The lateral extension is best controlled by using a guard ring which limits the active area of the device to the pad area. Tab. 6.6 summarizes the defect concentrations obtained with the DLTS, TSC and TSCap methods on the same sample (see last section) with connected guard ring. Since the TSC method is based on the measurement of current and the DLTS and TSCap methods are based on the measurement of capacitance, they can be regarded as independent measurement techniques. Thus the comparison gives an indication for the accuracy of the estimated defect concentrations. With these measurements a long lasting controversy within the ROSE collaboration between the Brunel University group and the Hamburg University group about defect introduction rates (the Brunel data were higher by a factor of 4 [Wat95, Wat96, Mol97]) were solved in the favor of the data published by the Hamburg group. Meanwhile the Brunel group has revised their introduction rates to values close to the ones obtained in this work [Wat98].

Looking at the data presented in Tab. 6.6 it becomes obvious that for the defect E(85) (point defect, close superposition of VO_i and C_iC_s(A), see Tab. 6.1) the defect concentrations determined with the different techniques are in good agreement within the given errors while for the two other peaks E(120) and E(205) discrepancies arise between the different methods. This can be understood if one takes into account that the defects giving rise to the peaks E(120) and E(205) are no isolated point defects. The observed defects seem to be a superposition of different defects leading to the observation of the broad peaks at 120 and 205 K. Therefore the evaluation methods using the peak maxima for the determination of the defect concentration (DLTS or I_{max} for TSC) lead to wrong results since they are only valid for single defect levels.
However, using the evaluation methods basing on the measurement of the total change in the effective doping concentration leads to far better results. Integrating the current over one peak in the TSC spectrum leads to the total amount of emitted charge Q_t. A corresponding result is obtained with the TSCap method. Here the total change in the effective doping concentration is monitored by the change in the reverse capacitance. In

other words, these two methods give the exact concentration of charge carriers stored in the defects and , if all defects are occupied at the beginning of the measurement, also the exact defect concentration.

In many experiments it is tried to count the overall number of vacancy and interstitial related defects generated after irradiation [Mac96a, Mol97]. In this section it has been demonstrated that the defect concentrations obtained with the DLTS method have to be treated with care in the case of superimposed defect levels as e.g. observed after irradiation with fast hadrons or after ion implantation.

6.3 Cooling and filling conditions (C_iC_s and VO_i)

In this section it will be demonstrated that the cooling condition (with or without applied reverse bias) and the duration of the filling pulse have a strong influence on the obtained spectrum. Furthermore it will be shown how a variation of the filling pulse duration can be used to separate the signals arising from the C_iC_s(A) and the VO_i at the same peak maximum temperature by making use of the bistability of the C_iC_s defect described already in Sec. 3.6.

In Fig. 6.4 four DLTS spectra obtained on the same sample with different cooling and filling conditions are shown. Either 0 V or -15 V reverse bias was applied during the cooling of the sample and either a short filling pulse of 100 μs duration or a long filling pulse of 100 ms duration was used. In the displayed temperature range 3 peaks are observed. At about 50 K a peak assigned to the C_iC_s in configuration B, at about 75 K a peak assigned to the superposition of the VO_i and the C_iC_s in configuration A and finally at about 110 K a peak attributed to the $VV^{(=/-)}$. As later on will be shown the changes in the peak heights of the peak at 75 K are solely due to the C_iC_s (A) while the signal arising from the VO_i is the same in all 4 shown spectra.

Only the peak at 50 K (C_iC_s (B)) is influenced by the different cooling conditions (with or without applied bias). This effect is due to the bistability of the C_iC_s defect. If the defect is occupied with an electron configuration A is the most stable one while for the neutral charge state configuration B is preferred (compare configurational coordinate diagram for the C_iC_s on page 56 (Fig. 3.9)). Thus, cooling the sample under zero bias (defect in negative charge state) to deep temperatures (e.g. 40 K) results in configuration A and no signal is observed at 50 K. However, cooling under reverse bias (defect in neutral charge state) results in configuration B at deep temperatures. Now the defect can be filled with electrons and the emission of the electrons gives rise to the signal at 50 K. At such low temperatures the activation energy for the configurational change from B to A cannot be overcome within the duration of the filling pulse.

The filling pulse duration has a strong influence on the peak heights of the signals corresponding to the $VV^{(=/-)}$ and the C_iC_s (A) levels. Independent of the cooling condition (with or without applied bias) the peaks are observed with the long filling pulse while with the short pulse no signal is observed. For the $VV^{(=/-)}$ this effect is explained by the very small electron capture cross section of the defect (compare

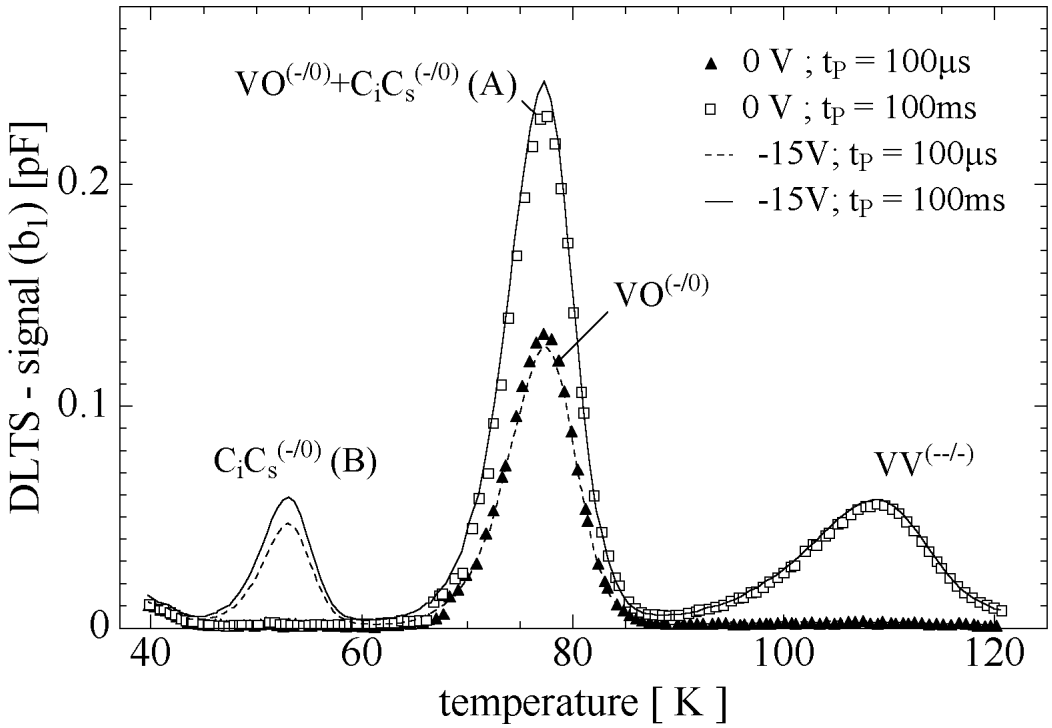

Figure 6.4: DLTS spectra obtained with different cooling and filling conditions (see text). Note that the time window was $T_W = 2$ s and not 200 ms as for most of the spectra shown in this work. Sample: n-type, WM2-3kΩcm, neutron irradiated (UKE) $\Phi_{eq} = 9.7 \times 10^{10}\,\mathrm{cm}^{-2}$, U_R = -10 V, $U_P = 0$ V.

Tab. 6.1). The filling time of 100 μs is not sufficient to fill the trap. However, for the C_iC_s (A) the observed dependence on the filling time is not due to a small capture cross section but due to the fact that an activation energy is needed for the configurational change of the defect from state B to state A in order to get a signal at 75 K. Under reverse bias the C_iC_s is not occupied with an electron and configuration B is the most stable one. During the filling pulse the defect captures an electron and is still in configuration B. Now, occupied with an electron, the most stable configuration is A. For the configurational change from state B to A an activation energy has to be overcome. This is demonstrated in Fig. 6.5. Here the DLTS peak height is plotted versus the filling time for various temperatures. Since the emission time constant is strongly temperature dependent different time windows had to be chosen for different temperatures. Most of the data where obtained on a low resistivity sample (6 Ωcm). Already with a filling pulse of 10 μs 70% of the peak heights are observed. This signal is due to the VO_i defect. With increasing filling time also the signal arising from the C_iC_s (A) is observed coming finally up for 30% of the overall signal. With increasing

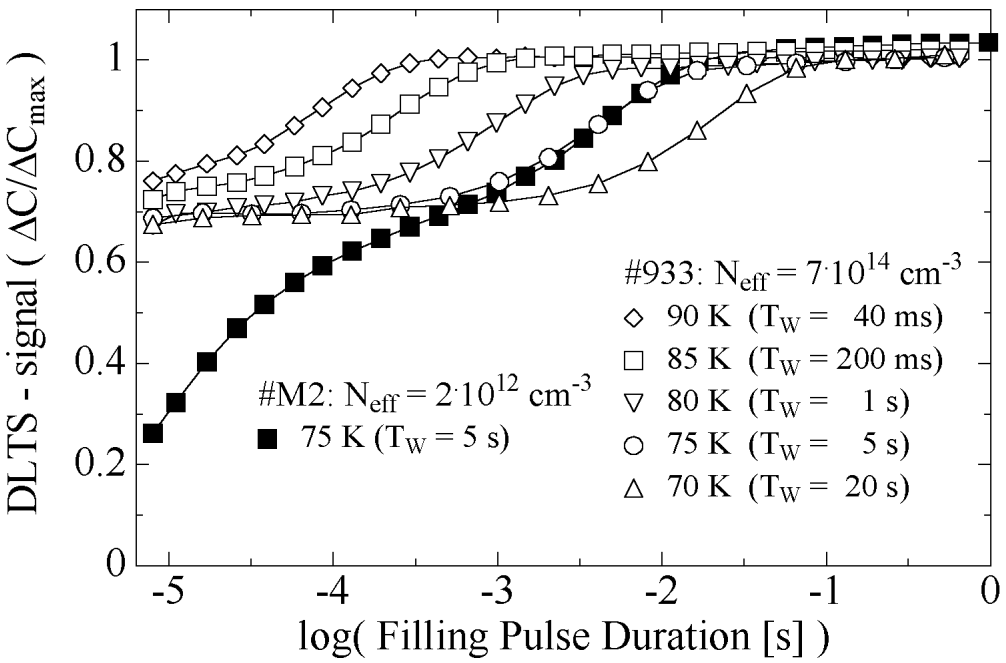

Figure 6.5: Peak height of the DLTS signal corresponding to the superposition of the VO_i and $C_iC_s(A)$ levels in dependence of filling pulse duration and temperature (T_W indicates the time window, see text). The signals are normalized to the saturation values obtained after very long filling times. Samples: a) # 933, WH-6Ωcm, neutron irradiated (PTB) $\Phi_{eq} = 8 \times 10^{12}\,\mathrm{cm}^{-2}$, b) # M2, WM2-3kΩcm, neutron irradiated (UKE) $\Phi_{eq} = 9.7 \times 10^{10}\,\mathrm{cm}^{-2}$; Measurement: U_R = -10 V, U_P = 0 V.

temperature the saturation of the DLTS signal is shifted to shorter filling times. The comparison with the data obtained for a high resistivity (3 kΩcm) sample clearly reveals that the observed effect is not due to a temperature dependent capture cross section. For this sample two steps in the data curve are observed. The first one is due to the electron capture of the VO_i defect. Since the carrier concentration in the high resistivity sample is by about a factor 500 smaller than in the low resistivity sample the filling times are expected to be 500 times longer. The calculated capture time constant for the VO_i defect in the high resistivity sample is $\tau_c = 7\ \mu$s ($1/\tau_c = n\sigma_n v_{th}$, σ_n from Tab. 6.1) and thus in a good agreement with the observed data. However, the second step in the DLTS signal occurs at exactly the same filling time as for the low resistivity material. Therefore this increase in the signal is independent of the free carrier concentration and hence not related to a capture process.

In Fig. 6.6 the extracted time constants for the configurational change C_iC_s(B) $\rightarrow$ C_iC_s (A) have been used to establish an Arrhenius plot. The corresponding activation

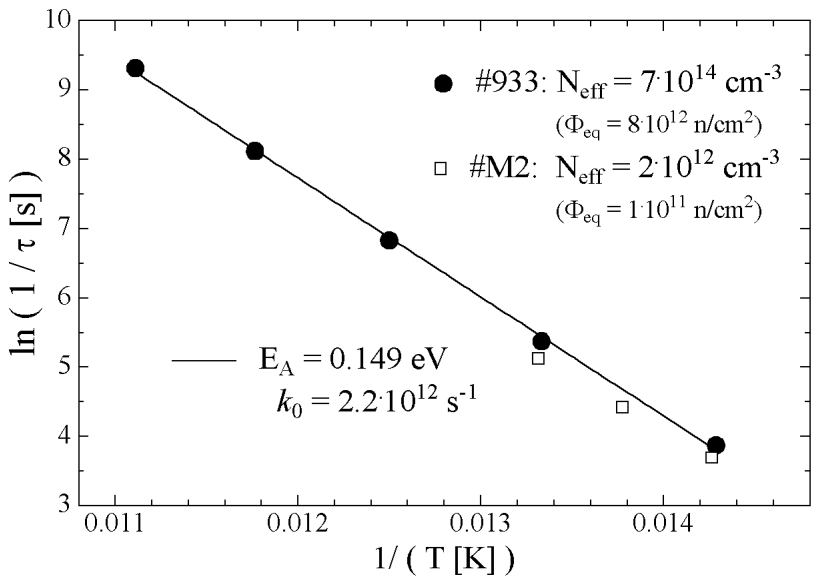

Figure 6.6: Arrhenius Plot for the conversion $C_iC_s^{(-)}(\mathrm{B}) \rightarrow C_iC_s^{(-)}(\mathrm{A})$.

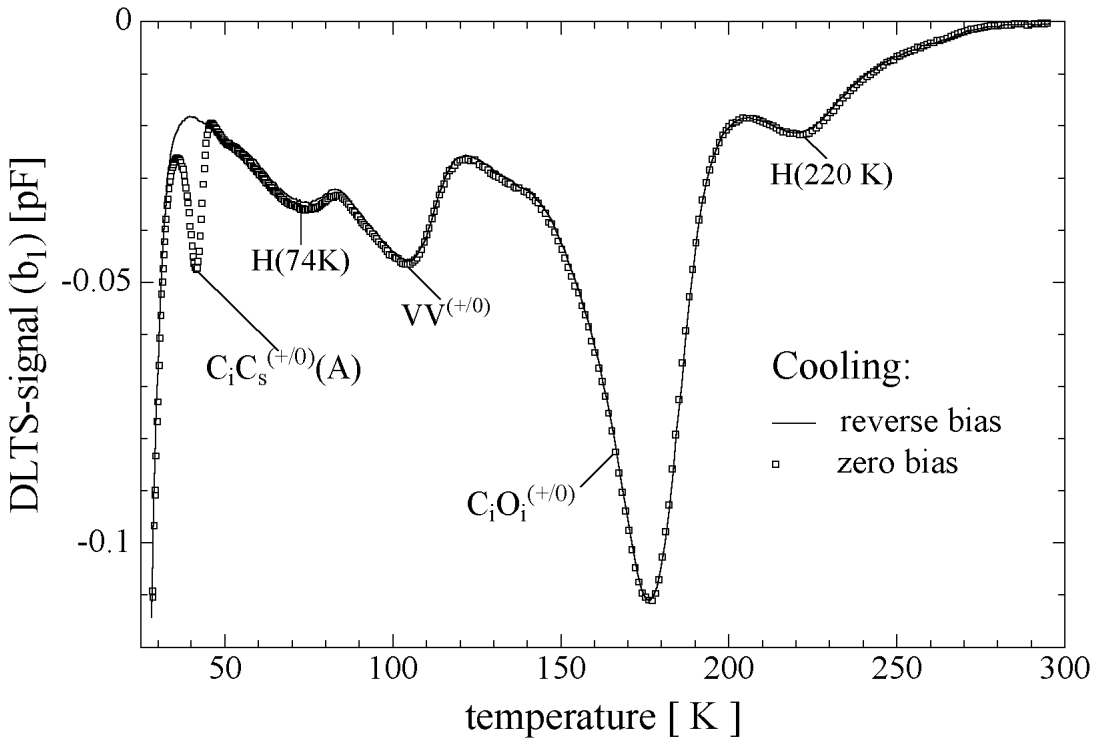

Figure 6.7: Bistability of the C_iC_s(A) donor level. Minority carrier spectrum in n-type material obtained after cooling down to 25 K with and without applied reverse bias. The DLTS spectra were obtained by minority carrier injection from the back side of the diode (laser illumination of rear side under reverse bias, 670 nm). Sample: n-type, WM2-3kΩcm, neutron irradiated (UKE) $\Phi_{eq} = 2 \times 10^{11}\,\mathrm{cm}^{-2}$, U_R = -10 V, U_P = -10 V + laser illumination, T_W = 200 ms.

Author	Method	Transition: $C_iC_s^{(-)}(\mathrm{B}) \longrightarrow C_iC_s^{(-)}(\mathrm{A})$	Ref.
this work	DLTS	$\tau = 4.5 \times 10^{-13}\mathrm{s} \cdot \exp(0.149\mathrm{eV}/k_BT)$	
Jellison 1982	DLTS	$\tau = 7.3 \times 10^{-13}\mathrm{s} \cdot \exp(0.145eV/k_BT)$	[Jel82]
Song et al. 1990	EPR	$\tau = 6.4 \times 10^{-13}\mathrm{s} \cdot \exp(0.15\mathrm{eV}/k_BT)$	[Son90b]

Table 6.7: Time constant for the transition $C_iC_s^{(-)}(\mathrm{B}) \longrightarrow C_iC_s^{(-)}(\mathrm{A})$.

energy and the frequency factor are given in the figure and are compared in Tab. 6.7 to data found in the literature. The agreement is very good.

The bistability of the C_iC_s in n-type material can also be observed on the C_iC_s donor level. This is displayed in Fig. 6.7. The shown spectra were obtained after cooling the sample down with zero bias (C_iC_s frozen in configuration A) or under reverse bias (C_iC_s frozen in configuration B) to 25 K. For the measurement a reverse bias of -10 V was applied and minority carriers were injected with a red laser (670 nm) from the rear side of the diode in order to fill only hole traps. As can be seen a signal arising from the $C_iC_s^{(+/0)}(A)$ is only observed if the sample was cooled down under zero bias. The C_iC_s(B) donor level is expected to be located at about 0.05 eV above the valence band [Son90b]. Thus it could not be observed with capacitance based DLTS within this experiment. Furthermore, the signal of the C_iC_s (A) was not observed after cooling down under zero bias if the diode was additionally switched to forward bias for a short period at low temperatures. An injection of 10 mA for 1 min at 23 K was sufficient to convert the C_iC_s(A) into configuration B. Therefore, it can be assumed from this experiment that also an recombination enhanced configurational change of the defect from state A to state B is possible.

Finally it should be mentioned that the filling pulse dependence as displayed in Fig. 6.6 was used in this work to separate the superimposed signals of the C_iC_s (A) and VO_i in order to determine the individual concentrations of these defects. In the presented example 70% of the signal is due to the VO_i and 30% due to the C_iC_s.

6.4 Capture cross sections of the C_iO_i

In order to calculate the impact of certain defects on the detector performance a complete characterization of the electrical defect properties is needed. Most often with DLTS or TSC only the activation energy $\Delta H'$ and the cross section of the defect level as calculated from an Arrhenius plot of the emission time constant are determined. However, for a full electrical characterization the capture cross sections for holes and electrons, the entropy factor X and the enthalpy ΔH are needed (Sec. 3.4). Due to the lack of such experimental data very often assumptions about the missing parameters have to be made which might not be true. Usually the entropy factor is set to 1 and the value of the missing carrier cross section is set to the value of the measured one

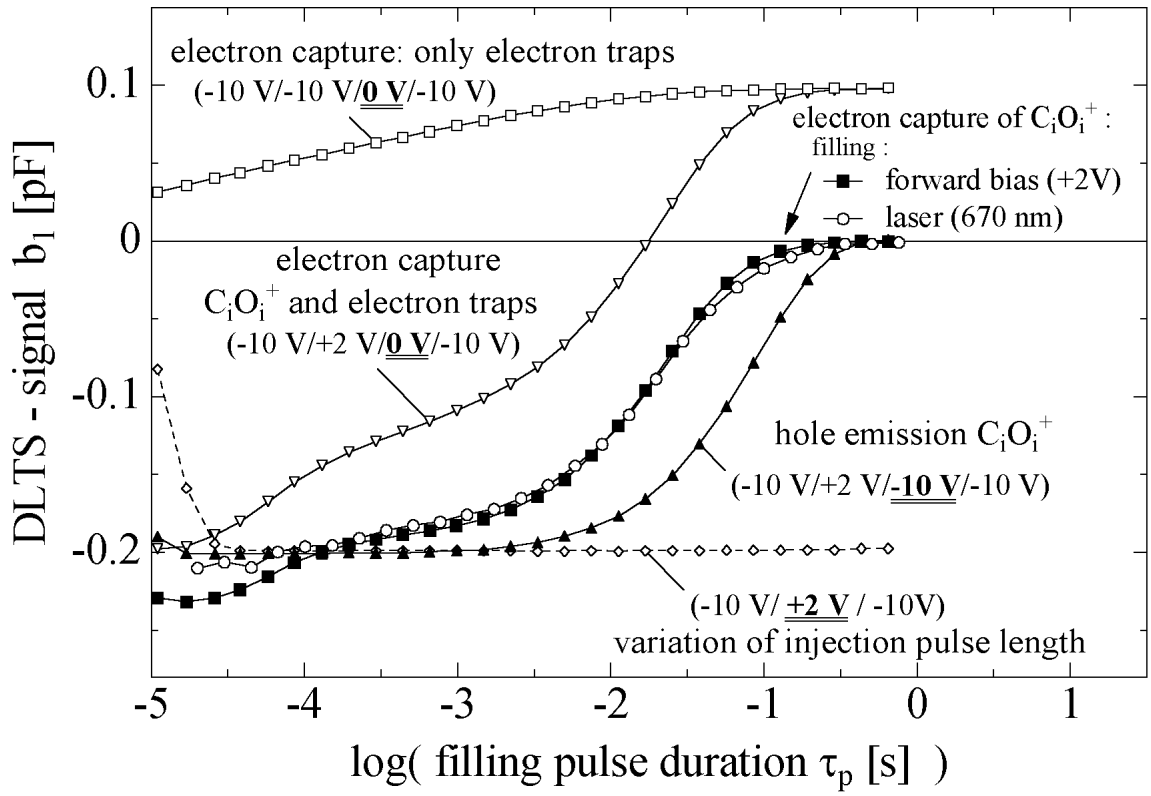

Figure 6.8: Measurement of the electron capture cross section of the $C_iO_i^+$ at 180 K. The DLTS signal (b_1) is plotted versus the filling time under various conditions. The bias values indicate the bias sequences during the different measurements. The bias corresponding to the filling pulse of variable length (abscissa) is underlined (see text).
Sample: n-type, WM2-3kΩcm, M20911, neutron irradiated (UKE) $\Phi_{eq} = 9.7 \times 10^{10}\,\mathrm{cm}^{-2}$, $T_W = 300$ ms, t_p(+2 V filling pulse) = 1 ms, delay between capture measurements: 300 ms.

(e.g. [Mac96a, Gil97]).
In this section it is demonstrated by the example of the dominant hole trap in irradiated silicon, the C_iO_i defect, that there can be drastic differences between the absolute values of electron and hole capture cross sections. Furthermore, it is shown that a capture cross section can have a strong temperature dependence. Thus care has to be taken if defect properties that have been measured at deep temperatures are extrapolated to room temperature in order to simulate macroscopic detector properties (see Chapter 7).

DLTS measurements

In Fig. 6.8 a set of isothermal DLTS measurements is displayed which is needed to

determine the electron capture coefficient c_n of the $C_iO_i^+$ at the given temperature of 180 K. The measurements were performed with a quiescent reverse bias of V_R = -10 V. In order to measure the capture of electrons at the C_iO_i level the defect has first to be occupied by holes. In n-type material this is either achieved by applying forward bias to the sample (high injection) or by illumination of the rear contact with a short wave length light source ($\approx$ 500 – 700 nm) under reverse bias. With the first filling method only hole traps with $c_p > c_n$ can be filled since electrons and holes are injected in the semiconductor bulk (see Sec. 3.4.4) while with the second method all hole traps independent of their electron capture cross section can be filled since only holes are injected into the depleted zone. The short wave length light has only a small penetration depth in which electron-hole pairs are generated (e.g. inverse absorption constant for 670 nm: 3.3 μm at 300 K and 7.7 μm at 77 K [Das55]). The electrons and holes diffuse through the neutral bulk but due to the applied field only holes are able to enter the depleted zone and fill the traps. The difference between the two filling methods becomes obvious by comparing the hole trap spectra displayed in Fig. 6.1 (forward bias) and Fig. 6.7 (red laser, 670 nm)). For example the signal of the $V_2^{(+/0)}$ ($c_p < c_n$) is not detected by applying forward bias to the sample while it is seen after injection of holes with the laser. Since the C_iO_i level is observed in both measurements it is already obvious that for this defect the hole capture coefficient c_p is bigger than the electron capture coefficient c_n (in the temperature range where the DLTS peaks are observed, see below).

In the present measurement the filling of the C_iO_i was performed by applying a forward bias of +2 V for t_p = 1 ms to the device. As can be seen from the variation of the +2 V filling pulse length – data labelled with (-10 V / **+2 V** / -10 V)[3] in Fig. 6.8 – already a filling pulse length of 100 μs is sufficient to get a saturation of the $C_iO_i^{(+/0)}$ DLTS signal.

When the C_iO_i is occupied by holes the capture process of electrons (recombination) can be measured by injecting electrons. In n-type material this is easily achieved by applying zero bias to the sample for various filling times. The corresponding measurement with the bias sequence (V_R = -10 V / $V_{\text{pulse 1}}$ = + 2 V / $V_{\mathbf{pulse\ 2}}$ **= 0 V** / V_R = -10 V) is shown in the figure. The hole traps are filled by applying forward bias to the sample (+ 2V for t_{pulse1} = 1 ms) and afterwards the electrons are injected during the second pulse (0 V for variable pulse duration $t_{\text{pulse 2}}$).

However, during an electron filling pulse the electrons are not only trapped at the $C_iO_i^+$ but also at electron traps giving rise to a positive DLTS signal at the temperature of 180 K. The signal due to the electron traps has to be subtracted from the capture measurement. Therefore another measurement with the same filling times but under filling conditions that only inject electrons has to be performed. This measurement is achieved with the bias sequence (V_R = -10 V / $V_{\text{pulse 1}}$ = - 10 V / $V_{\mathbf{pulse\ 2}}$ **= 0 V** / V_R = -10 V). The difference of the two measurements is shown in the figure and represents almost solely the electron capture of the $C_iO_i^+$ and an exponential fit to the data can be used to extract an *effective electron capture time constant* $\tau_{c,e}^*$. For comparison a measurement with hole injection by laser illumination instead of applying forward bias is shown. The agreement between the measurements with the different filling methods is very good.

[3]Notation: (-10 V / **+2 V** / -10 V) indicates a bias sequence of (a) quiescent reverse bias of -10 V (b) filling pulse at +2 V with variable length (c) measurement of the transient at -10 V.

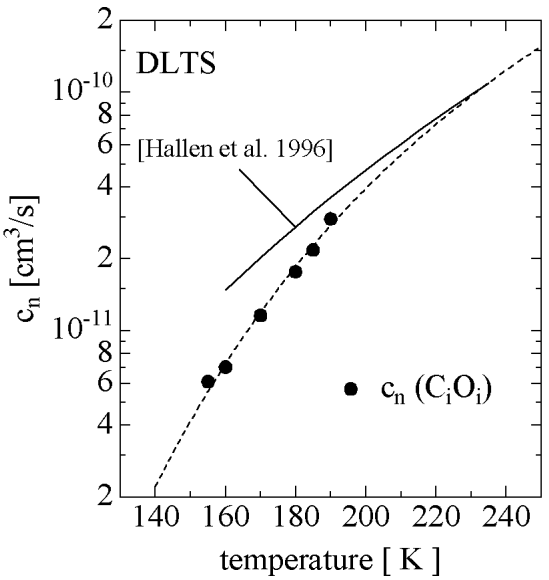

Figure 6.9: Electron capture coefficient c_n of the C_iO_i defect determined in n-type material with the DLTS method (see text). The solid line indicates the parameterization given in Ref. [Hal96] for the temperature range 160 K $< T <$ 238 K: $c_n = 5.1 \times 10^{23} \times T[K]^{5.2}\,\mathrm{cm}^3/\mathrm{s}$.
Sample: n-type, WM2-3kΩcm, neutron irradiated (UKE) $\Phi_{eq} = 1 \times 10^{11}\,\mathrm{cm}^{-2}$.

However, one has also to take into account that the DLTS signal of the C_iO_i during the electron filling pulse does not only decrease due to capture of electrons but also due to emission of holes. The measurement of the hole emission is indicated in the figure by the corresponding bias sequence (V_R = -10 V / $V_{\mathrm{pulse\ 1}}$ = + 2 V / $V_{\mathbf{pulse\ 2}}$ **= -10 V** / V_R = -10 V). Here C_iO_i is filled with holes during the first pulse while during the second pulse of variable duration already the reverse bias is applied. Since no free electrons or holes are present in the space charge region only the hole emission of the $C_iO_i^+$ is observed. The determined hole emission time constant $\tau_{e,h}$ is then used to correct the previously measured *effective electron capture time constant* $\tau^*_{c,e}$ for the hole emission

$$\frac{1}{\tau_{c,e}} = \frac{1}{\tau^*_{c,e}} - \frac{1}{\tau_{e,h}}$$

with $\tau_{c,e}$ representing the electron capture time constant of $C_iO_i^+$.

In Fig. 6.9 the resulting temperature dependent electron capture coefficient $c_n = 1/(n\tau_{c,e})$ of the $C_iO_i^+$ is displayed. The free electron concentration n was determined from CV measurements performed at the individual temperature. Compared to the data published in [Hal96] (solid line in figure) a stronger temperature dependence of c_n is found. The corresponding electron capture cross section was calculated from c_n according to Eq. 3.25 with $X_n = 1$ and $m^*_{dC} = 1.084$ (compare Sec. 3.4) and was fitted as function of temperature by

$$\sigma_n = 2.4 \times 10^{-15} \times \exp\left(-\frac{0.109\mathrm{eV}}{k_B T}\right)\ \mathrm{cm}^2 \qquad \text{for} \qquad 155\,\mathrm{K} < T < 190\,\mathrm{K}.$$

The corresponding parameterization for c_n is given by the dashed line in Fig. 6.9.

In conclusion the DLTS measurements reveal a very strong temperature dependence of the $C_iO_i^+$ electron capture cross section. The absolute value is about 3 orders of magnitude smaller than the hole capture cross section of the $C_iO_i^0$ in the temperature range from 155 K to 190 K (e.g. at T = 179 K: $\sigma_n = 2 \times 10^{-18}\,\mathrm{cm}^2$ and $\sigma_p = 2 \times 10^{-15}\,\mathrm{cm}^2$). Finally it should

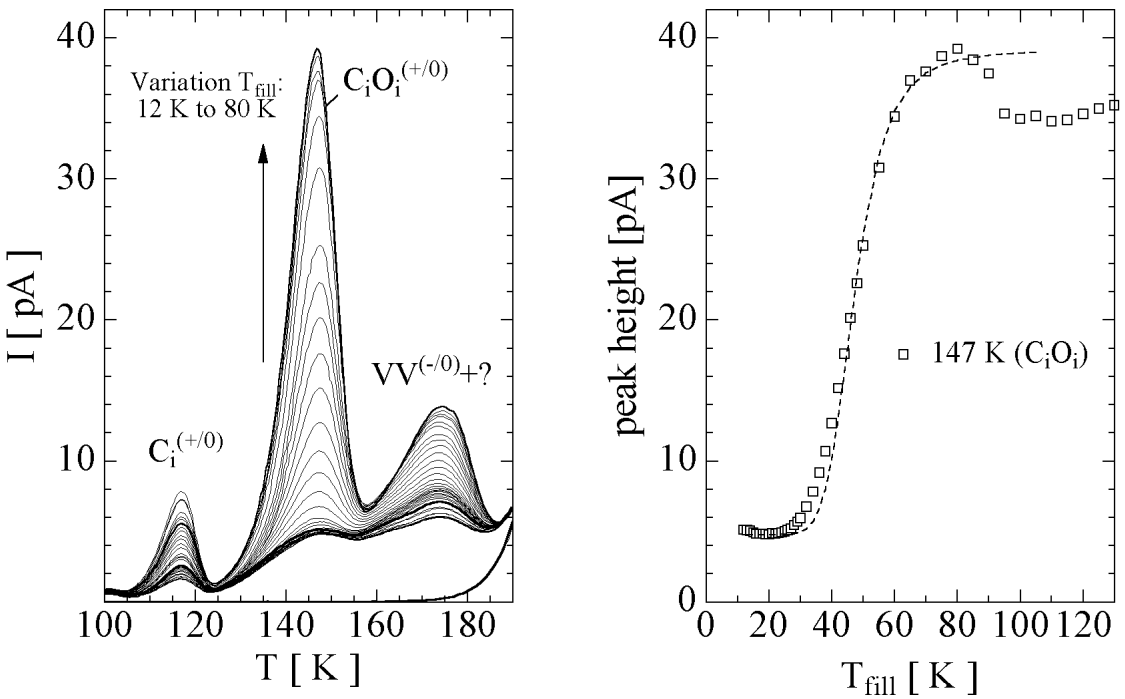

Figure 6.10: Peak height of the TSC signal at 147 K (C_iO_i) in dependence of the filling temperature T_{fill}. Left: TSC spectra obtained after filling of the traps by forward biasing of the diode at different temperatures T_{fill}. Right: Plot of the C_iO_i peak height measured at 147 K as function of the filling temperature T_{fill}. The dashed line indicates a fit to the data according to Eq. 6.1.
Sample: n-type, WM2-3kΩcm, neutron irradiated (UKE) $\Phi_{eq} = 1 \times 10^{13}\,\mathrm{cm}^{-2}$, annealing: one day at room temperature, filling: 1.7 mA for 30 s at given temperature, bias: 50 V, heating: $\beta = 0.183$ K/s.

be mentioned that according to DLTS measurements presented in [Hal96] the hole capture cross section is nearly independent of temperature (160 K to 238 K) and the entropy factor is close to one (for details see Tab. B.2 on page 225).

TSC measurements

Fig. 6.10 (left hand side) shows a series of TSC spectra obtained on a neutron irradiated detector ($\Phi_{eq} = 1\times10^{13}\,\mathrm{cm}^{-2}$) after filling of the defects at various temperatures T_{fill} between 12 K and 80 K by forward biasing (7 mA/cm^2 for 30 s). On the right hand side of the figure the corresponding TSC peak height of the C_iO_i donor level as function of filling temperature is presented. A strong dependence of the peak height on the filling temperature is observed. In [Fei97a] it was demonstrated that the measured peak height of the C_iO_i is governed by the fractional occupation of the defect with holes during the high injection (n = p) filling process ($p_t/N_t = (1+c_n/c_p)^{-1}$, compare Sec. 3.4.4). Thus the peak height as function of temperature gives an indication for the ratio between the electron and hole capture coefficient. The data thus reveal that c_p is bigger than c_n for temperatures above about 50 K which is in agreement

reference	Offset [pA]	Amplitude [pA]	a	E_b [meV]
this work	4.79	34.4	1.06×10^{-4}	37.3
[Fei97b]	1.21	19.2	1.07×10^{-3}	32.8
[Fei97b]	0.86	10.4	3.43×10^{-4}	37.4

Table 6.8: Fit parameters according to Eq. 6.1 for the data displayed in Fig. 6.10. For comparison also data published in [Fei97b] are shown.

with the DLTS measurements performed in the temperature range between 155 K and 190 K. However, for temperatures lower than about 50 K the opposite seems to be true. The defect is not filled any more which indicates that at deep temperatures c_n is bigger than c_p. In order to describe the observed behavior the following parameterization was chosen:

$$I_{max}(T_{fill}) = \text{Offset} + \text{Amplitude} \times \frac{1}{1+\frac{c_n}{c_p}} \qquad \text{with} \qquad \frac{c_n}{c_p} = a \exp\left(\frac{E_b}{k_B T_{fill}}\right). \tag{6.1}$$

The corresponding fit to the data is given by the dashed line in Fig. 6.10 and the free parameters are displayed in Tab. 6.8. For comparison also data published in [Fei97b] and obtained on similar material but irradiated with about 10 times smaller neutron fluences are shown. It should be mentioned that the temperature dependence of the filling by forward current injection was also observed on a ^{60}Co-gamma irradiated sample (compare Fig. 6.15) and is thus not depending on the type of irradiation. Furthermore, the level could also not be filled at 25 K by illumination of the sample with a laser of 980 nm wavelength (measurement not shown)[4]. This indicates that the observed filling behavior is not an artifact due to the filling by forward biasing of the diode.
In order to show that the C_iO_i defect can be filled at temperatures below 60 K at all, an experiment was performed in which solely hole traps were filled. This was achieved by illumination of the rear contact of a reverse biased weakly damaged sample ($\Phi_{eq} = 1 \times 10^{12}\text{cm}^{-2}$) with a red laser (670 nm). The dependence of the C_iO_i peak height on the filling temperature is shown in Fig. 6.11. The data clearly reveal that the defect can be occupied by holes even at 20 K. Thus it is obvious that the defect is electrical active at deep temperatures and the observed effect of the temperature dependent peak height displayed in Fig. 6.10 is most probably due to a ratio of $c_n/c_p > 1$ at temperatures below about 50 K.

Further defects

Further experiments for the determination of electron capture cross sections of hole traps were performed. However, these experiments result in the fact that the electron capture process was faster than the minimum pulse length of the used DLTS apparatus. Thus it was only possible to determine a lower limit for the electron capture cross section. The corresponding values are given in Tab. 6.1.

[4]Measurement performed on a neutron irradiated ($\Phi_{eq} = 1 \times 10^{12}\text{cm}^{-2}$) sample of type WM2-3k$\Omega$cm. Inverse absorption coefficient for 980 nm light at 25 K > 300 μm [Das55].

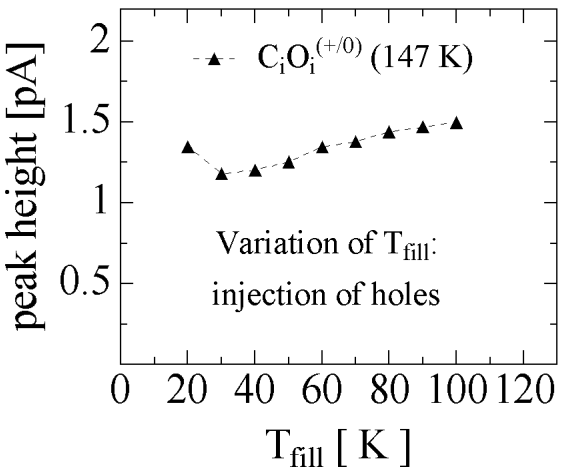

Figure 6.11: Plot of the C_iO_i peak height measured at 147 K as function of the filling temperature T_{fill}. Filling of the level was achieved by illumination of the rear contact with a red laser (670 nm) under reverse bias (100 V).
Sample: n-type, WM2-3kΩcm, neutron irradiated (UKE) $\Phi_{eq} = 1 \times 10^{12}\,\mathrm{cm}^{-2}$, annealing: 1000 min at room temperature, bias: 100 V, heating: $\beta = 0.183$ K/s, filling: illumination with red laser (670 nm) through a hole in the rear contact (5 min, 35 μA photocurrent).

6.5 Field strength dependence

An electron trap in the upper half of the band gap has only an influence on the effective doping concentration of a reverse biased diode if it is a donor (Sec. 3.4). However, it is not straight forward to distinguish between an acceptor and a donor level since both kind of defects give rise to peaks in the DLTS or TSC spectra. One possibility to identify an electron trap as a donor is the existence of a Poole-Frenkel effect which is explained in the following.

Theory

The thermal emission of charge carriers as studied with the DLTS or TSC method is observed in the space charge region of a reverse biased diode. Thus the emission process is monitored in an electric field E(x) (compare Fig. 2.7) which can have an influence on the emission process. If e.g. an electron is emitted from a donor the external field reduces the binding energy between the emitted electron and the remaining positive ion (Coulombic well) by the applied voltage drop across the binding potential (Poole-Frenkel effect [Fre38]). Thus the activation energy $\Delta H'$ for the carrier emission is reduced by a field strength dependent value ΔE_E resulting in an effective activation energy E_A of

$$E_A = \Delta H' - \Delta E_E. \tag{6.2}$$

The value ΔE_E for a simple 1-dimensional approach[5] (electron emission in opposite direction of electric field vector) is given by [Fre38]:

$$\Delta E_E = q_0 \sqrt{\frac{q_0 E}{\pi \epsilon \epsilon_0}} = 2.2 \times 10^{-4} \sqrt{E[V/cm]}\, eV. \tag{6.3}$$

Please note that for the emission of an electron from an acceptor no such effect can be observed since the acceptor is neutral after ionization i.e. there is no coulomb interaction between the

[5] A more detailed discussion with a 3-dimensional model taking into account different potentials for shallow and deep defects as well as phonon-assisted tunneling can be found in [Mar81].

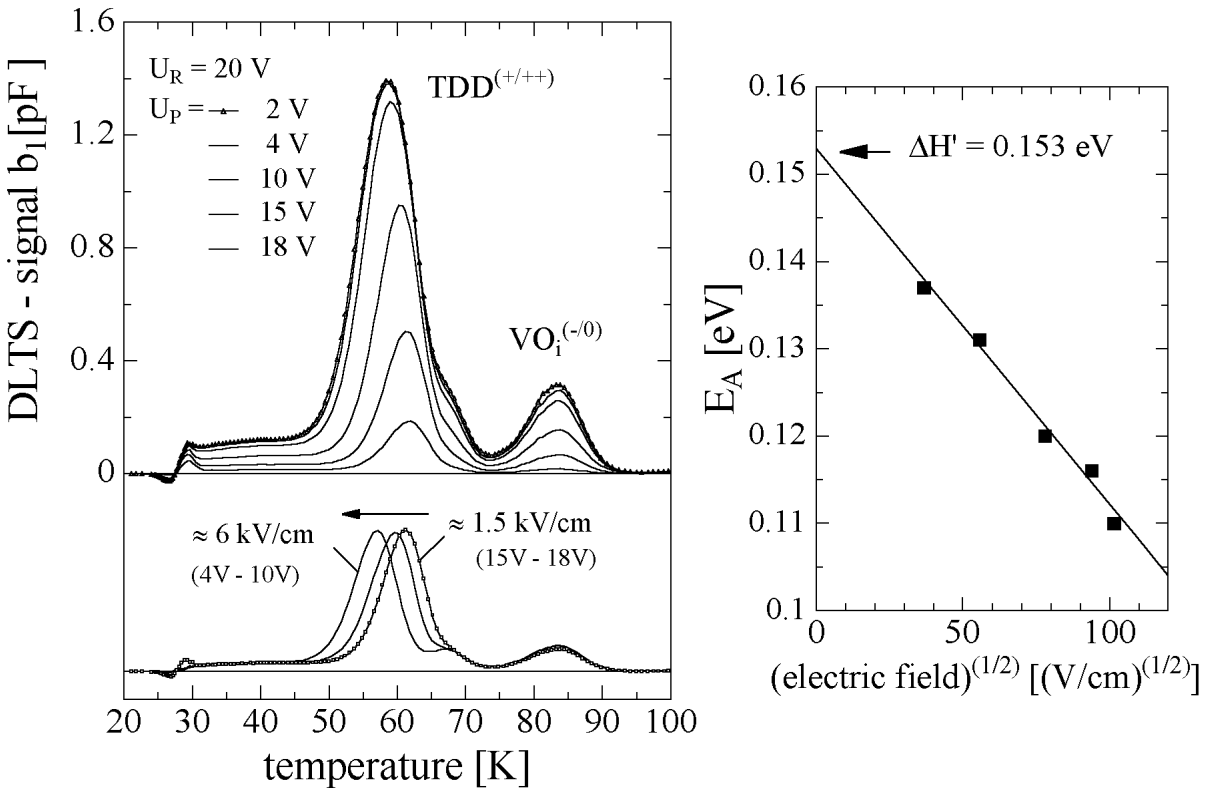

Figure 6.12: Poole-Frenkel effect observed on the Thermal Double Donor (TDD) in CZ silicon. Left: DLTS spectra and (lower part) corresponding difference spectra showing a shift in the TDD peak maximum to lower temperatures with increasing field strength. Right: Field strength dependent activation energy of the TDD (further details are given in the text). (PH-110Ωcm; $\Phi_{eq} = 1.3 \times 10^{12}\,\mathrm{cm}^{-2}$; $U_R = -20\,\mathrm{V}$; $U_P = 2...18\,\mathrm{V}$; $t_p = 100\,\mathrm{ms}$; $T_W = 200\,\mathrm{ms}$)

neutral defect and the emitted electron. Therefore the existence of a Poole-Frenkel shift in the activation energy of an electron trap is an evidence for the defect being a donor.

Measurement

Fig. 6.12 exhibits the data which confirm the Poole-Frenkel field emission process for the thermal double donor (TDD, Sec. 3.6.2). The displayed spectra were obtained on a neutron irradiated sample made from Czochralski silicon (PH-110Ωcm, $[O] = 9 \times 10^{17}\mathrm{cm}^{-3}$). However, the TDD and the defect E(67) visible in the right hand shoulder of the TDD peak were already present in the material before irradiation.
The spectra were obtained with a reverse bias U_R of 20 V and variable pulse voltages[6] U_P between 2 and 18 V, as indicated in the figure. Let W(U) be the voltage dependent depletion depth according to Eq. 2.6. After a filling pulse to U_P =2 V all defects in the region between

[6]It is noted again that the pulse voltage U_P was defined in Sec. 4.4 as the voltage applied to the sample during the filling pulse.

W(2 V) and W(20 V) are filled. Thus after a filling pulse to $U_P = 2$ V more defects are occupied by electrons than after a filling pulse to higher voltages. Correspondingly the heights of the peaks displayed in Fig. 6.12 decrease with increasing filling pulse voltage.
The difference between two spectra can be used to extract the signal origin from electrons emitted in a certain depth of the detector (left hand side of Fig. 6.12, lower part). If e.g. the spectrum with $U_P = 18$ V is subtracted from the spectrum with $U_P = 15$ V the resulting *difference spectrum* is only due to electrons emitted in a depth range between W(15 V) and W(18 V). In the displayed example the average field strength in this region during the emission process under $U_R = 20$ V is ≈ 1.5 kV/cm. Therefore the activation energy obtained from an Arrhenius plot based on this *difference spectrum* corresponds to the field strength of 1.5 kV/cm.

Results – Thermal donor

The field strength dependence of the $TDD^{(++/+)}$ activation energy is displayed on the right hand side of Fig. 6.12. The straight line in the figure represents a fit according to Eqs. 6.2 and 6.3:

$$E_A = \left(0.153 - 4.1 \times 10^{-4}\sqrt{E[V/cm]}\right)\ eV\,.$$

The zero field activation energy $\Delta H' = 0.153$ eV is in good agreement with the value of 0.15 eV published in [Ben83]. The prefactor of 4.1×10^{-4} is about two times higher than the theoretical predicted one of 2.2×10^{-4} (Eq. 6.3). However, taking into account that the defect is a double donor the theoretical value in Eq. 6.3 has to be multiplied with $\sqrt{2}$ which then results in a rather good agreement between theory and experiment.

Results – Radiation induced defects

As can be seen in Fig. 6.12 the peak maximum temperatures of the defects E(67) and VO_i do not depend on the field strength. This was also observed for the DLTS peaks E(120) and E(205). The variation of the peak maximum temperatures was below 1 K in the present experiment although e.g. a shift in activation energy of about 10 meV would already result in a shift in the peak maximum of about 5 K.
Furthermore, no difference in the peak maximum temperature was observed for the DLTS peaks E(85) and E(120) in low and high resistivity material (WM2-3kΩcm with an average field strength of $<E> = 0.75$ kV/cm and WH-6Ωcm with $<E> = 17.5$ kV/cm). In contrast to what would be expected by a Poole-Frenkel shift the peak E(205) was shifted to higher temperatures in the low resistivity material by about 2 K (203 K measured instead of 201 K after 320 min annealing at 60°C). This effect can be attributed to a contribution of the VP defect to the peak E(205) which is not present in the high resistivity material due to the very low phosphorus concentration.

In conclusion a significant contribution of a donor level to the DLTS signals E(85), E(120) and E(205) can be excluded. This, of course, is also not expected if one takes into account the radiation induced changes of the effective doping concentration described in Chapter 5. The defects described above are produced by neutron irradiation with introduction rates of about 0.2 to 1 cm^{-1}. If one of these defects would be a donor an increase of the effective space charge with the rate of 0.2 to 1 cm^{-1} should be observed (introduction of positive

Acronym	Assignment	$\Delta H'$ [eV]	σ_n, σ_p [cm^2]	Introduction rate [10^6 Gy^{-1} cm^{-3}]	Peak maximum DLTS [K]	TSC [K]
E(60b)	$C_iC_s(B)^{(-/0)}$	-0.109	2.39×10^{-15}	–	58	49
E(85a)	$VO_i^{(-/0)}$	-0.175	1.48×10^{-14}	55.0	84	70
E(85b)	$C_iC_s(A)^{(-/0)}$	-0.17	–	13.0	84	70
E(120)	$VV^{(=/-)}$	-0.224	7.14×10^{-16}	1.5	120	100
E(205b)	$VV^{(-/0)}$	-0.423	2.06×10^{-15}	1.6	204	167
H(180)	$C_iO_i^{(+/0)}$	+0.357	1.66×10^{-15}	46.0	181	147

Table 6.9: Ionization energies, cross sections, introduction rates and most probable assignments with defects for the levels found in the ^{60}Co-gamma-irradiated samples measured three months after irradiation.

space charge). Instead the experimental data show a decrease of the effective space charge (introduction of negative space charge) with a rate in the order of $2 \times 10^{-2}\,\mathrm{cm}^{-1}$ (compare Chapter 5).

6.6 ^{60}Co-gamma irradiations

In contrast to the radiation damage introduced by high energetic hadrons an irradiation with ^{60}Co-gammas can only produce point defects and no clusters (compare Sec. 3.1). Thus a comparison of DLTS measurements on neutron and ^{60}Co-gamma irradiated samples of the same material offers the possibility to clearly divide between point defects and defects related to clusters (which are assumed to be composed of higher order vacancy or interstitial related defects e.g. V_x or I_x with $x = 2, 3, ..$).
In this section investigations on defects observed after irradiation with ^{60}Co-gammas will be presented and compared in the next section to observations on neutron irradiated samples of the same type.

Four diodes of type WM2-3kΩcm (see Tab. 4.1) were irradiated at the BNL (see Sec. 4.2) with ^{60}Co-gammas in a dose range[7] from 1.5 kGy to 110 kGy. The corresponding DLTS spectra measured 3 months after irradiation are shown in Fig. 6.13. They were obtained using a time window of 20 ms and a filling pulse duration of 100 ms to completely fill all traps. The Arrhenius plots for the defect levels and the corresponding defect parameters as well as the defect introduction rates are given in Fig. 6.14 and Tab. 6.9, respectively.
It is already noted here that for all observed levels an assignment to a specific defect could be made and that all observed DLTS peaks could be perfectly reproduced by simulations with the defect parameters obtained from the Arrhenius plots. In the next section it will be shown that this is by no means the case for many of the levels observed after fast neutron irradiation.
During a DLTS measurement the VO_i acceptor level is negatively charged below about 100 K

[7] 1 Gy = 100 rad

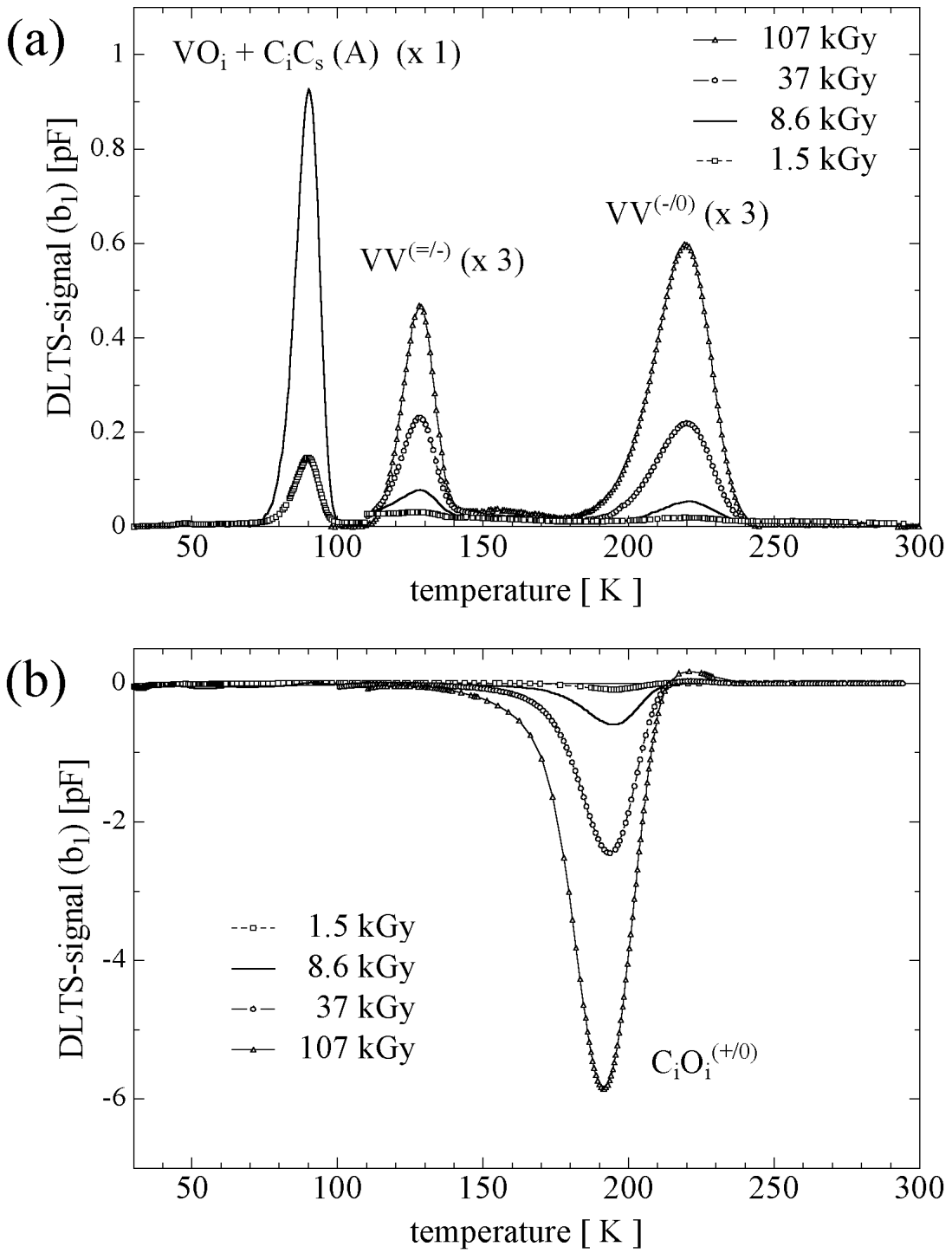

Figure 6.13: DLTS-spectra after (a) electron and (b) high injection of four samples irradiated with different ^{60}Co-gamma doses. Note that there are no data below 100 K for the heavily irradiated samples (dose > 10 kGy) and that the peaks above 100 K in (a) are enlarged by a factor 3 for better visibility. Samples: n-type, WM2-3kΩcm, annealing: 3 months at room temperature, T_W = 20 ms, t_p(+2 V) = 1 ms, t_p(0 V) = 100 ms.

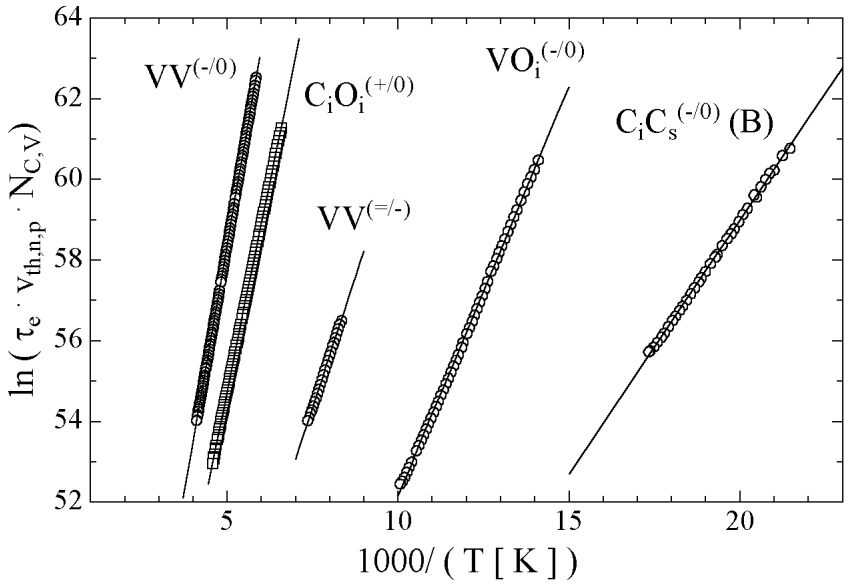

Figure 6.14: Arrhenius plot of defect levels detected in ^{60}Co-gamma irradiated samples obtained with the variable time window method (DLTS, Sec. 4.4.3).

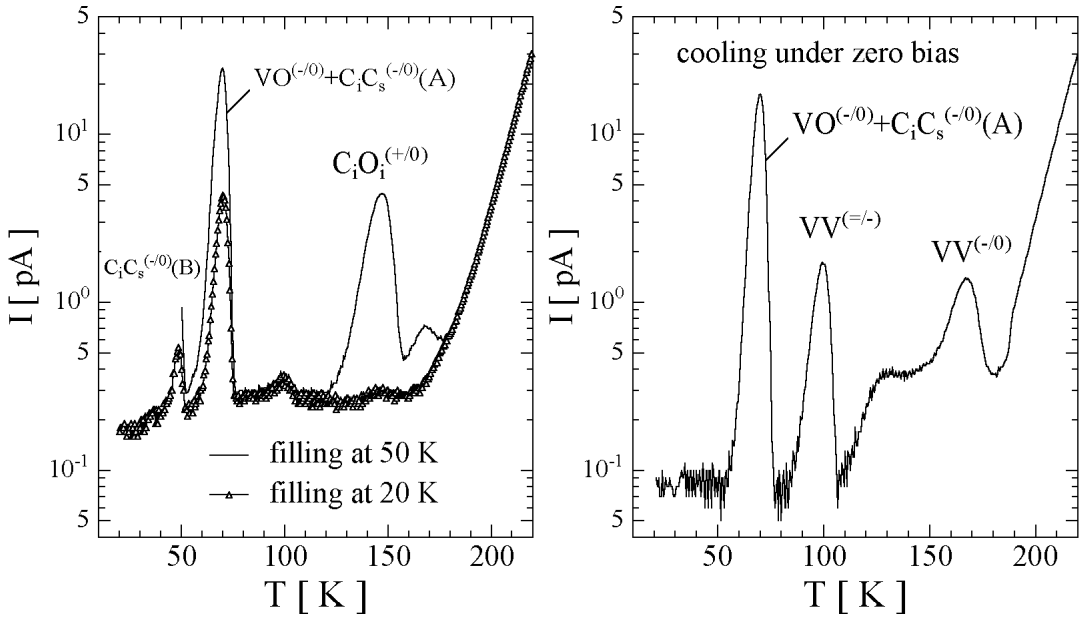

Figure 6.15: TSC spectra of a ^{60}Co-gamma irradiated sample. Left: Filling by applying forward bias at 20 K and 50 K. The dependence of the C_iO_i peak height on the filling temperature was already described in Sec. 6.4. Right: Filling by cooling down under zero bias (only electron traps are filled). Note that the concentration of the electron traps is higher than the effective doping concentration. Therefore the $VO_i + C_iC_s$ – level is only partly filled and detection of levels with peaks below 70 K is not possible. Sample: M21009; WM2-3kΩcm; dose: 107 kGy; bias: 90 V.

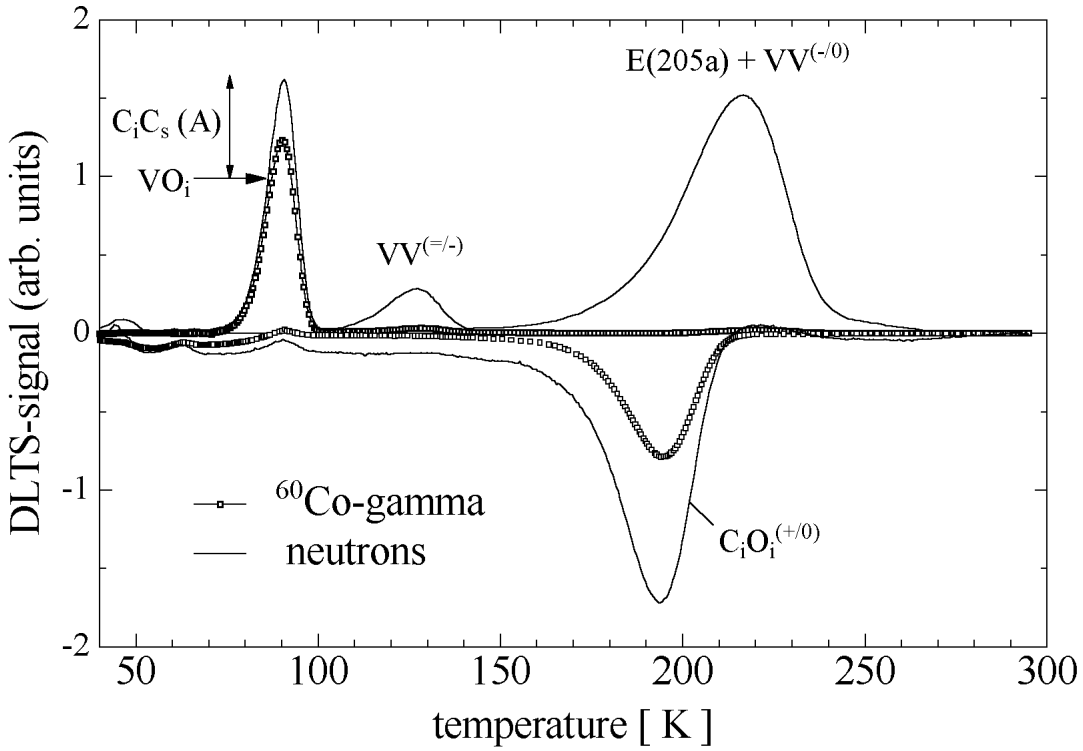

Figure 6.16: Comparison of DLTS-spectra after ^{60}Co-gamma and neutron irradiation obtained on identical samples. The spectra are scaled to the signal of the VO_i level which was set to the value of one on the ordinate. Samples: WM2-3kΩcm, $\Phi_{eq} = 1 \times 10^{11}$cm^{-2} (UKE), dose = 8.6 kGy (BNL), T_W = 20 ms, V_R = -10 V, V_P = (0 V/+2V), t_P = (10ms/1ms).

and therefore it compensates part of the positively charged shallow donors. For the heavily irradiated samples (37 kGy and 107 kGy) the concentration of the VO_i was in the order of the shallow doping concentration. Hence, DLTS measurements below 100 K were not possible any more. This effect is also seen in the reduced peak amplitude of the $VV^{(=/-)}$ level observed on the sample irradiated with a dose of 107 kGy. TSC spectra obtained on this sample are displayed in Fig. 6.15. An analysis of the peak heights of the TSC peaks corresponding to the $VV^{(=/-)}$ and $VV^{(-/0)}$ levels result in introduction rates of 1.40×10^3 Gy^{-1}cm^{-3} and 1.37×10^3 Gy^{-1}cm^{-3}, respectively. Thus, as expected for a single defect with two levels in the band gap, the observed introduction rates for both levels are the same.

6.7 Comparison: Neutron and ^{60}Co-gamma irradiations

The defects detected in neutron irradiated silicon during annealing studies at room temperature are displayed in Tab. 6.1 on page 133. All defects observed after ^{60}Co-gamma irradiation have also been observed after irradiation with neutrons. Additionally some defects were found that were not present in the gamma irradiated samples in detectable concentrations.

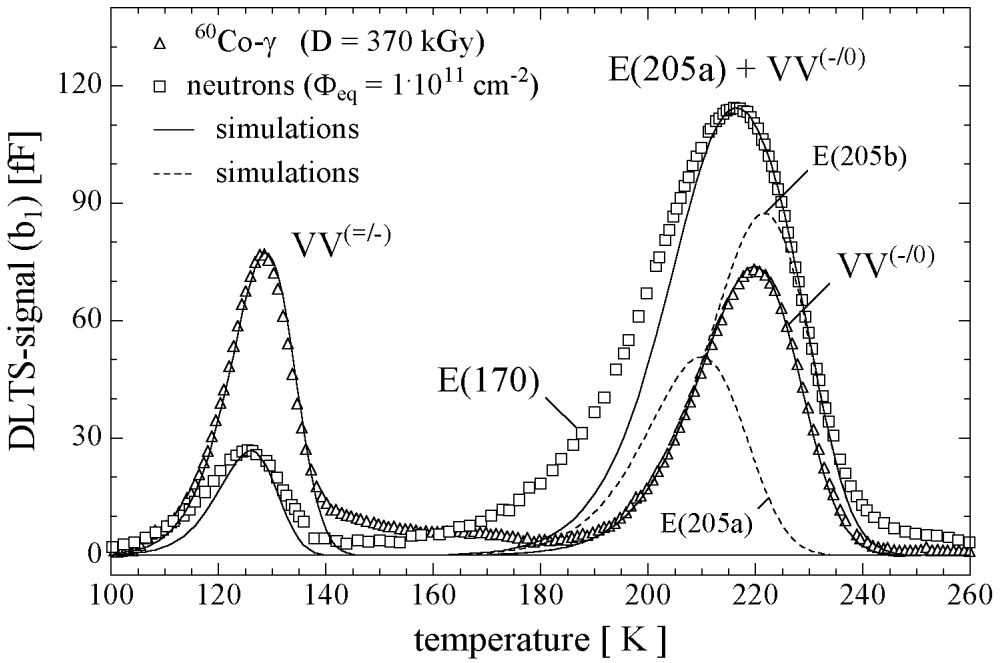

Figure 6.17: Comparison of DLTS-spectra after ^{60}Co-gamma and neutron irradiation (see text).

A comparison between the DLTS-spectra obtained on neutron and ^{60}Co-gamma irradiated devices originating from the same wafer is given in Fig. 6.16. Both spectra are normalized to the VO_i-signal[8] which was set to the value of 1 on the ordinate scale. The most obvious differences between the spectra are the two electron trap peaks at around 130 K and 210 K which can be seen for the neutron irradiated sample while they are far too small to be observed within the used scaling for the ^{60}Co-gamma irradiated one. In order to display further peculiarities of the two levels in the neutron irradiated material in Fig. 6.17 a part of the spectrum of the neutron irradiated sample is compared to another ^{60}Co-gamma irradiated sample (higher dose, same material). Most often these peaks are assigned in the literature to the two acceptor levels of the divacancy, $VV^{(=/-)}$ and $VV^{(-/0)}$, regardless of the type of particle used for irradiation (e.g. [Sve97]). However, in this work it will be argued that indeed for the ^{60}Co-gamma irradiated samples the peaks correspond to the divacancy levels, while after neutron irradiation additional defects (E(170), E(205a) and E(210)) contribute to the signal (see below and Secs. 6.8 and 6.9).

It is very instructive to compare the introduction rates of specific defects to each other in order to understand the differences between the damage mechanisms of fast neutrons and ^{60}Co-gammas. The absolute numbers are displayed in Tab. 6.10 and will be discussed in the following.

(1) The ratio between the $[C_iO_i]$ and the $[C_iC_s]$ is about the same after neutron and gamma irradiation. This indicates that the migrating C_i – produced by the interstitials

[8]Details about the separation of the VO_i and the C_iC_s signals are given in Sec. 6.3.

ratios of introduction rates		neutron irrad.	^{60}Co-γ irrad.	interpretation
(1)	$\frac{[C_iO_i]}{[C_iC_s]}$	2.8	3.2	C_i migration is not influenced by type of irradiation (in the investigated fluence/dose - range)
(2)	$\frac{[VO_i]}{[VV^{(-/0)}]}$	0.8	35	n-irradiation: many vacancies produced in a small region (i.e.VV creation is possible)
(3)	$\frac{[VO_i]}{[C_iC_s]+[C_iO_i]}$	0.5	0.9	n-irradiation: more V than I are captured in the primary damage region
(4)	$\frac{[VO_i]+2\times[VV^{(-/0)}]}{[C_iC_s]+[C_iO_i]}$	1.7	1.0	γ-irradiation: ratio of vacancy to interstitial related defects is 1:1
(5)	$\frac{[VV^{(-/0)}]}{[VV^{(=/-)}]}$	3.3	1.0	n-irradiation: VV are mostly localized in disordered regions (lattice strain or inter-center charge transfer ?)

Table 6.10: Ratios of introduction rates (defect concentrations) for the dominant defects after ^{60}Co-gamma and neutron irradiation. The absolute introduction rates are given in Tab. 6.9 for the γ-irradiated and Tab. 6.11 for the neutron irradiated material.

escaping the primary damage region (*Watkins replacement mechanism*, Sec. 3.6.1) – are not influenced by the type of irradiation. Such an influence is of course also not expected since the irradiation induced defect concentrations in the DLTS experiments are in the order of $10^{12}\,\mathrm{cm}^{-3}$ and thus are about 3 orders of magnitude smaller than the carbon and oxygen concentration in the material. Therefore a reaction of the C_i with carbon or oxygen is much more likely than the reaction with a radiation induced defect.

(2) The ratio of the generation rates of the divacancy (VV) and the A-centre (VO_i) is $1:35$ for the gamma and about $1:1$ for the neutron irradiated samples. This clearly reveals that a high number of vacancies is generated by fast neutron damage in a small crystal region. Only if the vacancies are produced close to each other within one PKA cascade they can form divacancies or even higher order vacancy defects ($V_3, V_4, ..$). Since only a small number of vacancies can be produced by the gamma induced Compton electrons (see Sec. 3.1) it is rather unlikely that divacancies form and most of the vacancies that are not recombined by a silicon interstitial in the primary damage process migrate through the lattice until they are captured by an oxygen atom.

(3) The most effective sink for interstitials I is the C_s with the reaction $I+C_s \rightarrow C_i$. The C_i later on form the defects C_iC_s and C_iO_i. The most effective sink for the vacancies is the oxygen with the reaction $V + O_i \rightarrow VO_i$. Thus the ratio of $([C_iC_s] + [C_iO_i]) : [VO_i]$ displays the ratio of diffusing interstitials to diffusing vacancies which escaped the recombination process in the primary damage regions. This ratio is $1 : 0.9$ for the

gammas and 1 : 0.5 for the neutrons showing that after neutron irradiations two times more interstitials escape from the primary damage regions than vacancies.

(4) Including the divacancies into the counting of interstitial and vacancy related defects[9] a ratio of 1:1 is found for the gamma irradiated samples. However, for the neutrons a problem arises since the origin of some defects is not known (e.g. E(170) and E(205a)). Taking into account only the levels assigned to known defects a ratio of vacancy to interstitial related defects of 1.7 : 1 is found. Since not necessarily all intrinsic defects have to be electrically active (e.g. V_6 is expected to give no DLTS signal at all [Has97]) no conclusion can be drawn about the origin of the unknown defects E(170) and E(205a). They might be composed of interstitials or vacancies.

(5) As expected for a defect with two levels in the bandgap the divacancy concentrations determined from the $VV^{(=/-)}$ and $VV^{(-/0)}$ levels are the same in the case of ^{60}Co-gamma irradiation. However, after neutron irradiation a strong discrepancy is observed. The signal of the $VV^{(=/-)}$ seems to be suppressed by a factor of about 3 compared to the signal of the $VV^{(-/0)}$. An even stronger suppression of the $VV^{(=/-)}$ signal compared to the $VV^{(-/0)}$ was detected after ion implantation in silicon [Sve97]. The suppression is depending on the ion mass and was found to range from a factor of about 3 for 44 keV ^{11}B ions to a factor of about 7 for 2.3 MeV ^{120}Sn ions.
So far two explanations have been suggested both basing on the fact that many lattice defects are generated in a small crystal volume. According to the first model by B.G. Svensson et al. [Sve91] the high concentration of defects in the clusters leads to lattice strain which reduces the signal of the double charged divacancy in DLTS spectra. The second model was proposed by S.J. Watts et al. [Wat96]. They assume that due to the high density of divacancies a so-called *intercenter charge transfer* is possible which suppresses the divacancy level by exchange of charge carriers between different divacancies and is furthermore responsible for the high leakage current observed after neutron irradiations (compare Sec. 5.1).

Fig. 6.18 displays another peculiarity of the double charged divacancy level in neutron irradiated silicon which is most probably related with the suppression of the signal. The figure shows a comparison of DLTS electron capture measurements obtained after irradiation with gammas and neutrons on the same material (WM2-3kΩcm). Furthermore, a capture measured for a neutron irradiated sample of lower resistivity (WH-90Ωcm) is given. As expected from the standard Shockley-Read-Hall theory (Sec. 3.4) and displayed by the dashed line in the figure the data for the gamma irradiated sample (triangles) can very well be fitted by an exponential function

$$b_1(t_p) = b_{1,max} \times (1 - \exp(-t_p/\tau_c)) \quad \text{with} \quad \tau_c^{-1} = \sigma_n v_{th} N_{eff} \quad \text{(see Eq. 4.14)}$$

resulting in an electron capture cross section of $\sigma_n = 2 \times 10^{-17} cm^{-2}$. For the neutron irradiated samples such a fit was not possible indicating that not only the $VV^{(=/-)}$ signal is suppressed after neutron irradiation but also the capture behavior is distorted. The difference between the capture measurements obtained on the low and high resistivity material clearly reveals that the observed process is depending on the free electron concentration (i.e. N_{eff})

[9]The concentration of divacancies has to be multiplied by a factor of 2 since divacancies contain two vacancies.

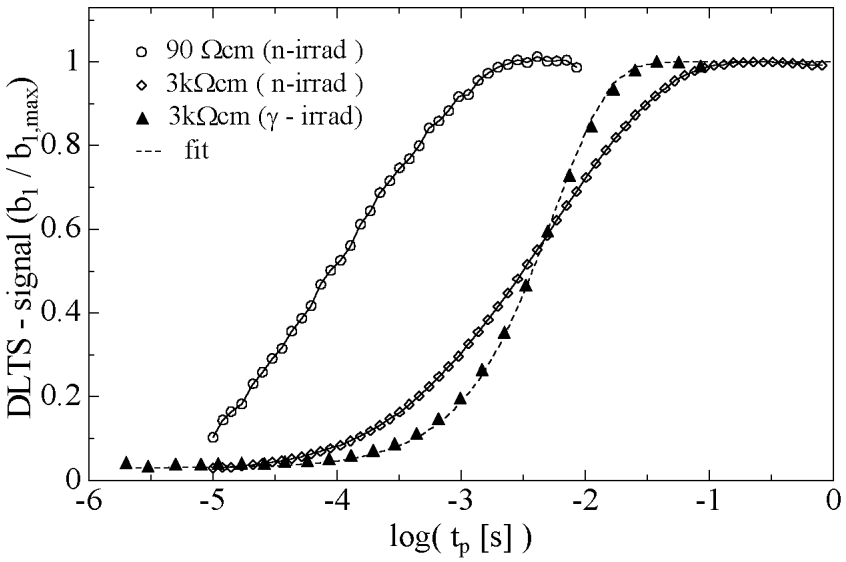

Figure 6.18: Electron capture of the $VV^{(=/-)}$-level after neutron and ^{60}Co-gamma irradiation. Materials: WM2-3kΩcm ($N_{eff} = 1.4 \times 10^{12}\,\mathrm{cm}^{-3}$) and WH-90Ωcm ($N_{eff} = 48 \times 10^{12}\,\mathrm{cm}^{-3}$).

as expected for a capture process. Therefore a configurational change like e.g. observed for the C_iC_s can be excluded.
It is noted here that similar capture properties (increase of the signal over several decades of filling pulse length) have been observed for the neutron induced level E(170) [Sch96b, Luc97]. Furthermore for both levels, $VV^{(=/-)}$ and E(170), the observed DLTS signals could only be poorly reproduced by simulations with the level parameters extracted from the corresponding Arrhenius-plots while simulations for the divacancy signals of gamma irradiated sample always perfectly reproduced the observed peaks (see Fig. 6.17).
Further properties of the defects located at around 0.4 eV below the conduction band (E(170), E(205) and E(210)) will be revealed by the annealing experiments presented in the next two sections.

6.8 Annealing at room temperature

In this section isothermal annealing studies at room temperature performed with the DLTS and TSC methods on neutron irradiated high resistivity FZ samples (WM2-3kΩcm) are presented. The results will be compared in Chapter 7 with the annealing studies on macroscopic detector properties described previously in Chapter 5 in order to detect or rule out relations between microscopic defects and macroscopic detector properties.

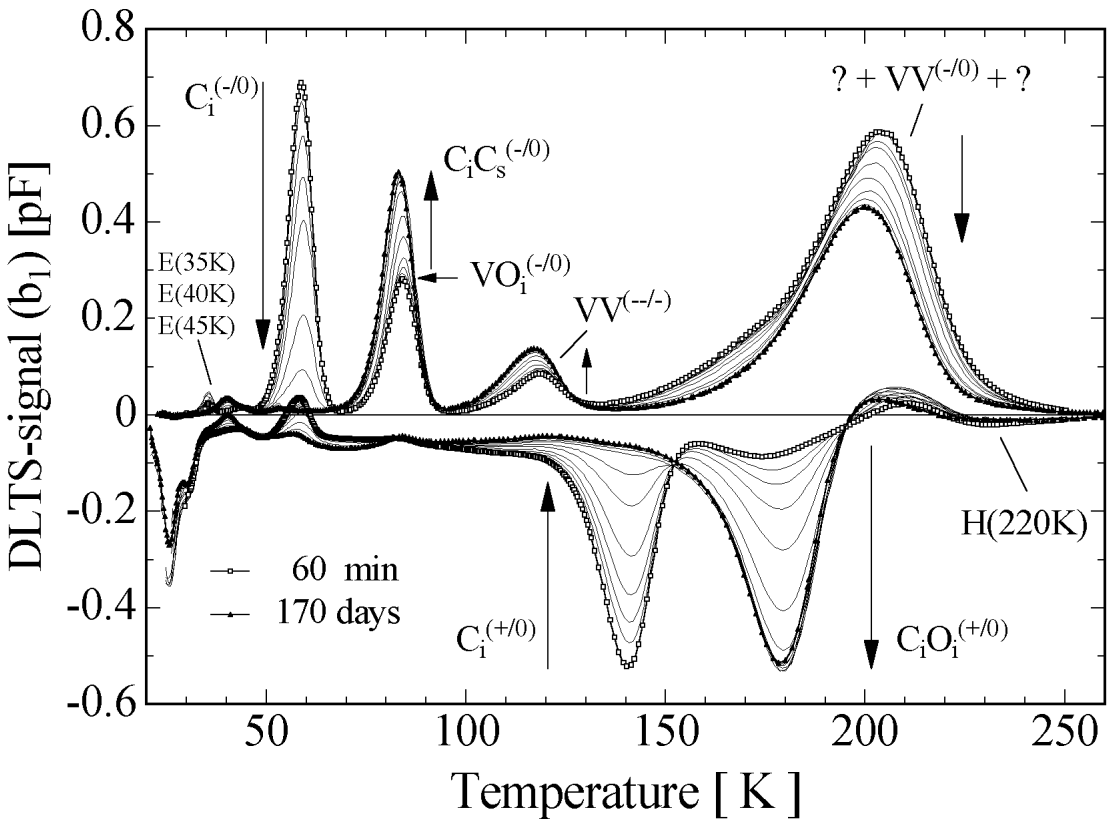

Figure 6.19: DLTS-spectrum transformation at room temperature within 170 days after neutron irradiation with a fluence of $\phi_{eq} = 2{\times}10^{11}\,\mathrm{cm}^{-2}$ (UKE). Sample of type WM2-3kΩcm, see Tab. 4.1, T_W = 200 ms, U_R = -10 V, U_P = (0 V/+2 V), t_P = 100 ms/ 1 ms.

6.8.1 DLTS measurements

In Fig. 6.19 the evolution of a DLTS spectrum at room temperature within an annealing period ranging from 60 min to 170 days after end of neutron irradiation[10] is shown. The level E(45), indicated in the figure, is not radiation induced[11]. The concentration of this defect was about $6 \times 10^9\,\mathrm{cm}^{-3}$ and the level parameters were $\Delta H' = 0.086$ eV and $\sigma_n = 1.5 \times 10^{-14}\,\mathrm{cm}^2$. All other DLTS peaks displayed in Fig. 6.19 change in peak heights during the annealing. The observed changes in the defect concentrations can roughly be divided into two different processes. A short term annealing of the carbon interstitial related defects (C_i, C_iC_s, C_iO_i) with a time constant of about 4 days and a long term annealing process of defects related to the broad electron-trap peak around 205 K (E205) with a time constant of about 1 month.

[10]After irradiation and before the first measurement the sample was stored in liquid nitrogen in order to prevent any annealing. The overall annealing time at room temperature was 60 min before the first measurement.

[11]In [Mol97] this defect was quoted erroneously as irradiation induced.

				Annealing at room temperature (21.5°C)	
Label (DLTS)	TSC [K]	Assignment	introduction rate [cm^{-1}]	DLTS ($\Phi_{eq} = 2 \times 10^{11}\,cm^{-2}$)	TSC ($\Phi_{eq} = 1 \times 10^{13}\,cm^{-2}$)
E(35)	30	?	≈ 0.14	$\uparrow$ 7h ; $\downarrow$ 91h	$\uparrow\approx$ 1h ; $\downarrow\approx$ 60h
E(40)	34	?	≈ 0.06	$\uparrow$ 40 d	$\uparrow\approx$ 22 d
E(60a)	49	$C_i^{(-/0)}$	1.55	$\downarrow$ 78h	–
E(85a)	70	$VO_i^{(-/0)}$	0.69	stable	stable
E(85b)	70	$C_iC_s^{(-/0)}$	0.40	$\uparrow$ 86h	$\uparrow\approx$ 93h
E(120)	100	$VV^{(=/-)}$	0.17$\rightarrow$0.28	increase $\uparrow$ 36 d	–
E(170)	(141)	?	0.18	$\downarrow$ 37 d	–
E(205)	(168)	–	$(1.49 \rightarrow 1.09)^{\dagger}$	–	–
E(205a)	(158)	?	0.58	stable	–
E(205b)	(167)	$VV^{(-/0)}$	0.92	stable	–
E(210)	(174)	?	0.55	$\downarrow$ 31 d	–
H(51)	43	?	≥ 0.05	–	$\downarrow\approx$ 23 d
H(140)	116	$C_i^{(+/0)}$	$(1.16)^{*}$	$\downarrow$ 80h	$\downarrow\approx$ 47h
H(180)	147	$C_iO_i^{(+/0)}$	1.10	$\uparrow$ 70h	$\uparrow\approx$ 77h
H(220)	(190)	?	≈ 0.08	introduction rate from p-type sample	

† E(205): Introduction rate obtained from peak height of the peak around 205 K (superposition of E(170), E(205a), E(205b) and E(210)).
* H(140): The defect cannot be fully occupied with holes by the used filling method (i.e. the extracted concentration is to small; see text).

Table 6.11: Defect introduction rates and annealing time constants observed on samples of type WM2-3kΩcm during annealing at room temperature. The corresponding defect parameters $\Delta H'$ and $\sigma_{n,p}$ can be found in Tab. 6.1.

The corresponding changes in the peak heights are displayed in Fig. 6.20 and Fig. 6.21 for the short and long term annealing process, respectively. The introduction rates and the annealing time constants resulting from exponential fits to the data are given in Tab. 6.11 (a first order kinetics is assumed for all annealing processes). In the following the two processes will be described in more detail.

Short term annealing

The decay of the $[C_i]$ and the built up of the $[C_iO_i]$ and $[C_iC_s]$ is displayed in Fig. 6.20. For better comparison the data are displayed in two different ways. The upper figure displays the DLTS-peak heights while the lower one shows the data normalized to the maximum peak height observed during annealing. The lines in the figures represent exponential fits with time constants and defect concentrations as displayed in Tab. 6.11.
The decrease of the $C_i^{(-/0)}$ and $C_i^{(+/0)}$ signals coincide very well with the increase of the C_iC_s

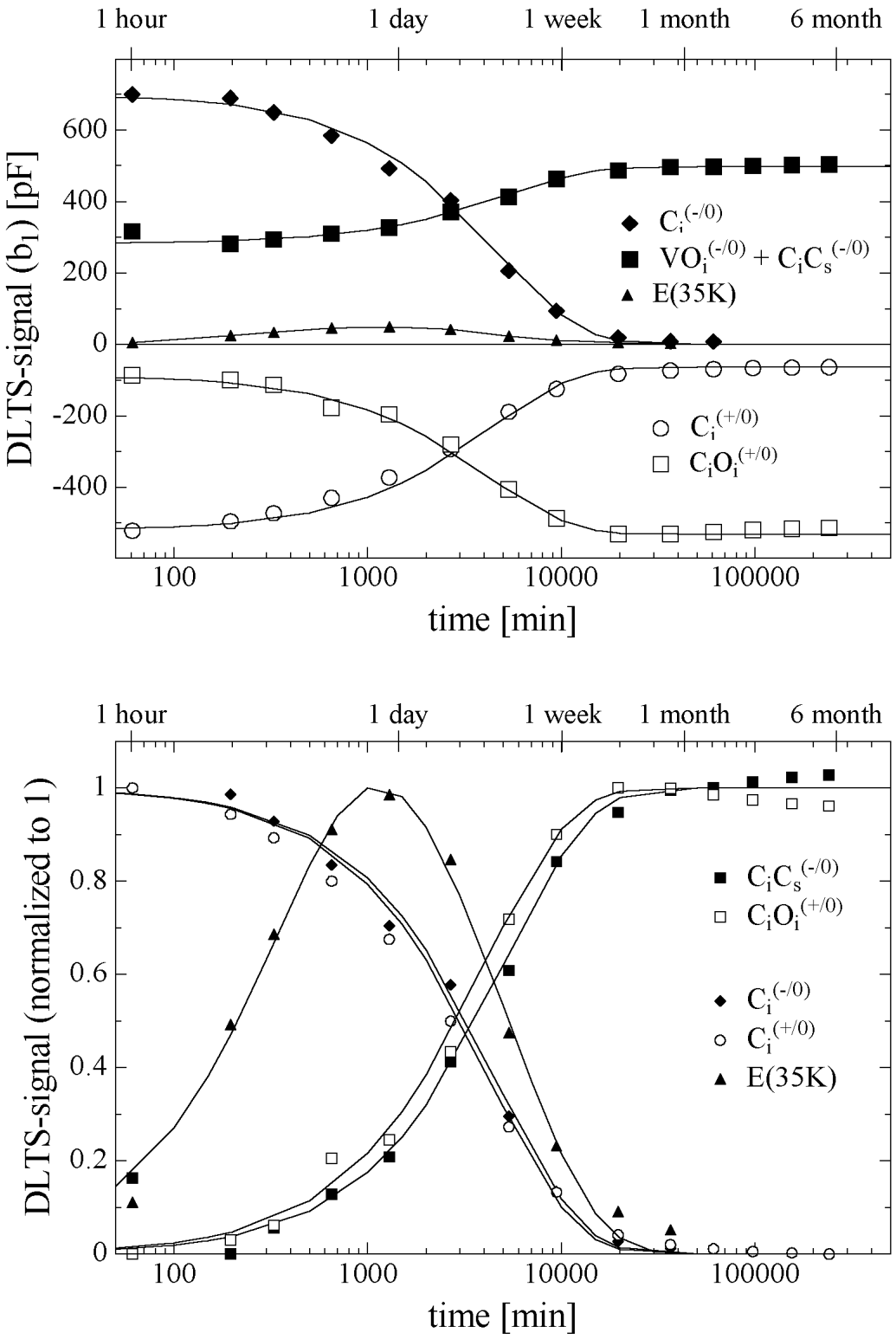

Figure 6.20: Evolution of the DLTS-peak heights during annealing at room temperature for the carbon related defects displayed in Fig. 6.19 (see text). Electron traps are indicated by filled and hole traps by open symbols.

and C_iO_i signals. However, comparing the introduction rates for the two C_i levels given in Tab. 6.11 a difference is observed although the signals arise from the same defect in a different charge state. This is due to the fact that the $C_i^{(+/0)}$ level cannot be fully occupied by holes by applying forward bias to the diode (i.e. not all C_i defects can be transferred into the positive charge state by the used filling method). Assuming a high injection filling process ($n = p$, compare Sec. 3.4.4) and using the measured capture cross sections of the C_i donor level for holes and electrons as given in Tab. 6.1 results in an occupancy with holes of 84 % during high injection. This value is in rather good agreement with the ratio between the measured introduction rates for the $C_i^{(+/0)}$ and $C_i^{(-/0)}$ levels: $1.16\,\mathrm{cm}^{-1}/1.55\,\mathrm{cm}^{-1} = 75\%$. In this context it has to be noted that in contrast to the C_i donor level the C_iO_i donor level can be fully occupied by holes since the electron capture cross section of this defect is by 3 orders of magnitude smaller than the hole capture cross section at the DLTS-peak maximum temperature of 180 K (Tab. 6.1 and Sec. 6.4). Thus the C_iO_i concentration determined from the DLTS signal obtained after forward biasing of the diode is giving the correct defect concentration, i.e. all C_iO_i defects are in the positive charge state after a forward bias filling pulse at 180 K. Hence the measured introduction rates of the C_iC_s and the C_iO_i level can be used to determine the C_i sharing between O_i and C_s which is approx. 70% : 30%. Using the value of the ratio between the capture radii $\mathrm{R}(C_i,C_s)/\mathrm{R}(C_i,O_i) = 3.1$ quoted in [Dav87b] suggests that $[O_i]/[C_s] \approx 7$ in the studied material. This information is valuable since the concentrations of the most abundant impurities O_i and C_s are not known for this material (both expected to be below $5 \times 10^{15}\mathrm{cm}^{-3}$).

During the annealing an up to now not reported electron trap, E(35K), was observed. It emerges during the initial stages of the short term annealing and disappears with a rate similar to the C_i (compare Fig. 6.20). If the defect causing the level is assumed to be the intermediate state B of a two stage reaction

$$A \xrightarrow{k_a} B \xrightarrow{k_b} C \tag{6.4}$$

the following differential equations can be used to describe the annealing behavior:

$$\frac{d}{dt}[A] = -k_a[A]\,, \tag{6.5}$$

$$\frac{d}{dt}[B] = -\frac{d}{dt}[A] - k_b[B] \tag{6.6}$$

$$\text{and} \quad \frac{d}{dt}[C] = -k_b[B]\,, \tag{6.7}$$

where [A], [B] and [C] are the defect concentrations and k_a and k_b the first order kinetics rate constants. The solution for the concentration of B as function of time can be written as

$$[B]\,(t) = \frac{k_a}{k_b - k_a}\left(\exp\left(-k_a t\right) - \exp\left(-k_b t\right)\right)[A]\,(t{=}0) \tag{6.8}$$

where $[A]\,(t{=}0)$ denotes the initial concentration of A. The reasonable fit of Eq. 6.8 to the data displayed in Fig. 6.20 justifies the model. The fitted parameters are given in Tab. 6.11 along with the spectroscopic information on E(35K). Eq. 6.4 might simply reflect a double decay. However, the similarity of the time constants encountered in the C_i annealing and the decay of E(35K) could indicate a close relation between the unknown defect and C_i, respectively C_iC_s or C_iO_i.

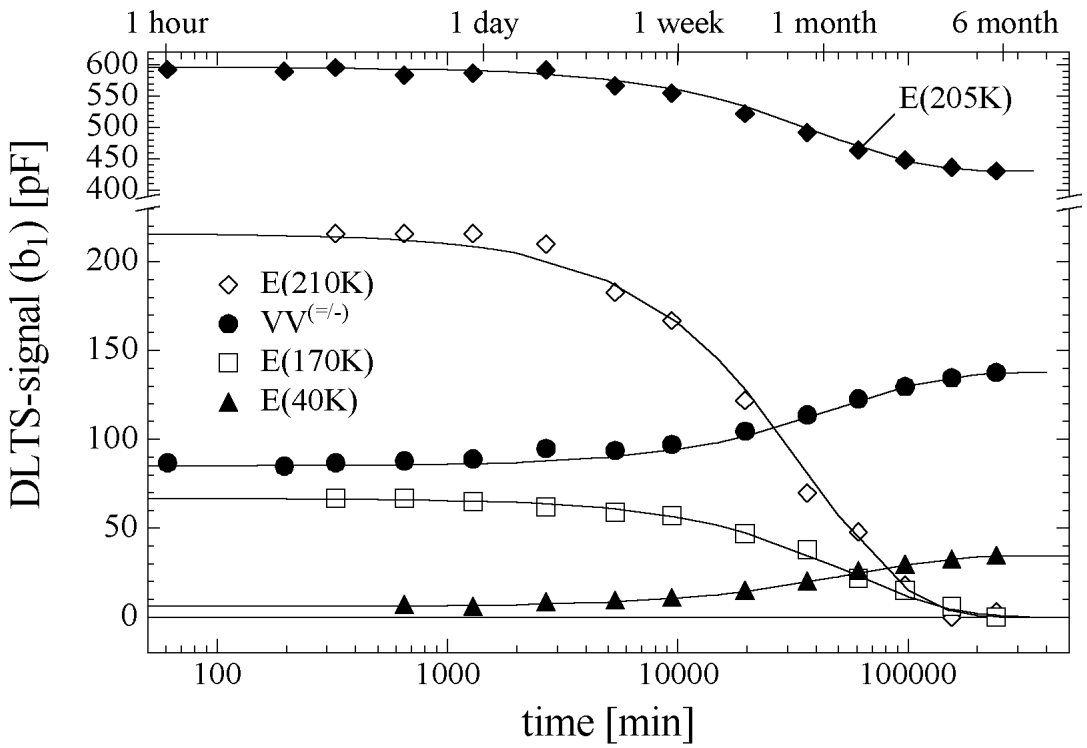

Figure 6.21: Evolution of the DLTS-peak heights during annealing at room temperature for defects displayed in Fig. 6.19 with annealing constants higher than 20 days. The DLTS signals for the levels E(170) and E(210) were extracted from *difference* spectra (see Fig. 6.22).

6.8.1.1 Long term annealing

The changes in the defect concentrations observed on a longer time scale are displayed in Fig. 6.21. In the same time interval the electron trap E(40) emerges, the $VV^{(=/-)}$ peak height increases and the height of the peak E(205) decreases. An analysis of the *difference spectra* reveals that the decrease of the E(205) peak height is due to the annealing of the levels E(170) and E(210). These levels give rise to peaks in the left and right hand shoulder of the E(205) peak, respectively. An example for a *difference spectrum* is displayed in Fig. 6.22. It was obtained by subtracting the DLTS spectrum measured after 70 days from the one measured 200 min after irradiation. Therefore the *difference spectrum* displays the spectrum of the defects that are annealed during this period of time. Using a full set of *difference spectra*[12] allows to determine the activation energy and the capture cross section of the annealed defect. The corresponding data for the levels E(170) and E(210) are given in Tab. 6.1. However, comparing simulations of the DLTS spectra with the parameters obtained from the Arrhenius plots (Fig. 6.22, right hand side) it becomes obvious that the level E(170) cannot be reproduced by assuming a single defect level while the level E(210) can. For this reason the parameters given in Tab. 6.1 for the level E(170) have to be treated with care. Whether the

[12]Difference spectra of all 18 DLTS coefficients for three different time windows T_W = 20, 200 and 2000 ms were used, compare Sec. 4.4.

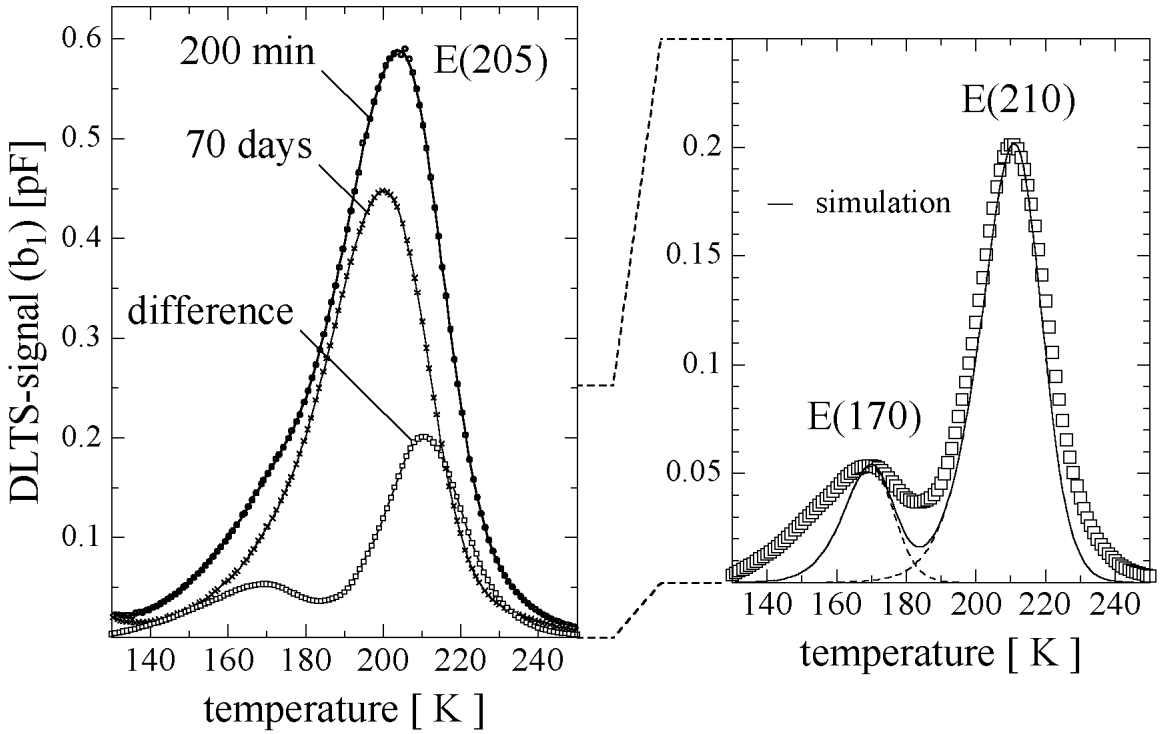

Figure 6.22: Example of a DLTS *difference spectrum*. Subtracting the spectrum measured after 70 days of annealing from the spectrum measured after 200 min results in a *difference spectrum* corresponding to defects that are annealed during this period of time. The right hand side of the figure displays an enlarged view of the difference spectrum with simulations for point defects (see text). Same sample and measurement parameters as displayed in Fig. 6.19.

deviation of the peak shape from the theoretically expected one is due to a superposition of defect levels with slightly different activation energies, the location of the defect in a volume that is exposed to lattice strain (clusters) [Sve97], the influence of an intercenter-charge exchange effect [Wat96] or another physical reason cannot be decided with the present data (see also discussion in Sec. 6.7 about the different peak heights of the divacancy levels after neutron irradiation).

Since the annealing of the levels E(210) and E(170) is taking place with the same time constant (this holds also for the annealing at 60°C, see Sec. 6.10) they may represent two different charge stages (double and single negative) of the same defect. In such a case it could be expected that the same mechanism which is responsible for the different peak heights of the $VV^{(=/-)}$ and $VV^{(-/0)}$ signals is leading to the difference in the peak heights of E(170) and E(210). This, however, are speculations that have to be proved by further experiments.

Finally it should be mentioned that in Sec. 6.9 some evidence will be given that the peak E(205) remaining after the annealing of E(170) and E(210) is composed of the two levels E(205a) and E(205b) (see Tab. 6.1). While the origin of E(205a) is unknown E(205b) is assigned to the $VV^{(-/0)}$.

6.8.2 TSC measurements

In parallel to the DLTS measurements described above the annealing at room temperature of a further neutron irradiated sample of the same type (WM2-3kΩcm) was investigated using the TSC method. Compared to the sample investigated with DLTS ($\Phi_{eq} = 2 \times 10^{11}\,\mathrm{cm}^{-2}$) the fluence was 50 times higher ($\Phi_{eq} = 1 \times 10^{13}\,\mathrm{cm}^{-2}$) in order to observe the evolution of the microscopic defects in a fluence range in which usually the changes of the effective doping concentration are monitored. It has to be mentioned again that TSC measurements on samples irradiated with a high fluence, like the one used here, can give only a qualitative figure of the defect kinetics since due to the very high defect concentration the sample cannot be kept fully depleted during a TSC scan. Thus the determination of defect concentrations is very difficult (compare Sec. 4.5 and Ref. [Fei97d])

Figs. 6.23 and 6.24 show the evolution of TSC spectra during annealing at room temperature within a time period ranging from 60 min to 145 days after irradiation. The filling was performed at 20 K (Fig. 6.23) or 50 K (Fig. 6.24) by applying forward bias to the sample (details are given in the figure captions). The normalized peak heights versus annealing time are depicted in Fig. 6.25 and the corresponding time constants for the exponential fits to the data (solid lines in Fig. 6.25) are given in Tab. 6.11. The time constants for the growth of the C_iO_i and the C_iC_s are in good agreement with the values extracted from the DLTS measurements. However, for the other defects a strong deviation in the time constants is observed. Due to the problems of TSC measurements in materials with high defect concentrations mentioned above the observed differences in the time constants are believed rather to be caused by an inaccuracy in the TSC measurement than by real physical effects. This is the reason why the time constants extracted from the TSC measurements are regarded as approximate values only (indicated by a $\approx$ in Tab. 6.11).

The most essential difference compared to the DLTS results is the observation of a further defect with a TSC peak maximum temperature of 43 K (labelled H(43K-TSC) in the spectra). This defect is not stable at room temperature. Its concentration decreases with a time constant of about 25 days. In the same period of time the electron trap E(40) (labelled E(34K-TSC) in the TSC spectra) emerges in the spectrum (see Fig. 6.25, lower part) indicating a relation between both defects. Since it is not possible to decide whether a defect is a hole or electron trap from the spectra obtained after filling of the traps by switching the diode to forward bias additional experiments were necessary.

A further detector of same type was irradiated with neutrons to a fluence of $\Phi_{eq} = 1 \times 10^{12}\,\mathrm{cm}^{-2}$ and annealed for 1000 min at room temperature. Since after such a small fluence the detector is not type inverted it is possible to inject only electrons into the silicon bulk by switching the diode to zero bias during the filling process.
The detector with a depletion voltage of 80 V was cooled down to 20 K under a reverse bias of 100 V. At 20 K zero bias was applied to the sample. Since under zero bias charge neutrality is required for the silicon bulk electrons drift into the material in order to compensate the positive space charge. The free electrons are immediately captured by the electron traps in the device with the highest capture cross section. After the electron injection the reverse bias of 100 V was applied again and the TSC spectrum was recorded. The resulting spectrum is displayed in Fig. 6.26 (solid line). While most of the electron traps are observed in the spectrum (E(30K-TSC), E(34K-TSC), $C_i^{(-/0)}$, $VO_i + C_iC_s$ and E(205)) no signal is observed at 43 K giving the first indication that the trap at 43 K is a hole trap. The evidence,

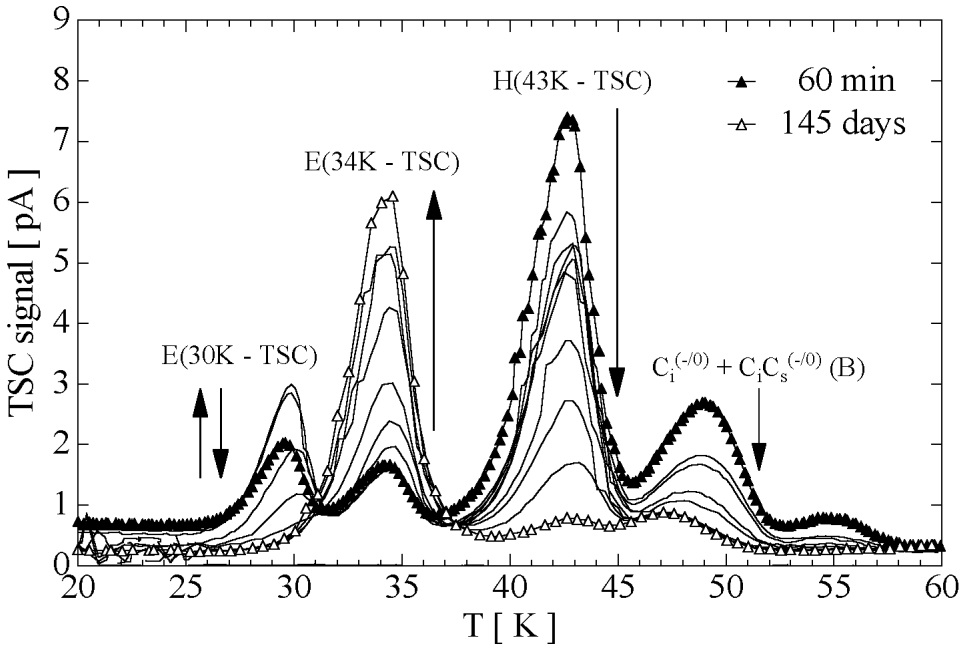

Figure 6.23: Evolution of the TSC spectra during annealing at room temperature within 145 days after neutron irradiation. The filling was performed at 20 K. (Sample: n-type, WM2-3kΩcm, neutron irradiated (UKE) $\Phi_{eq} = 1 \times 10^{13}\,\mathrm{cm}^{-2}$, filling: 1.7 mA for 30 s, bias: 100 V, heating: $\beta = 0.183$ K/s.)

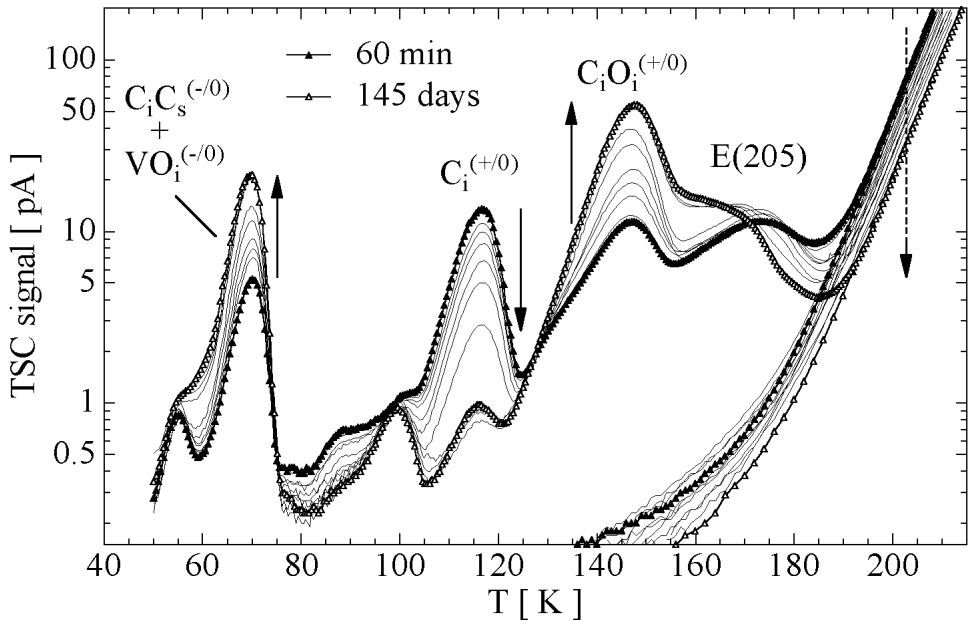

Figure 6.24: Evolution of the TSC spectra during annealing at room temperature within 145 days after neutron irradiation. The filling was performed at 50 K. (Sample: see Fig. 6.23)

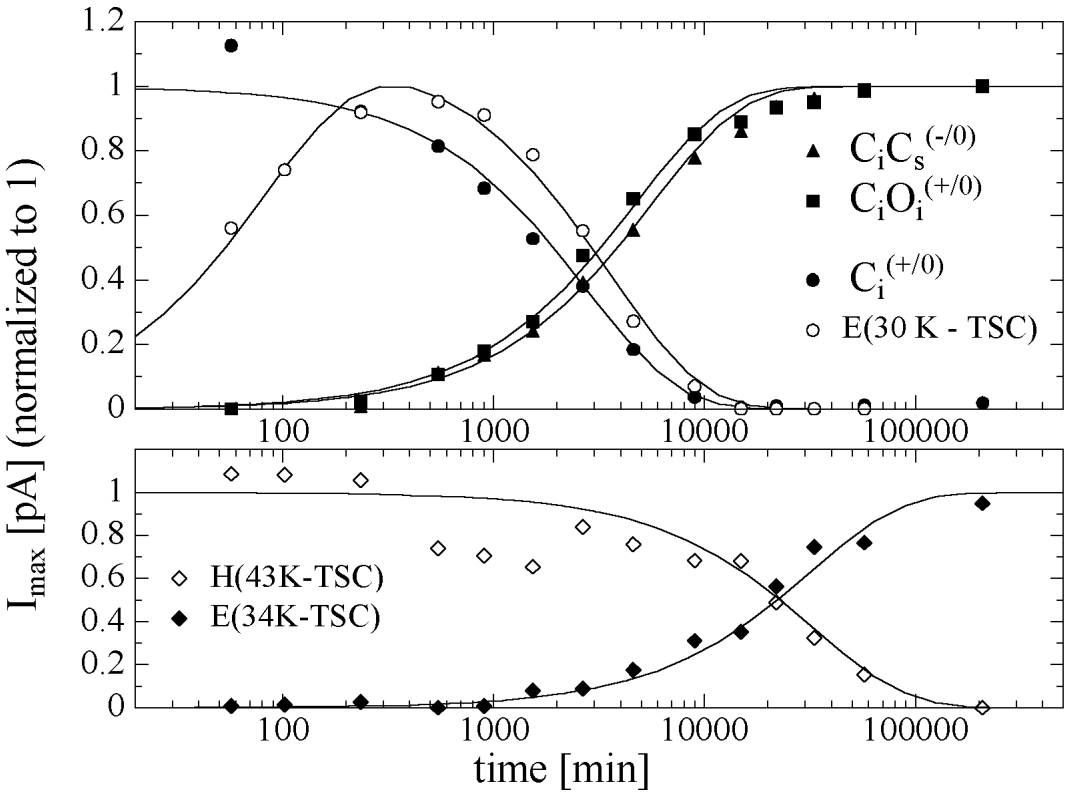

Figure 6.25: Evolution of TSC peak heights during annealing at room temperature within 145 days after neutron irradiation. The corresponding TSC spectra are shown in Figs. 6.23 and 6.24.

however, is given by the second measurement presented in Fig. 6.26. During the cooling of the sample under a reverse bias of 100 V the sample was illuminated from the rear side with a red light emitting diode (LED). At 20 K the LED was turned off and the spectrum was recorded. During the whole process the reverse bias of 100 V was applied to the sample.
As already explained in Sec. 6.4 the penetration depth of red light in silicon is only a few μm. Thus the electron-hole pairs are generated very close to the rear electrode. Due to the applied electric field the electrons drift to the rear electrode while the holes drift to the front electrode. Therefore only the holes traverse through the silicon bulk and can be captured by the defects. Consequently only hole traps are observed in the spectrum displayed in Fig. 6.26 (line with symbols). Along with the other hole trap signals the TSC peak at 43 K is observed clearly indicating that the defect is a hole trap.
The investigated sample was not type inverted. Hence the effective space charge density N_{eff} was positive. During the filling of the hole traps N_{eff} increases and consequently also the depletion voltage is increasing during the filling process. Therefore the applied voltage of $100V$ is not high enough to fully deplete the sample when all hole traps are occupied. This is the reason why only the lower limit of the defect introduction rate for the defect H(43K-TSC) (for DLTS: H(50)) could be given in Tab. 6.11.

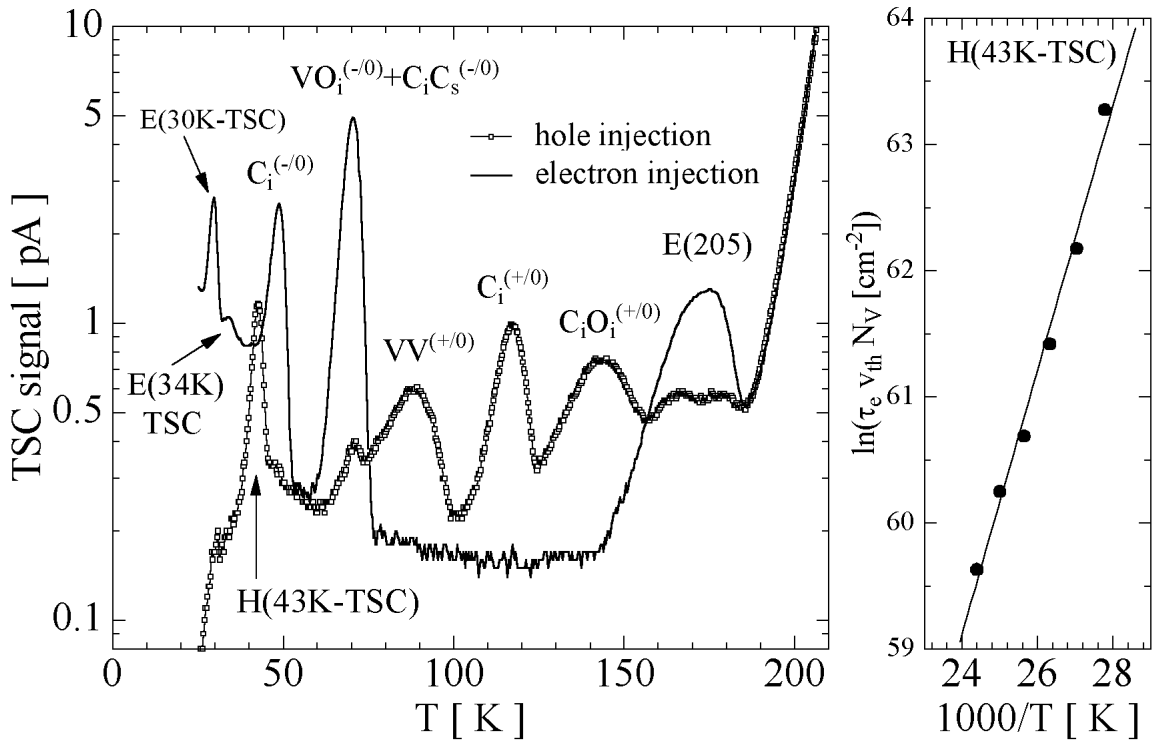

Figure 6.26: Left: TSC spectra obtained after hole or electron injection (see text). Right: Arrhenius plot for the hole trap H(43K-TSC) obtained with the delayed heating method. The resulting level parameters are $\Delta H' = 0.090\,\mathrm{eV}$ and $\sigma_p = 1.77 \times 10^{-15}\,\mathrm{cm}^2$.
(Sample: n-type, WM2-3kΩcm, neutron irradiated (UKE) $\Phi_{eq} = 1 \times 10^{12}\,\mathrm{cm}^{-2}$, annealing: 1000 min at room temperature, filling: see text, bias: 100 V, heating: $\beta = 0.183$ K/s.)

In order to determine the capture cross section and the activation energy for the defect a series of spectra was measured with the delayed heating method (compare Sec. 4.5). The resulting Arrhenius plot is shown in Fig. 6.26 and the corresponding defect parameters are $\Delta H' = 0.090\,\mathrm{eV}$ and $\sigma_p = 1.77 \times 10^{-15}\,\mathrm{cm}^2$.

6.9 Isochronal annealing

One detector of type WM2-3kΩcm, irradiated with 6×10^{11} n/cm^2 and stored for 6 months at room temperature, was studied in more detail using isochronal annealing. For this experiment a liquid nitrogen cryostat [AME] was used. Therefore levels with peaks below about 80 K (i.e. shallower than the VO_i level) could not be detected. The annealing temperature was increased from 353 to 633 K in 20 K steps each lasting 20 min. As can be seen in Fig. 6.27, a strong reduction of the E(205) peak amplitude was observed and up to 493 K this decrease was accompanied by a shift of the peak position to higher temperatures (Fig. 6.28). After the 493 K step an Arrhenius analysis of the remaining E(205b) peak and the annealed E(205a) peak (analysis of difference spectra shown in Fig. 6.28) result in the defect parameters given in

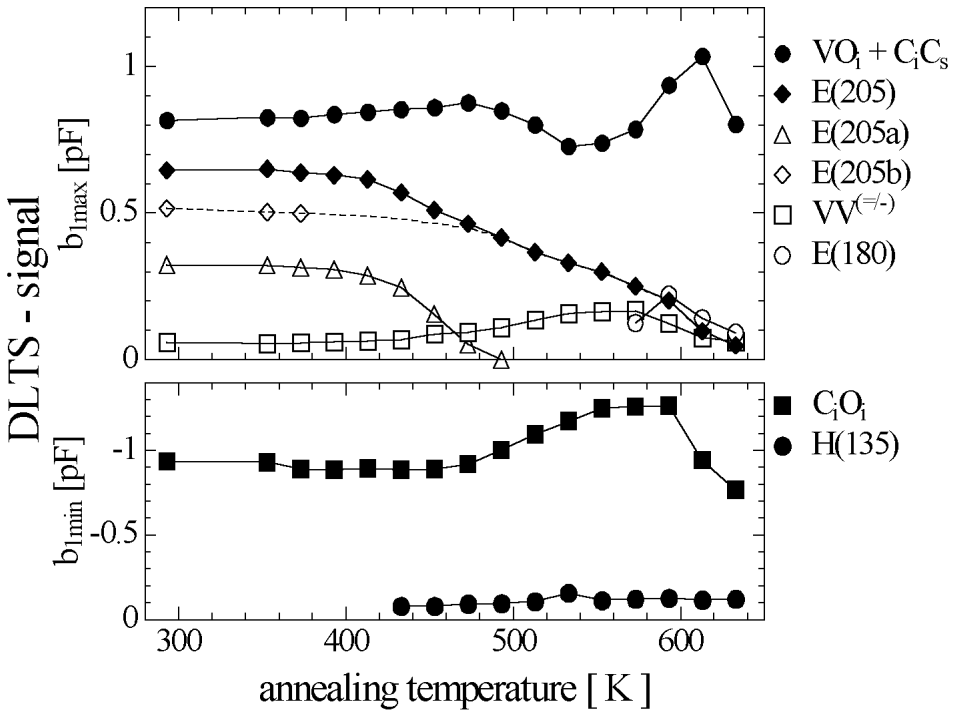

Figure 6.27: Changes of the DLTS-peak heights of the various electron (upper part) and hole traps (lower part) during the isochronal heat treatment. (WM2-2kΩcm; $\Phi_{eq} = 6 \times 10^{11}\,\mathrm{cm}^{-2}$; $U_R = -10V$;$U_P = 0\mathrm{V}$; $t_p = 1\,\mathrm{ms}$; $T_W = 200\,\mathrm{ms}$)

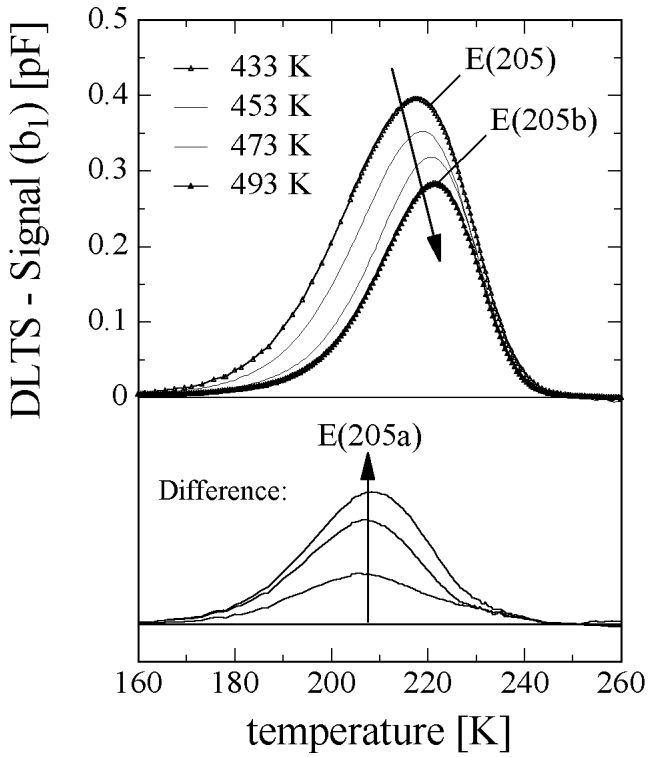

Figure 6.28: Evolution of the E(205) DLTS peak during an isochronal annealing experiment as observed after the annealing steps indicated in the legend. The DLTS signal remaining after the 493 K step is attributed to the level E(205b) which is assigned to $VV^{(-/0)}$. The lower part of the figure displays the difference spectra with respect to the spectrum measured after 433 K, i.e. the peak corresponding to the annealed level E(205a).
(WM2-3kΩcm, $\Phi_{eq} = 6 \times 10^{11}\,\mathrm{cm}^{-2}$; $t_p = 1\,\mathrm{ms}$; $T_W = 20\,\mathrm{ms}$)

This work				Defect	Data taken from literature				
Acronym	$\Delta H'$	T_{ann} [K]			$\Delta H'$	T_{ann} [K]	k_0	E_A	Reference
	[eV]	in	out		[eV]	out	[s^{-1}]	[eV]	
E(85a)	-0.18	–	>633	VO_i	-0.18	633	1.6×10^{15}	2.27	[Sve86, Kim77]
E(85b)	-0.17	≈300	533	C_iC_s	-0.17	533	2.5×10^{13}	1.70	[Son90b, Dav89]
E(180)	-0.35	573	633	V_2O(?)	-0.30	570...620	–	–	[Lee76, Awa86]
E(205a)	-0.39	–	473	unknown	–	–	–	–	–
E(205b)	-0.42	–	613	VV	-0.41	613	1.1×10^{9}	1.47	[Evw76]
H(135)	+0.28	≈ 433	>633	unknown	+0.31	-	–		[Fei98b]
H(180)	+0.36	≈300	>633	C_iO_i	+0.38	620...670	–	–	[Tro87, Moo77]

Table 6.12: Comparison of the annealing temperatures observed in this work with the ones taken directly from the literature or calculated by the activation energies E_A and frequency factors k_0 given in the literature. The annealing temperature T_{ann} is defined here as the temperature step at which the defect concentration drops below $1/e$ (37%) of the initial concentration (compare Sec. 3.5). Further data taken from the literature about the defects can be found in Appendix B.

Tab. 6.1 for E(205a) and E(205b). The same parameters have previously also been extracted from a two level fit to the peak E(205) in not annealed neutron irradiated silicon [Fre96]. Thus, the transformation of the E(205) peak in the temperature range up to 493 K can be attributed to the annealing of the E(205a) level, as indicated by the open triangles in Fig. 6.27. With further increasing temperature also the E(205b) level drops and is almost completely annealed after the last step at 633 K. Besides the good agreement of the level parameters with the ones obtained after ^{60}Co-gamma irradiation (Sec. 6.6) the annealing temperature further reassures the assignment of E(205b) level to the single charged divacancy $VV^{(-/0)}$ (see Tab. 6.12) because the trap is known to have an annealing temperature of about 610 K [Evw76]. Also the annealing behavior of the other observed defects tally with the defect assignments given in Tab. 6.12 where the annealing temperatures measured in this work are compared to the ones known from the literature. After the 573 K step a new level E(180) was observed which annealed out again after the 633 K step. This annealing behavior is consistent with that of the level attributed to the defect V_2O in [Awa86]. However, the ionization energy given for the level in [Awa86] is 0.30 eV while the one measured in this work is about 0.35 eV. Therefore, the assignment to V_2O is highly questionable and the origin of the level remains unknown. It has to be noted that for the isochronal heat treatment the used filling pulse duration of 1 ms was not sufficient to completely fill the $VV^{(=/-)}$ level.

6.10 Material dependence – Annealing at 60°C

In this section isothermal annealing studies on four different neutron irradiated materials are presented. The major differences between the investigated materials are the resistivity

and the oxygen concentration. The resistivity of the n-type materials ranged from 4 kΩcm to 6 Ωcm and the oxygen concentration from below $2 \times 10^{14}\,\mathrm{cm}^{-3}$ to $9 \times 10^{17}\,\mathrm{cm}^{-3}$ (the properties of the materials are summarized in Tab. 6.13 on page 182). All samples were annealed at 60°C in 4 annealing steps (cumulated annealing times of about 0, 80, 320, 1280 and 11000 min).
In the following (Secs. 6.10.1 to 6.10.4) the results on the individual materials will be briefly reported and compared in Sec. 6.10.5 with each other.

6.10.1 High resistivity FZ - 3 kΩcm

The evolution of the electron and hole trap spectra obtained on a neutron irradiated ($\Phi_{eq} = 2.8 \times 10^{11}\,\mathrm{cm}^{-2}$) high resistivity float zone sample of type WM3-3kΩcm during an isothermal annealing at 60°C is shown in Fig. 6.29. The corresponding difference spectra used for the analysis of the levels E(170) and E(210) are depicted in Fig. 6.30 and the defect introduction rates are listed in Tab. 6.14.

The present sample and the one used for the DLTS annealing study at room temperature (sample of type WM2-3kΩcm, see Sec. 6.8) were produced by the same manufacturer. Furthermore, the used silicon was obtained from the same company. Even the defect level E(45) was present in both samples before irradiation in comparable concentrations (here: $N_t = 5 \times 10^9\mathrm{cm}^{-3}$, in the other sample: $N_t = 6 \times 10^9\mathrm{cm}^{-3}$). Therefore the sample properties and especially the oxygen and carbon content of the material are regarded as very similar and the data obtained on both samples can be used to investigate the temperature dependence of the C_i annealing.
The averaged annealing time constant for the annealing of the C_i and the built up of C_iO_i and C_iC_s at room temperature (21°C) was $\tau_{21} = 78.5$ h (Sec. 6.8). For the annealing at 60°C the time constant is estimated to be $\tau_{60} \approx 120$ min. Using the two time constants a rough estimate of the activation energy for C_i migration can be calculated (Sec. 3.5). The analysis results in an activation energy of $E_A \approx 0.80\,\mathrm{eV}$ and a frequency factor of $k_0 \approx 2 \times 10^8\,\mathrm{s}^{-1}$. Although only two data points could be used for the analysis the result is in good agreement with the values of $E_A = 0.74\,\mathrm{eV}$ and $k_0 = 2 \times 10^8\,\mathrm{s}^{-1}$ published in [Son90a]. In the cited experiment the migration parameters were determined with the DLTS method on reverse biased low resistivity (0.7 Ωcm) electron irradiated n-type silicon diodes. Thus, as in the experiment presented here, the migration of the C_i was observed for the neutral charge state.

It has to be noted that the observation of the level $C_iC_s^{(-/0)}$(B) in the electron trap spectrum is due to the used measurement technique. The electron and hole trap spectra were measured during one temperature scan, i.e. at a certain temperature first the transient for the electron traps and then the one for the hole traps was recorded. The injection of holes during the hole trap filling process can lead to a configurational change of a fraction of the C_iC_s defect from configuration A to configuration B (details in Sec. 6.3). Thus the $C_iC_s^{(-/0)}(B)$ level can be observed in the following electron trap measurement. The electron and hole trap spectra presented in the previous sections were recorded separately during two independent temperature scans. Therefore the $C_iC_s^{(-/0)}$(B) level was not observed in those spectra unless, however, the sample was cooled down under reverse bias (compare Sec. 6.3).

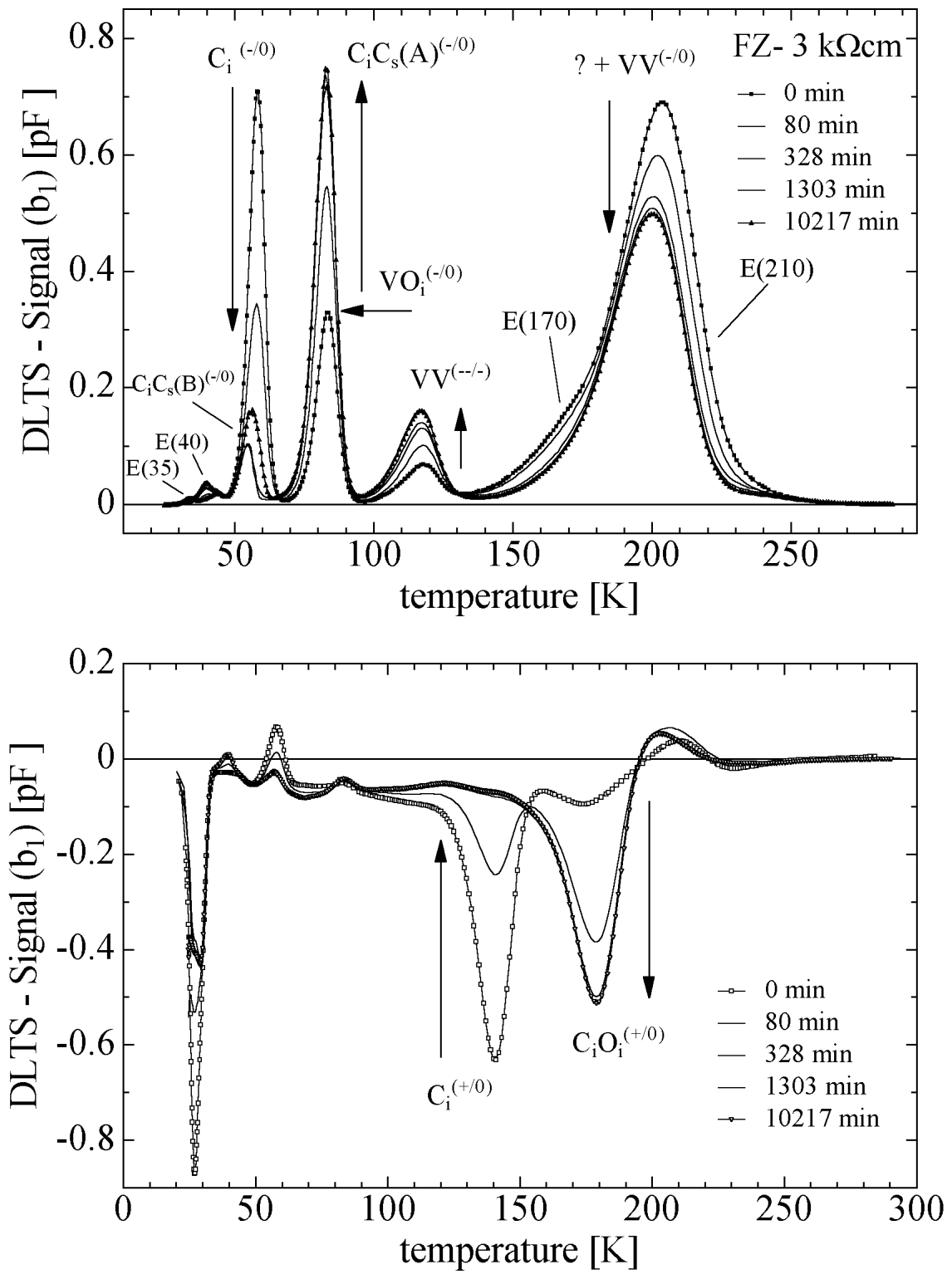

Figure 6.29: Evolution of DLTS-spectra at 60°C for a sample of type WM-3kΩcm. (M3D103; $\Phi_{eq} = 2.8 \times 10^{11}\,\mathrm{cm}^{-2}$(PTB); $U_R = -10\,\mathrm{V}$; $U_P = 0\,\mathrm{V}(+3\,\mathrm{V})$; $t_p = 100\,\mathrm{ms}(1\,\mathrm{ms})$; $T_W = 200\,\mathrm{ms}$)

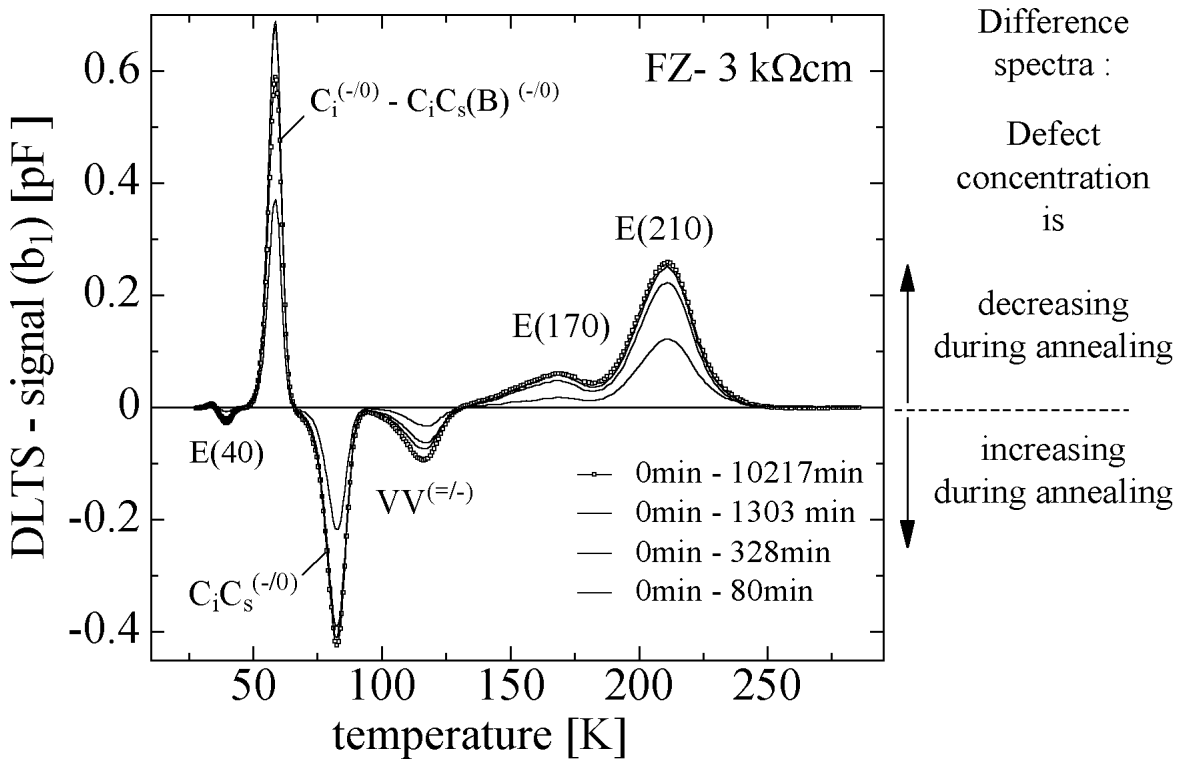

Figure 6.30: Difference spectra for electron traps obtained during 60°C annealing for a sample of type WM3-3kΩcm (see Fig. 6.29).

6.10.2 Low resistivity FZ - 6 Ωcm

In Fig. 6.31 DLTS spectra obtained during an isothermal annealing at 60°C on a neutron irradiated low resistivity (6 Ωcm) sample are shown. Since the used device was a Schottky-diode hole traps could not be measured by applying forward bias to the diode. In the lower part of the figure the difference spectrum between the measurement directly after irradiation and the one recorded after 11381 min annealing at 60°C is depicted. As for the high resistivity sample the annealing of two levels visible in the left and right hand shoulder of the peak around 205 K is observed. The introduction rates of all defects visible in Fig. 6.31 are displayed in Tab. 6.14 and will be compared in Sec. 6.10.5 to the introduction rates obtained on the other materials.
The negative signal of the DLTS spectrum below about 80 K is thought to be due to an up to now not understood problem with the Schottky contact. With increasing annealing time the perturbation by a negative DLTS signal becomes more pronounced. This was previously also observed on similar Schottky diodes during isochronal annealing studies [Luc97]. However, for devices with implanted or diffused junction such an effect has up to now not been reported.

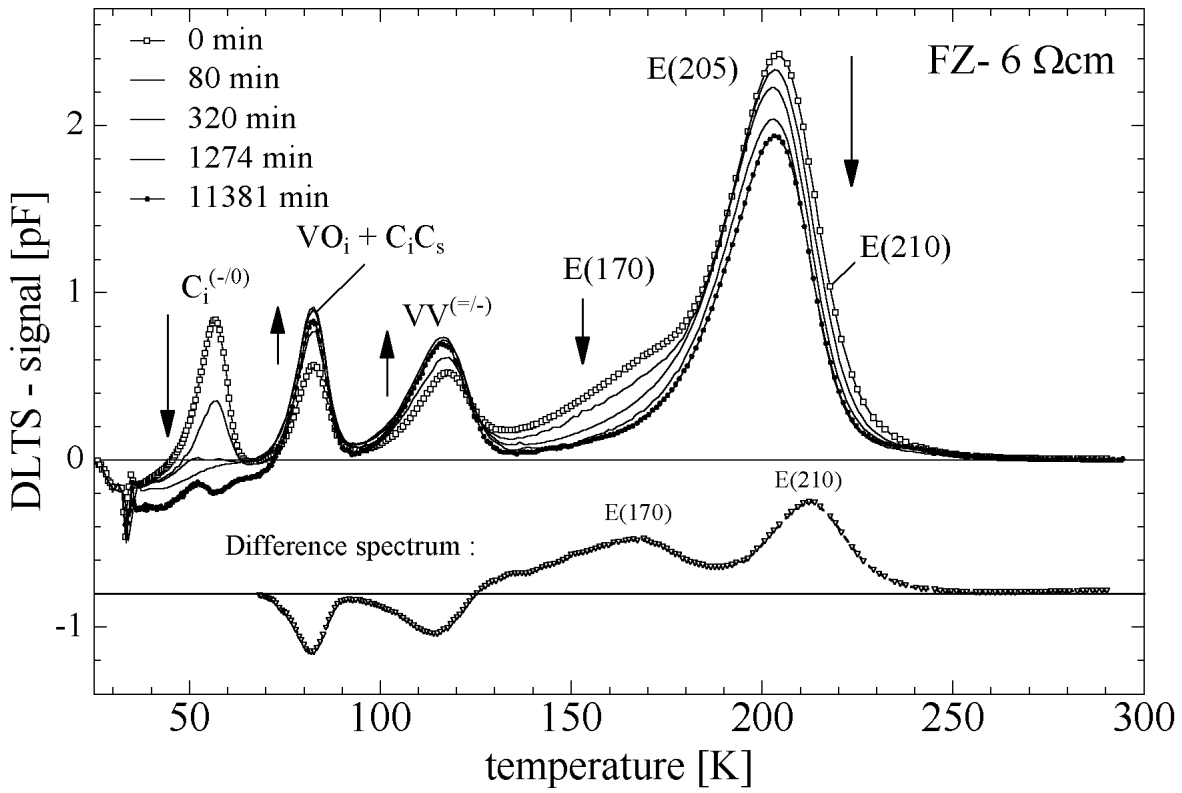

Figure 6.31: Upper part: Evolution of DLTS-spectra at 60°C for a sample of type WH-6Ωcm irradiated with fast neutrons. Lower part: Difference spectrum of spectra measured before annealing (0 min) and after 11381 min annealing at 60°C. (Sample: 933G06; WH-6Ωcm; $\Phi_{eq} = 1.35 \times 10^{13}\,\mathrm{cm}^{-2}$(PTB); $U_R = -10\,\mathrm{V}$; $U_P = 0\,\mathrm{V}$; $t_p = 100\,\mathrm{ms}$; $T_W = 200\,\mathrm{ms}$)

6.10.3 Cz silicon with high oxygen content - 110 Ωcm

The transformation of the DLTS spectrum of a neutron irradiated Schottky diode of type PH-110Ωcm (Czochralski silicon) during an annealing at 60°C is displayed in Fig. 6.32 together with the corresponding difference spectra. The oxygen concentration as measured by the SIMS method on a wafer of the same batch was $9 \times 10^{17}\,\mathrm{cm}^{-3}$ (see Sec. 4.1 on page 63). The huge peak at about 60 K is due to thermal double donors (TDD) that were already present in the material before irradiation. The theoretical aspects of these defects were described in Sec. 3.6.2 while the level parameters were topic of the discussion in Sec. 6.5. Although the peak superimposes the signal arising from the $C_i^{(-/0)}$ level, it was possible to determine the C_i concentration from the difference spectra. The C_i introduction rate together with the introduction rates for the other defects is given in Tab. 6.14.

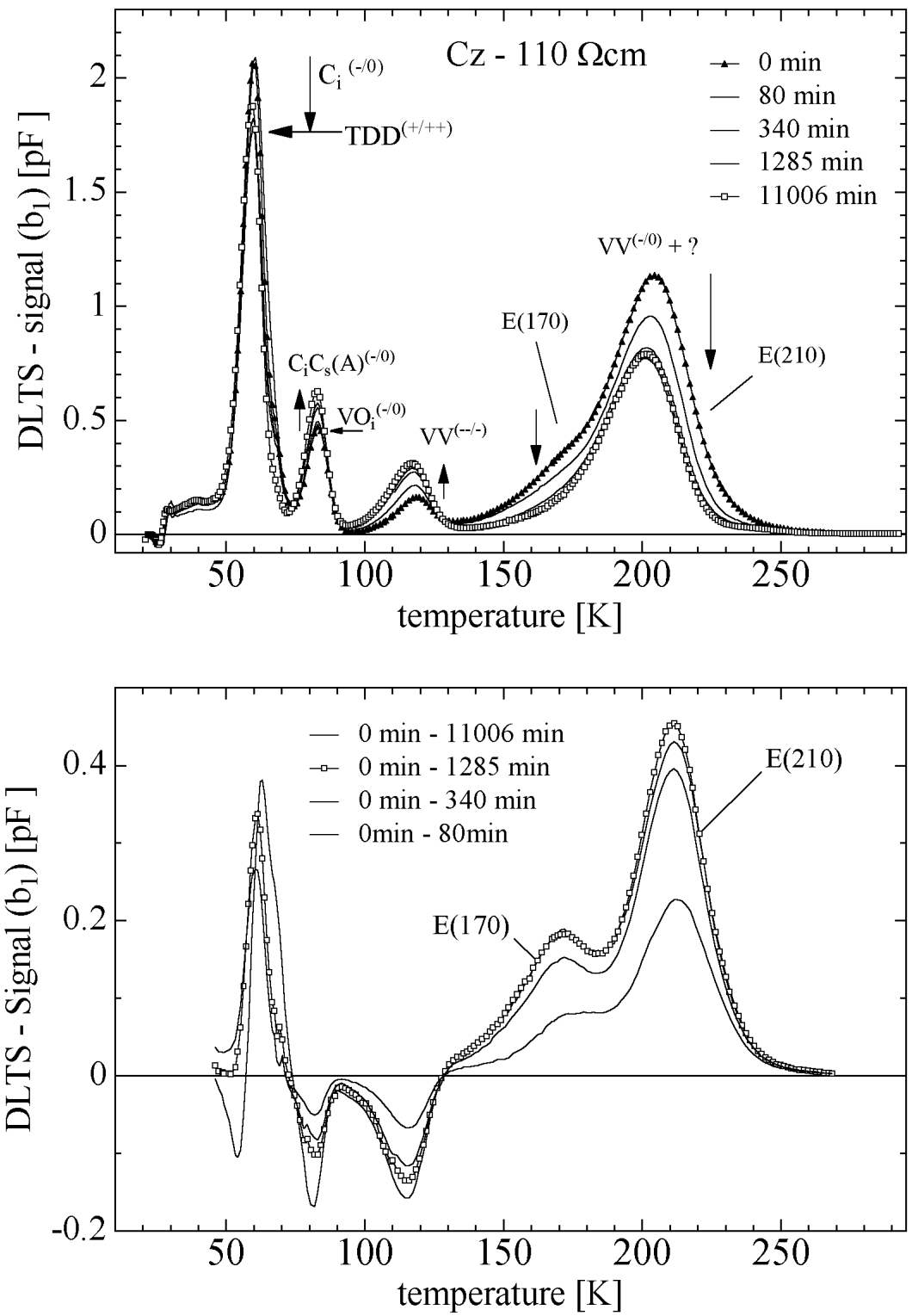

Figure 6.32: Evolution of DLTS-spectra at 60°C for a sample of type Cz-110Ωcm and corresponding difference spectra. (Sample: 963G17; PH-110Ωcm; $\Phi_{eq} = 1.3 \times 10^{12}\,\mathrm{cm}^{-2}$; $U_R = -10\,\mathrm{V}$; $U_P = 0\,\mathrm{V}$; $t_p = 100\,\mathrm{ms}$; $T_W = 200\,\mathrm{ms}$)

6.10.4 FZ silicon with low oxygen content - 4 kΩcm

Two Schottky diodes produced on high resistivity FZ silicon with a very low oxygen concentration ($[O_i] < 2 \times 10^{14}\,\mathrm{cm}^{-3}$, see Sec. 4.1) were irradiated with 24 GeV/c protons at the CERN - PS ($\Phi_{eq} = 7.1 \times 10^{10}\,\mathrm{cm}^{-2}$) and fast neutrons at the PTB ($\Phi_{eq} = 8.2 \times 10^{10}\,\mathrm{cm}^{-2}$). DLTS spectra obtained on the proton irradiated sample during an isothermal annealing at 60°C are shown in Fig. 6.33 along with the corresponding difference spectra. The most essential difference compared to the other materials is the emergence of the defect level E(240) during the isothermal annealing at 60°C and the very long annealing time constant for the C_i of 667 min (discussion in Sec. 6.10.5). The level parameters of E(240) were determined to be $\Delta H' = 0.463\,\mathrm{eV}$ and $\sigma_n = 3.5 \times 10^{-16}\,\mathrm{cm}^2$.
In Fig. 6.34 spectra measured on the neutron and proton irradiated sample after a heat treatment of 320 min at 60°C are compared with each other. Note that the presented data are not normalized to the fluence. All defects observed after the proton irradiation are also detected after the neutron irradiation. However, the introduction rates are different. The numbers displayed in the figure indicate the ratio between the defect concentrations observed after proton and neutron irradiation. For all defects the concentration observed after proton irradiation is higher than for the neutron irradiated sample although the equivalent fluence was lower for the proton irradiated one by about 15%. The most significant difference is found for the shallow level E(40) which was present in the proton irradiated sample in 7 times higher concentration.
However, it has to be noted that the measured introduction rates are not in agreement with recently published data in [Fre99]. In the cited article it was shown that the introduction rates for the level E(205) after 24 GeV proton and MeV neutron irradiation are about the same while for the levels E(120) and E(85) about 1.6 times more defects are produced after proton irradiation (measured after 80 min annealing at 60°C). The concentration of the levels E(40) and E(60) were not measured.
Since the experiment presented here is only based on one proton irradiated detector, an error in the proton fluence determination cannot be ruled out. According to the results presented in [Fre99] the introduction rate for the defect level E(205) is independent of the particle type. This would indicate that the proton fluence should be higher by a factor of 1.85 than the measured one ($\Phi_{eq} = 13.1 \times 10^{10}\,\mathrm{cm}^{-2}$ instead of $7.1 \times 10^{10}\,\mathrm{cm}^{-2}$). Using this fluence would result in a ratio of 1.7 between the introduction rate for the E(120) and E(85) levels between the proton and neutron irradiated sample which would be in good agreement with the value of 1.6 given in [Fre99].
In conclusion the discrepancies between the results presented here and the ones given in [Fre99] could be explained by a fluence calibration error. Thus, no statement about the introduction rates after proton irradiation will be given in this work. However, since the same defects are observed after neutron and proton irradiation, it is justified to use the annealing kinetics data extracted from the proton irradiated sample for the comparison of different materials in the next section.

6.10.5 Comparison

In Tab. 6.13 some properties of the devices used for the comparison of different materials are displayed. The defect introduction rates obtained from the spectra presented in the previous four sections are displayed in Tab. 6.14. Before discussing the differences between

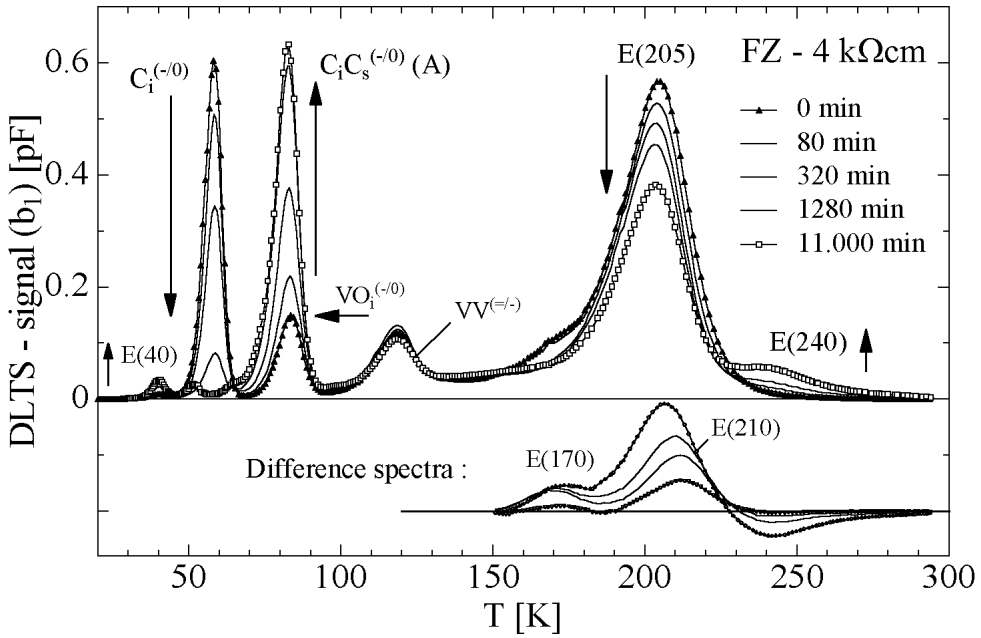

Figure 6.33: Evolution of DLTS-spectra at 60°C for a sample of type WH-4kΩcm irradiated with 24 GeV/c protons. (Sample: 972G01; WH-4kΩcm; $\Phi_{eq} = 7.1 \times 10^{10}\,\mathrm{cm}^{-2}$; $U_R = -10\,\mathrm{V}$; $U_P = 0\,\mathrm{V}$; $t_p = 100\,\mathrm{ms}$; $T_W = 200\,\mathrm{ms}$)

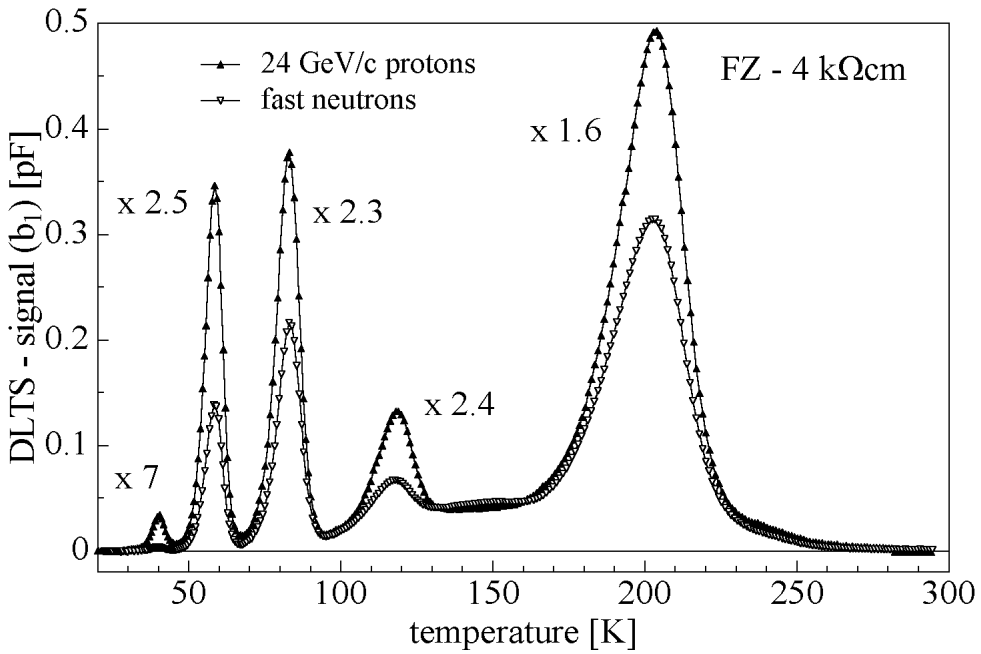

Figure 6.34: Spectra obtained after 24 GeV/c proton ($\Phi_{eq} = 7.1 \times 10^{10}\,\mathrm{cm}^{-2}$) and MeV neutron ($\Phi_{eq} = 8.2 \times 10^{10}\,\mathrm{cm}^{-2}$, PTB) irradiation of identical samples. Both samples were annealed for 320 min at 60°C. The numbers in the figure indicate the ratio between the defect concentrations in the proton and neutron irradiated sample. (Samples: WH-4kΩcm; annealing: 320 min at 60°C; $U_R = -10\,V$; $U_P = 0\,V$; $t_p = 100\,\mathrm{ms}$; $T_W = 200\,\mathrm{ms}$)

Sec.	Type of material		Producer of crystal	$[O_i]$ $\left[\frac{10^{16}}{\text{cm}^{-3}}\right]$	$[C]$ $\left[\frac{10^{16}}{\text{cm}^{-3}}\right]$	N_{eff} $\left[\frac{10^{12}}{\text{cm}^{-3}}\right]$	ρ $[k\Omega\text{cm}]$	Acronym of diode
6.10.1	high resistivity	n-FZ	Wacker	< 5	< 0.5	1.6	2.6	WM3-3k
6.10.2	low resistivity	n-FZ	Wacker	–	–	770	0.006	WH-6
6.10.3	high oxygen	n-Cz	Polovodice	90	0.5	39	0.11	PH-110
6.10.4	low oxygen	n-FZ	Wacker	< 0.02	< 3	1.0	4.3	WH-4k

Table 6.13: Properties and labelling of the materials used for the isothermal annealing studies at 60°C. Further details about the devices and materials can be found in Secs. 2.2.2 and 4.1.

Material	T_{ann}	C_i E(60)	VO_i E(85a)	C_iC_s E(85b)	$VV^{(=/-)}$ E(120)	? E(170)	$? + VV^{(-/0)}$ E(205)	? E(210)	C_iO_i H(180)
WM2-3kΩcm	21°C	1.55	0.69	0.41	0.28	0.18	1.09	0.55	1.10
WM3-3kΩcm	60°C	(1.17)	0.53	0.51	0.21	0.13	1.06	0.55	1.00
PH-110Ωcm	60°C	(0.34)	0.52	0.12	0.37	0.20	0.84	0.48	–
WH-6Ωcm	60°C	0.40	0.30	0.12	0.35	0.20	1.28	0.34	–
WH-4kΩcm	60°C	0.74	0.30	0.60	0.18	0.02	1.04	0.23	–

Table 6.14: Defect introduction rates in units of $[\text{cm}^{-1}]$ for neutron irradiated materials. T_{ann} indicates the annealing temperature. The values for C_i were measured directly after irradiation, the ones for C_iCs, C_iO_i and VO_i after annealing of the C_i and all other after a heat treatment of 320 min at 60°C, respectively 6 months after irradiation for the sample annealed at 21°C. Note that for Schottky diodes the C_iO_i introduction rate cannot be measured by standard DLTS (compare Sec. 2.3.3).

the materials it has to be mentioned again that the systematic errors in the determined defect introduction rates can easily reach 20% taking into account the errors in the fluence measurement and especially the problem of the lateral field extension discussed in Sec. 6.2.

The first important point to be noticed is that in all materials the same type of defects were found. The only exceptions were the levels E(240) in the material with the very low oxygen concentration (Sec. 6.10.4) and the not radiation induced thermal donors in the Czochralski silicon. The materials were obtained from different producers (Polovodice and Wacker). The devices were manufactured with different process technologies. The first two devices listed in Tab. 6.13 were processed by the MPI Munich and have implanted junctions while the other samples were Schottky diodes produced in our own laboratory without any high temperature step (Sec. 2.2.2).
Any influence of process induced defects or impurities should depend on the fabrication process of the materials and devices. Since different materials and devices have been used and the same type of defects were found it is e.g. not believed that process induced hydrogen or contaminations like transition metals play any major role in the presented data.

Introduction rates

Comparing the introduction rates of the two standard[13] materials WM2-3kΩcm and WM3-3kΩcm the data show a good agreement. The only difference is the introduction rate for the C_i which is lower in the sample WM3-3kΩcm. This sample was irradiated with a higher fluence ($\Phi_{eq} = 2.8 \times 10^{11}\,\mathrm{cm}^{-2}$) than the other one ($\Phi_{eq} = 2 \times 10^{11}\,\mathrm{cm}^{-2}$). The higher defect concentration leads to a higher compensation making the DLTS measurements at low temperatures difficult (see Sec. 6.2). Although the compensation effect is taken into account for the analysis, a systematic error cannot be ruled out. This is the reason why the value is given in brackets only.

Compared to the high resistivity standard FZ all other defects show a smaller introduction rate of C_i. For the Cz silicon (PH-110Ωcm) the measured concentration might be lower for two reasons. First, the material contains a very high oxygen concentration (Tab. 6.13) leading to a very fast transformation of C_i into C_iO_i. Therefore already at room temperature a significant fraction of the C_i could already be annealed before the first measurement. The second reason is the superposition of the C_i and the thermal donor peak (Fig. 6.32) which makes the analysis of the C_i difficult. However, these arguments do not hold for the other materials (WH-6Ωcm and WH-4kΩcm). The main difference compared to the standard material is the type of diode. While the first two diodes listed in Tab. 6.13 are devices with implanted contacts the later three devices were Schottky diodes. However, this fact is not thought to influence the defect concentration and thus the question why the C_i introduction rate is lower in these materials remains open.

For the low (6 Ωcm) and high resistivity (3 kΩcm) FZ silicon about 30% of the measured C_i concentration is transformed into C_iC_s while in the material with the very low oxygen concentration this is the case for about 80% of the C_i. As expected, in the material with the low oxygen concentration the rate for the reaction $C_i + O_i \longrightarrow C_iO_i$ is reduced while that of the reaction $C_i + C_s \longrightarrow C_iC_s$ is increased.

The introduction rate of the level E(205) as measured after 320 min annealing at 60°C are about the same in all materials. The slightly higher introduction rate in the low resistivity material WH-6Ωcm is attributed to a contribution of VP defects to the signal at 205 K [Luc97] while there is no explanation for the slightly lower introduction rate in the CZ material PH-110Ωcm.

The introduction rates for the levels E(170) and E(210) are strongly suppressed in the material with the very low oxygen content WH-4kΩcm. Furthermore the annealing of the level E(205) does not reach a saturation after the 320 min annealing step like for the other samples. So far, no explanation was found for this behavior.

Annealing kinetics

Although the defect annealing was only studied at two different temperatures (21°C and 60°C) the obtained annealing time constants can be used to roughly estimate the activation energy and the frequency factor for the defect annealing kinetics (compare Sec. 3.5). In

[13]Both materials are high resistivity (3 kΩcm) FZ. This kind of material is presently used for silicon detectors in HEP experiments.

	T_{ann}	C_i – annealing	E(170)	E(210)
WM2-3kΩcm	21°C	78.5 hours	37 days	31 days
WM3-3kΩcm	60°C	120 min	210 min	170 min
PH-140Ωcm	60°C	–	150 min	160 min
WH-6Ωcm	60°C	90 min	200 min	260 min
WH-4kΩcm	60°C	670 min	–	–

Table 6.15: Defect annealing time constants. T_{ann} indicates the annealing temperature. A first order kinetics is assumed for all annealing processes. In cases where a first order approach was not possible, no time constants are given.

Tab. 6.15 the time constants[14] for the C_i transformation into C_iC_s and C_iO_i are displayed. As can be seen, the time constant depends on the material. For the material with the very low oxygen content the time constant is about 6 times higher than in the standard material. This reflects the fact that the C_i has to migrate over longer distances in the material with the low oxygen content in order to react with a C_s or a O_i.
In Sec. 6.10.1 the activation energy and the frequency factor for the carbon annealing were determined:

$$C_i\text{-annealing:} \qquad E_A \approx 0.80\,\text{eV} \quad \text{and} \quad k_0 \approx 2 \times 10^8\,\text{s}^{-1}.$$

These data are in agreement with published data (Sec. 6.10.1) and it is noted again that the frequency factor reflects perfectly the long range migration of the C_i (see Sec. 3.5).

The time constants for the annealing of the defects E(170) and E(210) are also displayed in Tab. 6.15. As can be seen the time constants for for E(170) and E(210) agree very well indicating a close relation between both levels. The time constants for E(170) and E(210) averaged over all materials annealed at 60°C (192 min) and the average value obtained at room temperature (34 days) were used to determine the annealing parameters. The activation energy and the frequency factor were found to be:

$$\text{E(170), E(210) - annealing:} \qquad E_A \approx 1.03\,\text{eV} \quad \text{and} \quad k_0 \approx 1 \times 10^{14}\,\text{s}^{-1}.$$

The frequency factor is in the order of the most abundant phonon frequency and thus clearly indicates a *single jump process*. The most probable explanation for the decrease of the levels E(170) and E(210) is therefore the decay of a defect. A long range migration like observed for the C_i annealing can be ruled out.
In the next chapter it will be shown that the annealing of the levels E(210) and E(170) is most probably related to the short term annealing of the effective doping concentration and the leakage current.

[14]It is noted that the time constants at 60°C are a rough estimate since only a few annealing steps have been undertaken during the isothermal heat treatments: ≈ 0, 80, 320 , 1280 and 11000 min at 60°C.

Chapter 7

Relation between Macroscopic Detector Properties and Microscopic Defects

The microscopic investigations presented in the last chapter led to the detection and characterization of about 20 different radiation induced defect levels. Now the question arises how these defects are related with the radiation induced changes in the leakage current, the effective doping concentration and the charge collection efficiency.

In order to reveal such relations two different approaches will be followed. On the one hand the annealing studies are used to compare the microscopic defect kinetics with the results of the annealing experiments on macroscopic parameters. On the other hand absolute macroscopic properties are calculated by using the measured defect properties.
However, for the second approach severe problems arise. It is necessary to know all defect properties and especially the electron and the hole capture cross section (σ_n and σ_p). These could unfortunately only be measured for a few defects within this work (see Tab. 6.1). For most of the defects only one cross section is known. Furthermore, the radiation induced changes in the macroscopic detector properties were investigated at room temperature while the features of the microscopic defects were – depending on their individual level position – measured at much lower temperatures. Therefore, the defect properties have to be extrapolated to room temperature. As was shown in Sec. 6.4 the capture cross sections of the defects can exhibit a strong temperature dependence. Thus, the extrapolated defect parameters might be afflicted with errors.

Recently level parameters obtained on proton irradiated silicon have been reported by Hallén et al. [Hal96]. They have measured the electron and hole capture coefficients $c_{n,p}$ ($c_{n,p} = \sigma_{n,p} \cdot v_{th,n,p}$, see Sec. 3.4) for the dominant defects VO_i, CO_i and VV over a wide range in temperature (see Tab. B.2 on page 225). The corresponding defect properties as extrapolated to 20°C are given in Tab. 7.1. In Sec. 6.4 the temperature dependence of the $C_iO_i^{(+)}$ electron capture coefficient was measured. An extrapolation to 20°C results in a value of $c_n(C_iO_i^+) = 4 \times 10^{-10}\mathrm{cm}^3\,\mathrm{s}^{-1}$ which is in good agreement with the value of $c_n(C_iO_i^+) = 3.4 \times 10^{-10}\,\mathrm{cm}^3\mathrm{s}^{-1}$ extrapolated from the data published by Hallén et al. (see Tab. 7.1).

Defect	$VO_i^{(-/0)}$	$VV^{(-/0)}$	$C_iO_i^{(+/0)}$
$\Delta H_{n,p}$[eV]	-0.164	-0.421	+0.339
X	0.29	0.33	0.89
$c_n[\mathrm{cm^3 s^{-1}}]$	2.40×10^{-7}	5.24×10^{-8}	3.44×10^{-10}
$c_p[\mathrm{cm^3 s^{-1}}]$	4.27×10^{-6}	3.64×10^{-7}	3.84×10^{-9}
$e_n[\mathrm{s^{-1}}]$	2.90×10^{9}	2.76×10^{4}	3.30×10^{-4}
$e_p[\mathrm{s^{-1}}]$	1.33×10^{-2}	2.61×10^{1}	1.51×10^{5}
(a) $f_{e,h} = \frac{e_{p,n}}{e_n + e_p}$	4.57×10^{-12}	9.45×10^{-4}	2.19×10^{-9}
(b) $\frac{e_n \cdot e_p}{e_n + e_p}$ [$\mathrm{s^{-1}}$]	1.33×10^{-2}	2.61×10^{1}	3.30×10^{-4}
(c) $\frac{c_{n,p} \cdot e_{p,n}}{e_n + e_p}$ [$\mathrm{cm^3 s^{-1}}$]	2.40×10^{-7}	5.23×10^{-8}	3.84×10^{-9}

(a) Fraction of defects occupied with electrons (holes for C_iO_i).
(b) Gives generation current density if multiplied with $q_0\, N_t$.
(c) Gives inverse electron (hole for C_iO_i) trapping time if multiplied with N_t.

Table 7.1: Parameters of defects at 20°C as extrapolated from the data given in [Hal96]. Further details can be found in Tab. B.2 on page 225.

In the following discussion the defect properties at 20°C for the defects VO_i, C_iO_i, and for the single charged divacancy $VV^{(-/0)}$ are taken from [Hal96] (Tab. 7.1). Furthermore, the C_iC_S defect is treated like the VO_i defect, i.e. the level parameters given for the VO_i in [Hal96] are used. For all other defects the properties measured in this work are used (Tab. 6.1). The capture cross sections are assumed to be temperature independent and the (electron resp. hole) cross section that could not be measured is set to the value of the (hole resp. electron) cross section that was measured. The defect introduction rates are taken from the investigations on the high resistivity FZ silicon as listed in Tab. 6.11 for the neutron irradiations and in Tab. 6.9 for the ^{60}Co-gamma irradiations.

For all calculations presented in this chapter the standard Shockley-Read-Hall theory for defects in semiconductors (Sec. 3.4) is used. It has however to be mentioned that recently another approach has been suggested for the description of the defects related with *cluster damage*, namely the levels $VV^{(=/-)}$, E(170), E(205a), $VV^{(-/0)}$ and E(210). This so-called *intercenter charge transfer model* [Wat96] is not used here.

		Neutron irradiation		^{60}Co–gamma irradiation	
Defect	$\frac{e_n \cdot e_p}{e_n + e_p}$ [s^{-1}]	g_t [cm^{-1}]	α_t [A cm^{-1}]	g_t [Gy^{-1}cm^{-3}]	α_t [A Gy^{-1}cm^{-3}]
$VO^{(-/0)} + C_iC_s^{(-/0)}$	1.3×10^{-2}	1.09	2.3×10^{-21}	68×10^{6}	1.5×10^{-13}
E(170)	$> 4.1 \times 10^{-2}$	0.18	$> 1.2 \times 10^{-21}$	–	–
E(205a) + $VV^{(-/0)}$	2.6×10^{1}	1.50	6.3×10^{-18}	1.6×10^{6}	6.7×10^{-12}
E(210)	$> 2.3 \times 10^{0}$	0.55	$> 2.1 \times 10^{-19}$	–	–
$C_iO_i^{(+/0)}$	3.3×10^{-4}	1.10	5.8×10^{-23}	46×10^{6}	2.4×10^{-15}
H(220) – 0.48 eV	$< 1.5 \times 10^{1}$	0.08	$< 2.0 \times 10^{-19}$	–	–
H(220) – 0.53 eV	$< 5.3 \times 10^{2}$	0.08	$< 6.8 \times 10^{-18}$	–	–
	$\sum_t \alpha_t$:		$\approx 1.3 \times 10^{-17}$		6.8×10^{-12}

Table 7.2: Calculated contributions of the different defects to the leakage current (α–value) at 20°C. Note that the hole capture cross section for the levels E(170) and E(210) and the electron capture cross section for the level H(220) were assumed to be equal to the measured electron, respectively hole, capture cross section in order to make a calculation possible (see text). For the defect H(220) two different sets of level parameters have been measured (see Sec. 6.1). For completeness both sets have been taken into account here.

7.1 Leakage current

7.1.1 Magnitude of current

The contribution α_t of a defect to the α-value (Sec. 5.1) is given by

$$\alpha_t = g_t \, q_0 \, \frac{e_n \cdot e_p}{e_n + e_p} \tag{7.1}$$

with g_t being the generation rate and e_n and e_p the electron and hole emission rates (for details see Secs. 3.4 and 3.7). In Tab. 7.2 the expected contributions of the different defects to the α–value at room temperature are summarized.

^{60}Co-gamma irradiation

After gamma irradiation the divacancy is expected to be the main source for the bulk generation current while the contributions of the defects VO_i, C_iC_s and C_iO_i are negligible. Compared to the measured value of $\alpha = (1.4 \pm 0.2) \times 10^{-11}$ A/cm^3 Gy (Sec. 5.2) the calculated value of $\alpha \approx 7 \times 10^{-12}$ A/cm^3 Gy is by a factor of two smaller. This difference could of course arise from an uncertainty in the defect parameters but may also be due to a contribution from an up to now not detected defect close to the middle of the band gap. This possibility is supported by very recent experiments reported by Fretwurst et al. [Fre98]. The authors showed that the value of the leakage current after ^{60}Co-gamma irradiation is depending on the oxygen concentration of the material. With increasing oxygen content a decrease

in leakage current is observed. This can be interpreted as an evidence for a further impurity related defect contributing to the leakage current. The existence of such a defect is also the basis of a theoretical model describing the increase in leakage current as well as the changes in the effective doping concentration of materials with different oxygen content after ^{60}Co-gamma irradiation [Mac99]. In this model the defect is assumed to be the divacancy-oxygen complex (V_2O). However, the definite identification of this defect is still missing.

Neutron irradiation

The accuracy of the calculated α-value for neutron irradiations suffers from the not known temperature dependence of the defect properties for the levels E(170), E(210) and H(220). Furthermore, it is noted again that the unknown values of the hole, respectively electron, capture cross sections were set to the measured electron, respectively hole, capture cross sections for the calculation. Since the only information from the experiments was $\sigma_p > \sigma_n$ for all three defects (Sec. 6.1) the values given in Tab. 7.2 correspond to the lower (E(170) and E(210)) or upper (H(220)) limit for the current generation.
Under the assumptions given above the calculated α-value $\alpha_{80/60}$ (i.e. after an annealing of 80 min at 60°C) is $\approx 1.3 \times 10^{-17}$ A/cm which is only about 3 times smaller than the measured value of 4×10^{-17} A/cm.

7.1.2 Annealing

^{60}Co-gamma irradiation

Within a time period ranging from 3 days to 200 days after ^{60}Co-gamma irradiation no annealing of the leakage current was observed [Fei97a]. Furthermore in this work the same divacancy concentration was measured 3 months and one year after ^{60}Co-gamma irradiation. These experimental facts agree with the conclusion drawn above about the divacancy being at least a significant contributor to the observed leakage current.

Neutron irradiation

The annealing of the leakage current after neutron irradiation was discussed in Sec. 5.1.3. There it was shown that the long term current annealing can be parameterized with a function consisting of an exponential and a logarithmic term (Eq. 5.4). While no microscopic defect was observed to anneal with a logarithmic time dependence four defect levels were found to anneal with about the same time constant as measured for the exponential term in the leakage current annealing. The level E(40) emerges and the levels H(50), E(170) and E(210) vanish within the same period of time (compare Tab. 6.1). However, only the two levels closest to the middle of the band gap, namely E(170) and E(210), can contribute significantly to the leakage current.
The annealing parameters k_0 (frequency factor) and E_A (activation energy) for the *macroscopic* current annealing and the *microscopic* defect annealing process are displayed in Tab. 7.3. The last two columns in the table give the corresponding references to the individual sections. The similar annealing parameters obtained for the annealing of E(170) and E(210) and the macroscopic properties α_I (short term annealing of leakage current) and N_A (short term annealing of effective doping concentration) can be interpreted as a strong indication that all three processes are closely related to each other.

Property	$k_0[s^{-1}]$	$E_A[eV]$	Section	Page
macroscopic property:				
α_I – current annealing	$1.2^{+5.3}_{-1.0} \times 10^{13}$	(1.11 ± 0.05)	5.1.3	99
N_A – *beneficial annealing*	$2.4^{+1.2}_{-0.8} \times 10^{13}$	(1.09 ± 0.03)	5.3.2	112
N_Y – *reverse annealing*	$1.5^{+3.4}_{-1.1} \times 10^{15}$	(1.33 ± 0.03)	5.3.3	115
microscopic defects:				
C_i – annealing	$\approx 2 \times 10^8$	≈ 0.80	6.10.1	175
E(170), E(210) – annealing	$\approx 1 \times 10^{14}$	≈ 1.03	6.10.5	180

Table 7.3: Annealing parameters k_0 (frequency factor) and E_A (activation energy) for macroscopic detector properties (α_I, N_A, N_Y) and microscopic defects (see text and referred section in last column).

A relation between the level E(210) and the leakage current was previously also reported by Watts et al. [Wat96]. During an isochronal annealing experiment ($\Delta T = 10°C$; $\Delta t = 15$ min) the authors observed the annealing of the level E(210)[1] and a drop in leakage current at about 70°C. Furthermore, very recently the same correlation was demonstrated by an isothermal annealing study at 60°C by Fretwurst et al. [Fre99]. They demonstrated that the annealing of the level E(210)[2] in a CZ silicon sample is related with the annealing of the leakage current.

Now the question arises whether the annealing of this level is only related or responsible for the observed changes in the leakage current. The absolute change in the α-value is $\alpha_I = (1.23 \pm 0.06) \times 10^{-17}$ A/cm (Sec. 5.1.3) and the introduction rate of E(210) is $0.55\,cm^{-1}$ (Tab. 6.11). Assuming a temperature independent electron capture cross section for E(210) ($\sigma_n = 5.02 \times 10^{-15}cm^2$, Tab. 6.11) it is possible to calculate the hole capture cross section needed to come up for the experimentally observed leakage current. The resulting value of $\sigma_p(E(210)) = 3 \times 10^{-13}\,cm^2$ is not unreasonable. Taking into account the strong correlation in the microscopic and macroscopic annealing behavior, it is very likely that the defect E(210) is *generating* the leakage current corresponding to the fraction α_I of the overall α-value.

The annealing experiments presented in Sec. 5.1.3 indicated a saturation value of $\alpha = 6 \times 10^{-18}$ A/cm after a 2 months lasting annealing at 106°C (compare Fig. 5.2). This value coincides very well with the calculated value of $6.3 \times 10^{-18}\,A/cm$ for the contribution of the defects E(205a) and $VV^{(-/0)}$.
In Tab. 7.2 a further contribution of the defect H(220) of about the same value is indicated. However, the electron capture cross section of this defect is unknown and the other level parameters are afflicted with an uncertainty (Sec. 6.1). Furthermore, the annealing behavior of this defect is not known. It could already be annealed after a 2 months lasting heat treatment at 106°C.

[1] Labelled E70 in [Wat96]; Given level parameter: $E_C - (0.45 \pm 0.02)\,eV$.
[2] Labelled E4b in [Fre99]; Given level parameters: $E_C - 0.46\,eV$, $\sigma_n = 1 \times 10^{-14}\,cm^2$.

		Neutron irradiation		^{60}Co–gamma irradiation	
Defect	$f_{e,h}$	g_t [cm^{-1}]	$f_{e,h} \times g_t$ [cm^{-1}]	g_t [Gy^{-1}cm^{-3}]	$f_{e,h} \times g_t$ [Gy^{-1}cm^{-3}]
Introduction of negative space charge:					
$VO^{(-/0)} + C_iC_s^{(-/0)}$	4.6×10^{-12}	1.09	5.0×10^{-12}	68×10^6	3.1×10^{-4}
E(170) ($\sigma_p \equiv \sigma_n$)	$> 4.7 \times 10^{-8}$	0.18	$> 8.5 \times 10^{-9}$	–	–
E(205a) + $VV^{(-/0)}$	9.5×10^{-4}	1.50	1.4×10^{-3}	1.6×10^6	1.5×10^3
E(210) ($\sigma_p \equiv \sigma_n$)	$> 9.4 \times 10^{-5}$	0.55	$> 5.2 \times 10^{-5}$	–	–
Introduction of positive space charge:					
$C_iO_i^{(+/0)}$	2.2×10^{-9}	1.10	2.4×10^{-9}	46×10^6	1.0×10^{-7}
H(220) - 0.48 eV ($\sigma_p \equiv \sigma_n$)	$< 3.4 \times 10^{-3}$	0.08	$< 2.7 \times 10^{-4}$	–	–
H(220) - 0.53 eV ($\sigma_p \equiv \sigma_n$)	$< 1.7 \times 10^{-1}$	0.08	$< 1.4 \times 10^{-2}$	–	–

Table 7.4: Calculated contributions of various defects to the effective doping concentration N_{eff} at 20°C (see text). Note that the levels E(170) and E(210) are assumed to be acceptors while the level H(220) is a assumed to be a donor.

7.2 Effective doping concentration

With the electron and hole emission rates e_n and e_p and the defect introduction rate g_t the introduction rate of the effective doping concentration (N_{eff}/Φ_{eq}) can be calculated by

$$N_{eff}/\Phi_{eq} = \sum_{\text{donors}} g_t \underbrace{\frac{e_n}{e_n + e_p}}_{f_h = 1 - f_e} - \sum_{\text{acceptors}} g_t \underbrace{\frac{e_p}{e_n + e_p}}_{f_e}. \tag{7.2}$$

Here f_h and f_e denote the fractions of the defects occupied by holes or electrons, respectively (for details see Secs. 3.4 and 3.7). Donors not occupied by electrons (≡ occupied by holes) contribute positive space charge while acceptors occupied by electrons contribute negative space charge. In Tab. 7.4 the expected fluence normalized contributions of the defects to the effective doping concentration at 20°C are summarized.

As discussed for the leakage current the contributions of the VO_i, the C_iC_s and the C_iO_i to the effective doping concentration are negligible. For the carbon related defects this finding is also supported by the observed annealing behavior. In Sec. 6.10 it was shown that the annealing time constant for the carbon related defects is strongly depending on the carbon and oxygen concentration of the material. However, such a dependence was not observed for the annealing time constants of the macroscopic changes in the leakage current and the effective doping concentration. Thus a significant influence of the carbon related defects on the leakage current or the effective doping concentration after neutron irradiation can be ruled out.

7.2.1 Short term annealing

As shown in Tab. 7.3 and discussed already in the last section the annealing parameters for the short term annealing of the leakage current, the short term annealing of the effective doping concentration and the annealing of the defects E(210) and E(170) are very similar suggesting a correlation between these three processes. Under the assumption that the annealing of the defect E(210) is responsible for the observed changes in the leakage current the hole capture cross section was calculated to be $\sigma_p(E(210)) = 3 \times 10^{-13}\,\mathrm{cm}^2$. Taking this value for granted the occupation of the defect with electrons at room temperature can be calculated. The resulting introduction rate of negative space charge is $3.1 \times 10^{-3}\,\mathrm{cm}^{-1}$. Compared to the experimentally determined introduction rate for the short term annealing of the effective doping concentration of $g_a = (1.81 \pm 0.14) \times 10^{-2}\,\mathrm{cm}^{-1}$ (Sec. 5.3.2) the value is by a factor of 6 too small.
This could indicate that the defect is only contributing a small part to the observed changes in the effective doping concentration or that the electron capture cross section is temperature dependent.
In the latter case the electron capture cross section at room temperature is an unknown value. However, under the assumption that the defect is responsible for the changes in N_{eff} as well as for the observed changes in the leakage current both capture cross sections can be calculated. Using the measured macroscopic parameters g_a and α_I, the defect introduction rate g_t and the defect level position $\Delta H'$ the cross sections are determined to be (Eqs. 7.1, 7.2 and 3.27):

$$\text{E(210) at 20°C}: \qquad \sigma_n = 8.6 \times 10^{-16}\,\mathrm{cm}^2 \quad \text{and} \quad \sigma_p = 3.1 \times 10^{-13}\,\mathrm{cm}^2.$$

In conclusion a perfect agreement between microscopic and macroscopic observations would be given if the electron capture cross section at room temperature is about 6 times smaller than the value measured in this work at about 210 K ($\sigma_n = 5.0 \times 10^{-15}\,\mathrm{cm}^2$). Such a prediction needs however to be checked by a measurement of the temperature dependence of the electron capture cross section.

7.2.2 Stable damage – Donor removal

The radiation induced changes of the effective doping concentration after neutron irradiation that do not anneal after irradiation were named *stable damage* in Chapter 5. The *stable damage* consists of a so-called *incomplete donor removal* and an introduction of negative space charge proportional to fluence (see Sec. 5.3.4).

^{60}Co-irradiation

The observed changes in the effective doping concentration after ^{60}Co-irradiation show a similar behavior like the ones measured after neutron irradiation. A *donor removal* and the introduction of negative space charge is observed leading to the reduction of the positive space charge in n-type material and finally to type inversion, i.e. the effective space charge changes its sign from positive to negative (see e.g. [Fre98, Mac96a]).
There exist only a few measurements of the negative space charge introduction rate. In [Fre98] introduction rates of $2.3 \times 10^3\,\mathrm{cm}^{-3}\mathrm{Gy}^{-1}$ and $1.0 \times 10^4\,\mathrm{cm}^{-3}\mathrm{Gy}^{-1}$ have been reported for high resistivity FZ silicon. As for the leakage current (Sec. 7.1) the calculated introduction rate

for the negative space charge of $1.5 \times 10^3\,\mathrm{cm}^{-3}\mathrm{Gy}^{-1}$ is too small to explain the experimental data giving a further hint that so far not all defects relevant for the macroscopic changes in the detector properties have been detected.

Neutron irradiation: Stable damage

The introduction rate of (*stable*) negative space charge was determined in Sec. 5.3.4 to be $g_c = (1.49 \pm 0.04) \times 10^{-2}\,\mathrm{cm}^{-1}$. It was found that the introduction rate does not depend on the oxygen concentration of the material after neutron irradiation. Therefore, it can be assumed that the defect (or defects) responsible for the negative space charge observed after neutron irradiation are related to the *cluster damage*. They are located inside or near clusters and are composed of vacancies and/or interstitials only. They are not impurity related.
Taking into account only defects not annealing (*stable*) at room temperature the calculated introduction rate of negative space charge is $1.4 \times 10^{-3}\,\mathrm{cm}^{-1}$ (Tab. 7.4). This value is one order of magnitude smaller than the experimentally observed effect. Furthermore, contrary to the observed experimental facts, the parameters measured for the hole trap H(220) suggest an introduction of positive space charge with a rate of about $1.4 \times 10^{-2}\,\mathrm{cm}^{-1}$. However, the defect H(220) could also be an acceptor and not a donor as assumed in (Tab. 7.4). In such a case the introduction rate of negative space charge would be about $8 \times 10^{-2}\,\mathrm{cm}^{-1}$ and thus much higher than the experimentally observed value of $1.49 \times 10^{-2}\,\mathrm{cm}^{-1}$.
In conclusion the level H(220) might be a good candidate for the introduction of the negative space charge. However, the uncertainty in the level parameters of this defect make a clear statement about its role for the macroscopic detector properties so far impossible.

Neutron irradiation: Donor removal - Role of oxygen

The experimental data presented in Sec. 5.3.4 clearly revealed the increased radiation hardness of oxygen rich material with respect to the *stable damage* component of the effective doping concentration. In order to understand the mechanisms that lead to this improvement one has to take a closer look on the microscopic defect kinetics that underly the macroscopic changes of the detector properties.

High energy hadron irradiation generates two basically different kinds of defects in silicon.
On the one hand there are the so-called *disordered regions* or *clusters* which arise at the end of the range of any heavy recoil atom. They are composed of divacancies, diinterstitials and higher order intrinsic defect complexes. The maximum impurity concentration in the silicon is in the order of $10^{18}\,\mathrm{cm}^{-3}$ (oxygen rich Cz). Since the size of a disordered region is expected to be in the order of $10^{-19}\,\mathrm{cm}^3$ [Mes92] it is very unlikely that more than one impurity atom is located inside a cluster. Therefore no or only a minor influence of the impurities on the disordered regions is expected.
On the other hand there are the migrating interstitial silicon atoms (I) and vacancies (V) that have escaped the disordered regions or the recoil tracks and migrate through the silicon lattice. They are almost completely trapped at the impurity atoms and form point defects. Therefore the influence of oxygen is expected to be seen in those components of the radiation damage that are caused by point defects as e.g. the donor removal.
Besides oxygen interstitial (O_i) the most abundant non dopant impurity in detector grade silicon is carbon substitutional (C_s). Therefore the main reactions for the migrating silicon interstitials (I), vacancies (V) and carbon interstitials (C_i), all mobile at room temperature,

are:

I **reactions**	V **reactions**	C_i **reactions**
$I + C_s \rightarrow C_i$	$V + O \rightarrow VO$	$C_i + C_s \rightarrow C_iC_s$
$I + V_2 \rightarrow V$	$V + P_s \rightarrow VP$	$C_i + O_i \rightarrow C_iO_i$
$I + VP \rightarrow P_s$	$V + VO \rightarrow V_2O$	$(C_i + P_s \rightarrow C_iP_s)$
$I + VO \rightarrow O$	$V + V_2O \rightarrow V_3O$	
$I + V_3O \rightarrow V_2O$	$V + V_2 \rightarrow V_3$	
$(I + P_s \rightarrow P_i)$		

The relevant reactions for the donor (phosphorus) removal at room temperature are $V + P_s \rightarrow$VP and $C_i + P_s \rightarrow C_iP_s$. Both reactions remove the shallow donor P_s into a defect that is not charged in the space charge region and therefore has no influence on the effective doping concentration. Because V and C_i do also react with oxygen and carbon it is easy to understand that with a high oxygen concentration the phosphorus removal is strongly suppressed since most of the V and C_i are gettered at O_i and not at a phosphorus atom.

To corroborate these considerations with more quantitative values simulations of the defect kinetics taking into account all reactions listed above and described in very detail in [Mac96a] have been performed. The calculations were realized with the algorithm and the capture radii taken from [Mac96a], the impurity concentrations as given in Tab. 4.1 and the primary introduction rates for vacancies, divacancies and interstitials as measured in this work (Chapter 6). The reactions $C_i + P_s \rightarrow C_iP_s$ and $I + P_s \rightarrow P_i$ were omitted because their experimental evidence in detector grade silicon is still missing (for details see [Mac96a]). With such a model the parameter N_C can be calculated by:

$$N_C = [VP] + g_c \times \Phi_{eq}. \tag{7.3}$$

Here [VP] denotes the concentration of VP resp. the removed phosphorus concentration. The second term stands for the generation of an up to now unknown acceptor (see discussion about *stable damage*).
To compare the model with the experimental data it is very instructive to concentrate on the donor removal since the acceptor generation ($g_c \times \Phi_{eq}$) could up to now not be correlated with any microscopic defect and is therefore not integrated in the modeling. This is done in Fig. 7.1. Here the remaining donor concentration N_{donor} is plotted versus the fluence. The values were extracted from the experimental data plotted in Fig. 5.18 by subtracting the individual acceptor concentration $g_C \times \Phi_{eq}$ (see Tab. 5.9) for each data point. This gives the removed donor concentration. Consequently the remaining donor concentration N_{donor} in the material is obtained by subtracting this value from the initial effective doping (donor)concentration $N_{eff,0}$:

$$\begin{aligned} N_{donor} &= N_{eff,0} - (N_C - g_C\Phi_{eq}) \\ &= N_{eff,0} - N_{C0} \times (1 - \exp(-c\Phi_{eq})). \end{aligned} \tag{7.4}$$

The solid lines in Fig. 7.1 represent fits to the data points and the dashed ones the model predictions calculated by subtracting the VP concentration from the initial phosphorus concentration $[P]_{initial}$ (set to $N_{eff,0}$):

$$[P](\Phi_{eq}) = [P]_{initial} - [VP](\Phi_{eq}). \tag{7.5}$$

Two essential differences between the experimental and simulated data become obvious which will be described under A) and B) in the following:

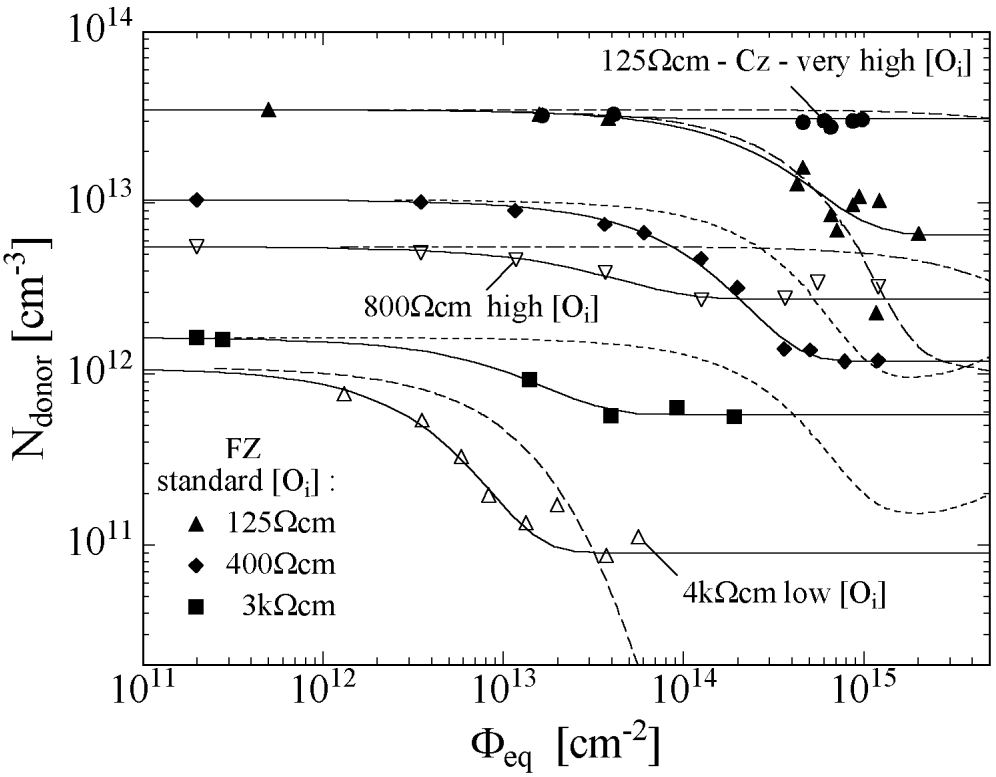

Figure 7.1: Donor concentration N_{donor} plotted versus fluence for some of the used materials (see Tab. 4.1). The solid lines represent fits to the data points while the dashed ones display the model predictions. For the FZ material with only an upper limit of impurity contents given in Tab. 4.1 (filled symbols) $[O_i]$ and $[C_s]$ were set to $5 \times 10^{15}\,\mathrm{cm}^{-3}$.

A) The non removable donor concentration

In contrast to the experimental data the simulations for standard $[O_i]$ material always lead to an almost complete donor removal. After high fluences, depending on the oxygen and carbon concentration, a small fraction of electrically active phosphorus due to the reaction $I + VP \rightarrow P_S$ is predicted. This, however, cannot explain the experimental data for most of the materials as e.g. is demonstrated in Fig. 7.1 for the 125 Ωcm (filled triangles) and 3 kΩcm (filled squares) FZ silicon. Here the data and the simulations (dashed lines) differ significantly in the high fluence range.

To explain the non removable fraction of donors one could think about a reservoir of other donors than phosphorus that are not influenced by the migrating I and V. Another possibility could be that a fraction of the phosphorus atoms is removed into an up to now unknown oxygen related complex defect that anneals out during the first days after irradiation. Thereby it releases the phosphorus back into its original role of a donor. If this should be true, a second irradiation of the sample would lead to a further removal of donors. Due to the lack of experimental data with repeated irradiations and annealing procedures performed on oxygen rich samples such a *rate dependence* can at this time not be ruled out.

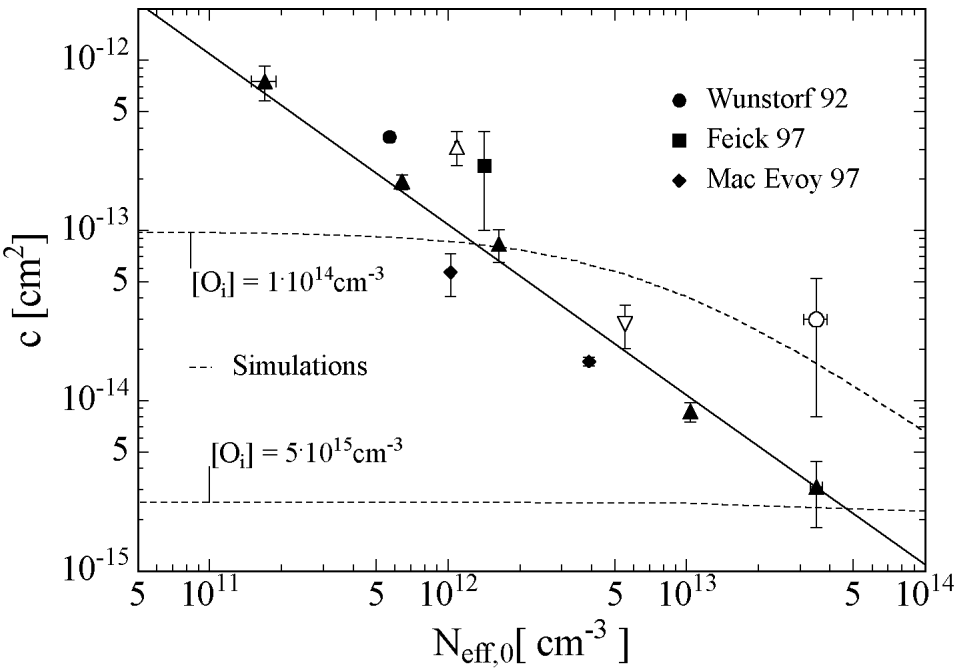

Figure 7.2: Donor removal constant c plotted versus the initial effective doping concentration $N_{eff,0}$ (same symbols used as in Fig. 5.20). The dashed lines represent the model predictions for materials with $[C_s] = 5 \times 10^{15}\,\mathrm{cm}^{-3}$. Since the donor removal in the model is not necessarily exponential c has been taken as the reciprocal fluence where a fraction of 1/e (37%) of the initial donor concentration is removed. The external data are taken from [Fei97a, Wun92] and [Mac96a].

B) The donor removal constant c

In Fig. 7.1 it can also be seen that for most of the materials the donor removal process is much faster than expected by the model (dashed lines). The donor removal is described by Eq. 7.4 as an exponential exhaustion of a donor concentration N_{C0}. Therefore it is very instructive to take a closer look at the exponential term, governed by the donor removal constant c, which determines the speed of the donor removal. In Fig. 5.20 on page 126 the removal constant c is plotted versus the *removable* donor concentration N_{C0}. The experimental data clearly display a reciprocal dependence on the donor concentration, correspondingly $c \times N_{C0}$ is a constant (see also Tab. 5.9). A weighted fit to the data of the FZ material with the standard oxygen concentration (filled triangles) reveals $N_{C0} \times c = (7.5 \pm 0.6) \times 10^{-2}\,\mathrm{cm}^{-1}$. This value has also a physical meaning. For small fluences Eq. 7.4 can be approximated by $N_{donor} \approx N_{eff,0} - (N_{C0} \times c)\Phi_{eq}$. Therefore $N_{C0} \times c$ denotes the *initial donor removal rate*[3]. In comparison with the model the initial donor removal rate should correspond to the initial rate for the process $V + P \rightarrow VP$.
However, in order to compare the experimental and the simulated data a problem arises since for the model $N_{eff,0}$ is used as input parameter and not N_{C0}. Therefore the removal constant c is plotted in Fig. 7.2 against the effective doping concentration $N_{eff,0}$. This representation also offers the possibility to include experimental data taken from the literature where most

[3]Not to be confused with the donor removal constant (c).

often the parameter N_{C0} is not used or given. A weighted fit to the data of the FZ material with the standard oxygen concentration (filled triangles) reveals a value of $N_{eff,0} \times c = (10.9 \pm 0.8) \times 10^{-2}\,\mathrm{cm}^{-1}$. As can be seen, it is expected from the simulation (dashed lines) that the donor removal constant is nearly independent of the initial donor concentration and increases with decreasing oxygen concentration. The expectation of a constant removal rate c is obvious: The probability for a vacancy to be captured at a phosphorus atom (donor removal process) and not at an oxygen atom in the case of $[O] \gg [P]$ is roughly proportional to the ratio $[P]/[O]$. Therefore also the initial generation of VP defects ($c \times [P]_{initial} \equiv c \times N_{eff,0}$) is proportional to the ratio $[P]/[O]$. In conclusion c is expected to be $\propto 1/[O]$ and independent of $[P]$.
The observed dependence on the oxygen concentration is not in accordance with such a theoretical prediction (see Fig.5.20). While for the FZ with the low $[O_i]$ content the removal constant is, as expected, higher than for the standard FZ, for the material with the high and very high $[O_i]$ concentration the values are not lower than in the standard material.
However, the main discrepancy between model and experiment is the reciprocal dependence of c on N_{C0} (resp. $N_{eff,0}$). Such a behavior means from the microscopic defect kinetics point of view that the initial generation of VP defects is independent of the phosphorus concentration itself. Such a behavior is only expected when phosphorus has the highest impurity concentration in the material as indicated by the simulation with the very low oxygen concentration in Fig. 7.2. Here phosphorus is the main getter for vacancies and the generation of VO defects is negligibly small. However, in such a case a linear fluence dependence is expected. This is by no means displayed by the experimental data. Without any exception an exponential fluence dependence is observed (see e.g. the exponential fits in Figs. 5.18 and 7.1).
Supplementation of the microscopic model with the so far neglected defect reactions leading to C_iP_s and P_i (see above) will, of course, lead to higher removal rates. However, the reciprocal dependence of the donor removal constant c on the effective doping concentration cannot be explained with such additional reactions. In other words: the observed donor removal in the oxygenated materials and the reciprocal dependence of the removal constant on the doping concentration remains a riddle giving indication that the present understanding of the microscopic processes and their impact on the detector properties is still incomplete or some systematic errors, not yet taken into account, may play an important role.

7.2.3 Reverse annealing

The increase of negative space charge on a long time scale at room temperature ($\tau_Y \approx 1.5$ years) was subject of the investigations presented in Sec. 5.3.3. In order to find a correlation between this so-called *reverse annealing* and microscopic defects a sample of type WM2-3kΩcm was irradiated with a neutron fluence of $\phi_{eq} = 1 \times 10^{13}\,\mathrm{cm}^{-2}$ (UKE). Subsequently the annealing of the radiation induced changes in the effective doping concentration ΔN_{eff} and TSC spectra were monitored in parallel.
Fig. 7.3 displays the evolution of ΔN_{eff} during a 290 days lasting annealing period at room temperature (left hand side) and a subsequent isothermal heat treatment at 80°C (right hand side). After 10 days at 80°C the measured depletion voltage was 3.5 V. Since the determination of such small depletion voltages is not very accurate (e.g. it could not be determined whether the detector is inverted or not) the last point is afflicted with a big error. However, the overall annealing is in good agreement with the parameterization given in Sec. 5.3.

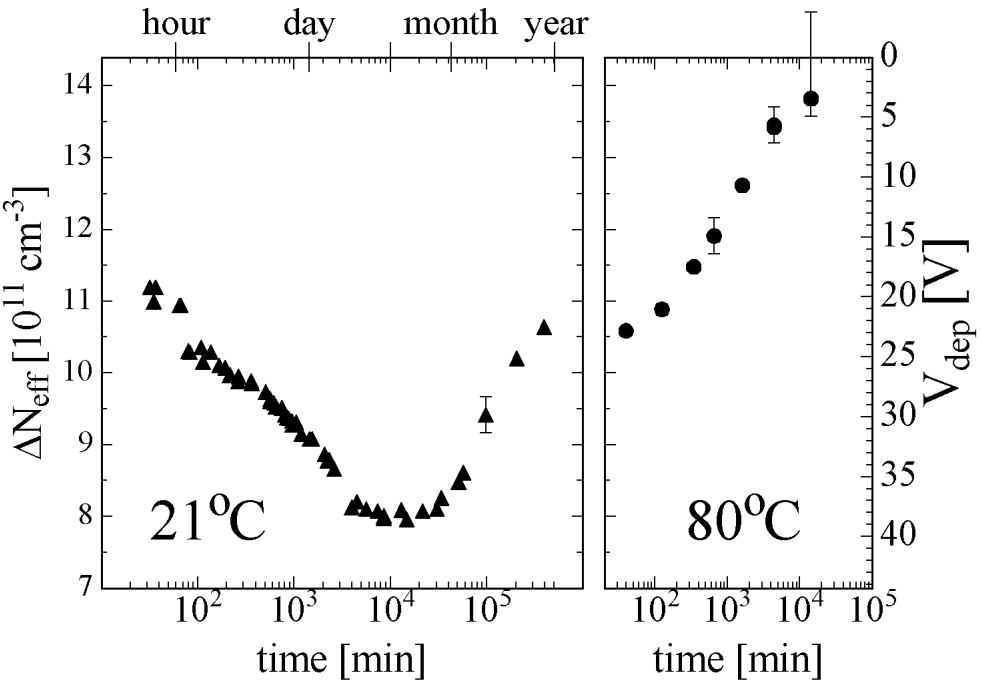

Figure 7.3: Development of ΔN_{eff} at room temperature (left) and during a subsequent isothermal heat treatment at 80°C (right) (sample of type WM2-3kΩcm; $\phi_{eq} = 1 \times 10^{13}\,\mathrm{cm}^{-2}$ (UKE)).

The evolution of the TSC spectra at room temperature was already the subject of the investigations in Sec. 6.8 here the interest is focused on the evolution during the *reverse annealing*. The TSC spectra obtained during the isothermal heat treatment at 80°C are shown in Fig. 7.4. All peaks are labelled according to the assignments given in Tab. 6.1. The major transformations are observed on H(116K)[4] and the right hand side of this peak.
At this point it has to be emphasized that for the considered fluence of $1 \times 10^{13}\,\mathrm{cm}^{-2}$ the interpretation of the spectra is not straightforward. Of prime importance is the variation of the active depletion layer width with the TSC measuring temperature. This results from the large concentration of the dominant defect levels which, depending on their state of occupation during the TSC temperature scan, determine the charge concentration in the depletion region (for details see Sec. 4.5 and Ref. [Fei97d]). This problem could only be overcome if the applied reverse bias were always sufficient to fully deplete the device, which however for the particular sample studied here would require in the order of 500 V. The above mechanism implies that the TSC signal recorded at a certain temperature depends on the history of the measurement, i.e. on all peaks observed at lower temperature. Therefore, one can conclude from Fig. 7.4 that H(116K) indeed is growing during the course of isothermal heat treatment and that the variations noticed between 120 and 180 K are likely second-order effects.
In Fig. 7.5 the increase of the integrated TSC signal ΔQ_t of the H(116K) level is plotted versus the change in the effective doping concentration due to reverse annealing N_Y. The data obtained during the annealing at room temperature are indicated by open triangles while the

[4]To be strict the level should be labeled H(116K-TSC) since the peak maximum of 116 K corresponds to the TSC spectrum.

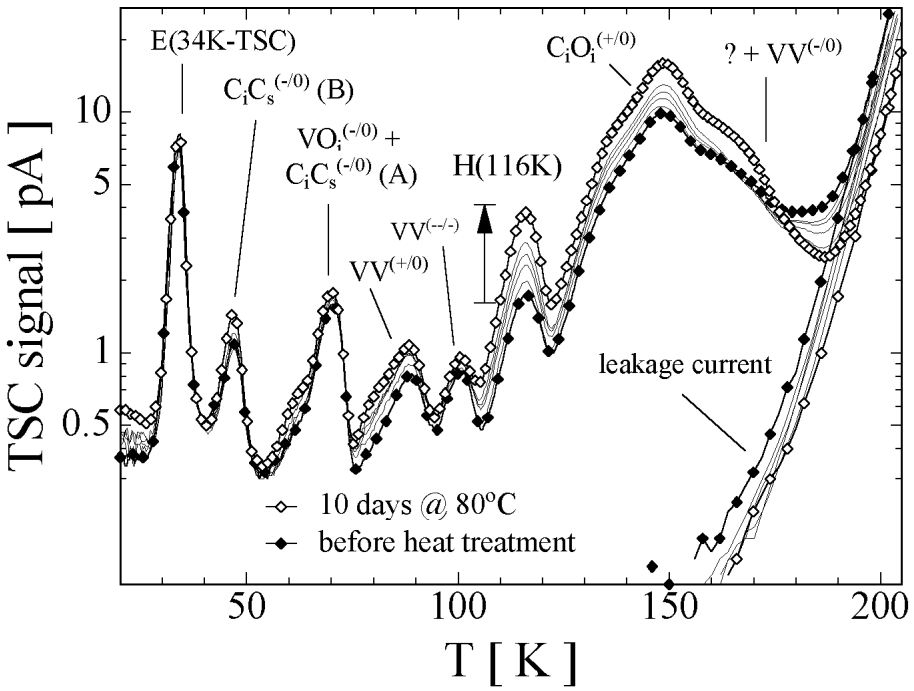

Figure 7.4: Evolution of the TSC spectrum during the isothermal heat treatment at 80°C. All spectra were obtained with a reverse bias of 100 V and a heating rate of $\beta = 0.183\,\mathrm{K/s}$. Filling of the defect levels was achieved by applying forward bias to the diode: 1.7 mA for 30 s at 20 K (sample M20713 of type WM2-3kΩcm; $d = 280\,\mu\mathrm{m}$; $\phi_{eq} = 1 \times 10^{13}\,\mathrm{cm}^{-2}$(UKE)).

ones measured during the isothermal annealing at 80°C are indicated by the filled circles. Except for the last data point, supplied with a bigger error bar for the reasons mentioned above, a good linear correlation is found providing clear evidence for this level to be related with the reverse annealing effect.

The simplest explanation for the observed relation would be to assume that the hole trap H(116K) is an acceptor. In this case the level would be negatively charged in the depletion zone. This view is also compatible with the concentration of H(116K). Due to the high defect concentration the depletion depth might not be sufficient to fully deplete the device and the integrated TSC current Q_t can only be used to determine a lower limit for the defect concentration $N_{t,min}$. The observed changes in $N_{t,min}$ during the reverse annealing ($\Delta N_{t,min}$) give 30% of the changes in the effective doping concentration (N_Y) (see upper scale in Fig. 7.5). This discrepancy could easily be accounted for by a smaller depletion width at 116 K (i.e. 30% of thickness). The level H(116K) has already been studied in [Fei97c], where the ionization energy and cross section were quoted to be $\Delta H' = 0.32\,\mathrm{eV}$ and $\sigma_p = 1.7 \times 10^{-13}\,\mathrm{cm}^2$, respectively. Moreover, strong evidence was provided for the correlation of H(116K) and the negative space charge related to a bistable defect which is introduced by annealing at higher temperatures (> 100°C) [Mol95b]. In this work these level parameters could not be reproduced. Values of $\Delta H' = 0.285\,\mathrm{eV}$ and $\sigma_p = 4.1 \times 10^{-15}\,\mathrm{cm}^2$ were obtained by the delayed heating method. While the large cross section reported in [Fei97c] would have supported the assignment to an acceptor, the much smaller value found here rather indicates that H(116K) is neutral after hole emission and therefore might be a donor. In such case the level cannot

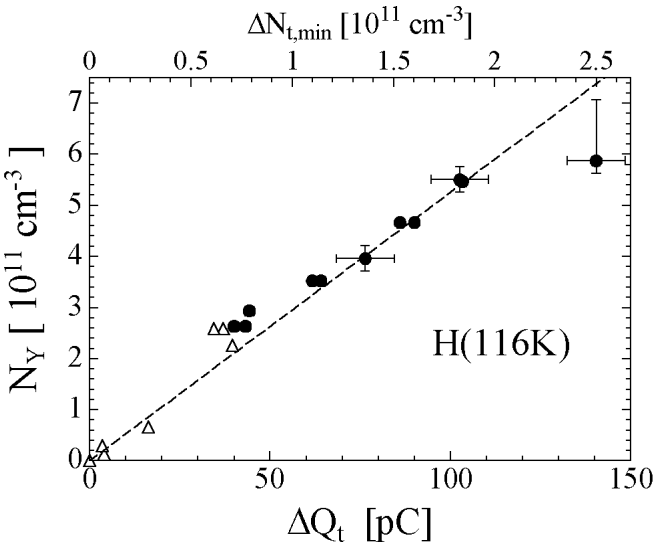

Figure 7.5: Change in the effective doping concentration due to the reverse annealing N_Y versus the change of the integrated TSC signal of the H(116K) hole trap ΔQ_t. The upper scale gives the corresponding lower limit of the increase of the H(116K) concentration ΔN_t calculated under the assumption of a fully depleted detector.

account for the *reverse annealing*. In fact, the level parameters observed here match precisely to those known for the transition $C_i^{(+/0)}$ (Tab. 6.1). It is however not believed that the observed level is the C_i defect because C_i levels were observed to anneal out at room temperature with a time constant of about 80 h in this particular sample (Sec. 6.8).

In conclusion, there is no indication for the chemical nature of the defect causing the TSC signal H(116K). However, it was demonstrated that the defect is a measure of the negative space charge corresponding to the *reverse annealing*.

7.3 Charge collection efficiency

The charge collection efficiency depends on the trapping time constants for electrons and holes. The overall trapping times for electrons ($\tau_{T,n}$) and holes ($\tau_{T,p}$) can be calculated by (Sec. 3.7)

$$\frac{1}{\tau_{T,n}} = \Phi_{eq} \sum_{traps} g_t \, c_{n,t} \underbrace{\frac{e_{n,t}}{e_{p,t} + e_{n,t}}}_{f_{h,t}} \quad \text{and} \quad \frac{1}{\tau_{T,p}} = \Phi_{eq} \sum_{traps} g_t \, c_{p,t} \underbrace{\frac{e_{p,t}}{e_{p,t} + e_{n,t}}}_{f_{e,t}}. \tag{7.6}$$

Compared to Eq. 3.65 the defect concentration N_t was replaced by $N_t = \Phi_{eq} \, g_t$ with g_t being the defect introduction rate and Φ_{eq} the 1 MeV neutron equivalent fluence. The terms f_e and f_h give the fractional occupation of the defects by electrons and holes, respectively.
The experimentally determined trapping times as function of fluence are usually described by a damage parameter γ_T

$$\frac{1}{\tau_{T,n}} = \Phi_{eq} \gamma_{T,n} \quad \text{and} \quad \frac{1}{\tau_{T,p}} = \Phi_{eq} \gamma_{T,p}. \tag{7.7}$$

where $\gamma_{T,n}$ and $\gamma_{T,p}$ stand for the sums in Eq. 7.6. The calculated γ_t values for the individual defects are given in Tab. 7.5. However, for a comparison with measured trapping time constants the detrapping time has to be taken into account. If the trapped charge carrier is

Defect	g_t $[cm^{-1}]$	$\gamma_{t,n,p}$ $[cm^2 s^{-1}]$	$1/e_{n,p}$ (detrapping)
electron trapping:			
$VO^{(-/0)} + C_i C_s^{(-/0)}$	1.09	2.6×10^{-7}	0.4 ns
E(170)	0.18	9.0×10^{-9}	1 μs
E(205a) + $VV^{(-/0)}$	1.50	7.9×10^{-8}	36 μs
E(210)	0.55	3.4×10^{-8}	40 μs
hole trapping:			
$VV^{(+/0)}$	0.92	1.1×10^{-8}	24 ns
$C_i O_i^{(+/0)}$	1.10	4.2×10^{-9}	7 μs
H(220) – 0.48 eV	0.08	6.5×10^{-9}	220 μs
H(220) – 0.53 eV	0.08	2.9×10^{-8}	330 μs

Table 7.5: Impact of various defects on the charge collection efficiency at 20°C (see text).

released (detrapped) within the shaping time of the measurement no charge collection deficiency will be observed. For example electrons trapped in VO_i defects will be released again with a time constant of $\tau_e = 0.4\,\text{ns}$ at 20°C (Tab. 7.5). Therefore the VO_i has no effect on the charge collection efficiency at room temperature. Taking into account only defects with detrapping time constants higher than 10 ns at 20°C values of

$$\gamma_{T,n} = 1.2 \times 10^{-7}\,\text{cm}^2\text{s}^{-1} \qquad \text{and} \qquad \gamma_{T,h} = 4.4 \times 10^{-8}\,\text{cm}^2\text{s}^{-1}$$

are found for electron and hole trapping, respectively. It is noted again that the contribution of the H(220) defect to the later value might be afflicted with a big error due to the uncertainty in the H(220) level parameters (Sec. 6.1).
In [Wun92] a value of $\gamma_{T,h} = 2.4 \times 10^{-7}\,\text{cm}^2\text{s}^{-1}$ is given for the hole trapping which is by a factor of 5 bigger than the one calculated here. For $\gamma_{T,n}$ two values are given in [Wun92]. For low fluences a value of $\gamma_{T,n} = 2.4 \times 10^{-7}\,\text{cm}^2\text{s}^{-1}$ was measured while for fluences above $\Phi_{eq} = 8.8 \times 10^{12}\,\text{cm}^2$ a value of $\gamma^*_{T,n} = 1.01 \times 10^{-6}\,\text{cm}^2\text{s}^{-1}$ was found to describe the change in the trapping time constant ($\Delta\,(1/\tau_{T,n}) = \Delta\Phi_{eq} \cdot \gamma^*_{T,n}$). Such a fluence dependence is not expected from the data found in this work. However, the calculated value is at least by a factor of two smaller than the experimental values.
Finally, it is noted again that the defect properties were measured at low temperatures and had to be extrapolated to 20°C in order to perform this comparison. Therefore, a discrepancy between the measured and calculated values does not necessarily mean that the defects presented here are not responsible for the observed macroscopic properties. The differences could also be due to an uncertainty in the extrapolated defect parameters.

Chapter 8

Radiation Hard Material - Outlook

The detailed discussions presented in the previous chapters about the *macroscopic* and *microscopic* radiation damage and their relation to each other lead to the question how this knowledge can be used to produce radiation harder silicon detectors. In order to answer this question from the present point of view three irradiation experiments performed with different types of material will be discussed in this chapter. However, only the first material will be of practical interest for the near future.

8.1 Oxygen enriched FZ silicon

The beneficial influence of a high oxygen concentration on the radiation hardness with respect to neutron damage was discussed in very detail in Sec. 5.3.4. The presented investigations led to a parameterization of the macroscopic effects that can be used to model the behavior in high energy physics experiments. Furthermore, the investigations on the particle dependence presented in Sec. 5.3.5 showed – based on data measured by the CERN group – that an even more pronounced radiation hardness compared to standard silicon is observed after high energetic proton or pion irradiation. However, the data were obtained with another measurement technique that does not allow to extract all damage parameters necessary for the modeling (Sec. 5.3.5).

In order to verify the results reported by the CERN group and to extract the damage parameters for the modeling two sets of detectors produced with standard and oxygenated silicon were irradiated with 23 GeV protons at the CERN PS (Sec. 4.2.3). Subsequently these detectors were exposed to an isothermal heat treatment at 60°C as described in Sec. 5.3. Here, a provisional set of parameters will be given but should be taken with caution since the full analysis is still under way and will be published soon [Lin99b].

Throughout this section the 1 MeV neutron equivalent fluence as determined by the α-method (see Sec. 5.2) is used for the presentation of the data and calculation of the damage parameters. It has however to be noted that in this experiment the hardness factor for the 23 GeV protons was measured to be 0.62 and not 0.51 as determined in Sec. 5.2. This discrepancy is attributed to a problem in the nominal fluence determination by the activation foil method between the two beam-times (8/97 and 4/99) at the CERN PS that up to now could not be solved. Please note that the hardness factor has no influence on the given damage parameters since they are normalized to the 1 MeV neutron equivalent fluence

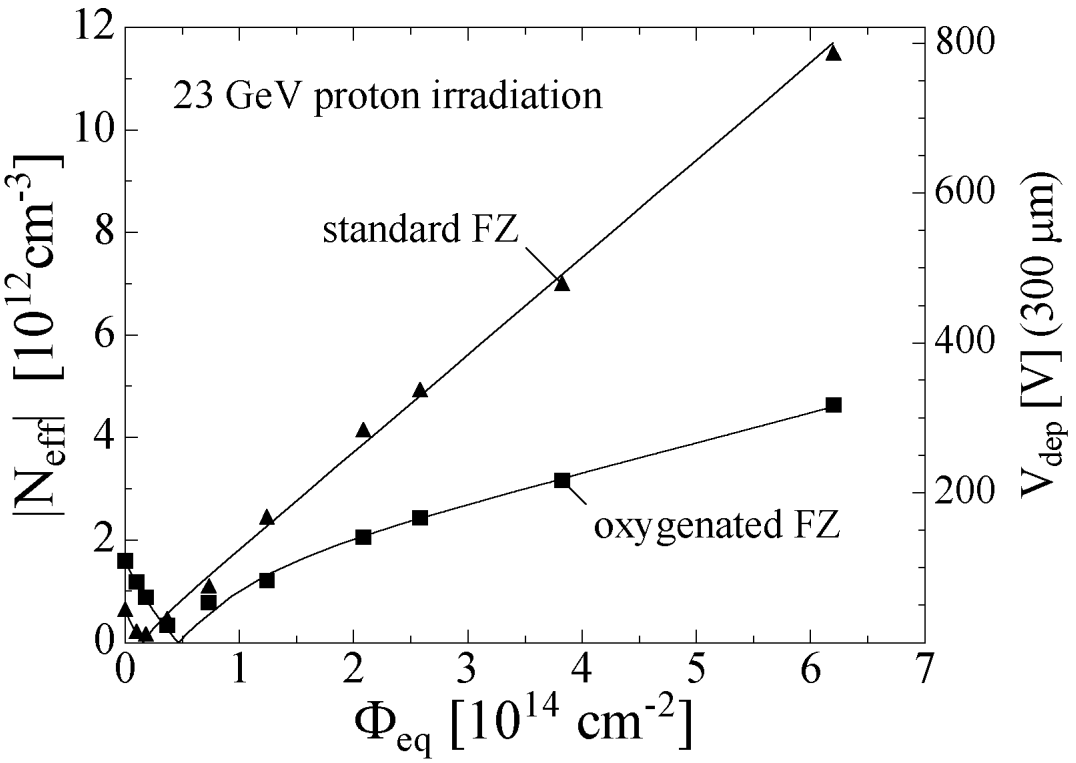

Figure 8.1: Absolute effective doping concentration of standard and oxygenated FZ silicon as measured after 23 GeV proton irradiation and a subsequent annealing at 60°C for 80 min. Each point corresponds to an individual sample (see text).

by the α-method.

The standard FZ silicon was of type WE-7kΩcm and the oxygenated of type WS-3kΩcm (see Tab. 4.1). The latter material was produced by Wacker [WAC] and enriched with oxygen by Sintef [SIN]. After oxidation the wafers were heated in an N_2 atmosphere for 72 h at 1150°C in order to diffuse the oxygen from the surface into the bulk. The oxygen concentration as measured by SIMS and IR was $[O] = [O_i] = 1.5 \times 10^{17}\,\mathrm{cm}^2$ while the carbon concentration was below $1 \times 10^{16}\,\mathrm{cm}^2$ [Mol99].

The absolute effective doping concentrations for the standard and oxygenated material as measured after an 80 min lasting heat treatment at 60°C are presented in Fig. 8.1 as function of the 1 MeV neutron equivalent fluence. As expected from the data provided by the CERN group (see Sec. 5.3.5) an improved radiation hardness of the oxygenated silicon is observed. After e.g. a fluence of $6 \times 10^{14}\,\mathrm{cm}^{-2}$ the depletion voltage of a 300 μm thick detector is lower by about 500 V. The main reason for this effect is found in a strongly reduced introduction rate g_c for the *stable damage* component N_C which is displayed in Fig. 8.2. The solid lines in the figure represent fits according to Eq. 5.8 (page 111). The extracted parameters for the proton irradiations are:

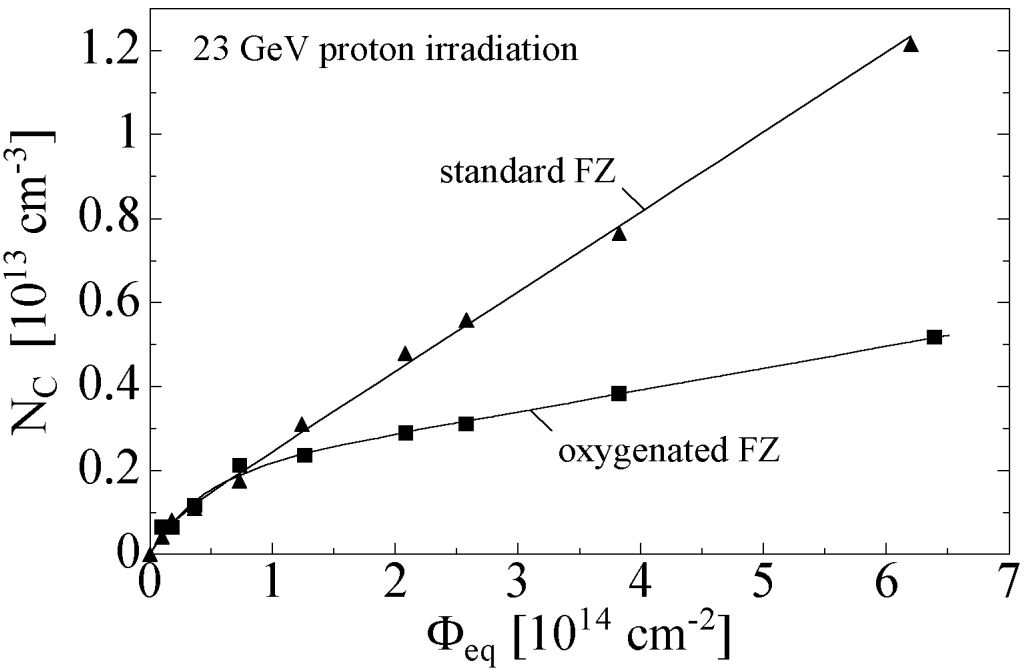

Figure 8.2: Stable damage component N_C for standard and oxygenated FZ silicon as measured after 23 GeV proton irradiation. Each point corresponds to an individual sample (see text).

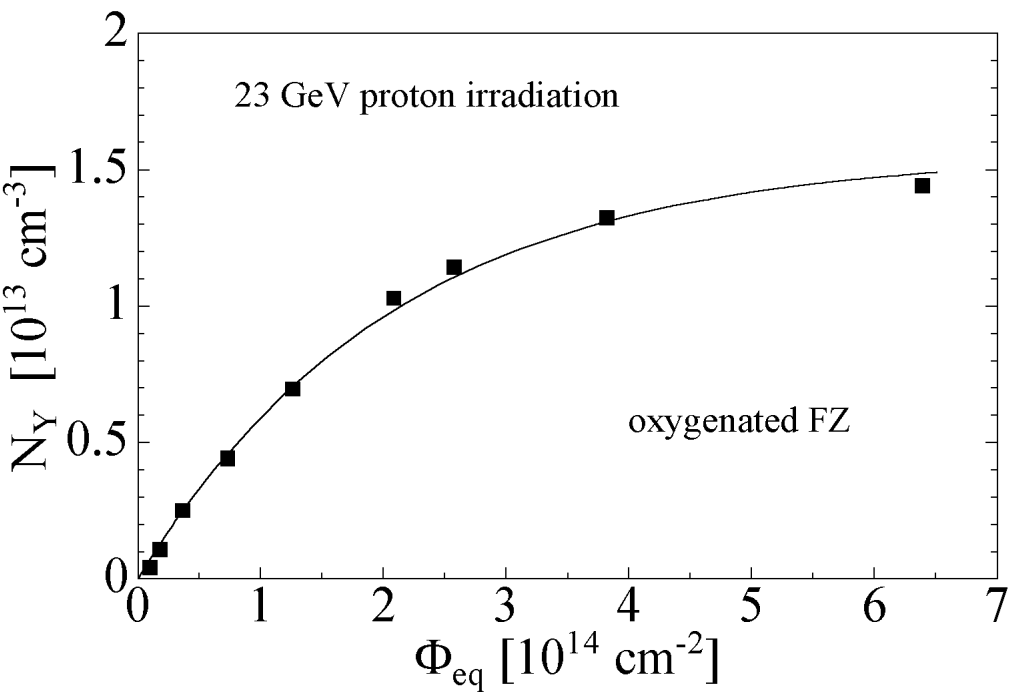

Figure 8.3: Reverse annealing amplitude for the oxygen enriched FZ silicon as measured after 23 GeV proton irradiation. Each point corresponds to an individual sample (see text).

oxygen enriched silicon	**standard silicon**
$N_{C0} = 1.74 \times 10^{12}\,\mathrm{cm}^{-3}$,	$N_{C0} = 6.03 \times 10^{11}\,\mathrm{cm}^{-3}$,
$c = 2.24 \times 10^{-14}\,\mathrm{cm}^{2}$,	$c = 5.23 \times 10^{-14}\,\mathrm{cm}^{2}$,
$g_c = 0.55 \times 10^{-2}\,\mathrm{cm}^{-1}$,	$g_c = 1.86 \times 10^{-2}\,\mathrm{cm}^{-1}$,
$N_{eff,0} = 1.59 \times 10^{12}\,\mathrm{cm}^{-3}$,	$N_{eff,0} = 6.54 \times 10^{11}\,\mathrm{cm}^{-3}$,
$N_{C0}/N_{eff,0} = 1.09$,	$N_{C0}/N_{eff,0} = 0.92$.

The value of $g_c = 1.86 \times 10^{-2}\,\mathrm{cm}^{-1}$ for the standard silicon is in agreement with the value of $g_c = (1.66 \pm 0.35) \times 10^{-2}\,\mathrm{cm}^{-1}$ given in Sec. 5.3.5 for 23 GeV proton irradiated standard material. However, the oxygen enriched material shows a 3.4 times smaller introduction rate which – of course – has an important impact for the operability of the detectors (see below). After neutron irradiation no influence of the oxygen concentration on the parameter g_c was observed (Sec. 5.3.4). A further difference between neutron and proton irradiations is seen in the *donor removal*. In Sec. 5.3.4 it was shown that after neutron irradiation the ratio $N_{C0}/N_{eff,0}$ (*removable donor concentration*) is depending on the oxygen concentration. However, for the proton irradiations presented here this ratio is close to 1 for the standard and the oxygen enriched silicon indicating that all donors are *removed*. It is noted that such a *complete donor removal* is expected from the microscopic defect kinetics simulations presented in Sec. 7.2.2 while the observations after neutron irradiation so far could not be explained.

The dependence of the reverse annealing amplitude on the fluence is depicted in Fig. 8.3 for the proton irradiations. Obviously a saturation of the amplitude at high fluences is observed and was paramterized as

$$N_Y(\Phi_{eq}) = N_{Y0}\,(1 - \exp(-c_Y \Phi_{eq}))\,. \tag{8.1}$$

The parameters corresponding to the fit shown in the figure are $N_{Y0} = 1.56 \times 10^{13}\,\mathrm{cm}^{-3}$ and $c_Y = 4.79 \times 10^{-15}\,\mathrm{cm}^{2}$. For small fluences ($\Phi_{eq} \ll 1/c_Y$) the above given parameterization can be approximated by $N_Y(\Phi_{eq}) \approx N_{Y0} c_Y \Phi_{eq} = g_Y \Phi_{eq}$ with $g_Y = 7.5 \times 10^{-2}\,\mathrm{cm}^{-1}$. This value is about 50% higher than the value observed after neutron irradiation in the low fluence range ($g_Y(\mathrm{neutron}) = 5.16 \times 10^{-2}\,\mathrm{cm}^{-1}$, page 120).
Up to now it is not clear whether or not the saturation effect depends on the oxygen concentration. Due to its higher introduction rate g_c and a larger thickness of the devices it was not possible to investigate the reverse annealing of the standard material in the high fluence range. Also after neutron irradiation only a few samples of low resistivity could be investigated in the high fluence range (compare Fig. 5.15 on page 121). However, the reduced reverse annealing amplitude of the Czochralski silicon does indicate that there is also after neutron irradiation a saturation of the reverse annealing amplitude in highly oxygenated material. The average reverse annealing amplitude for the three Cz samples was found to be about $1.7 \times 10^{13}\,\mathrm{cm}^{-3}$ and thus is close to the value measured here.

Although there are still some open questions regarding the reverse annealing effect in standard material and especially the fluence normalization for the proton irradiations the improvement of the radiation hardness is evident.
As an example the ATLAS pixel detector is chosen. This detector component is located very close to the beam line. It consists of three barrels with average radii of $R \approx 4$, 10 and 13 cm and 5 end-cap disks on each side between radii of 13 and 19 cm [ATL98]. Therefore,

the expected particle fluence is very high and dominated by pions (compare Fig. 1.1). At e.g. a distance of 10 cm from the beam line a cumulated 1 MeV equivalent fluence of about $\Phi_{eq} \approx 7 \times 10^{14}\,\mathrm{cm}^2$ is expected for the envisaged 10 year operational period [ATL98]. Roughly 70% ($\approx 5 \times 10^{14}\,\mathrm{cm}^2$) of the overall equivalent fluence is due to charged hadrons and about 30% ($\approx 2 \times 10^{14}\,\mathrm{cm}^2$) due to neutrons (compare Fig. 1.1).
Assuming that the NIEL hypothesis can still be used to scale the damage produced by charged hadrons with respect to the introduction of negative space charge a prediction for the impact of the high oxygen concentration on the depletion voltage can be given. In other words: It is assumed that the 1 MeV equivalent neutron fluence can be used to calculate the introduction of the stable negative space charge for charged hadrons of different type and energy. This assumption is supported by the fact that also after irradiation with 236 MeV pions a reduced *stable damage* was observed in oxygen enriched silicon (compare Sec. 5.3.5).
Taking into account only the beneficial effect of the suppressed *stable damage* generation the negative space charge for a detector produced from oxygenated silicon compared to a standard detector at $R = 10\,\mathrm{cm}$ (Layer 1) will be lower by

$$\Delta N_{eff} = (g_c(\text{standard}) - g_c(\text{oxygenated})) \cdot 5 \times 10^{14} cm^{-2} = 6.6 \times 10^{12}\,\mathrm{cm}^{-3}.$$

This corresponds to a reduction in depletion voltage of about 300 V ($d = 250\,\mu\mathrm{m}$) after 10 years of operation. Instead of a value in the order of 800 V predicted in [ATL98] the depletion voltage would be around 500 V which is below the operating voltage of 600 V and thus would assure the operability of the detectors in this layer over the whole 10 years.
Finally, it is mentioned that of course the improvement for the layer closest to the beam line (B-layer at a radius of 4 cm) would be even more pronounced. The expected cumulated fluence after 10 years of operation at this position is $\Phi_{eq} = 2.8 \times 10^{15}\,\mathrm{cm}^{-2}$ resulting in a depletion voltage of about 2100 V for a $200\,\mu\mathrm{m}$ thick detectors produced from standard silicon. It is expected that the detectors will be operable for about five years taking already into account an operation in partial depletion (see [ATL98]). Roughly 90% of the overall fluence at this position is due to charged hadrons (compare Fig. 1.1). Hence, it is expected that the depletion voltage with oxygen enriched silicon would be about 1000 V smaller after 10 years. Therefore the operational lifetime of the B-layer would be significantly enlarged.

Presently first pixel detectors for ATLAS and strip detectors for ATLAS, CMS and HERAB are produced with oxygenated silicon in order to verify the improved radiation hardness – so far measured only on test structures – in irradiation tests of *"real"* detectors [Wun99, Lut99, Ton99]. If these tests are successful the oxygenated silicon will be implemented in the experiments.

8.2 Magnetic Czochralski silicon (MCz)

The essential difference between Czochralski and float zone silicon is the very high oxygen concentration of Cz silicon (see Sec. 2.1). Therefore, it seems natural to use Cz silicon in order to get material with a high oxygen content. Unfortunately the resistivity is usually lower than 100 Ωcm. However, new developments in the Cz production technique (e.g. the MCz technology) allow for better control of the melt flow during the growth process and enable also the production of higher resistivity material (see Sec. 2.1).
In this work a prototype high resistivity (4 kΩcm) p-type MCz silicon produced by Komatsu [KOM] was investigated after neutron irradiation (KIP-4kΩcm in Tab. 4.1). The

oxygen concentration as measured by SIMS was $[O] = 5 \times 10^{17}\,\mathrm{cm}^{-3}$. Unfortunately TSC measurements revealed that the material was contaminated with iron in a concentration of $[Fe] \approx 1 \times 10^{12}\,\mathrm{cm}^{-3}$ [Lin98]. The iron influenced the effective doping concentration during the isothermal heat treatment and made the analyses of the reverse annealing process impossible. Furthermore, only an approximative determination of the stable damage component could be achieved. A value of $g_c \approx 1.75 \times 10^{-2}\,\mathrm{cm}^{-1}$ was measured which is above the average value of $g_c = 1.49 \times 10^{-2}\,\mathrm{cm}^{-1}$ given in Sec. 5.3.4. However, these studies clearly showed that it is possible to produce high resistivity ($\rho > 1$ kΩcm) Cz silicon for detector applications.
Very recently it was demonstrated by Z. Li et al. [Li 99] that it is possible to enrich FZ silicon with an oxygen concentration of $4 \times 10^{17}\,\mathrm{cm}^{-3}$ by a very long lasting very high temperature diffusion (216 hrs at 1200°C). This value is only slightly below the oxygen concentration of the MCz. Since in this moment the dependence of the improved radiation hardness on the oxygen concentration with respect to charged hadron damage is not very well known it is also unclear whether the oxygen concentration achievable by diffusion of FZ silicon (presently up to $4 \times 10^{17}\,\mathrm{cm}^{-3}$) is sufficient or whether an even higher oxygen concentration is leading to a further improvement. In such a case the MCz silicon could become of interest.

8.3 Compensated silicon

One aspect of the radiation induced changes in the effective doping concentration in n-type material is the *donor removal* (Secs. 5.3.4 and 7.2) while in p-type material an *acceptor removal* is observed [Wun92, Dez97]. Thus the idea arises to produce a compensated material with a high boron and phosphorus concentration and influence the donor and acceptor-removal in such a way that the acceptor removal rate is slightly higher than the donor removal rate in order to counterbalance the radiation induced negative space charge.
Such a *defect engineering* approach has to take into account the reactions that lead to the removal of phosphorus and boron. On the one hand migrating vacancies (V) can react with both shallow dopants, with phosphorus in the reaction $V + P \rightarrow VP$ and with boron in the reaction $V + B \rightarrow VB$. However, the VB defect is not stable at room temperature [Wat92] and thus only phosphorus is removed by vacancies. On the other hand it is well known that the interstitials react with boron $I + B_s \rightarrow B_i$. The B_i is mobile at room temperature and can e.g. react with oxygen or carbon to form the defects B_iO_i or B_iC_s, respectively, which are stable at room temperature (see Sec. 3.6 and Tab. B.1). Such reactions are not reported in the literature for the phosphorus and thus the following idea arises:
In a compensated material with a high oxygen concentration and a low carbon concentration the acceptor removal rate should be higher than the donor removal rate. On the one hand the high oxygen concentration getters the vacancies by the reaction $V + O \rightarrow VO$ and thus prevents the donor removal via the reaction $V + P \rightarrow VP$. Furthermore, oxygen does not influence the migrating interstitials since the IO_i defect is not stable at room temperature (Tab. B.1). On the other hand carbon is a getter for migrating interstitials ($I + C_s \rightarrow C_i$) and thus can suppress the acceptor removal ($I + B_s \rightarrow B_i$). In consequence for a material with a high oxygen and a low carbon content the acceptor removal should be more pronounced than the donor removal.

In collaboration with B. Falster from MEMC–Italy [MEM] a compensated Cz silicon was produced (MIP-650Ωcm in Tab. 4.1). The oxygen and carbon concentrations as measured by SIMS were $[O] = 7.3 \times 10^{17}\,\mathrm{cm}^{-3}$ and $[C] < 5 \times 10^{15}\,\mathrm{cm}^{-3}$. The phosphorus and boron

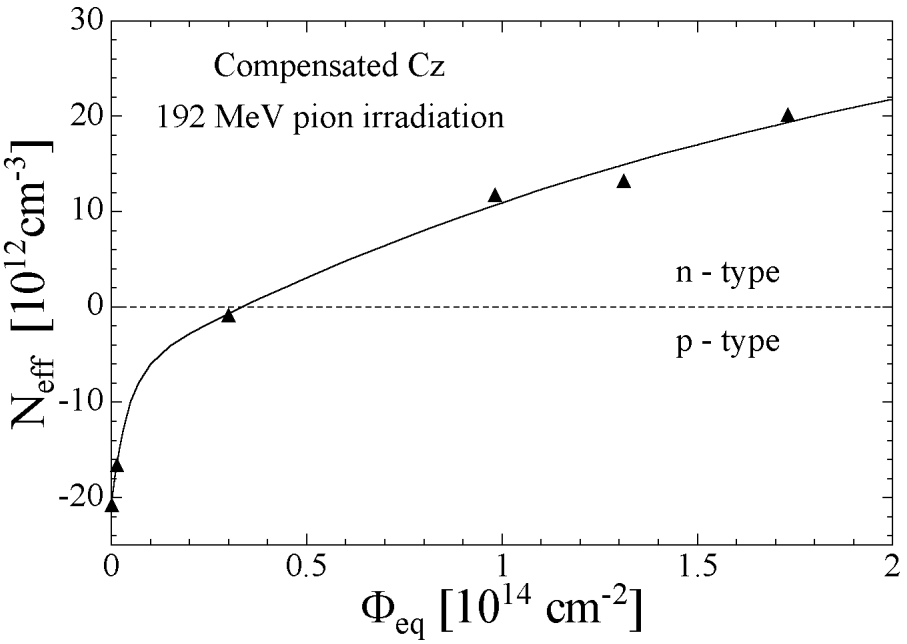

Figure 8.4: Effective doping concentration of compensated p-type Cz silicon as measured after 192 MeV pion irradiation and a subsequent annealing at 60°C for 80 min. Note that the material undergoes a type inversion from p- to n-type. Each point corresponds to an individual sample (see text).

concentrations were determined with the PL method to be, both, about $5 \times 10^{13}\,\mathrm{cm}^{-3}$ (see Sec. 4.1). The measurement of the effective doping concentration at room temperature gave a value of $N_{eff,0} = -2.07 \times 10^{13}\,\mathrm{cm}^2$ (650 Ωcm p-type) and thus indicates that the boron concentration should be higher by this value than the phosphorus concentration. This discrepancy to the PL measurement could so far not be solved.
In Fig. 8.4 the effective doping concentration as measured after a 192 MeV pion (π^+) irradiation and a subsequent annealing of 80 min at 60°C is shown. The solid line corresponds to a double exponential fit:

$$N_{eff}(\Phi_{eq}) = N_{eff,0} + N_{A1}(1 - \exp(-c_{A1}\Phi_{eq})) + N_{A2}(1 - \exp(-c_{A2}\Phi_{eq}))$$

with $N_{eff,0} = -2.07 \times 10^{13}\,\mathrm{cm}^{-3}$,
$N_{A1} = 1.37 \times 10^{13}\,\mathrm{cm}^{-3}$, $c_{A1} = 2.46 \times 10^{-13}\,\mathrm{cm}^2$,
$N_{A2} = 4.55 \times 10^{13}\,\mathrm{cm}^{-3}$ and $c_{A2} = 5.03 \times 10^{-15}\,\mathrm{cm}^2$.

However, this fit is up to now not based on a physical model and thus the line in Fig. 8.4 only serves to guide the eye. Nevertheless, the difference to all other materials investigated so far is obvious. With increasing fluence the space charge becomes more positive and a type inversion from p-type to n-type is observed. This behavior is in agreement with the idea of a higher boron than phosphorus removal rate in material with high oxygen concentration.

Although the behavior of the compensated Cz silicon is so far not understood in a quantitative way it serves as an excellent example that there are still possibilities for *defect engineering* approaches in order to produce even radiation harder material than the oxygenated high resistivity FZ silicon presented in this chapter.

Chapter 9

Summary and Conclusions

The aim of this thesis was threefold. First, to establish a comprehensive parameterization of radiation induced changes of silicon detector properties in order to make damage projections for HEP experiments possible. Second, to get a more fundamental understanding of the microscopic mechanisms leading to the deterioration of the detector properties and, third, to develop – based on the understanding of the damage mechanism – radiation hard material.

For these purposes the radiation induced changes in the leakage current and the effective doping concentration of silicon detectors as well as the properties of the radiation induced defects in the silicon bulk have been studied. These *macroscopic* and *microscopic* features were investigated as a function of particle fluence, annealing time and annealing temperature as well as of the resistivity and oxygen concentration of the material. The oxygen concentration ranged from below $2 \times 10^{14}\,\mathrm{cm}^{-3}$ to $9 \times 10^{17}\,\mathrm{cm}^{-3}$ and the resistivity from $6\,\Omega$cm to $25\,\mathrm{k}\Omega$cm for n-type and from $400\,\Omega$cm to $4\,\mathrm{k}\Omega$cm for p-type material. Most irradiations were performed with fast neutrons and a few with ^{60}Co-gammas or 23 GeV protons. In a single experiment detectors were exposed to 192 MeV pions (π^+).

Macroscopic features - Detector performance

- Leakage current

The current related damage rate α was investigated in isothermal annealing experiments ranging from 21°C to 106°C. The measurements clearly revealed that there is no saturation value α_∞ at room temperature. This is in contradiction to earlier publications in which the proper use of guard rings was not yet established. Consequently a new parameterization for the annealing of α was suggested. It consists of an exponential and a logarithmic term

$$\alpha(t) = \alpha_I \exp\left(-t/\tau_I\right) + \alpha_0 - \beta \cdot \ln\left(t/t_0\right) \qquad \text{(see Eq. 5.4, page 101)}$$

and is valid for the time and temperature range described in Sec. 5.1.3. While about the physical meaning of the logarithmic term so far only speculations could be given the annealing parameters extracted for the exponential component, $E_I = (1.11 \pm 0.05)$ eV and $k_{0I} = 1.2^{+5.3}_{-1.0} \times 10^{13}\,\mathrm{s}^{-1}$, are consistent with a first order decay of a defect. The corresponding defect was most probably also identified in this work (see below). The overall annealing behavior as well as the value of α were found to be independent of the oxygen content and the resistivity. Furthermore, α was found to be independent of the fluence in a range from

$\Phi_{eq} = 1 \times 10^{11}\,\mathrm{cm}^{-2}$ to $\Phi_{eq} = 1 \times 10^{14}\,\mathrm{cm}^{-2}$. Therefore it was concluded that the leakage current after hadron irradiation is generated by intrinsic defects, i.e. the defects responsible for the leakage current are only composed of vacancies and silicon interstitials.

- Determination of hardness factors

It was shown that the α-value determined in a well defined annealing state provides an excellent tool for measuring the 1 MeV neutron equivalent fluence (Φ_{eq}). With this method the hardness factors for 23 GeV protons (CERN PS) and the neutron spectrum of the TRIGA research reactor in Ljubljana were determined to be 0.51 ± 0.01 and 0.90 ± 0.05, respectively. However, it was also demonstrated that this method cannot be used for ^{60}Co-gamma irradiations. The reason is found in the completely different damage mechanism. While ^{60}Co-gamma irradiations lead only to the generation of point defects hadron irradiations also cause so-called *clusters*. Therefore, damage parameters related to *cluster* formation, e.g. the leakage current after hadron irradiation, do not scale in the same way with the NIEL as damage parameters related to point defects, e.g. the donor removal. Furthermore, the damage caused by point defects is usually influenced by the impurity content of the material. In conclusion the NIEL hypothesis, i.e. the concept of hardness factors, has to be treated with great care since the ratio between the generated point defects and clusters is not only a function of the NIEL but also depends on the type of particle and its energy.

- Changes in the effective doping concentration

The radiation induced changes in the effective doping concentration were parameterized according to the *Hamburg model*[1] which was critically reviewed, changed in some aspects (e.g. the *reverse annealing*) and complemented with respect to the dependence on the bulk material and the type of particle used for irradiation.

The introduction rate $g_a = (1.81 \pm 0.14)\ \mathrm{cm}^{-1}$ and the annealing time constant of the *beneficial annealing* were found to be independent of the used material. It can be described as a first order process with an activation energy of $E_{aa} = (1.09 \pm 0.03)$ eV and a frequency factor of $k_{0a} = 2.4^{+1.2}_{-0.8} \times 10^{13}\,\mathrm{s}^{-1}$ indicating a decay of a defect. The corresponding defect is most probably the same as the one responsible for the *exponential* annealing component of the leakage current (see below).

The *stable damage* consists of a so-called *donor removal* and a fluence proportional introduction of stable acceptors (introduction of negative space charge).
Significant differences were observed after irradiation with protons or neutrons:
After irradiation with high neutron fluences the fraction of *removed* (inactive) donors is strongly depending on the oxygen content of the material. About 10% of the initial doping concentration is removed in material with $[O_i] = 9 \times 10^{17}\,\mathrm{cm}^{-3}$ while for standard detector grade silicon with $[O_i]$ below $5 \times 10^{16}\,\mathrm{cm}^{-3}$ that value is 60–90%. The defect kinetics that might lead to such an effect was discussed and a relation between the non removable donor concentration N_{C0} and the donor removal constant c was found ($N_{C0} \times c = (7.5 \pm 0.6) \times 10^{-2}\,\mathrm{cm}^{-1}$). Furthermore, the introduction rate of *stable* negative space charge (g_c) was found to be independent of the oxygen concentration. An average value of $g_c = (1.49 \pm 0.04) \times 10^{-2}\mathrm{cm}^{-1}$ was measured after neutron irradiation. Only one material

[1] *Hamburg model*: Parameterization according to the Hamburg University group [Chi95, Fei97a].

exhibited a significantly smaller introduction rate of about $g_c = 0.6 \times 10^{-2}\text{cm}^{-1}$ indicating that it is possible to suppress the radiation induced creation of negative space charge by material modification.
In contrast to the findings after neutron irradiation a strong influence of the oxygen content on the parameter g_c was observed for 23 GeV proton irradiations. Compared to standard silicon with $[O_i]$ below $5 \times 10^{16}\,\text{cm}^{-3}$ the introduction rate of negative space charge was suppressed by a factor of about three in oxygen enriched FZ silicon with $[O_i] = 1.5 \times 10^{17}\,\text{cm}^{-3}$. Furthermore, the measurements revealed that after proton irradiation independently of the oxygen concentration all donors are removed.

A systematic study of the *reverse annealing* process definitely revealed that the underlying microscopic defect kinetics is not a second but a first order process. However, individual annealing curves are best described by an equation originating from the second order approach and thus as a pragmatic compromise the following parameterization was suggested:

$$N_Y(t) = g_Y \times \Phi_{eq} \times \left(1 - \frac{1}{1 + t/\tau_Y}\right) \qquad \text{(see Eq. 5.15, page 117)}$$

with a time constant $\tau_Y(T) = 1/k_{0Y} \times \exp(E_Y/(k_B T))$. The measured activation energy and frequency factor are $E_Y = (1.33 \pm 0.03)\,\text{eV}$ and $k_{0Y} = 1.5^{+3.4}_{-1.1} \times 10^{15}\,\text{s}^{-1}$, respectively. The average introduction rate for the reverse annealing in samples irradiated with neutron fluences below $1 \times 10^{14}\,\text{cm}^{-2}$ is $g_Y = (5.16 \pm 0.09) \times 10^{-2}\,\text{cm}^{-1}$. However, for oxygen rich Czochralski silicon ($[O] = 9 \times 10^{17}\,\text{cm}^{-3}$) irradiated with fluences higher than $\Phi_{eq} = 5 \times 10^{14}\,\text{cm}^{-2}$ a significantly reduced introduction rate was observed. Furthermore, a systematic investigation of oxygen rich material after proton irradiations definitely showed a saturation of the reverse annealing amplitude above about $\Phi_{eq} = 2 \times 10^{14}\,\text{cm}^{-2}$. Since standard material with low oxygen content could up to now not be investigated after such high fluences due to the their lower radiation tolerance with respect to the *stable damage*, the question whether or not the only recently observed saturation effect depends on the oxygen content so far remains open.

Microscopic defects analysis

- Characterization

The microscopic techniques *Deep Level Transient Spectroscopy* (DLTS) and *Thermally Stimulated Current* (TSC) were used to study the microscopic defects. A comparison of the defect concentrations determined with both techniques on the same neutron irradiated sample showed very good agreement with respect to the measurement of isolated point defects while in the case of superimposed defect levels the concentrations obtained with the DLTS method have to be treated with care.
About 20 radiation induced defect levels were detected and characterized (Tab. 6.1). Besides the well known defects VO_i, C_iC_s, C_iO_i and the divacancy VV also defects were found that so far have not been reported in the literature. For some levels both capture cross sections, for holes and electrons, could be measured. Here, special interest was put on the electron capture cross section of the $C_iO_i^+$ that displayed a very strong temperature dependence. It was demonstrated how the bistability of the C_iC_s defect can be used to separate the superimposed DLTS signals of the VO_i and the C_iC_s defect. Furthermore, a strong dependence of the thermal double donor DLTS signal on the field strength (*Poole Frenkel effect*) was observed on oxygen rich Cz silicon. In the same sample the signals arising from the dominant

neutron radiation induced electron traps[2] E(85), E(120) and E(205) (see Tab. 6.1) were not influenced by the field strength. Hence it could be concluded that non of those defects is a donor.
A comparison of the spectra obtained on ^{60}Co-gamma and neutron irradiated samples of the same type and material were used to investigate the differences in the primary damage mechanisms. Roughly, the defects could be divided into two categories. On the one hand there are defects which are observed after both kinds of irradiation (VO_i, C_iC_s, C_iO_i, VV). These defects are well known from the literature and can be described as isolated point defects. On the other hands there are the defects only found in the neutron irradiated samples (see Tab. 6.1). Those defects were attributed to be related to the *cluster* formation. A detailed discussion of the defect introduction rates after neutron and ^{60}Co-gamma irradiation showed e.g. that after neutron irradiation more interstitials than vacancies escape the primary damage regions (*clusters*), an important fact that gives a further hint about the topology of clusters.

- Annealing

The annealing behavior of the defects at room temperature was monitored on neutron irradiated high resistivity (standard) FZ samples. Furthermore an isochronal annealing study on standard and various isothermal annealing experiments at 60°C on samples produced from different materials were performed.
At room temperature all DLTS peaks changed in peak heights during the first 170 days after irradiation. The changes in the defect concentrations could be roughly divided into two processes. A short term annealing of the carbon interstitial related defects (C_i, C_iC_s, C_iO_i) with a time constant of about 4 days and a long term annealing of defects related to the broad electron-trap peak E(205) with a time constant of about one month.

The time constant of the first process depends on the oxygen and carbon concentration in the material, e.g. the isothermal annealing experiments at 60°C showed a six times larger time constant for a material with a very low oxygen concentration compared to the standard material. An analysis of the temperature dependence of the annealing process on identical material revealed an activation energy of $E_A \approx 0.80\,\mathrm{eV}$ and a frequency factor of $k_0 \approx 2 \times 10^8\,\mathrm{s}^{-1}$ for the carbon migration in high resistivity FZ. The frequency factor is in consistence with a long range migration of the C_i. During the annealing an up to now not reported defect level E(35) was detected. It emerges during the initial stages of the short term annealing and disappears with a rate similar to the C_i, thus indicating that it might be a carbon related defect.

The time constant for the second process was found to be independent of the material. In about the same period of time the electron trap E(40) ($E_C - 0.08\,\mathrm{eV}$) emerges, the hole trap H(50) ($E_V + 0.09\,\mathrm{eV}$) and the deep electron traps E(180) ($\approx E_C - 0.36\,\mathrm{eV}$) and E(210) ($E_C - 0.46\,\mathrm{eV}$) vanish and the peak heights of the level E(120) ($E_C - 0.22\,\mathrm{eV}$) increases. The activation energy and frequency factor for this annealing process were found to be $E_A \approx 1.03\,\mathrm{eV}$ and $k_0 \approx 1 \times 10^{14} s^{-1}$, respectively. The frequency factor indicates a *single jump process* and thus a break up of a defect is the most probable explanation for the observed annealing.

[2]In this work the defect levels are labelled with an E or H for an electron or hole trap followed by the DLTS peak-maximum temperature for a time window of 200 ms (see Sec. 6.1).

In an isochronal annealing study the annealing of the peak E(205) was investigated. It was shown that the annealing of the left hand side of the peak at around 200°C can be attributed to the annealing of a defect labelled E(205a). The remaining peak E(205b) was attributed to the single charged divacancy level and annealed around 350°C which is in accordance with data reported for this defect after electron irradiation. Furthermore, also the annealing behavior of the defects VO_i, C_iC_s and C_iO_i were found to tally with data given in the literature for electron irradiated silicon which can be interpreted as a further proof for the correct assignment of levels to defects in this work.

Relations between macroscopic and microscopic features

In principle the knowledge of all defect parameters (energy level, cross sections, introduction rate, type of defect: acceptor or donor) enables the calculation of the impact of the defect on the macroscopic detector properties. However, these parameters could not be determined for all defects. Furthermore, assumptions about the temperature dependence of the defect parameters had to be made since the defect properties are measured at very low temperatures while the macroscopic parameters are determined at room temperature. Therefore, the values calculated from the measured defect properties are afflicted with errors.

From the level parameters and the introduction rate of the divacancy in ^{60}Co-gamma irradiated silicon an α-value of $7 \times 10^{-12}\,\mathrm{AGy^{-1}cm^{-3}}$ was calculated which is only a factor of two below the measured value of $1.4 \times 10^{-11}\,\mathrm{AGy^{-1}cm^{-3}}$. However, after neutron irradiations a higher deviation was observed. The calculations suffer from the uncertainty in the level properties of the deep hole trap H(220) at around $E_V + 0.5\,\mathrm{eV}$. The calculated value was at least by a factor of four too small at an annealing state of 80 min at 60°C. Nevertheless, it could be shown that the calculated contribution $\alpha(E205) = 6.3 \times 10^{-18}\,\mathrm{Acm^{-1}}$ of the levels E(205a) and the divacancy (E(205b)) are in very good agreement with the value of $\alpha = 6 \times 10^{-18}\,\mathrm{Acm^{-1}}$ observed after a 2 months lasting annealing at 106°C.

Very strong indications for a correlation between the annealing of the defects E(210) and E(170), the *beneficial annealing* of the effective doping concentration and the short term annealing of the leakage current were found. All three processes showed very similar annealing parameters (Tab. 7.3). Under the assumption that the annealing of the level E(210) ($E_C - 0.46\,\mathrm{eV}$) is responsible for the observed changes in the macroscopic detector properties both capture cross sections of the defect at room temperature could be predicted. The values are $\sigma_n = 8.6 \times 10^{-16}\,\mathrm{cm^2}$ and $\sigma_p = 3.1 \times 10^{-13}\,\mathrm{cm^2}$.

The *donor removal* observed after neutron irradiation was discussed in very detail from the defect kinetics point of view including also numerical simulations of the defect kinetics. However, in conclusion it had to be stated that the experimental data so far cannot be explained in the scope of present defect kinetics models.

In parallel the effective doping concentration and TSC spectra were measured on a neutron irradiated sample during an isothermal heat treatment at 80°C. A defect at $E_V + 0.29\,\mathrm{eV}$ was found to increase in concentration in close relation to the *reverse annealing*. Although it could not be determined whether the defect is responsible for the increase of negative space charge or not (i.e. whether the defect is an acceptor or donor) it was clearly demonstrated that this defect is a measure for the negative space charge.

Compared to experimental data the *trapping times* calculated from the defect properties were

found to be 5 times higher for holes and at least 2 times higher for electrons, a discrepancy which still needs to be resolved.

Radiation hard material – Outlook

The experimental data presented in this work – and the results of other workers cited in the previous chapters – clearly revealed the beneficial effect of a high oxygen concentration on the radiation hardness of silicon detectors. However, it was also demonstrated that a high oxygen concentration has no influence on the leakage current and the saturation of the *reverse annealing* is only reached for fluences above $2 \times 10^{14}\,\mathrm{cm}^{-2}$. Therefore, cooling of the detectors is inevitable. On the one hand the leakage current has to be reduced during detector operation and on the other hand the *reverse annealing* must be suppressed. For the latter effect the detectors have to be kept cold even in non operational periods.

In an outlook the present and future possibilities for the production of radiation hard material were discussed on the basis of irradiation experiments with three different oxygen rich materials. However, only one material, namely the oxygen enriched FZ silicon, was found to be of interest for the near future.

A high resistivity *Magnetic Czochralski* (MCz) silicon and a highly compensated high resistivity Czochralski silicon, could be of future interest for further improvements of the radiation hardness. The MCz offers the possibility of a higher oxygen content than the enriched FZ (i.e. $[O] > 2 \times 10^{17}\,\mathrm{cm}^{-3}$) and on the example of the compensated Cz it was demonstrated that there are further promising possibilities for a *defect engineering* of silicon.

However, the radiation hard material for the present and the near future is the oxygen enriched FZ silicon. Here, the oxygen is diffused into the material by a long lasting heat treatment of an oxidized standard FZ silicon wafer in an oxygen or nitrogen atmosphere (e.g. 72 h at 1150°C). In contrast to other methods which incorporate the oxygen during the silicon production process this one is far more practical. It can be applied independent of the wafer diameter, the material so far used can still be taken, the diffusion process can be done in the oxidation ovens of the detector producers, and the additional cost of this process is rather low.

For fast neutron irradiation it was found that the oxygen prevents the donor removal and leads to a higher fraction of the so-called *non-removable* donor concentration while the so-called *stable damage* was not influenced by the oxygen concentration. Therefore, the improved radiation hardness is depending on the resistivity, resp. the donor concentration, of the material. A material with as low as possible resistivity and as high as possible oxygen concentration is therefore the best choice with respect to neutron irradiations. As a further advantage it should be mentioned that the type inversion in such a material is shifted to higher fluences. This has two impacts. First, the junction is on the front side of the device for a longer time and, second, the power consumption is reduced. Detectors with low resistivity bulk material have a high depletion voltage in the beginning. However, since the leakage current is initially small this has no dramatic impact on the power consumption. During irradiation the leakage current is increasing independently of the resistivity. For small fluences the depletion voltage is decreasing in both kind of devices. However, the high resistivity material will undergo type inversion at lower fluences than the low resistivity material. Thus after a certain exposure when the leakage current has reached high values the depletion voltage of the high resistivity

sample will be higher and so will be the power consumption.

In contrast to the findings after neutron irradiation a *complete donor removal* was observed after irradiation with 23 GeV protons. Consequently, the beneficial effect of an *incomplete donor removal* observed after neutron irradiation are most probably of no use any more in applications where detectors are exposed to irradiation fields with neutrons and charged hadrons. However, the introduction of negative space charge (*stable-damage*) was observed to be strongly suppressed in oxygen rich material. Compared to standard FZ silicon the introduction rate was found to be lower by about a factor of three in oxygen enriched FZ silicon. It is emphasized again that the *stable damage* is the most important damage component regarding the operability of detectors in High Energy Physics experiments since it cannot be influenced by the operational temperature. Furthermore, it is noted that the radiation damage in the devices exposed to the highest particle fluence, i.e. the detectors closest to the interaction point, is dominated by charged hadrons. Therefore, the reduced introduction rate of negative space charge in oxygen enriched silicon corresponds to a distinctive improvement of the radiation hardness.

This is best clarified by examples:

Detectors fabricated from oxygen enriched and standard FZ silicon were exposed to a 23 GeV proton fluence of $\Phi_{eq} = 6 \times 10^{14}\,\mathrm{cm}^{-2}$. The depletion voltages of the 300 μm thick devices measured in an annealing state corresponding to about two weeks storage at room temperature were measured to be 300 V for the oxygen enriched and 800 V for the standard material.

The impact of the damage parameters obtained for the oxygen enriched material on a 10 year LHC operational szenario was demonstrated (Sec. 8.1) and it was shown that with this new material the operability of e.g. Layer 1 of the ATLAS Pixel detector can now be assured without any problem.

Appendix A

Constants and Silicon Properties

A.1 Fundamental constants

Quantity	Symbol	Value
Boltzmann constant	k_B	1.380 658(12) $\times 10^{-23}$ J/K
		8.617 385(73) $\times 10^{-5}$ eV/K
Elementary charge	q_0	1.602 177 33(49) $\times 10^{-19}$ C
Electron rest mass	m_0	9.109 389 7(54) $\times 10^{-31}$ kg
Neutron mass	m_n	1.674 928 6(10) $\times 10^{-27}$ kg
Proton mass	m_p	1.672 623 1(10) $\times 10^{-27}$ kg
Atomic mass constant	m_u	1.660 540 2(10) $\times 10^{-27}$ kg
Permittivity in vacuum	ϵ_0	8.854 187 817 $\times 10^{-14}$F/cm
Planck constant	h	6.626 075 5(40) $\times 10^{-34}$ J s
		4.135 669 2(12) $\times 10^{-15}$ eV s
Avogadro constant	N_A	6.022 136 7(36) $\times 10^{23}$ mol^{-1}
Speed of light in vacuum	c	2.997 924 58$\times 10^{10}$ cm/s

Table A.1: Fundamental constants as recommended by the CODATA Task Group [Coh87] (CODATA = Committee on Data for Science and Technology).

A.2 Basic properties of silicon

Note that some silicon properties are displayed in Tab. 2.3 on page 27.

Temperature dependence of the band gap

It is important to keep in mind that the bandgap $E_g = E_C - E_V$ is temperature dependent and that the defect level positions in the bandgap are measured normally with respect to the nearest band edge E_C or E_V. The change of the bandgap E_g with temperature is a

T[K]	n_i[cm^{-3}]	N_C[cm^{-3}]	N_V[cm^{-3}]	E_g[eV]	m^*_{dC}/m_0	m^*_{dV}/m_0
20	1.66×10^{-130}	4.73×10^{17}	2.08×10^{17}	1.1689	1.062	0.614
50	1.97×10^{-41}	1.87×10^{18}	9.78×10^{17}	1.1675	1.063	0.690
100	2.22×10^{-11}	5.31×10^{18}	3.66×10^{18}	1.1627	1.066	0.831
150	3.47×10^{-1}	9.82×10^{18}	8.16×10^{18}	1.1555	1.070	0.946
200	5.34×10^{4}	1.52×10^{19}	1.43×10^{19}	1.1463	1.076	1.033
250	7.83×10^{7}	2.15×10^{19}	2.20×10^{19}	1.1354	1.083	1.100
273.15	9.58×10^{8}	2.47×10^{19}	2.60×10^{19}	1.1298	1.086	1.126
293.15	6.14×10^{9}	2.76×10^{19}	2.97×10^{19}	1.1248	1.090	1.146
300	1.10×10^{10}	2.86×10^{19}	3.10×10^{19}	1.1230	1.091	1.153
350	3.99×10^{11}	3.65×10^{19}	4.13×10^{19}	1.1095	1.100	1.194
400	6.17×10^{12}	4.51×10^{19}	5.26×10^{19}	1.0949	1.109	1.228

Table A.2: Calculated temperature dependence of the silicon intrinsic carrier concentration n_i, the effective densities of states, N_C and N_V, the band gap E_g and the density-of-states effective masses, m^*_{dC} and m^*_{dV}.

result of two different processes. The first one arises from the change in bond lengths with temperature and the second from the electron-phonon interaction. The latter dominates at temperatures above $\approx$ 100 K, decreasing the band-gap energy with increasing temperature. In this work the so-called Varshni equation [Var67]

$$E_g(T) = E_g(0) - \frac{\alpha_g \cdot T^2}{T + \beta_g} \tag{A.1}$$

was used with $E_g(0) = 1.1692\,\text{eV}$, $\alpha_g = (4.9 \pm 0.2) \cdot 10^{-4}\,\text{eV/K}$ and $\beta_g = (655 \pm 40)\,\text{K}$ taken from [Ale96]. Some calculated values are given in Tab. A.2.

Density-of-state effective masses

In this work the density-of-state effective masses for electrons m^*_{dC} and holes m^*_{dV} as given in the review article of M.A. Green [Gre90] have been used if not mentioned otherwise. Some temperature dependent values can be found in Tab. A.2. The following parameterizations were used for m^*_{dC} and m^*_{dV}:

$$m^*_{dC} = 6^{2/3} \left(m_t^{*2} m_l^*\right)^{1/3} \qquad \text{(Eq. 3.10)}$$

$$\text{with} \quad m_t^*/m_0 = 0.1905 \times \frac{E_g(0)}{E_g(T)} \quad \text{and} \quad m_l^*/m_0 = 0.9163 \tag{A.2}$$

and

$$\frac{m_{dV}*}{m_0} = \left(\frac{a + bT + cT^2 + dT^3 + eT^4}{1 + fT + gT^2 + hT^3 + iT^4}\right)^{2/3} \tag{A.3}$$

with the parameters

a = 0.443 587 0	b = 0.360 952 8 $\times 10^{-2}$	c = 0.117 351 5 $\times 10^{-3}$
d = 0.126 321 8 $\times 10^{-5}$	e = 0.302 558 1 $\times 10^{-8}$	f = 0.468 338 2 $\times 10^{-2}$
g = 0.228 689 5 $\times 10^{-3}$	h = 0.746 927 1 $\times 10^{-6}$	i = 0.172 748 1 $\times 10^{-8}$.

A.3 DLTS - Determination of trap concentration

The considered semiconductor is of n-type with a shallow donor concentration N_D. The calculations are based on the hypothesis that the distributions of free electrons is completely determined by the quasi-Fermi level for electrons E_{Fn} that is assumed to be constant throughout the space charge region and equal to the bulk Fermi level (see Fig. 4.7). Furthermore it is assumed that the defect under investigation is an acceptor level (negatively charged if occupied with an electron and neutral if not) with concentration N_t. In such a case the Poisson equation (2.3) can be written as

$$-\frac{d^2\Phi(x,t)}{dx^2} = \frac{q_0}{\epsilon\epsilon_0}\left(N_D - N_t + p_t(x,t) - n(x,t)\right) \tag{A.4}$$

where $p_t(x,t)$ denotes the concentration of neutral acceptors (see Eq. 3.36) and n(x,t) the free electron concentration. A double integration with the boundary conditions $\Phi(x > W, t) = 0$ and $\frac{d}{dx}\Phi(x,t)|_{x=W} = 0$ (see Fig. 4.7) leads to

$$\Phi(0,t) = -\frac{q_0}{\epsilon\epsilon_0}\int_0^\ell x\,\left[N_D - N_t + p_t(x,t) - n(x,t)\right]\,dx. \tag{A.5}$$

Here $\Phi(0,t)$ is the potential at the interface, equal to the sum of the externally applied reverse bias V_R and the constant built-in voltage V_{bi}. ℓ denotes a point deep in the neutral bulk ($\ell > W$) where the overall charge is zero during the whole emission process. Since the bias is kept constant during the emission process the time derivative of Eq. A.5 yields

$$\frac{d}{dt}\left(\int_0^\ell x\,n(x,t)\,dx\right) = \frac{d}{dt}\left(\int_0^\ell x p_t(x,t)\,dx\right). \tag{A.6}$$

Since the concentration of free electrons is zero in the space charge region ($x < W$) and $N_D - N_t$ in the neutral bulk ($x > W$) does not depend on time, the left hand side of Eq. A.6 results in

$$\frac{d}{dt}\left(\int_0^\ell x\,n(x,t)\,dx\right) = -W(N_D - N_t)\frac{dW}{dt}. \tag{A.7}$$

Combining Eqs. A.6 and A.7 and integration over the time ($t = 0$ denotes the beginning of the transient directly after the filling pulse) leads to

$$-\int_{t=0}^{t} W(N_D - N_t)\frac{dW}{dt'}dt' = \int_{t=0}^{t}\left(\int_0^\ell x\frac{d}{dt'}(p_t(x,t'))\,dx\right)dt'. \tag{A.8}$$

which finally gives

$$\int_0^\ell x\,\Delta p_t(x,t)\,dx = -(N_D - N_t)\frac{1}{2}\left(W^2(t) - W_0^2\right) \tag{A.9}$$

with $\Delta p_t(x,t) = p_t(x,t=0) - p_t(x,t)$ and $W_0 = W(t=0)$. Using the definition of the dynamic junction capacitance $C = \frac{dQ}{dV} = \frac{\epsilon\epsilon_0 A}{W}$ this can be written as

$$\frac{C^2(t)}{C_0^2} - 1 = \frac{2}{(N_D - N_t)\,W(t)^2} \int_0^\ell x\,\Delta p_t(x,t)\,dx. \tag{A.10}$$

With $C(t) = C_0 + \Delta C(t)$ and the assumption of $\Delta C(t) \ll C_0$ the left hand site can be approximated by

$$\frac{C^2(t)}{C_0^2} - 1 \approx -2\frac{\Delta C(t)}{C(t)}. \tag{A.11}$$

Integration of Eq. A.10 leads finally to

$$\frac{\Delta C(t)}{C(t)} = -\frac{1}{2}\frac{\Delta p_t^*(t)}{N_D - N_t}\frac{(W(t)-\lambda)^2 - (W_P - \lambda)^2}{W^2(t)} \tag{A.12}$$

with W_P being the width of the space charge region during the filling pulse (see Fig. 4.7) and λ the width of the edge region (Eq. 4.7). $\Delta p_t^*(t)$ denotes the concentration of acceptors occupied by holes in the region between $W_P - \lambda$ and $W(t) - \lambda$. For $t \to \infty$ all electrons are emitted from the acceptors, the capacitance relaxes into the steady state reverse bias capacitance C_R and the space charge region width becomes $W_R = L_R + \lambda$. Therefore the amplitude of the capacitance transient ΔC_0 divided by C_R is given by

$$\frac{\Delta C_0}{C_R} = -\frac{1}{2}\frac{N_t}{N_D}\frac{L_R^2 - L_P^2}{W_R^2}. \tag{A.13}$$

Here it has been assumed that during the filling pulse all acceptors have been filled with electrons and that the trap concentration is small compared to the donor concentration $N_D - N_t \approx N_D$. It should be noted that Eq. A.13 is valid for a donor level without the assumption of $N_D - N_t \approx N_D$. This is easily shown by replacing $N_D - N_t$ with N_D in Eq. A.4. For the use in experiments it is more convenient to express the equation with capacitance values that can directly be extracted from the measured capacitance transients

$$\frac{\Delta C_0}{C_R} = -\frac{1}{2}\frac{N_t}{N_D}\left[1 - \left(\frac{C_R}{C_P}\right)^2 - \frac{2\lambda C_R}{\epsilon\epsilon_0 A}\left(1 - \frac{C_R}{C_P}\right)\right]. \tag{A.14}$$

Appendix B

Review:
Defects and Impurities in Silicon

In Table B.1 a review of some identified defects is given. It has to be noted that the review is by far not complete but may prove very useful as a reference to further literature. The first four columns display the most probable identification of the defect and its charge state, the abbreviation for the Electron Paramagnetic Resonance (EPR) spectrum, the local vibrational mode (LVM) for infrared absorption and the zero phonon line for Photo Luminescence (PL) measurements. For further particulars about these measurement methods the reader is referred to [Mad89] and literature cited therein. The column in the middle gives information about the annealing (out $\downarrow$ or in $\uparrow$, frequency factor k_0, activation energy E_A, annealing temperature T_{ann}), the diffusion ($\leftrightarrow$, diffusion coefficient D_0, activation energy E_D), or the configurational change ($\rightarrow$,frequency factor k_0, activation energy E_A, activation temperature T_{ann}) of a defect or impurity. Here, the annealing temperature T_{ann} is defined as the temperature at which the defect concentration decreases to 1/e (37%) of the initial concentration during a 20 min lasting heat treatment. Further abbreviations are: ZB = zero bias, RB = reverse bias, inj = high injection. The last column gives the properties of the transition between two charge states of the defects: activation Energy $\Delta H'$, cross section for electrons (acceptors) or holes (donors) and peak maximum temperatures for the TSC (T_{TSC}) and DLTS (T_{DLTS}) methods. The peak maximum temperatures for TSC and DLTS measurements are calculated for a heating rate of $\beta = 0.183K/s$ and a time window of 200 ms, respectively (see Eqs. 4.36 and 4.18). Level parameters marked with a (*) indicate that the temperature dependence of the displayed capture cross section is known or that both capture cross sections (for electrons and holes) have been measured. In such cases the corresponding values can be found in in Tab. B.2. More information about the specific defects can be found in the given references.

Defect	EPR	IR LVM [cm^{-1}]	PL 0 phonon line [eV]	Ref.	Annealing ($\uparrow,\downarrow$) / Diffusion ($\leftrightarrow$) k_0, E_{ann}, T_{ann} / D_0, E_D [s^{-1}, eV, °C] / [$cm^2 s^{-1}$, eV]	Ref.	Emission Parameters $\Delta H'$, $\sigma, T_{TSC}, T_{DLTS}$ [eV, cm^2, K, K]	Ref.
Impurities								
O_i		1106 (RT)			$\leftrightarrow 0.17, 2.54$	[Åbe98]	not electrically active	
O_2		1012, 1060, 1105 (10K)		[Mur98]	$\leftrightarrow 3\times10^{-4}, 1.26$	[Åbe98]		
C_s		607 (RT)			kick out mechanism $C_s :\leftrightarrow 0.95, 3.04$ ($C_i :\leftrightarrow 0.44, 0.87$)	[Wer98]	not electrically active	
N_2		766, 962		[Jon94]	main configuration		not electrically active	[Jon94]
N_s	Si-SL5	653		[Jon94]			-0.19 d	[Mad89]
P_s							-0.045 d	[Mad89]
Sb_s							-0.043 d	[Mad89]
As_s							-0.054 d	[Mad89]
B_s							+0.044 a	[Mad89]
Al_s							+0.067 a	[Mad89]
Fe^0					$(\leftrightarrow, 1\times10^{-2}, 0.84)$	[Hei92]	$(0.42, 6\times10^{-16}, 176, 220)^*$	[Bro85]
Fe^+					$(\leftrightarrow, 1.4\times10^{-3}, 0.69)$	[Hei92]		
Mg							-0.108 d -0.257 d	[Mad89]
Li_i							-0.034 d	[Mad89]
Primary radiation induced defects								
I^-	Si-G25			[Wat79]	$\downarrow$ {annealing observed at 4.2K / recombination enhanced}			
I					$\downarrow$ about 150K in n-type	[Wat79]		
I_2^+	Si-P6				$\downarrow\approx 170$°C	[Lee98]		
V^{--}					0.18eV	[Wat92]		
V^-								
V^0					0.45eV	[Wat92]		
V^+					negative–U	[Wat80]	+0.05	
V^{++}					0.32eV	[Wat92]	+0.13	

Defect	EPR	IR LVM [cm^{-1}]	PL 0 phonon line [eV]	Ref.	Annealing ($\uparrow,\downarrow$) / Diffusion ($\leftrightarrow$) k_0, E_{ann}, T_{ann} / D_0, E_D [s^{-1}, eV, °C] / [$cm^2 s^{-1}$, eV]	Ref.	Emission Parameters $\Delta H'$, $\sigma, T_{TSC}, T_{DLTS}$ [eV, cm^2, K, K]	Ref.
V_2^{--}								
V_2^{-}	Si-G7			[Wat65]			$(-0.235, 2.2\times10^{-15}, 98, 119)^*$	[Hal96]
V_2^{0}					$\downarrow 1.1\times10^{9}, 1.47, 340$°C	[Evw76]	$(-0.420, 1.5\times10^{-15}, 168, 206)^*$	[Hal96]
V_2^{+}	Si-G6			[Wat65]			$(+0.196, 6.1\times10^{-15}, 88, 108)^*$	[Hal96]
V_4	Si-P3			[Lee73]	(V_4-planar) $\downarrow\approx 150$°C			
V_5^{-}	Si-P1			[Lee73]	(V_5-nonplanar) $\uparrow\approx 150$°C			

Vacancy related defects

VO_i^{-}	Si-B1 (Si-A)	877 RT 885 $\leq 70K$		[Wat61]				
VO_i^{0}		830 RT 835 $\leq 70K$		[Cor61]	$\downarrow 1.6\times10^{15}, 2.27, 350$°C	[Sve86]	$(-0.164, 6.1\times10^{-15}, 68, 82)^*$	[Hal96]
VP^{-}					$\downarrow, 4\times10^{10}, 1.25, 190$°C ($ZB$)	[Kim75]		
VP^{0}	Si-G8 (Si-E)			[Wat64]	$\downarrow, 7\times10^{8}, 0.95, 130$°C ($RB$) $\downarrow 0.48eV$ under forward bias	[Kim75] [Bar86]	$(-0.456, 3.7\times10^{-15}, 176, 215)$	[Bro82]
VSn^0					$\downarrow\approx 200$°C (charge state not specified)	[Wat92]		
VSn^{+}							+0.32	[Wat80]
VSn^{++}							+0.07	[Wat80]
VAs					$\downarrow\approx 170$°C (charge state not specified)	[Wat92]		
VGe					$\downarrow\approx 220K$ (charge state not specified)	[Wat92]		
VAl					$\downarrow\approx 250$°C (charge state not specified)	[Wat92]		
VSb					$\downarrow\approx 190$°C (charge state not specified)	[Wat92]	-0.44 a	[Mad89]
VB					$\downarrow\approx 260K$ (charge state not specified)	[Wat92]	+0.50 +0.36	[Mad89]
$VO + O_i$		914,1000		[Lon94]	$\uparrow 290$°C			
VO_2		889		[Sve86]	$\uparrow 350$°C ,$\downarrow 500$°C	[Lon97]	no levels expected	[Sve86]
VO_3		962,899,993		[Lon94]	$\uparrow 450$°C ,$\downarrow 520$°C	[Lon94]		
VO_4		1032,1043		[Lon94]	$\uparrow 520$°C $\downarrow 660$°C	[Lon94]		

Defect	EPR	IR LVM [cm^{-1}]	PL 0 phonon line [eV]	Ref.	Annealing ($\uparrow,\downarrow$) / Diffusion ($\leftrightarrow$) k_0, E_{ann}, T_{ann} / D_0, E_D [s^{-1}, eV, °C] / [$cm^2 s^{-1}$, eV]	Ref.	Emission Parameters $\Delta H'$, σ, T_{TSC}, T_{DLTS} [eV, cm^2, K, K]	Ref.
V_2O^0	Si-A14	839		[Lee76] [Sar97]	$\downarrow \approx 350$°C	[Lee76]		
$V_2O_2^0$	Si-P2	824		[Lee76] [Sar97]	$\uparrow \approx 350$°C , $\downarrow \approx 400$°C	[Lee76]		
V_3O^0	Si-P4			[Lee76]	$\uparrow \approx 350$°C , $\downarrow \approx 450$°C	[Lee76]		
$V_3O_2^0$	Si-P5	833		[Lee76] [Sar97]	$\uparrow \approx 400$°C	[Lee76]		
$V_3O_3^0$	Si-A15			[Lee76]	$\uparrow \approx 400$°C	[Lee76]		

Interstitial related defects

IO_i^0	A^0			[Abd96]				
IO_i^+	A^+	Si-A18		[Abd96]	$A^+ \rightarrow B^0 : 160 - 190K$	[Abd96]	$\approx +0.4$	[Abd96]
IO_i	B^-	Si-AA13		[Abd96]	$B^- \rightarrow AA12 : 2 \times 10^{12}, 0.75, 250K$	[Abd96]		
IO_i^0	B^0			[Abd96]	$B \rightarrow A$: illumination at 77K	[Abd96]	≈ -0.19	[Abd96]
IO_i^+	B^+	Si-AA14		[Abd96]	$\downarrow 2 \times 10^{12}, 0.75, 250K$	[Abd96]	$\approx +0.13$	[Abd96]
$I - O_i^-$	(?)	Si-AA12		[Abd96]	$\downarrow 10 - 80$°C release of I	[Abd96]	-0.39	[Abd96]
I_nX	(?)		$W1.018$	[Dav87a]	$\uparrow -, -, 150$–250°C $\downarrow -, -, 330$°C	[Dav87a]	probably isoelectronic	[Dav97]
B_i^-					anneal at RT			
B_i^0					negative–U	[Wat80]	-0.45	[Wat80]
B_i^+					anneal at RT		-0.13	[Wat80]
B_iB_s							$+0.30$	[Mad89]
B_iC_s					$\downarrow$ recombination enhanced dissociation	[Sch98]	$+0.306, 3 \times 10^{-15}, 126, 154$ X-center: $+0.037$ (?)	[Tra95] [Mad89]
B_iO_i					≈ 175°C	[Sch98]	$\left\{ \begin{array}{l} (-0.24, 4 \times 10^{-15}, 98, 118) \\ (-0.27, 3 \times 10^{-13}, 96, 113)^* \end{array} \right\}$ $+0.26$(?)	$\left\{ \begin{array}{l} [\text{Tra95}] \\ [\text{Sch98}] \end{array} \right\}$ [Mad89]

Defect	EPR	IR LVM [cm^{-1}]	PL 0 phonon line [eV]	Ref.	Annealing ($\uparrow,\downarrow$) / Diffusion ($\leftrightarrow$) k_0, E_{ann}, T_{ann} / D_0, E_D [s^{-1}, eV, °C] / [$cm^2 s^{-1}$, eV]	Ref.	Emission Parameters $\Delta H'$, $\sigma, T_{TSC}, T_{DLTS}$ [eV, cm^2, K, K]	Ref.
C_i^-	Si-L6			[Son90a]				
C_i^0		930, 921			$\downarrow 5\times10^7, 0.74, 30$–$70$°C	[Son90a]	$-0.110, 6\times10^{-15}, 48, 57$	[Mol97]
C_i^+	Si-G12		0.856	[Wat76]	$\downarrow 1\times10^8, 0.75, 30$–$70$°C	[Son90a]	$+0.280, 2\times10^{-15}, 117, 144$	[Mol97]
$C_iC_s^-$ A^-	Si-G17			[Son90b]				
$C_iC_s^0$ A^0					$A^0 \rightarrow B^0, 1.1\times10^{11}, 0.16, 55K(RB)$	[Son90b]	-0.17 (compare VO_i)	[Son90b]
$C_iC_s^+$ A^+	Si-G11			[Son90b]			$+0.086, \geq 10^{-16}$	[Son90b]
$C_iC_s^-$ B^-	Si-L7				$B^- \rightarrow A^-, 1.4\times10^{12}, 0.145, 50K(ZB)$	[Jel82]		
$C_iC_s^0$ B^0			G 0.969	[Son90b]	$\downarrow, 2.5\times10^{13}, 1.7, 250$°C	[Dav89]	-0.11	[Son90b]
$C_iC_s^+$ B^+					$B^+ \rightarrow A^+, 2.5\times10^{12}, 0.21, 70K(ZB)$		+0.05	[Son90b]
$C_iP_s^-$ IA				[Zha93]	$\downarrow -, -, \approx 130$°C ($\approx 10$°C ($inj$))	[Zha93]		
$C_iP_s^0$ IA	Si-L8			[Zha93]	$IA \rightarrow III, 0.54eV, 240K$(inj)	[Gür92]	-0.38	[Gür92]
$C_iP_s^+$ IA				[Zha93]	$IA \rightarrow IB, 0.22eV, 140K$(inj)	[Gür92]	+0.48	[Gür92]
$C_iP_s^-$ IB				[Zha93]	$IB \rightarrow IA, 2.0\times10^{12}, 0.49, 160K(ZB)$	[Gür92]		
$C_iP_s^0$ IB	Si-L9			[Zha93]			-0.07	[Gür92]
$C_iP_s^+$ IB				[Zha93]			-0.39	[Gür92]
$C_iP_s^-$ IIA				[Zha93]	$IIA \rightarrow IA, 2.8\times10^{16}, 1.25, 50$°C ($ZB$)	[Gür92]		
$C_iP_s^0$ IIA	Si-L10			[Zha93]	$IIA \rightarrow IIB, 1.5\times10^{12}, 0.70, 230K(RB)$	[Gür92]	-0.26	[Gür92]
$C_iP_s^+$ IIA				[Zha93]			-0.57	[Gür92]
$C_iP_s^0$ IIB				[Zha93]	$IIB \rightarrow IIA, 9.2\times10^{12}, 0.86, 270K(ZB)$	[Gür92]		
$C_iP_s^+$ IIB				[Zha93]			-0.32	[Gür92]
$C_iP_s^0$ III				[Zha93]	$III \rightarrow IIB, 1.7\times10^{13}, 0.77, 240K(ZB)$	[Gür92]		
$C_iP_s^+$ III				[Zha93]			-0.23	[Gür92]
$C_iO_i^0$								
$C_iO_i^+$	Si-G15		C 0.79	[Tro87]			$(0.348, 9.4\times10^{-16}, 146, 181)^*$	[Hal96]
C_iAs	Si-L11			[Zha93]				
C_iSb	Si-L12			[Zha93]				
C_iHC_s			T0.935	[Saf96]	$\uparrow$ irradiation + 450°C	[Saf96]	-0.2 a midgap d	[Saf96]

Defect	EPR	IR LVM [cm^{-1}]	PL 0 phonon line [eV]	Ref.	Annealing ($\uparrow,\downarrow$) / Diffusion ($\leftrightarrow$) k_0, E_{ann}, T_{ann} / D_0, E_D [s^{-1}, eV, °C] / [$cm^2 s^{-1}$, eV]	Ref.	Emission Parameters $\Delta H'$, $\sigma, T_{TSC}, T_{DLTS}$ [eV, cm^2, K, K]	Ref.
Some non irradiation induced defects								
$TDD1$		975		[Åbe98]	([O_4], see Sec. 3.6.2)		$-0.07d$ $-0.15dd$	[Ben83]
$TDDx$	Si-NL8	988 (TDD2)		[Åbe98]	(for further information on TDD's see references in Sec. 3.6.2)		single donor level -0.0530 to -0.0693	[Ewe97]
STD	Si-NL10			[Ewe97]	(for further information on STD's see references in Sec. 3.6.2)		-0.0347 to -0.0374	[Ewe97]
FeB							$-0.23a$ $+0.10d$	[Mad89]
BH					$\downarrow >$ 240°C	[Mad89]		

Table B.1: Review of identified defects (see text for details.)

Transition	ΔH[eV]	X	$c_n[cm^3s^{-1}]$	$c_p[cm^3s^{-1}]$	$T_{\text{range}}[K]$	Ref.
$VO_i^{(-/0)}$	-0.164	0.29	$1.4\times10^{-8}\times T^{0.5}$	$8\times10^{-8}\times T^{0.7}$	80–108	[Hal96]
$VV^{(--/-)}$	-0.225	4.6	$1.6\times10^{-12}\times T^{1.4}$	7×10^{-7}	105–155	[Hal96]
$VV^{(-/0)}$	-0.421	0.33	$5.4\times10^{-9}\times T^{0.40}$	$2\times10^{-6}\times T^{-0.3}$	182–226	[Hal96]
$VP^{(-/0)}$			$1.3\times10^{-11}\times T^{0.5}$		182–226	[Hal96]
$C_iO_i^{(+/0)}$	0.339	0.89	$5.1\times10^{-23}\times T^{5.2}$	$1.2\times10^{-10}\times T^{0.61}$	160–238	[Hal96]
$VV^{(+/0)}$	0.194	0.56	$\gg c_p$	$2.1\times10^{-9}\times T^{0.20}$	104–146	[Hal96]

Transition	$\Delta H'$[eV]	σ_n[cm^2]	σ_p[cm^2]	T_{range}[K]	Ref.
$B_iO_i^{(-/0)}$	-0.27	3×10^{-13}	$0.45-1.2\times10^{-15}$	RT	[Sch98]
$Fe^{(+/0)}$	0.37	$1\times10^{-10}\times T^{-1.5}$	$5.6\times10^{-16}\exp(-\frac{0.048}{k_BT})$	100-300	[Lem81] [Bro85]

Table B.2: Enthalpy (ΔH), capture coefficients for electrons (c_n) and holes (c_p) and the temperature range in which these data have been obtained for various defect levels. In the second part of the table only the activation energy $\Delta H'$ and both capture cross sections (σ_n and σ_p) are given.

As explained in Sec. 3.4 there exist two different formulations for the defect level emission coefficients (Eqs. 3.24 and 3.27). This is also expressed in Tab. B.2 where the data are given as published in the literature. Since the emission coefficients are measured parameters the two formulations must be equal:

$$e_{n,p} = c_{n,p}\, X_{n,p}\, N_{C,V}\, \exp\left(-\frac{\Delta H_{n,p}}{k_B T}\right) \qquad \text{(Eq. 3.24, page 43)}$$

$$= \sigma_{n,p}\, v_{th,n,p}\, N_{C,V} \exp\left(-\frac{\Delta H'_{n,p}}{k_B\, T}\right) \qquad \text{(Eq. 3.27)}$$

with

$$v_{th,n,p} = \sqrt{\frac{3k_BT}{m^*_{dC,dV}}} = 6.743\times10^5\,\frac{\text{cm}}{\text{s}}\cdot(T[\text{K}])^{0.5}\cdot\left(\frac{m_0}{m^*_{dC,dV}}\right)^{0.5}.$$

List of Figures

1.1 Expected particle fluences for the ATLAS detector. 2

2.1 Schematic setup of a Czochralski crystal puller. 7
2.2 Schematic setup for the Float zone process. 10
2.3 The planar process for detector fabrication. 14
2.4 Schematic cross section of a MPI München $p^+-\nu-n^+$ structure. 15
2.5 Schematic cross section of a ITE $p^+-\nu-n^+$ structure. 16
2.6 Schematic cross section of a Schottky diode. 18
2.7 Schematic figure of a p^+-n abrupt junction. 22
2.8 Schematic cross section of a microstrip detector. 30

3.1 Simulation of a PKA track with primary energy of 50 keV. 32
3.2 Damage functions for neutrons, protons, pions and electrons. 34
3.3 Charge states of donors acceptors and amphoteric levels. 37
3.4 Fermi level as function of temperature and defect concentrations. 41
3.5 Emission and capture rates of an energy level E_t. 42
3.6 Schematic representation of defect annealing mechanisms. 49
3.7 Schematic representation of vacancy and vacancy-defect pair annealing. . . . 53
3.8 Hierarchy and stability of self-interstitial related defects. 55
3.9 Configurational co-ordinate diagram for the C_iC_s complex. 56
3.10 Thermal donor formation kinetics. 58

4.1 Neutron flux as function of target distance (PTB). 67
4.2 Dependence of κ on the distance from the target (PTB). 68
4.3 Dependence of α on the distance from the target (PTB). 68
4.4 Examples for C/V and I/V characteristics of type inverted detectors. 72
4.5 Electrical setup for C/V and I/V measurements. 74
4.6 Principle of C-DLTS operation. 76
4.7 Band bending diagram explaining the λ region. 78
4.8 Time axis used for analysis of capacitance transients. 81
4.9 Illustration of DLTS rate window by means of double-boxcar integrator. . . . 82
4.10 Correlator functions used for *maximum evaluation*. 83
4.11 DLTS spectra with different correlators. 84
4.12 DLTS spectra obtained with a_1, b_1, a_2 and b_2 correlators. 86
4.13 Arrhenius plot obtained with the variable time window method. 87
4.14 Schematic representation of the TSC measurement. 89
4.15 Typical TSC spectrum ($\Phi_{eq} = 1 \times 10^{13}\,\mathrm{cm}^{-2}$). 90
4.16 Principle of operation: Delayed heating method. 92

4.17 Schematic view of the cryostat cold station. 94
4.18 Electrical setup for DLTS and TSC measurements. 95

5.1 Leakage current increase. 99
5.2 Leakage current annealing at different temperatures. 100
5.3 Arrhenius plot for time constant τ_I. 103
5.4 Parameter α_0 versus inverse temperature. 103
5.5 α values as function of cumulated annealing time at 60°C. 105
5.6 α values measured after 80 min at 60°C for various materials. 105
5.7 $\alpha(80\,\text{min}, 60°\text{C})$ versus fluence for various irradiation sources. 107
5.8 Change in the bulk material as measured immediately after irradiation 111
5.9 Annealing behavior of ΔN_{eff}. 112
5.10 Fluence dependence of the short term annealing amplitude N_A. 114
5.11 Arrhenius Plot of annealing time constant τ_a. 114
5.12 Comparison between first and second order fit to the *reverse annealing*. . . . 116
5.13 Half life period of the reverse annealing as function of fluence. 118
5.14 Fluence dependence of 2^{nd}-order rate constant k_{2Y}. 118
5.15 Reverse annealing amplitude $N_{Y,\infty}$ versus fluence. 121
5.16 Arrhenius Plot of reverse annealing time constant τ_Y. 121
5.17 Fluence dependence of N_{eff} for low resistivity (100Ωcm) FZ and Cz silicon. . 123
5.18 Damage parameter N_C plotted against the fluence. 124
5.19 Incomplete donor removal (plot of $N_{C0}/N_{eff,0}$ versus fluence). 126
5.20 Donor removal constant c plotted versus N_{C0}. 126
5.21 Improved radiation hardness of oxygen rich silicon. 129

6.1 DLTS spectra obtained with floating and grounded guard ring. 136
6.2 Determination of defect concentrations with TSC measurements. 138
6.3 TSCap measurements with floating and connected guard ring. 140
6.4 DLTS spectra obtained with different cooling and filling conditions. 143
6.5 Observation of the configurational change C_iCs (B) $\rightarrow$ C_iC_s (A). 144
6.6 Arrhenius Plot for the conversion $C_iC_s^{(-)}$(B) $\rightarrow$ $C_iC_s^{(-)}$(A). 145
6.7 Bistability of the C_iC_s(A) donor level. 145
6.8 Electron capture of the C_iO_i donor level. 147
6.9 Electron capture coefficient c_n of the C_iO_i defect. 149
6.10 Dependence on TSC filling temperature: C_iO_i (high injection). 150
6.11 Dependence on TSC filling temperature: C_iO_i (hole injection) 152
6.12 Poole-Frenkel effect observed on the TDD in CZ silicon. 153
6.13 DLTS-spectra of ^{60}Co-gamma irradiated samples. 156
6.14 Arrhenius plot of defect levels in ^{60}Co-gamma irradiated samples. 157
6.15 TSC spectra of a ^{60}Co-gamma irradiated sample. 157
6.16 Comparison of DLTS-spectra after ^{60}Co-gamma and neutron irradiation. . . . 158
6.17 DLTS-spectra after ^{60}Co-gamma and neutron irradiation: The VV levels. . . 159
6.18 Electron capture of the $VV^{(=/-)}$-level. 162
6.19 DLTS-spectrum evolution at room temperature after n-irradiation. 163
6.20 DLTS-peak heights evolution at room temperature: short term annealing. . . 165
6.21 DLTS-peak heights evolution at room temperature: long term annealing. . . . 167
6.22 Example of a DLTS difference spectrum. 168

6.23 Evolution of TSC spectra after neutron irradiation (Filling at 20 K). 170
6.24 Evolution of TSC spectra after neutron irradiation (Filling at 50 K). 170
6.25 TSC peak heights during room temperature annealing for various defects. . . 171
6.26 TSC spectra: Electron and hole injection. 172
6.27 Changes of DLTS-peak heights during an isochronal heat treatment. 173
6.28 Evolution of the E(205) DLTS signal during an isochronal heat treatment. . . 173
6.29 Evolution of DLTS-spectra at 60°C for a sample of type WM3-3kΩcm. 176
6.30 Difference spectra for a sample of type WM-3kΩcm. 177
6.31 Evolution of DLTS-spectra at 60°C for a sample of type WH-6Ωcm. 178
6.32 Evolution of DLTS-spectra at 60°C for a sample of type Cz-110Ωcm. 179
6.33 Evolution of DLTS-spectra at 60°C for a sample of type WH-4kΩcm. 181
6.34 Comparison: 24 GeV/c proton and MeV neutron irradiation. 181

7.1 Donor concentration N_{donor} plotted versus fluence for various materials. . . . 194
7.2 Donor removal constant c plotted versus $N_{eff,0}$. 195
7.3 Development of ΔN_{eff} during annealing at 21 and 80°C. 197
7.4 Evolution of TSC spectrum during heat treatment at 80°C. 198
7.5 Increase of N_Y plotted against increase of H(116K) concentration. 199

8.1 Oxygen enriched and standard FZ: $|N_{eff}|$ after 23 GeV proton irradiation. . . 202
8.2 Oxygen enriched and standard FZ: N_C after 23 GeV proton irradiation. . . . 203
8.3 Oxygen enriched FZ: N_Y after 23 GeV proton irradiation. 203
8.4 Compensated p-type Cz silicon: N_{eff} after 192 MeV pion irradiation. 207

List of Tables

2.1 Equilibrium segregation coefficients for some elements. 8
2.2 Properties and labelling of the used test structures. 20
2.3 Basic properties of Si, Ge, GaAs and Diamond. 27

4.1 Properties and labelling of the used materials. 64

5.1 Parameters of leakage current annealing after [Wun92]. 101
5.2 Parameters of current annealing at different annealing temperatures. 102
5.3 α values measured after 80 min at 60°C for various materials. 106
5.4 Experimental determination of hardness factors for various sources. 108
5.5 α values obtained on "standard" material after ^{60}Co-gamma irradiation. . . . 109
5.6 *Beneficial* and *reverse annealing* parameters for different materials. 113
5.7 Temperature dependence of the *beneficial annealing* time constant τ_a. 115
5.8 Temperature dependence of the *reverse annealing* time constant τ_Y. 122
5.9 Damage parameters g_c, N_{C0} and c for different n-type materials. 125
5.10 Particle dependence of damage parameters g_Y and g_C. 128

6.1 Labelling of electron and hole traps. 133
6.2 Geometrical capacitance with floating and connected guard ring. 137
6.3 Defect concentrations (DLTS) with floating or connected guard ring. 137
6.4 Defect concentrations (TSC) with floating or connected guard ring. 139
6.5 Defect concentrations (TSCap) with connected guard ring. 140
6.6 Defect concentrations obtained with TSC, DLTS and TSCap. 141
6.7 Time constant for the transition $C_iC_s^{(-)}$(B) $\longrightarrow$ $C_iC_s^{(-)}$(A). 146
6.8 Fit parameters for the temperature dependent C_iOi filling factor. 151
6.9 Defect parameters measured after ^{60}Co-gamma irradiation. 155
6.10 Ratios of introduction rates for defects after γ and n - irradiation. 160
6.11 Defect parameters observed during room temperature annealing. 164
6.12 Annealing temperatures measured during an isochronal annealing study. . . . 174
6.13 Properties and labelling of the used materials. 182
6.14 Defect introduction rates measured on neutron irradiated samples. 182
6.15 Defect annealing time constants at 60°C. 184

7.1 Parameters of defects at 20°C. 186
7.2 Contribution of various defects to the leakage current at 20°C. 187
7.3 k_0 and E_A for microscopic and macroscopic annealing processes. 189
7.4 Contribution of various defects to N_{eff} at 20°C. 190
7.5 Impact of various defects on the CCE at 20°C. 200

A.1 Fundamental constants. 215
A.2 Temperature dependence of n_i,N_C,N_V,m^*_{dC}, E_g and m^*_{dV} 216

B.1 Review of identified defects 219
B.2 Capture cross sections for various defects. 225

List of publications

Listed in reverse chronological order:

1. E.Fretwurst, M.Kuhnke, M.Moll, G.Lindström
   Relation between microscopic defects and macroscopic changes in silicon detector properties after hadron irradiation. Paper submitted to the "First International Workshop on Defect Engineering of Advanced Semiconductor Devices" of the ENDEASD, held in Santorini -Greece, 21-22 APRIL 1999.

2. M.Moll, E.Fretwurst and G.Lindström.
   Investigation on the Improved Radiation Hardness of Silicon Detectors with High Oxygen Concentration. Paper presented at the "8^{th} European Symposium on Semiconductor Detectors, New Developments in Radiation Detectors", held at Schloss Elmau, June 14 - 17, 1998, accepted for publication in Nucl. Instr. & Meth. in Phys. Res. A.

3. G.Lindström, M.Moll and E.Fretwurst.
   Radiation Hardness of Silicon Detectors - A Challenge from High Energy Physics. Nucl. Instr. & Meth. in Phys. Res. A 426 (1999) 1-15.

4. M.Moll, E.Fretwurst, G.Lindström.
   Leakage current of hadron irradiated silicon detectors - material dependence. Paper presented at the "2^{nd} International Conference on Radiation Effects on Semiconductor Materials, Detectors and Devices" held at the Grand Hotel Mediterraneo, Firenze, Italy, March 4-6, 1998; Nucl. Instr. & Meth. in Phys. Res. A 426 (1999) 87-93.

5. E. Fretwurst, H. Feick, G. Lindström, M. Moll.
   A comprehensive model for the effective doping concentration of irradiated silicon detectors. Paper presented at "The Third International (Hiroshima) Symposium on the Development and Application of Semiconductor Tracking Detectors" at Melbourne 9-12th , December, 1997; to be published in Nucl. Instr. & Meth. in Phys. Res. A.

6. M. Moll, H. Feick, E. Fretwurst, and G. Lindström.
   Correlation between a deep hole trap and the reverse annealing effect in neutron-irradiated silicon detectors. Paper presented at the Seventh Pisa Meeting on Advanced Detectors, La Biodola, Isola d'Elba, Italy, May 25-31, 1997; Nucl. Instr. & Meth. in Phys. Res. A 388 (1998) 194-197.

7. H. Feick and M. Moll.
   Microscopic Studies of Radiation Damage-Induced Defects Responsible for the Deterioration of High-Resistivity Silicon Detectors. Proceedings of the 7th International

Autumn Meeting GADEST '97, Spa Belgium, Oct. 5-10, 1997; Solid State Phenomena Vols. 57-58 (1997) 233-238, Scitec Publications, Switzerland.

8. H. Feick, E. Fretwurst, G. Lindström, and M. Moll.
Correlation of Radiation Damage Effects in High Resistivity Silicon Detectors with Results from Deep Level Spectroscopy. IEEE Trans. Nucl. Sci. NS-44 (1997) 825–833.

9. H. Feick, E. Fretwurst, P. Heydarpoor, G. Lindström, M. Moll.
Analysis of TSC spectra measured on silicon pad detectors after exposure to fast neutrons. Nucl. Instr. & Meth. in Phys. Res. A 388 (1997) 323-329.

10. M. Moll, H. Feick, E. Fretwurst, G. Lindström, and C. Schütze.
Comparison of defects produced by fast neutrons and ^{60}Co gammas in high resistivity silicon detectors using Deep Level Transient Spectroscopy. Proceedings of the International Conference on Radiation Effects on Semiconductor Materials, Detectors and Devices, Florence, Italy, March 6-8, 1996; Nucl. Instr. & Meth. in Phys. Res. A 388 (1997) 335-339.

11. G.N. Taylor, F. Fares, S. Bates, C. Furetta, M. Glaser, F.Lemeilleur, E. León-Florián, C. Gössling, B. Kaiser, A. Rolf, R. Wunstorf, H. Feick, E. Fretwurst, G. Lindström, M. Moll, A. Chilingarov.
Radiation induced bulk damage in silicon detectors Nucl. Instr. & Meth. in Phys. Res. A 383 (1996) 144-154.

12. S.J. Bates, C. Furetta, M. Glaser, F. Lemeilleur, E. León-Florián, C. Gößling, B. Kaiser, A. Rolf, R. Wunstorf, H. Feick, E. Fretwurst, G. Lindström, M. Moll, G. Taylor, A. Chilingarov.
Pion-induced damage in silicon detectors. Nucl. Instr. & Meth. in Phys. Res. A 379 (1996) 116-123.

13. E. Fretwurst, C. Dehn, H. Feick, P. Heydarpoor, G. Lindström, M. Moll, C. Schütze, T. Schulz.
Neutron induced defects in silicon detectors characterized by DLTS and TSC methods. Nucl. Instr. and Meth. in Phys. Res. A 377 (1996) 258-264.

14. H. Feick, E. Fretwurst, G. Lindström, and M. Moll.
Long term damage studies using silicon detectors fabricated from different starting materials and irradiated with neutrons, protons, and pions. Nucl. Instr. and Meth. in Phys. Res. A 377 (1996) 217-223.

15. M. Moll, H. Feick, E. Fretwurst, G. Lindström, and T. Schulz.
Observation of a bistable defect generated and activated by heat treatments in irradiated high resistivity silicon detectors. Nucl. Phys. B 44 (Proc. Suppl.) (1995) 468-474.

16. M. Moll.
Temperungsexperimente an strahlengeschädigten Silizium- Detektoren. Diploma thesis, University of Hamburg (1995).

17. T. Schulz, H. Feick, E. Fretwurst, G. Lindström, M. Moll, and K.H. Mählmann.
Long Term Reverse Annealing in Silicon Detectors. IEEE Trans. Nucl. Sci. 41 (1994) 791-795.

Bibliography

[Abd96] Kh.A. Abdullin, B.N.Mukashev and Yu.V.Gorelkinskii. Metastable oxygen-silicon interstitial complex in crystalline silicon. *Semicond. Sci. Technol.*, 11:1696–1703, 1996.

[Åbe98] D. Åberg, B.G.Svensson, T.Hallberg and J.L.Lindström. Kinetic study of the oxygen dimer and thermal donor formation in silicon. *Physical Review B*, 58(19):12944–12951, 1998.

[Ale96] V. Alex, S. Finkbeiner, and J. Weber. Temperature dependence of the indirect energy gap in crystalline silicon. *J. Appl. Phys.*, 79:6943, 1996.

[Als93] P. Alscher. Untersuchungen zu den elektronischen Eigenschaften von Siliziumdetektoren. Diploma thesis, Universität Hamburg, 1993.

[AME] AME-Cryostat Cryodyn 91, Almer Mater Electronics, Labormessanlagen GmbH Berlin, Germany.

[Amm84] W. von Ammon and H.Herzer. The production and availability of high resistivity silicon for detector application. *Nucl. Instr. & Meth. in Physics Research*, 226:94–102, 1984.

[And98] L. Andricek, T.Gebhart, D.Hauff, J.Kemmer, E.Koffeman, G. Lutz, R.H. Richter, T. Rohe, R. Wunstorf. Single-sided p^+n and double-sided silicon strip detectors exposed to fluences up to $2 \times 10^{14}/cm^2$ 24 GeV protons. *Nucl. Instr. & Meth. in Physics Research*, A 409:184–193, 1998.

[AST93] ASTM E722-85. Standard practice for characterizing neutron fluence spectra in terms of an equivalent monoerergetic neutron fluence for radiation hardness testing of electronics. *ASTM E772-93 (revision)*, 1993.

[ATL97] ATLAS. Inner Detector Technical Design Report (ATLAS TDR 4-5). *CERN/LHCC/97-16 and 17*, 1997.

[ATL98] ATLAS. Pixel Detector - Technical Design Report. *CERN/LHCC/98-13*, 1998.

[Awa86] O.O. Awadelkarim, H.Weman, B.G.Svensson, J.L.Lindström. Deep-level transient spectroscopy and photoluminescence studies of electron-irradiated Czochralski silicon. *J. Appl. Phys.*, 60(6):1974–1979, 1986.

[Bal92] A. Baldini and M. Bruzzi. Thermally stimulated current spectroscopy: Experimental techniques for the investigation of silicon detectors. *Rev. Sci. Instrum.*, 64(4):932–936, 1992.

[Bar86] C.E. Barnes and G.A.Samara. Forward bias induced annealing of the E center in silicon. *Appl. Phys. Lett.*, 48(14):934–936, 1986.

[Bea98a] L.J. Beattie, T.J. Brodbeck, A. Chilingarov, G.Hughes, P.Ratoff, T.Sloan. Charge collection efficiency in heavily irradiated silicon diodes. *Nucl. Instr. & Meth. in Physics Research*, A412:238–246, 1998.

[Bea98b] L.J. Beattie, T.J. Brodbeck, A. Chilingarov, G.Hughes, S.A. McGarry. The electric field in irradiated silicon detectors. *Nucl. Instr. & Meth. in Physics Research*, A418:314–321, 1998.

[Beh98] T. Behnke, P.Hüntemeyer, A.Oh, J.Steuerer, A.Wagner and W.Zeuner. The Charge Collection Properties of CVD Diamond. *accepted for publication in NIMA*, 1998.

[Ben83] J.L Benton, L.C.Kimerling and M.Stavola. The oxygen related donor effect in silicon. *Physica*, 116B:271–275, 1983.

[Ber68] G. Bertolini and A.Coche, editor. *Semiconductor Detectors*. North–Holland Publishing Company, Amsterdam, 1968.

[Big94] U. Biggeri, E.Borchi, M.Bruzzi, Z.Li and S.Lazanu. Studies of Deep Levels in High Resistivity Silicon Detectors Irradiated by High Fluence Fast Neutrons Using a Thermally Stimulated Current Spectrometer. *IEEE Transactions on Nuclear Science*, 41(4):964–970, 1994.

[Big97] U. Biggeri, E.Borchi, M.Bruzzi, S.Pirollo, S.Scortino, S.Lazanu, Z.Li. Hall effect measurements on proton-irradiated ROSE samples. *Nucl. Instr. & Meth. in Physics Research*, A 400:113–123, 1997.

[BNL] Brookhaven National Laboratory (BNL), Upton NY 11973-5000 USA.

[Boc88] A. Bock. Charakterisierung tiefer Störstellen mit dem DLTS-Verfahren. Diploma thesis, Universität Kassel, 1988.

[Bor94] E. Borchi and M.Bruzzi. Radiation Damage in Silicon Detectors. *La Rivista del Nuovo Cimento della Societa Italiana di Fisica*, 17(11), 1994.

[Bou83] J. Bourgoin and M.Lannoo. *Point Defects in Semiconductors II*, volume 35 of *Springer Series in Solid-State Sciences*. Springer Verlag, 1983. ISBN 0-387-11515-3.

[Brä79] P. Bräunlich, editor. *Thermally Stimulated Relaxation in Solids*, volume 37 of *Topics in Applied Physics*. Springer-Verlag, Berlin, Heidelberg, New York, 1979.

[Bre86] H.J. Brede, G.Dietze, K.Kudo, D.Schlegel-Bickmann. Spectral neutron yield of an intense Be + d source. *Nuclear Data for Basic and Applied Science, Vol.I, Gordon and Breach Science Publishers, New York*, pages 803–806, 1986.

[Bre97a] H.J. Brede, 1997. Private communication with H.J.Brede [PTB]. To be published in NIMA: *R.Böttger et al., Radiation Damage Studies of High-Resistivity Silicon Detectors at Various Neutron Energies.*

[Bre97b] H.J. Brede, 1997. Private communication with H.J.Brede [PTB]. The MCNP4A code was used for the Monte Carlo simulations. (J.F. Briesmeister, Ed., MCNP, Version 4A, Los Alamos-Report LA-12626-M (1993)).

[Bro82] S.D. Brotherton and P.Bradley. Defect production and lifetime control in electron and γ-irradiated silicon. *J. Appl. Phys.*, 53(8):5720–5732, 1982.

[Bro85] S.D. Brotherton, P.Bradley, and A.Gill. Iron and the iron-boron complex in silicon. *J. Appl. Phys.*, 57(6):1941–1943, 1985.

[Bru95] Mara Bruzzi. TSC data-analysis on heavily irradiated silicon detectors. *Nucl. Instr. & Meth. in Physics Research*, A 352:618–621, 1995.

[Bue72] M.G. Buehler. Impurity centers in pn junctions determined from shifts in the thermally stimulated current and capacitance response with heating rate. *Solid State Electronics*, 15:69–79, 1972.

[Cah59] J.H. Cahn. Irradiation Damage in Germanium and Silicon due to Electrons and Gamma Rays. *J. Appl. Phys.*, 30:1310, 1959.

[CAN] CANBERRA Semiconductor, Lemmerdries 25, 2250 Olen, Belgium.

[Can71] C. Canalli et. al. Drift velocity of electrons and holes and associated anisotropic effects in silicon. *J.Phys.Chem.Solids*, 32:1707, 1971.

[Cas98a] C. Caso et al., (Particle Data Group). Review of Particle Physics. *The European Physical Journal*, C3:1, 1998.

[Cas98b] G. Casse. *The effect of hadron irradiation on the electrical properties of particle detectors made from various silicon materials.* PhD thesis, University Joseph Fourier - Grenoble 1, 1998.

[Cas99] G. Casse. Introduction of high oxygen concentrations into silicon wafers by high temperature diffusion. *ROSE Internal Note*, ROSE/TN-99/1, 1999.

[Chi95] A. Chilingarov et al. Radiation studies and operational projections for silicon in the ATLAS inner detector. *Nucl. Instr. & Meth. in Physics Research*, A 360:432, 1995.

[Chi97] A. Chilingarov, J.S.Meyer, T.Sloan. Radiation damage due to NIEL in GaAs particle detectors. *Nucl. Instr. & Meth. in Physics Research*, A395:35–44, 1997.

[Cin98] V. Cindro and M. Mikuž, 1998. Jožef Stefan Institute, Ljubljana, Slovenia, private communication.

[Cla97] 1997. P. Clauws, University of Gent, Belgium (IR measurements).

[CMS94] CMS. CMS Technical Proposal. *CERN/LHCC/94-38,1994*, 1994.

[Coh87] E.R. Cohen and B.N.Taylor. National Bureau of Standards, The 1986 CODATA Recommended Values of the Fundamental Physical Constants. *Journal of Research of the National Bureau of Standards*, 2:92, 1987.

[Cor61] J.W. Corbett, G.D.Watkins, R.M.Chrenko, and R.S. McDonald. Defects in Irradiated Silicon. II.Infrared Absorption of the Si-A Center. *Physical Review*, 4(121):1015–1022, 1961.

[Cor66] J.W. Corbett. *Electron Radiation Damage in Semiconductors and Metals.* Academic Press, New York and London, 1966.

[Cro96] N. Croitoru, A.Gambirasio, P.G.Rancoita, A.Seidman. Current-voltage and impedance characteristics of neutron irradiated silicon detectors at fluences up to $10^{16} n/cm^2$. *Nucl. Instr. & Meth. in Physics Research*, B111:297–302, 1996.

[Czo18] J. Czochralski. *Metalle. Z.Phys.Chem.*, 92:219, 1918.

[Dab89] W. Dabrowski and K. Korbel. Effects of deep imperfection levels on the capacitance of semiconductor detectors. *Nucl. Instr. & Meth. in Physics Research*, A276:270–279, 1989.

[Das55] W.C. Dash and R. Newman. Intrinsic optical absorption in single-crystal germanium and silicon at 77 K and 300 K. *Physical Review*, 99:1151, 1955.

[Dav87a] G. Davies, E.C. Lightowlers and Z.E. Ciechanowska. The 1018 meV (W or I_1) vibronic band in silicon. *J.Phys.C: Solid State Phys.*, 20:191–205, 1987.

[Dav87b] G. Davies et al. A model for radiation damage effects in carbon-doped crystalline silicon. *Semicond.Sci.Tech.*, 2:524–532, 1987.

[Dav89] G. Davies and K.T. Kun. Annealing the di-carbon radiation damage centre in silicon. *Semicond. Sci. Tech.*, 4:327–330, 1989.

[Dav97] G. Davies, Physics Department, King's College, London, UK, 1997. Private communication of B.MacEvoy with G.Davies, as cited in [Mac96a].

[Dav98] G. Davies, Physics Department, King's College, London, UK, 1998. Photo Luminescence measurements at 4.2K and 2.1K. The calibration factors ([P], [B]) for 4.2K were taken from: PMc Colley and E.C.Lightowlers, Semiconductor Science and Technology 2 (1987) 157.

[Deh95] C. Dehn. Untersuchung strahleninduzierter Defekte in Silizium-Detektoren mit Hilfe des DLTFS-Verfahrens (Deep-Level Transient Fourier Spectroscopy). Master's thesis, University of Hamburg, August 1995.

[DEM] National Center For Scientific Research "Demokritos", Institute of Nuclear Technology – Radiation Protection, Athens, Greece.

[Dez97] B. Dezillie. *Radiation hardness studies of epitaxial silicon particle detectors for applications at the CERN Large Hadron Collider.* PhD thesis, University Joseph Fourier - Grenoble 1, 1997. Contains data about SIMS and IR measurements on materials that also have been used in this work.

[DIO] DIOTEC, Družstevná ul. č 109 SK-95605 Radošina, Slovakia .

[DLT] DLTFS–Program; Release 3.2.5–17.7.95 by S.Weiss, University of Kassel, Institute for Technical Physics.

[Dob94] L. Dobaczewski, I. D. Hawkins, and A. R. Peaker. Laplace transform deep level transient spectroscopy: a new insight into defect microscopy. *Material Science and Technology*, 11:1071, 1994.

[ELM] ELMA, 103460 Moscow, Zelenograd, Russia.

[Ere96] V. Eremin, N.Strokan, E.Verbitskaya, Z.Li. Development of transient current and charge techniques for the measurement of effective net concentration of ionized charges (n_{eff}) in the space charge region of p-n junction detectors. *Nucl. Instr. & Meth. in Physics Research*, A372:388–398, 1996.

[EVA] EVANS EUROPA, Uxbridge, UK (SIMS measurements) .

[Evw76] A.O. Evwaraye. Electron-irradiation-induced divacancy in lightly doped silicon. *J. Appl. Phys.*, 47(9):3776–3780, 1976.

[Ewe97] C.P. Ewels. *Density Functional Modelling of Point Defects in Semiconductors.* PhD thesis, University of Exeter, 1997.

[Fei93] H. Feick. Temperaturabhängigkeit der Langzeitausheilung neutronengeschädigter Silizium-Detektoren. Master's thesis, University of Hamburg, 1993.

[Fei97a] H. Feick. *Radiation Tolerance of Silicon Particle Detectors for High-Energy Physics Experiments.* PhD thesis, University of Hamburg, 1997.

[Fei97b] H. Feick and M. Moll. Microscopic studies of radiation damage-induced defects responsible for the deterioration of high-resistivity silicon detectors. *Proceedings of the 7th International Autumn Meeting GADEST '97, Spa Belgium, Oct. 5-10, 1997; Solid State Phenomena Vols. 57-58, Scitec Publications, Switzerland*, pages 233–238, 1997.

[Fei97c] H. Feick, E.Fretwurst, G.Lindström, and M.Moll. Correlation of Radiation Damage Effects in High Resistivity Silicon Detectors with Results from Deep Level Spectroscopy. *IEEE Transactions on Nuclear Science*, 44:825–833, 1997.

[Fei97d] H. Feick, E.Fretwurst, P.Heydapoor, G.Lindström, M.Moll. Analysis of TSC spectra measured on silicon pad detectors after exposure to fast neutrons. *Nucl. Instr. & Meth. in Physics Research*, A 388:323–329, 1997.

[Fei98a] H. Feick, ROSE/CERN - RD48 Collaboration. Analysis of the Radiation Tolerance of the LHC-B Silicon Vertex Detector. *LHC-B technical note LHCb-98-043*, 1998.

[Fei98b] H. Feick, ROSE/CERN - RD48 Collaboration. First results from correlative studies using DLTS, PL, and EPR. *CERN/LEB 98-11, 4th ROSE Workshop, RD48, December 1998*, pages 503–521, 1998.

[For71] L. Forbes and C.T.Sah. On the determination of deep level center energy and concentration by thermally stimulated conductivity measured using reversed-biased p-n junctions. *Solid-State Electronics*, 14:182–183, 1971.

[Fre38] J. Frenkel. ON Pre-Breakdown Phenomena in Insulators and Electronic Semi-Conductors. *Physical Review*, 54:647–648, 1938.

[Fre87] E. Fretwurst, R.Grube, G.Lindström and J.Nagel. Development of large area silicon detectors – special properties and radiation stability. *Nucl. Instr. & Meth. in Physics Research*, A253:467–477, 1987.

[Fre90] E. Fretwurst, H. Herdan, G. Lindström, U. Pein, M. Rollwagen, H. Schatz, P. Thomsen and R. Wunstorf. Silicon detector developments for calorimetry: Technology and radiation damage. *Nucl. Instr. & Meth. in Physics Research*, A288:1–12, 1990.

[Fre94] E. Fretwurst, H. Feick, M. Glaser, C. Gössling, E.H.M. Heijne, A. Hess, F. Lemeilleur, G. Lindström, K.H. Mählmann, A. Rolf, T. Schulz, C. Soave. Reverse annealing of the effective impurity concentration and long term operational scenario for silicon detectors in future collider experiments. *Nucl. Instr. & Meth. in Physics Research*, A342:119–125, 1994.

[Fre96] E. Fretwurst, C. Dehn, H. Feick, P. Heydarpoor, G. Lindström, M. Moll, C. Schütze, T. Schulz. Neutron induced defects in silicon detectors characterized by DLTS and TSC methods. *Nucl. Instr. & Meth. in Physics Research*, A377:258–264, 1996.

[Fre97] E. Fretwurst, V.Eremin, H.Feick, J.Gerhardt, Z.Li, G.Lindström. Investigation on damage-induced defects in silicon by TCT. *Nucl. Instr. & Meth. in Physics Research*, A388:356–360, 1997.

[Fre98] E. Fretwurst, M.Kuhnke, G.Lindström, M.Moll, Z.Li. Damage results from Co-60 gamma irradiation in Si-diodes fabricated from several different materials. *4^{th} ROSE Workshop on Radiation Hardening of Silicon Detectors; CERN 2-4 December 1998; CERN/LEB 98-11*, pages 221–231, 1998.

[Fre99] E. Fretwurst, M.Kuhnke, G.Lindström, M.Moll. Relation between microscopic defects and macroscopic changes in silicon detector properties. *Proceedings of the 1^{st} International Workshop on Defect Engineering of Advanced Semiconductor Devices, held in Santorini, Greece, 21-22 April;* to be published in *Materials Science in Semiconductor Processing*, pages 39–49, 1999.

[Fri98] M. Friedl et. al. (RD42). CVD Diamond Detectors for Ionizing Radiation. *Presented at the "7th International Workshop on Vertex Detectors" held at Santorini, Greece, Sep. 98, to be published in NIMA*, 1998.

[FTE] Royal Institute of Technology, Solid State Electronics (FTE), Dept. of Electronics, Electrum 229, S-164 40 Kista (Stockholm), Sweden, (SIMS measurements).

[Ful54] C.S. Fuller, N.B.Ditzenberger, N.B.Hannay and E.Buehler. *Physical Review*, 96:833, 1954.

[Gil92] K. Gill, G.Hall, S.Roe, S.Sotthibandhu, R.Wheadon, P.Giubellino and L.Ramello. Radiation damage by neutrons and photons to silicon detectors. *Nucl. Instr. & Meth. in Physics Research*, A322:177–188, 1992.

[Gil97] K. Gill, G.Hall and B. MacEvoy. Bulk damage effects in irradiated silicon detectors due to clustered divacancies. *J. Appl. Phys.*, 82(1):126–136, 1997.

[Gin89] A. van Ginneken. Non ionizing energy deposition in silicon for radiation damage studies. Technical Report FN-522, Fermi National Accelerator Laboratory, 1989.

[Gos59] B.R. Gossick. Disordered Regions in Semiconductors Bombarded by Fast Neutrons. *J. Appl. Phys.*, 30:1214, 1959.

[Gös82] U. Gösele, and T.Y.Tan. *Appl.Phys.A.: Solid Surf.*, 28:79, 1982.

[Göt92] W. Götz, G.Pensl and W.Zulehner. *Physical Review B*, 46:4312, 1992.

[Gre90] Martin A. Green. Intrinsic concentration, effective densities of states, and effective mass in silicon. *J. Appl. Phys.*, 67:2944, 1990.

[Gri96] P. Griffin et al. SAND92-0094 (SANDIA Natl. Lab., Nov.93), 1996. neutron cross sections taken from ENDF/B-VI, ORNL, unpublished but available from G.Lindström, Hamburg (gunnar@sesam.desy.de).

[Gür92] E. Gürer, B.W. Benson and G.D. Watkins. Configurational metastability of carbon-phosphorus pair defects in silicon. *Materials Science Forum*, 83–87:339–344, 1992.

[Hal52] R.N. Hall. Electron-Hole Recombination in Germanium. *Physical Review B*, 87:387, 1952.

[Hal94] G. Hall. Semiconductor particle tracking detectors. *Rep. Prog. Phys.*, 57:481–531, 1994.

[Hal96] A. Hallén, N. Keskitalo, F. Masszi, V. Nágl. Lifetime in proton irradiated silicon. *J. Appl. Phys.*, 79(8):3906–3914, 1996.

[Has97] J.L. Hastings, S.K.Estreicher, P.A.Fedders. Vacancy aggregates in silicon. *Physical Review B*, 56(16):10215–10220, 1997.

[HB95] HERA-B. An Experiment to Study CP Violation in the B System Using an Internal Target at the HERA proton Ring – Design Report. *DESY-PRC 95/01*, 1995.

[Hei76] H.M. Heijne, J.C.Muller and P.Siffert. TSC defect level in silicon produced by irradiation with muons of GeV-energy. *Radiation Effects*, 29:25–26, 1976.

[Hei92] T. Heiser and A.Mesli. Charge-State-Dependent Diffusion and Carrier-Emission-Limited Drift of Iron in Silicon. *Physical Review Letters*, 68(7), 1992.

[Hey96] Parwin Heydarpoor. Spektroskopische Untersuchung von Kristallschäden in Silizium–Detektoren nach Neutronenbestrahlung mit Hilfe des TSC–Verfahrens. Diploma thesis, University of Hamburg, 1996.

[Hol94] A. Holmes-Siedle and L.Adams. *Handbook of Radiation Effects.* Oxford University Press, reprint with corrections edition, 1994. ISBN 0-19-856347-7.

[Huh93a] M. Huhtinen and P. Aarino. Estimation of pion induced desplacement damage in silicon. *HU-SEFT R 1993-02*, 1993.

[Huh93b] M. Huhtinen and P.A.Aarnio. Pion induced displacement damage in silicon devices. *Nucl. Instr. & Meth. in Physics Research*, A 335:580, 1993. (see also [Huh93a]).

[Ike83] K. Ikeda and H.Takaoka. Analysis of transient response by means of discrete Fourier transformation. *J. Appl. Phys.*, 54:6031, 1983.

[ITE] Institute of Electron Technology (ITE), Al. Lotnikow 32/46, 02-668 Warsaw, Poland.

[ITM] Institute of Electronic Materials Technology (ITME), ul Wólczyńska 133, 01-919 Warsaw, Poland.

[Jel82] G.E. Jellison, Jr. Transient capacitance studies of an electron trap at $E_C - E_T = 0.105$ eV in phosphorus-doped silicon. *J. Appl. Phys.*, 53:5715, 1982.

[Jon94] R. Jones, S.Öberg, F.B.Rasmussen and B.B.Nielsen. Identification of the Dominant Nitrogen Defect in Silicon. *Physical Review Letters*, 72(12):1882–1885, 1994.

[Kai58] W. Kaiser, H.L. Frisch, H. Reiss. *Physical Review*, 112:1546, 1958.

[Kem80] J. Kemmer. Farbrication of low noise silicon radiation detectors by the planar process. *Nucl. Instr. & Meth. in Physics Research*, 169:499–502, 1980.

[Kem84] J. Kemmer. Improvement of detector fabrication by the planar process. *Nucl. Instr. & Meth. in Physics Research*, 226:89–93, 1984.

[Kim75] L.C. Kimerling, H.M. DeAngelis and J.W. Diebold. On the role of defect charge state in the stability of point defects in silicon. *Solid State Communications*, 16:171–174, 1975.

[Kim77] L.C. Kimerling. Defect states in electron-bombarded silicon: capacitance transient analyses. *Inst.Phys.Conf.Ser.No.31*, pages 221–230, 1977.

[Kno89] G.F. Knoll. *Radiation Detection and Measurement.* John Wiley & Sons, second edition, 1989. ISBN 0-471-81504-7.

[KOM] Komatsu Silicon USA, Inc.,101 Metro Drive, Suite 750, San Jose, CA 95110-1317.

[Kon92] A.Yu. Konobeyev et al. Neutron displacement cross-sections for structural materials below 800 MeV. *J.Nucl.Mater.*, 186:117, 1992.

[Kra93] H.W Kraner et al. *Nucl. Instr. & Meth. in Physics Research*, A326:350, 1993.

[Lam62] M.A. Lampert. Double injection in insulators. *Physical Review*, 125:126, 1962.

[Lan74] D.V. Lang. Deep-level Transient Spectroscopy: A new method to characterize traps in semiconductors. *J. Appl. Phys.*, 45:3023, 1974.

[Laz87] M.S. Lazo, D.M. Woodall and P.J. McDaniel. Silicon and silicon dioxide neutron damage functions. *In Proc. Fast Burt React. Workshop,1986. Sandia National Laboratories,1987. [Tech.Rep.] SAND, SAND87-0098 Vol.1.*, pages 85–103, 1987.

[Lee73] Y.H. Lee and J.W.Corbett. EPR Studies in Neutron-Irradiated Silicon: A Negative Charge State of a Nonplanar Five-Vacancy Cluster (V_5^-). *Physical Review B*, 8(6):2810, 1973.

[Lee76] Y.H. Lee and J.W. Corbett. EPR studies of defects in electron-irradiated silicon: A triplet state of vacancy oxygen complexes. *Physical Review B*, 13(6):2653–2666, 1976.

[Lee98] Y.H. Lee. Silicon di-interstitial in ion-implanted silicon. *Appl. Phys. Lett.*, 73(8):1119–1121, 1998.

[Lem81] H. Lemke. Dotierungseigenschaften von Eisen in Silizium. *phys.stat.sol.(a)*, 64:215–224, 1981.

[Lem95] F. Lemeilleur et al. Study of characteristics of silicon detectors irradiated with 24 GeV/c protons between -20°C and +20°C. *Nucl. Instr. & Meth. in Physics Research*, A 360:438, 1995.

[Leó95] E. León-Florián, C.Leroy and C.Furetta. Particle fluence measurements by activation technique for radiation damage studies. *CERN/ECP 95-15*, 1995.

[Li 92] Z. Li and H. Kraner. *Journal of Electronic Materials*, 21:701, 1992.

[Li 94] Z. Li . Modeling of the frequency dependent C-V characteristics of neutron irradiated p^+-n silicon detectors after the type inversion in the space charge region. *IEEE Transactions on Nuclear Science*, 41(4):948, 1994.

[Li 95a] Z. Li . Experimental comparison among various models for the reverse annealing of the effective concentration of ionized space charge (n_{eff}) of neutron irradiated silicon detectors. *IEEE Transactions on Nuclear Science*, 42(4):224–234, 1995.

[Li 95b] C.J. Li and Z.Li. Development of current-based microscopic defect analysis methods and associated optical filling techniques for the investigation on highly irradiated high resistivity silicon detectors. *Nucl. Instr. & Meth. in Physics Research*, A 364:108–117, 1995.

[Li 96] Z. Li, C.J.Li and E.Verbitskaya. Study of Bulk Damage in High Resistivity Silicon Detectors Irradiated by High Dose of ^{60}Co γ–Radiation. *IEEE Nuclear Science Symposium, Conference Record, November 2-9 1996, Anaheim California*, pages 251–255, 1996.

[Li 97] Z. Li, C.J.Li, V.Eremin, E.Verbitskaya. Direct observation and measurements of neutron-induced deep levels responsible for N_{eff} changes in high-resistivity silicon detectors using TCT. *Nucl. Instr. & Meth. in Physics Research*, A 388:297–307, 1997.

[Li 99] Z. Li, B.Dezillie and V.Eremin. BNL High Temperature Long Time (HTLT) oxygen Diffusion process. *CERN / LEB 99-8, ROSE Meeting RD48, June 1999*, pages 161–173, 1999.

[Lin80] V.A.J. van Lint, T.M. Flanagan, R.E.Leadon, J.A. Naber, V.C.Rogers. *Mechanisms of Radiation Effects in Electronic Materials.* John Wiley & Sons, 1980.

[Lin94] Wen Lin. *Oxygen in Silicon*, volume 42 of *Semiconductors and Semimetals*, chapter The incorporation of oxygen into silicon crystals, pages 9–52. Academic Press Inc., Boston, San Diego, New York, London, Sydney, Tokyo, Toronto, 1994. ISBN 0-12-752142-9.

[Lin98] G. Lindström. Some Observations in Annealing Studies for Standard and Non-standard Silicon after Neutron irradiation. *CERN / LEB 98-11, 4^{th} Rose Workshop, RD48, December 1998*, pages 232–260, 1998.

[Lin99a] G. Lindström, 1999. Private communication with G.Lindström, Institut für Experimentalphysik, University of Hamburg.

[Lin99b] G. Lindström et al., 1999. The data will be included in the ROSE (RD48) Final Report (1999/2000). A publication previous to this report by the Hamburg group is foreseen.

[LJU] Jožef Stefan Institute and Department of Physics, University of Ljubljana, SI-1000 Ljubljana, Slovenia.

[Lon94] C.A. Londos, G.I.Georgiou, L.G.Fytros, K.Papastergiou. Interptreatation of infrared data in neutron-irradiated silicon. *Physical Review B*, 50(16):11531–11534, 1994.

[Lon97] C.A. Londos, N.V.Sarlis and L.G.Fytros. An IR Study of the Annealing Behaviour of A-Center in Silicon. *Solid State Phenomena*, 57–58:245–250, 1997.

[Luc97] Jörn Luckow. Untersuchung des Einflusses der Phosphorkonzentration auf die Bildung von strahleninduzierten Defekten in Siliziumdetektoren durch die Charakterisierung der Niveaus tiefer Störstellen mit Hilfe des DLTS-Verfahrens (Deep-Level Transient Spectroscopy). Diploma thesis, University of Hamburg, December 1997.

[Lut96] G. Lutz. Effect of deep level defects in semiconductor detectors. *Nucl. Instr. & Meth. in Physics Research*, A377:234–243, 1996.

[Lut99] G. Lutz. Oxygenized silicon at MPI and CIS. *CERN/LEB 99-8; ROSE Meeting, RD48, June 1999*, pages 295–296, 1999.

[Ma 89] T.P. Ma and P.V.Dressendorfer, editor. *Ionizing Radiation Effects in MOS Devices and Circuits.* John Wiley & Sons, Inc., 1989.

[Mac96a] B.C. MacEvoy. *Defect Kinetics in Silicon Detector Material for Application at the Large Hadron Collider.* PhD thesis, Imperial College, London, November 1996. RAL-TH-97-003.

[Mac96b] B.C. MacEvoy, G.Hall, K.Gill. Defect evolution in irradiated silicon detector material. *Nucl. Instr. & Meth. in Physics Research*, A 374:12–26, 1996.

[Mac99] B.C. MacEvoy and G.Hall. Defect kinetics in novel detector materials. *Proceedings of the 1st International Workshop on Defect Engineering of Advanced Semiconductor Devices, held in Santorini, Greece, 21-22 April; to be published in* Materials Science in Semiconductor Processing, pages 57–74, 1999.

[Mad89] O. Madelung and M.Schulz, editor. *Landolt-Börnstein, Numerical Data and Functional Relationships in Science and Technology*, volume 22 b Semiconductors, Impurities and Defects in Group IV Elements and III-V Compounds of *New Series, Group III: Crystal and Solid State Physics.* Springer-Verlag, Berlin, Heidelberg, NewYork, London, Paris, Tokyo, HongKong, 1989.

[Mar81] P.A. Martin B.G.Streetman, and K.Hess. Electric field enhanced emission from non-coulombic traps in semiconductors. *J. Appl. Phys.*, 52(12):7409–7415, 1981.

[Mat95] J. Matheson, M.S.Robbins, S.J.Watts. The effect of radiation defects on the performance of high resistivity silicon diodes. *RD20 Technical Report TN/36*, 1995.

[McP97] M. McPherson, B.K.Jones and T.Sloan. Effects of radiation damage in silicon p-i-n photodiodes. *Semicond. Sci. Technol.*, 12:1187–1194, 1997.

[McW90a] P.J. McWhorter, S.L. Miller, and T.A. Dellin. Modeling the memory retention characteristics of silicon-nitride-oxide-silicon nonvolatile transistors in a varying thermal environment. *J. Appl. Phys.*, 68(4):1902–1909, 1990.

[McW90b] P.J. McWhorter, S.L.Miller, and W.M.Miller. Moeling the anneal of radiation-induced trapped holes in a varying thermal environment. *IEEE Transactions on Nuclear Science*, 37(6):1682–1689, 1990.

[Mei92] E. Meijer and H.G. Grimmeiss. Transient current measurements for the characterization of deep defects in semiconductors. *Semicond. Sci. Technol.*, 7:188–197, 1992.

[MEM] MEMC Electronic Materials, S.p.A., Viale Gherzi, 31 28100 Novara, Italy.

[Mes92] G.C. Messenger. A summary review of displacement damage form high energy radiation in silicon semiconductors and semiconductor devices. *IEEE Transactions on Nuclear Science*, 39:468–473, 1992.

[Mic94] J. Michel and L.C.Kimerling. *Oxygen in Silicon*, volume 42 of *Semiconductors and Semimetals.* Academic Press Inc., 1994. ISBN 0-12-752142-9.

[Mil77] G.L. Miller, D.V. Lang, and L.C. Kimerling. Capacitance Transient Spectroscopy. *Ann. Rev. Mater. Sci.*, pages 377–448, 1977.

[Mol95a] M. Moll. Temperungsexperimente an strahlengeschädigten Silizium- Detektoren. Diploma thesis, University of Hamburg, 1995.

[Mol95b] M. Moll, H. Feick, E. Fretwurst, G. Lindström, and T. Schulz. Observation of a bistable defect generated and activated by heat treatments in irradiated high resistivity silicon detectors. *Nucl. Phys.*, B 44 (Proc. Suppl.):468–474, 1995.

[Mol97] M. Moll, H. Feick, E. Fretwurst, G. Lindström, and C. Schütze. Comparison of defects produced by fast neutrons and Co-60 gammas in high resistivity silicon detectors using Deep Level Transient Spectroscopy. *Nucl. Instr. & Meth. in Physics Research*, A388:335–339, 1997.

[Mol99] M. Moll, E.Fretwurst, M.Kuhnke, G.Lindström. New results on oxygenated materials. *CERN/LEB 99-8; ROSE Meeting, RD48, June 1999*, pages 51–80, 1999. Including SIMS and IR measurements performed by ITME [ITM].

[Moo77] P.M. Mooney, L.J. Cheng, M.Süli, J.D.Gerson, J.W.Corbett. Defect energy levels in boron-doped silicon irradiated with 1-MeV electrons. *Physical Review B*, 15(8):3836–3843, 1977.

[Moz97] A.P. Mozer. Silicon Wafer Technology: The Challenges towards the Gigabit Era. *Solid State Phenomena*, 57–58:9–18, 1997.

[MPI] MPI Halbleiterlabor; Paul-Gerhardt-Allee 42; D-81245 München; Germany. The MPI Halbleiterlabor is a common facility of the Max-Planck-Institute for Extraterrestial Physics (Garching) and the Max-Planck-Institute for Physics (Munich).

[Mue82] G.P. Mueller and C.S. Guenzer. Simulation of cascade damage in silicon. *IEEE Transactions on Nuclear Science*, NS-27(6):1493, 1982.

[Mul74] J.C. Muller, R.Stuck, R.Berger and P.Siffert. Thermally Stimulated Current Measurement on Silicon Junctions Produced by Implantation of Low Energy Boron Ions. *Solid State Electronics*, 17:1293–1297, 1974.

[Mur98] L.I. Murin, T.Hallberg, V.P.Markevich, and J.L.Lindström. Experimental evidence of the oxygen dimer in silicon. *Physical Review Letters*, 80(1):93–96, 1998.

[Nic82] E.H. Nicollian and J.R. Brews. *MOS (Metal Oxide Semiconductors) Physics and Technology.* John Wiley & Sons, 1982.

[Nos98] E. Nossarzewska (ITME – Poland). ITME silicon for detectors. *Presented on the "4th ROSE Workshop on Radiation Hardening of Silicon Detectors", held at CERN, 2–4 December 1998, to be published as CERN–proceedings*, 1998.

[Oku83] M. Okuyama, H. Takakura and Y. Hamakawa. Fourier-transformation analysis of deep level transient signals in semiconductors. *Solid State Electronics*, 26(7):689–694, 1983.

[Osi95] C. Osius. Untersuchung von Silizium-Detektoren verschiedener Herstellungstechnologie mit einer 2 MeV Scanning-Protonen-mikrostrahlsonde. Diploma thesis, Universität Hamburg, May 1995.

[Oug90] A.M. Ougouag, J.G.Williams, M.Danjaji, S.Y.Yang, J.L.Meason. Differential displacement kerma cross sections for neutron interactions in Si and GaAs. *IEEE Transactions on Nuclear Science*, 37(6):2219, 1990.

[Pal98] V.G. Palmieri, K.Borer, S.Janos, C.Da Viá, L.Casagrande. Evidence for charge collection efficiency recovery in heavily irradiated silicon detectors operated at cryogenic temperatures. *Nucl. Instr. & Meth. in Physics Research*, A 413:475–478, 1998.

[Pas98] D. Passeri, G.M.Bilei and P.Ciampolini. A Comprehensive Analysis of Low-Resistivity Radiation Detectors. *Presented on the Nuclear Science Symposium 1998, 12.Nov 98, Toronto, to be published.*, 1998.

[POL] Polovodice, Vovodvorská 994, 142 21 Prague 4, Czech Republic.

[PTB] Physikalisch-Technische Bundesanstalt (PTB), Bundesallee 100, D-38116 Braunschweig, Germany.

[R39] Cryogenic Tracking Detectors, CERN-RD39 Collaboration, http://www.cern.ch/RD39.

[R42] CVD Diamond Radiation Detector Development, CERN-RD42 Collaboration, http://www.cern.ch/RD42.

[R48] The ROSE Collaboration (R & d On Silicon for future Experiments), CERN-RD48 Collaboration, http://www.brunel.ac.uk/research/rose/.

[Rho88] E.H. Rhoderick and R.H.Williams. *Metal-Semiconductor Contacts*, volume 19 of *Monographs in Electrical and Electronic Engineering.* Oxford University Press, Oxford, New York, second edition, 1988.

[Rie96] K. Riechmann et al. Pion and proton induced radiation damage to silicon detectors. *Nucl. Instr. & Meth. in Physics Research*, A377:276, 1996.

[Rog97a] M. Rogalla. *Systematic Investigation of Gallium Arsenide Radiation Detectors for High Energy Physics Experiments.* PhD thesis, Albert-Ludwigs-Universität Freiburg i. Brg., 1997. Shaker Verlag Aachen, 1998, ISBN 3-8265-3920-6.

[Rog97b] M. Rogalla, Th. Eich, N. Evans, R. Geppert, R. Göppert, R. Irsigler, J. Ludwig, K. Runge, Th. Schmid, D.G. Marder. Radiation studies for GaAs in the ATLAS inner detector. *Nucl. Instr. & Meth. in Physics Research*, A395:45–48, 1997.

[ROS97] RD48 STATUS REPORT, 1997. Status Report/RD48, CERN/LHCC 97-39.

[ROS98a] 2nd RD48 STATUS REPORT, 1998. LEB Status Report / RD48, CERN / LHCC 98-39.

[ROS98b] Proceedings of the "4th ROSE Workshop on Radiation Hardening of Silicon Detectors", held at CERN, 2–4 December 1998, to be published as CERN–proceedings , 1998.

[Ruz99a] A. Ruzin et al. Radiation hardness of silicon detectors processed on various oxygen-enriched wafers. *ROSE Meeting on Radiation Hardening of Silicon Detectors, CERN, 14-15 June, CERN/LEB 99-8*, pages 13–50, 1999.

[Ruz99b] A. Ruzin, G.Casse, M.Glaser, F.Lemeilleur. Studies of radiation hardness of oxygen enriched silicon detectors. *Nucl. Instr. & Meth. in Physics Research*, A426:94–98, 1999.

[Ruz99c] A. Ruzin, G.Casse, M.Glaser, F.Lemeilleur, J.Matheson, S.Watts, A.Zanet. Radiation effects in silicon detectors processed on carbon and oxygen rich substrates. *Paper submitted to the 1^{st} International Workshop on Defect Engineering of Advanced Semiconductor Devices, held in Santorini, Greece, 21-22 April*, 1999.

[Saf96] A.N. Safanov, E.C. Lightowlres, G. Davies, P. Leary, R. Jones, S. Öberg. Interstitial-Carbon Hydrogen Interaction in Silicon. *Physical Review Letters*, 77(23):4812–4815, 1996.

[Sar97] N.V. Sarlis, C.A.Londos, and L.G. Fytros. Origion of infrared bands in neutron-irradiated silicon. *J. Appl. Phys.*, 81(4):1645–1650, 1997.

[Sch78] R. Schmidt. *Neutronensosimetrie in gemischten Neutronen-Gamma-Feldern eines medizinisch genutzten $^3H(d,n)^4He$-Generator.* PhD thesis, University of Hamburg, 1978. (See also Schmidt et al., Med. Phys. 7 (1980) 507).

[Sch90] D.K. Schroder. *Semiconductor Material and Device Characterization.* John Wiley & Sons, 1990.

[Sch94] T. Schulz, H.Feick, E.Fretwurst, G.Lindström, M.Moll, K.H.Mählmann. Long term reverse annealing in silicon detectors. *IEEE Transactions on Nuclear Science*, 41(4), 1994.

[Sch96a] T. Schulz. *Investigations on the Long Term Behaviour of Damage Effects and Corresponding Defects in Detector Grade Silicon after Neutron Irradiation.* PhD thesis, University of Hamburg, November 1996.

[Sch96b] Christian Schütze. Vergleich von strahleninduzierten Defekten in Silizium-Detektoren nach Neutronen und Gamma-Bestrahlung mit Hilfe des DLTFS-Verfahrens. Diploma thesis, University of Hamburg, August 1996.

[Sch98] J. Schmidt, C. Berge, and G.Aberle. Injection level dependence of the defect-related carrier lifetime in light-degraded boron-doped Czochralski silicon. *Appl. Phys. Lett.*, 73(15):2167–2169, 1998.

[Shi90] Y. Shi, D.X.Shen, F.M.Wu and K.J.Cheng. A numerical study of cluster center formation in neutron-irradiated silicon. *J. Appl. Phys.*, 67:1116, 1990.

[Shi94] F. Shimura, editor. *Oxygen in Silicon*, volume 42 of *Semiconductors and Semimetals.* Academic Press, INC., 1994. ISBN 0-12-752142-9.

[Sho52] W. Shockley and W. T. Read, JR. Statistics of the Recombinations of Holes and Electrons. *Physical Review*, 87:835, 1952.

[SIA94] Semiconductor Industry Association SIA. The National Technology Roadmap for Semiconductors, 1994. San Jose, CA.

[Sim71] J.G. Simmons and G.W.Taylor. High-Field Isothermal Currents and Thermally Stimulated Currents in Insulators having Discrete Trapping Levels. *Physical Review B*, 5:1619, 1971.

[SIN] SINTEF Electronics and Cybernetics, Forskningsveien 1, P.O.Box 124 Blindern, N-0314 Oslo, Norway.

[Son90a] L.W. Song and G.D.Watkins. EPR identification of the single-acceptor state of interstitial carbon in silicon. *Physical Review B*, 42(9):5759–5764, 1990.

[Son90b] L.W. Song, X.D. Zhan, B.W. Benson, and G.D. Watkins. Bistable interstitial-carbon-substitutional-carbon pair in silicon. *Physical Review B*, 42:5765, 1990.

[Sum93] G.P. Summers et al. Damage correlations in semiconductors exposed to gamma, electron and proton radiations. *IEEE Transactions on Nuclear Science*, NS-40:1372, 1993.

[Sve86] B.G. Svensson and J.L. Lindström. Kinetic study of the 830- and 889-cm^{-1} infrared bands during annealing of irradiated silicon. *Physical Review B*, 34(12):8709–8717, 1986.

[Sve91] B.G. Svensson, B.Mohadjeri, A.Hallén, J.H.Svensson and J.W.Corbett. Divacancy acceptor levels in ion-irradiated silicon. *Physical Review B*, 43(3):2292–2298, 1991.

[Sve97] B.G. Svensson, C.Jagadish, A.Hallén, J.Lalita. Generation of vacancy-type point defects in single collision cascades during swift-ion bombardment of silicon. *Physical Review B*, 55(16):10498–10507, 1997.

[Sze81] S.M. Sze. *Physics of semiconductor devices.* John Wiley & Sons, 2^{nd} edition, 1981.

[Sze85] S.M. Sze. *SEMICONDUCTOR DEVICES Physics and Technology.* John Wiley & Sons, 1985.

[Tea50] G.K. Teal and J.B.Little. *Physical Review*, 78:647, 1950.

[The62] H.C. Theuerer. U.S. patent. *3,060,123*, 1962.

[Ton99] G. Tonelli on behalf of the CMS collaboration. Update on R&D Activity on Silicon Detectors in CMS. *CERN/LEB 99-8; ROSE Meeting, RD48, June 1999*, pages 243–274, 1999.

[TOP] TOPSIL Semiconductor Materials A/S, Linderupvej 4, P.O.BOX 93; DK-3600 Frederissund, Denmark.

[TOP98] 1998. Private Communication with P.E. Schmidt, TOPSIL [TOP].

[Tra95] M.-A. Trauwaert. *Radiation and Impurity Related Deep Levels in Si: A Deep Level Transient Spectroscopy Study Correlated with other Spectroscopic Techniques.* PhD thesis, Katholieke Universiteit Leuven, 1995.

[Tro87] J.M. Trombetta and G.D. Watkins. Identification of an interstitial carbon – interstitial oxygen complex in silicon. *Appl. Phys. Lett.*, 51(14):1103–1105, 1987.

[Var67] Y.P. Varshni. Temperature dependence of the energy gap in silicon. *Physica*, 34:149, 1967.

[Vas97a] A. Vasilescu. The NIEL scaling hypothesis applied to neutron spectra of irradiation facilities and in the ATLAS and CMS SCT. *ROSE Internal Note*, ROSE/TN-97/2, 1997.

[Vas97b] 1997. Private communication with A.Vasilescu, Institute of Nuclear Physics and Engineering (INPE) Bucharest, Romania. The MC simulations were performed by A. Ferrari (CERN) and are included in [ATL97]. An updated calculation for the total equivalent fluence for the pixel detector can be found in [ATL98].

[Vas98] 1998. Private communication with A.Vasilescu, Institute of Nuclear Physics and Engineering (INPE) Bucharest, Romania. For the hardness factor calculations the damage functions displayed in Sec. 3.2 have been used.

[Vec76] J.A. van Vechten and C.D.Thurmond. Entropy of ionization and temperature variation of ionization levels of defects in semiconductors. *Physical Review B*, 14:3539, 1976.

[WAC] Wacker Siltronic, Burghausen, Germany.

[WAC99] 1999. Point Defect/Impurity Concentrations of CVD-Poly-Si and FZ-Si, Typical values, state 1998; Information provided by Wacker [WAC] in a private comunication with H.Herzer.

[Wai57] T.R. Waite. Theoretical treatment of the kinetics of diffusion–limited reactions. *Physical Review*, 107:463, 1957.

[Wat61] G.D. Watkins and J.W.Corbett. Defects in Irradiated Silicon. I.Electron Spin Resonance of the Si–A Center. *Physical Review*, 121(4):1001–1014, 1961.

[Wat64] G.D. Watkins and J.W.Corbett. Defects in Irradiated Silicon: Electron Paramagnetic Resonance and Electron-Nuclear Double Resonance of the Si-E Center. *Physical Review*, 134(5A):A1359–1377, 1964.

[Wat65] G.D. Watkins and J.W.Corbett. Defects in Irradiated Silicon: Electron Paramagnetic Resonance of the Divacancy. *Physical Review*, 138(2A):A543–555, 1965.

[Wat76] G.D. Watkins and K.L. Brower. EPR Observation of the Isolated Interstitial Carbon Atom in Silicon. *Physical Review Letters*, 36(22):1329–1332, 1976.

[Wat79] G.D. Watkins, J.R.Troxell, A.P. Chatterjee. Vacancies and interstitials in silicon. *Inst.Phys.Conf.Ser. No.46*, pages 16–30, 1979.

[Wat80] G.D. Watkins and J.R. Troxell. Negative-U Properties for Point Defects in Silicon. *Physical Review Letters*, 44(9):593–596, 1980.

[Wat92] G. Watkins. *Deep Centers in Semiconductors*, chapter The Lattice Vacancy in Silicon, pages 177–213. Gordon and Breach Science Publishers S.A., Yverdon (CH), Philadelphia, Berlin, Paris, Amsterdam, Tokyo, second edition, 1992. ISBN 2-88124-562-5 (first edition published in 1986).

[Wat95] S.J. Watts, J. Matheson. Irradiation and DLTS studies on sample M101. *Brunel University (UK) Internal Note*, 1995.

[Wat96] S.J. Watts, J. Matheson, I. H. Hopkins-Bond, A. Holmes-Siedle, A. Mohammadzadeh, and R.Pace. A new model for generation-recombination in silicon depletion regions after neutron irradiation. *IEEE Transactions on Nuclear Science*, 43(6):2587, 1996.

[Wat98] S.J. Watts, M.Ahmed. DLTS studies of defect production in various Si substrates. *CERN/LEB 98-11, 4th ROSE Workshop*, 1998.

[Weg98] M. Wegrzecki, W.Slysz, S.Krzeminski, B.Jaroszewicz. PIN silicon structures processed at ITE. *Presented on the "4th ROSE Workshop on Radiation Hardening of Silicon Detectors", held at CERN, 2–4 December 1998, to be published as CERN–proceedings*, 1998.

[Weg99] 1999. Private communication with M.Wegrzecki, ITE-Poland (see [ITE]).

[Wei68] L.R. Weisberg and H.Schade. A Technique for Trap Determinations in Low-Resistivity Semiconductors. *J. Appl. Phys.*, 39(11):5149–5151, 1968.

[Wei88] S. Weiss and R.Kassing. Deep level transient Fourier spectroscopy (DLTFS)-A technique for the analysis of deep level properties. *Solid State Electronics*, 31(12):1733–1742, 1988.

[Wei91] S. Weiss. *Halbleiteruntersuchungen mit dem DLTFS– (Deep-Level Transient Fourier Spectroscopy–) Verfahren.* PhD thesis, University Kassel, January 1991.

[Wer98] P. Werner, H.-J.Gossmann, D.C.Jacobson, U.Gössele. Carbon diffusion in silicon. *Appl. Phys. Lett.*, 73(17):2465–2467, 1998.

[Wun91] R. Wunstorf, M.Benkert, E.Fretwurst, G.Lindström, T.Schulz, N.Croitoru, R.Darvas, M.Mudrik, R.Böttger, H.Schölermann. Radiation damage of silicon detectors by monoenergetic neutrons and electrons. *Nuclear Physics B (Proc. Suppl.) 23A*, pages 324–332, 1991.

[Wun92] R. Wunstorf. *Systematische Untersuchungen zur Strahlenresistenz von Silizium–Detektoren für die Verwendung in Hochenergiephysik-Experimenten.* PhD thesis, University of Hamburg, October 1992.

[Wun96] R. Wunstorf, H. Feick, E. Fretwurst, G. Lindström, G. Lutz, C. Osius, R.H. Richter, T. Rohe, A. Rolf, P. Schlichthärle. Damage-induced surface effects in silicon detectors. *Nucl. Instr. & Meth. in Physics Research*, A 377:290–297, 1996.

[Wun99] R. Wunstorf. Oxygenated Silicon for ATLAS Pixel Sensors. *CERN/LEB 99-8; ROSE Meeting, RD48, June 1999*, pages 275–289, 1999.

[Zha93] X.D. Zhan and G.D.Watkins. Electron parametic resonance of multistable interstitial-carbon–substitutional-group-V-atom pairs in silicon. *Physical Review B*, 47(11):6363–6380, 1993.

[Zio94] H.-J. Ziock et al. Temperature dependence of the radiation induced change of depletion voltage in silicon PIN detectors. *Nucl. Instr. & Meth. in Physics Research*, A 342:96–104, 1994.

[Žon99] D. Žontar, V.Cindro, G.Kramberger, M.Mikuž. Time development and flux dependence of neutron-irradiation induced defects in silicon pad detectors. *Nucl. Instr. & Meth. in Physics Research*, A 426:51–55, 1999.

Acknowledgements

First of all I like to express my thanks to Prof. Dr. Dr. h.c. Gunnar Lindström and Dr. Eckhart Fretwurst for supervising this thesis and their continuous support, advice and encouragement.

I am grateful to all members of the *Gruppe Nukleare Meßtechnik* for the good co-operation and the friendly and pleasant working atmosphere. Especially, I like to thank Prof. Dr. Robert Klanner for supporting me, Dr. Torsten Schulz for writing my first paper and Dr. Henning Feick for the competition in detecting defects, long lasting discussions about *Peak J* and of course for all the wonderful computer programs that made measurements and data analysis so easy. Furthermore, I am thankful to Uwe Pein, Peter Buhmann and Christa Nickel for supplying an infrastructure that I have so far not seen in any other institute including their tireless technical support and the measurement of hundreds of C/V and I/V curves. I like to thank Christian Schütze, Jörn Luckow, Parwin Heydarpoor, Uwe Bokelbrink, Carsten Dehn, Carsten Osius, Philipp Schlichthärle, Martin Kuhnke and all other diploma students who became *Diplom Physiker* during the time I worked on this thesis for the fun we had and the good team-work.

There are many people without whom this work would not have been possible. I like to thank all the people that provided irradiation facilities or irradiated samples. Among them my special thanks go to R.Böttger, H.J.Brede (PTB), Gianluigi Casse, Britta Dezillie, Maurice Glaser, Francois Lemeilleur, Arie Ruzin (CERN), Zheng Li (BNL), Marko Mikuž, Vlado Cindro (Ljubljana) and George Fanourakis (Demokritos). Moreover, I like to thank Angela Vasilescu (Bucharest) for the calculation of various hardness factors.
I am grateful to all material and device producers and especially to the people from MPI-Halbleiterlabor Munich for supplying test structures, to Bob Falster from MEMC for the production of the compensated Cz and to the people from ITE for the very fast processing of samples – here I also like to thank Maciej Wegrzecki for providing me with detailed information about the diode production process. Furthermore, I am indebted to Elzbieta Nossarzewska-Orlowska and Barbara Surma from ITME and Gordon Davies from King's College for material characterization.

I wish to thank all members of the ROSE collaboration for the interesting workshops and discussions and for continuously bringing up new ideas and models. In this context I must mention Steve Watts and Barry MacEvoy.

Finally, I like to thank Renate Wunstorf and Alexander Oh for helpful comments and Ioanna Pintilie for long lasting discussions about hole and electron traps.